Sask Polytech Library Moose Jaw
3 2293 000881733

CANMET

Canada Centre for Mineral and Energy Technology

Centre canadien de la technologie des minéraux et de l'énergie

Efficiency and Alternative Energy Technology Branch

Direction de la technologie de l'efficacité énergétique et des énergies de remplacement

627
TC
543
.D458
1992

Energy, Mines and Resources Canada

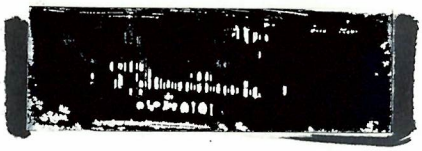
Énergie, Mines et Ressources Canada

Canada

THE ENERGY OF OUR RESOURCES - THE POWER OF OUR IDEAS

L'ÉNERGIE DE NOS RESSOURCES - NOTRE FORCE CRÉATRICE

543
.D458
1992



DESIGN OF LOW-COST FLOWTHROUGH ROCKFILL DAMS AND SPILLWAYS

PREPARED FOR:

Efficiency and Alternative Energy Technology Branch
Energy, Mines and Resources Canada
DSS File No. 55SZ.23283-7-6138
Ottawa, Ont.
April, 1990

PREPARED BY:

University of Ottawa
Department of Civil Engineering
161 Louis Pasteur
Ottawa, Ont. K1N 6N5

SIAST, PALLISER CAMPUS
LIBRARY
MOOSE JAW, SASK.

SCIENTIFIC AUTHORITY:

Tony Tung
Efficiency and Alternative Energy Technology Branch
Energy, Mines and Resources Canada
580 Booth Street
Ottawa, Ont. K1A 0E4

	DATE DUE		

SIAST
Palliser Campus

Learning Resources Centre
P.O. Box 1420
Moose Jaw, Saskatchewan
S6H 4R4

Phone: 694-3255

SIAST PALLISER CAMPUS
LIBRARY
MOOSE JAW, SASK

Citation

Garga, V.K., R. Townsend, D. Hansen, Department of Civil Engineering, University of Ottawa. *Design of Low-Cost Flowthrough Rockfill Dams and Spillways*. DSS Contract No. 55SZ.23283-7-6138. Efficiency and Alternative Energy Technology Branch, Energy, Mines and Resources Canada, Ottawa, Ontario. 1990 (317 pp.)

Copies of this report may be obtained through the following:

Efficiency and Alternative Energy Technology Branch
Energy, Mines and Resources Canada
580 Booth Street, 7th Floor
Ottawa, Ont.
K1A 0E4

or

Document Delivery Service
Library and Documentation Services Division
CANMET
Energy, Mines and Resources Canada
562 Booth Street
Ottawa, Ont.
K1A 0G1

Disclaimer

This report is distributed for informational purposes only and does not necessarily reflect the views of the Government of Canada nor constitute an endorsement of any commercial product or person. Neither Canada nor its ministers, officers, employees or agents makes any warranty in respect to this report or assumes any liability arising out of this report.

Note

Funding for this project was provided by the Federal Panel on Energy Research and Development, Energy, Mines and Resources Canada.

© Minister of Supply & Services Canada 1992
Catalogue No. M91-7/171-1992E
ISBN. 0-662-19577-9

Acknowledgements

The work described in this report was undertaken at the Department of Civil Engineering of the University of Ottawa by Mr. David Hansen, P.Eng. (Nfld.), under the supervision of Dr. Vinod K. Garga, P.Eng., and Dr. D. Ron Townsend, P.Eng. Assistance in experimental work at the University of Ottawa was provided by Vincent O'Shaughnessy, Victor Luk, and by the Technical Staff in the Machine Shop and the Hydraulics and Geotechnical Laboratories: Mr. Claude Lavigne, Mr. Robert Moore and Mr. Richard Moore. In connection with research performed at the Low Temperature Laboratory of the National Research Council, the assistance and cooperation of Dr. Bruce Pratt and Dr. Garry Timco are gratefully acknowledged. The excellent support of the technical staff at the National Research Council is also acknowledged, particularly that of Dr. Gordon Priest, Mr. Boyd Aitkin and Mr, Jeff Farnand. Finally, the project group wishes to express its appreciation for the continued interest and support of Mr. Tony Tung, Technology Coordinator, Hydraulic Energy Research and Development Program, Efficiency and Alternative Energy Technology Branch, Energy, Mines and Resources Canada.

Preface

This report consists of an investigation of the hydraulic and stability characteristics of flowthrough rockfill dams for low-cost small hydro projects. The study described in this report relates to the objective of Energy, Mines and Resources Canada to incorporate new technologies in the design of facilities to harness renewable sources of energy. Flowthrough rockfill dams are perceived to be an attractive alternative for the design of low head hydro schemes because they may reduce the costs of civil works for such projects. This report is intended for civil engineers involved in the design of low head hydro dams.

The information herein will have incidental usefulness in the characterization of the hydraulics of rock drains. Such drains are used in the open-pit mining industry.

Abstract

The hydraulic behaviour and stability characteristics of flowthrough rockfill dams was investigated in this study. The experimental investigations consisted of one dimensional flow studies in a packed column, and of two dimensional flow studies on model dams in three flumes, including a flume study at the low temperature laboratory of the National Research Council.

An investigation was made of the choice of non-Darcy flow equation, and on the estimation of the empirical parameters in such an equation. The overall hydraulic behaviour of flowthrough rockfill dams was characterized, including development of stage discharge curves and computation of the phreatic surface. Modifications to methods appearing in the literature are proposed. The stability of the downstream slope of flow through rockfill dams was investigated, including physical measurements of the force needed to prevent failure. A means of modelling non-Darcy pore pressures is presented. It was found that when non-Darcy pore pressures were used for rotational failure analyses the results of such analyses appear to be very conservative. It is suggested that the mechanism of failure assumed in methods such as Bishop's Simplified Method, namely, rotational failure along a limit-equilibrium slip circle, is often invalid for flowthrough rockfill dams. A new method of analysing the stability of flowthrough rockfill dams is presented. This method emphasizes the detailed consideration of seepage forces within two adjacent wedges.

A study of a model flowthrough embankment in the low temperature laboratory of the National Research Council of Canada, combined with a theoretical examination of the heat flux budget for flowthrough rockfill dams, indicated that flowthrough rockfill dams are not usually prone to significant changes in hydraulic capacity due to ice accretion.

DESIGN OF LOW-COST FLOWTHROUGH ROCKFILL DAMS AND SPILLWAYS

Hydraulic Energy Research and Development Program
Energy Mines and Resources Canada

CONTENTS

Acknowledgements i
Disclaimer i
Preface ii
Abstract iii
Contents iv
List of Figures vii
List of Tables xi
List of Appendices xii
Executive Summary xiii
Résumé xvi

1.0 INTRODUCTION 1

1.1 SCOPE 3

1.2 BASIC NOMENCLATURE USED FOR FLOWTHROUGH ROCKFILL DAMS 4

2.0 REVIEW OF PREVIOUS WORK 6

2.1 LITERATURE REVIEW 6

2.1.1 Research on non-Darcy Flow through Porous Media 6

2.1.1.1 Expressions describiong 1-D non-Darcy Flow 7
2.1.1.2 The Onset of Turbulence 15
2.1.1.3 The Wall Effect 18

2.1.2 Characterization of the Porous Media 18

2.1.3 Empirical Research on Model Rockfill Dams 21

2.1.3.1 The Research of Wilkins and Parkin 21
2.1.3.2 Location of the Phreatic Surface 28
2.1.3.3 Pore Pressure Modelling 34

2.1.4 Erosion of the Downstream Face 44

2.1.4.1 The Initiation of Motion Approach 47
2.1.4.2 Quantifying Shear Stress in Spatially Varied Flow 52
2.1.4.3 Quantifying Seepage Forces 54

2.1.5 Classical Slope Stability Analysis 55

2.1.6 Behaviour of Flowthrough Rockfill in Subzero Temperatures 60

2.2 CASE HISTORIES 64

2.2.1 Related References 73

3.0 EXPERIMENTAL PROGRAM 75

3.1 PACKED COLUMN TESTS 75

3.1.1 Apparatus 75

3.1.2 Methodology 75

3.1.3 Characterization of the Porous Media 77

3.1.3.1 Characterizing individual particles 78

3.1.3.2 Hydraulic mean radius 81

3.2 STUDIES IN GLASS-WALLED FLUME 83

3.3 STUDIES IN LARGE FLUME 88

3.4 LOW TEMPERATURE FLUME EXPERIMENTS 91

4.0 DESIGN CONSIDERATIONS I: INTERNAL FLOWS 96

4.1 DEVELOPMENT OF THE STAGE-DISCHARGE CURVE

4.1.1 Estimating of the Hydraulic Mean Radius 96

4.1.2 Parameter Estimation for the non-Darcy Flow Equation 100

4.1.3 Computing the Stage-Discharge Curve 104

4.1.3.1 The Case of No Impermeable Facing and No Tailwater 104

4.1.3.2 Rating Curve when Impermeable Facing Present 110

4.1.3.3 Effect of Tailwater on Rating Curve 113

4.2 POSITION OF THE PHREATIC SURFACE 113

4.2.1 Computing the Exit Height h_e 113

4.2.2 Computing the Phreatic Surface 121

5.0 DESIGN CONSIDERATIONS II: SLOPE STABILITY 135

5.1 EVALUATION OF POSSIBLE UNRAVELLING FAILURE 135

5.1.1 Erosion Potential of the Downstream Face 135

5.1.2 Discussion of the Summation of Particle Moments 165

5.2 EVALUATION OF POSSIBLE MASSIVE DEEP-SEATED FAILURE 169

5.2.1 Modelling of Pore Pressures for non-Darcy Flow 169

5.2.2 Analysis of Possible Rotational Failure 182

5.2.3 Description of Wedge Method & Comparison of Results 194

6.0 BEHAVIOUR IN SUB-ZERO TEMPERATURES 207

6.1 EXPERIMENTAL RESULTS 207

6.2 ESTIMATING ICE GROWTH AT THE PHREATIC SURFACE 210

6.3 HEAT EXCHANGE WITH THE ENVIRONMENT 216

6.4 CONCLUDING REMARKS 222

7.0 DESIGN GUIDELINES 224

8.0 SUMMARY AND CONCLUSIONS 229

9.0 REFERENCES 233

APPENDICES 243

List of Figures

FIGURE		PAGE
Figure 1-1.	Nomenclature used in this report for a flowthrough rockfill dam.	5
Figure 2-1.	Examples of friction-factor versus Reynolds number plots for flow through porous media.	8
Figure 2-2.	Zones of flow within a self-spillway flowthrough rockfill dam (after Parkin, 1963a).	25
Figure 2-3.	Comparison of Darcy and non-Darcy flow nets (after Wilkins, 1956).	35
Figure 2-4.	Finite difference stars for 5 point and 9 point schemes.	38
Figure 2-5.	Illustration of flowthrough occurring in a dam primarily designed for overflow.	
Figure 2-6.	Forces acting on a single particle located on the downstream face.	51
Figure 2-7.	Considerations in preventing failure.	58
Figure 2-8.	The San Ildefonso Dam in Mexico, described by Weiss (1951).	66
Figure 2-9.	Osceola rockfill spillway in Iowa, (Barr and Rosene 1958).	67
Figure 2-10.	Hellhole Dam in California before and after failure (after Leps, 1973).	69
Figure 2-11.	Cethana Dam in Tasmania, 1969.	71
Figure 2-12.	Cross-sections of rockfill dams constructed in Tasmania.	72
Figure 3-1.	Packed column apparatus.	76
Figure 3-2.	Material used in selected column tests.	79
Figure 3-3.	Characterization of particle shape.	80
Figure 3-4.	Nickel coating technique applied to crushed rock.	82
Figure 3-5.	Typical model dam in glass-walled flume.	84
Figure 3-6.	Rise in phreatic surface with increasing discharge.	86
Figure 3-7.	Nixon probe used for measuring velocity within the flow making up the seepage surface.	89

FIGURE		PAGE
Figure 3-8.	Model flowthrough rockfill dam in large flume.	90
Figure 3-9.	Force-measurement system in large flume.	92
Figure 3-10.	Arrangment of model dam and force-measurement system in large flume.	93
Figure 3-11.	Layout of flume experiment in the NRCC low-temperature laboratory.	94
Figure 4-1.	Comparison of mass-specific surface area results for crushed rock.	99
Figure 4-2.	Comparison of observed values of a in equation [2-3c] with values computed using Wilkins' (1956) equation.	102
Figure 4-3.	Comparison of observed and computed rating curves for tests GF27a and GF28a.	106
Figure 4-4.	Comparison of observed and computed rating curves for tests GF29d and GF30a.	107
Figure 4-5.	Comparison of observed and computed rating curves for tests GF31c and GF32a.	108
Figure 4-6.	Comparison of observed and computed rating curves for test FF17.	109
Figure 4-7.	Comparison of techniques for estimating the stage-discharge rating curves when an upstream impermeable facing (UIF) is present.	111
Figure 4-8.	Illustration of technique for estimating rating curve when tailwater present, tests GF29c and GF31d.	114
Figure 4-9.	Illustration of the concept of the angle of the emergent flow field.	117
Figure 4-10.	Comparison of observed and computed rating curves for the downstream face.	118
Figure 4-11.	Comparison of observed and computed rating curves for the downstream face.	119
Figure 4-12.	Observed and computed phreatic surfaces for GF29d.	126
Figure 4-13.	More observed and computed phreatic surfaces for GF29d.	127
Figure 4-14.	Observed and computed phreatic surfaces for GF31c.	128

FIGURE		PAGE
Figure 4-15.	More observed and computed phreatic surfaces for GF31c.	129
Figure 4-16.	Observed and computed phreatic surfaces for FF17d.	130
Figure 5-1.	Threshold discharge Q_T versus angle of the downstream toe θ; a test of Olivier's equation.	136
Figure 5-2.	Failed model dam in large flume.	137
Figure 5-3.	Schematic for seepage-surface definitions.	141
Figure 5-4.	Consideration of the Froude Number at the toe of the dam.	144
Figure 5-5.	Data of Sharp & James (1963) for a seepage wedge.	146
Figure 5-6.	Attempted simplifications in modelling the seepage wedge.	149
Figure 5-7.	Inferred variation in Manning's n for Sharp and James data.	152
Figure 5-8.	Variation in shear, emergent hydraulic gradient, and particle moment, beneath the seepage surface for GF29d	157
Figure 5-9.	Variation in shear, emergent hydraulic gradient, and particle moment, beneath seepage surface for a prototype.	158
Figure 5-10.	Variation in shear, emergent hydraulic gradient, and particle moment, beneath the seepage surface for GF31c.	159
Figure 5-11.	Finite difference stars for non-internal nodes.	173
Figure 5-12.	Configurations of model dams GF25 and GF26 showing piezometric tapping points.	175
Figure 5-13.	Comparison for computed and observed piezometric heads for model tests GF25 and GF26.	178
Figure 5-14.	Convergence characteristics of numerical simulation of piezometric heads for model tests GF25 and GF26.	181
Figure 5-15.	Slope stability for test GF29d.	188
Figure 5-16.	Slope stability for test GF31c.	189

FIGURE	PAGE
Figure 5-17. Slope stability for test FF18a.	190
Figure 5-18. Slope stability for test FF19b.	191
Figure 5-29. Slope stability for prototype with N=2.	192
Figure 5-20. Schematic diagrams pertaining to the wedge method.	196
Figure 5-21. Variation in P' for four model tests.	203
Figure 5-22. Reinforcement schemes implied by rotational and wedge failure analyses.	206
Figure 6-1. Temperature and piezometric data collection arrangements for model dam in the low temperature laboratory of the NRCC.	208
Figure 6-2. Observed temperatures in and above model dam for Test 1 in low temperature laboratory.	209
Figure 6-3. Observed temperatures in and above model dam for Test 2 in low temperature laboratory.	211
Figure 6-4. Ice growth for Tests 1 & 2 in low temperature laboratory.	212
Figure 6-5. Observed temperatures in and above model dam for Test 3 in low temperature laboratory.	213
Figure 6-6. Ice growth for Test 3 in low temperature laboratory.	214

List of Tables

TABLE		PAGE
Table 2-1.	Velocities needed for Fully-Developed Turbulence.	17
Table 2-2.	Estimates of the Wall Effect.	18
Table 2-3.	Historical Summary of Research on Flow Through Rockfill.	22
Table 2-4.	Influence of Particle Diameter and σ_3 on the Angle of Internal Friction.	56
Table 2-5.	Some Prototype Flowthrough Rockfill Dams/Spillways.	65
Table 3-1.	Tests in the Glass-walled Flume.	87
Table 4-1.	Comparison of Particle Surface Area Efficiencies.	98
Table 4-2.	Computed Coefficient a' in non-Darcy Flow Equations.	101
Table 4-3.	Four Cases of the Ratio H/d.	120
Table 4-4.	Values of Empirical non-Darcy Flow Parameters used in Phreatic Surface Calculations.	125
Table 5-1.	Comparison of Depth-at-toe Using Numerical Method (Eqn 5-9) and using Eqautions [5-4] and [5-5].	155
Table 5-2.	Summary of Estimated Positions of First Particle Turn-out.	165
Table 5-3.	Reynolds No. at h_e for Selected Dam Configurations.	169
Table 5-4.	Comparison of Observe Discharges with Finite Difference Modelling Results.	177
Table 5-5.	Observed and Computed Piezometric Heads.	179
Table 5-6.	Comparison of Convergence Characteristics.	180
Table 5-7.	Comparison of Actual and Theoretical Moments.	179
Table 5-8.	Comparison of Observed and Computed Bursting Forces at Incipient Failure.	201
Table 6-1.	Ice Growth for Low Temperature Flume Tests.	215

List of Appendices

APPENDIX		PAGE
1	Selected Data and Test Results.	244
2	Derivations Pertaining to Pore Pressure Determinations.	253
3	Appendices Pertaining to the Wedge Method.	261
4	Appendices Pertaining to the Phreatic Surface.	270
5	Appendices Pertaining to Unravelling Theory.	281
6	Worked Example: Analysis and Design of a Hypothetical Prototype.	288
7	Q-Budget Heat Flux Computer Program.	313
8	On Using a Spreadsheet for non-Darcy Pore Pressure Computations.	316

This report deals with the hydraulics and stability of "flowthrough" rockfill embankments. This class of embankments is unique in that, unlike ordinary earth embankments, the volume of water moving through the embankment is relatively large. This report provides new information in the following seven areas:

1. A multi-disciplinary consideration of most of the available equations describing one-dimensional non-Darcy flow. Such flow is characterized by a non-linear dependence of velocity on the rate of degradation of piezometric head with distance (the hydraulic gradient). The nature of this dependence is often expressed in terms of such factors as the porosity of the porous media and the size and shape of the individual particles making up this media. In the context of flowthrough rockfill embankments, the coefficient of variation for the selected empirical parameter (used as an indicator) was about 20%, with this variability decreasing to about 15% for prototype-sized particles. New data is also presented to assist in the evaluation of the effect of particle irregularity, as compared to perfect spheres.

2. A new computational method to estimate the quantity of flow moving through a rockfill embankment, as a function of the upstream water level, is presented. The general applicability of this method was developed from a parametric study on dams having a variety of configurations. The key equation derived from this parametric study can be used in conjunction with any power-function-form of non-Darcy flow equation.

3. If some minimum upstream water level is required, an impermeable element (in the form of a wall-like hydraulic barrier) will be needed. The hydraulics of an upstream impermeable facing (UIF) was studied in this research program. The hydraulics of the control section through the lip of the UIF exhibited unusual behaviour which could not be described by any single formula. However, the relative efficacy of a range of methods, both new and those presented by

previous researchers, is presented and discussed. Some guidance is also presented as to how to account for the effect of an elevated downstream water level on the stage-discharge rating curve of a flowthrough rockfill embankment.

4. Three distinct analytical methods for computing the position of the phreatic line are presented and evaluated. For a given amount of discharge passing through the dam, the phreatic line represents the internal division between the wet and dry portions of the dam. This phreatic line is of interest for two reasons. First, it is needed as a boundary condition to permit internal pore pressure modelling. Second, it may be used to develop a stage-discharge rating curve, which can be compared with that obtained using the more direct method mentioned in item (2) above. The validity of the Dupuit assumption, which is inherent in all three of the analytic methods, is also discussed. For non-prismatic river channels the engineer must resort to numeric, rather than analytic, expressions to compute the phreatic line, and the general approach for this class of problems is described.

5. A detailed computational framework is presented to make possible the prediction of the minimum elevation over which mesh protection is needed to prevent erosion of the downstream face of the dam. Computational methods are presented for evaluating the combined destabilizing effects of the spatially-varied overflow and the emergent seepage on individual 'loose' rock particles residing on the downstream face. These methods are relatively general and are valid irrespective of the size of the dam; however, further research is needed on the role of roughness and on making independent predictions of the depth of water at the toe of the dam.

6. As distinct from erosion of the downstream face (sometimes called unravelling failure), the possibility of massive deep-seated failure was investigated in detail. As a first step to permit such evaluations, non-Darcy pore-pressure modelling was performed. An efficient method for executing such modelling on an electronic spreadsheet is presented. Two types of massive failure were

considered. The first, based on classical rotational failure, was found to predict relatively deep-seated failures involving a relatively large fraction of the dam in question. This implied extensive and potentially expensive anchor reinforcement. The second, a wedge-type failure, generally implied mass-movement of considerably less material than did rotational failure. In an innovative series of experiments it was found that the *measured* bursting force at incipient failure was far closer to that theoretically predicted by the wedge method than that predicted by a classical rotational slip-circle method (Bishop's Simplified Method). The superiority of the wedge method was also qualitatively confirmed by laboratory observation of the relative amount of material mobilized, as compared to Bishop's Method. This wedge method emphasizes consideration of seepage forces, but can only be applied to cases in which the foundation beneath the dam is not part of the failure zone.

7. Most existing prototype-scale flowthrough rockfill dams and spillways have been constructed and operated in countries warmer than Canada, such as Mexico, Venezuela, and Australia. Prior to this report, the behaviour of this type of dam in sub-zero temperatures was therefore a matter of speculation. In another innovative series of experiments, this low-temperature behaviour was investigated using the Low Temperature Laboratory of the National Research Council of Canada. Based on this research a simple method for estimating the rate of growth of ice at the phreatic surface is presented. Ice was *not* observed to form in the voids within the body of the dam, except in one case in a small mixing zone (the base of Parkin's zone 3) below the lip of the UIF. A detailed theoretical framework for performing heat budget calculations is also presented, together with a short computer program to facilitate these calculations. It is quantitatively demonstrated that the viscous dissipation of hydraulic energy plays an important role in preventing ice formation in the voids.

Résumé

Au cours de ce travail, on a étudié le comportement hydraulique et les caractéristiques de stabilité des barrages en enrochements avec écoulement. La recherche expérimentale a consisté en des études d'écoulement unidimensionnel à travers une colonne solide. Des modèles de barrages à deux dimensions ont été placés dans trois bassins d'essais, dont une étude dans l'installation à basse température du Conseil National de Recherche du Canada.

On a d'abord effectué une recherche sur le choix d'une loi d'écoulement différente de celle de Darcy et sur la détermination des paramètres empiriques à introduire dans une telle équation. Le comportement hydraulique général des barrages en enrochement avec écoulement a été défini, y compris le tracé des courbes de débit par étapes et le calcul de la surface phréatique. On propose des modifications aux méthodes existant dans la littérature. La stabilité du parement aval a été étudiée, avec la mesure physique de la force nécessaire pour empêcher la rupture. On propose une méthode pour modéliser les pressions interstitielles n'obéissant pas à la loi de Darcy. On a trouvé que lorsqu'on utilisait de telles pressions dans les analyses de rupture circulaire, les résultats semblaient très conservateurs. On suggère que le mécanisme de rupture intervenant dans des méthodes comme celle de Bishop modifiée, à savoir une rupture circulaire le long d'un arc de glissement en équilibre limite, est souvent inexact pour les barrages en enrochement avec écoulement. On présente une nouvelle méthode d'analyse de la stabilité de tels ouvrages. Cette méthode considère de façon détaillée les forces d'écoulement entre deux tranches adjacentes.

Une étude d'un modèle de remblai avec écoulement dans le laboratoire à basse température du Conseil National de Recherche du Canada, combinée avec un examen théorique du bilan du flux calorifique pour les barrages en enrochement avec écoulement a démontré que ces ouvrages ne sont habituellement pas sujets à des changements significatifs de capacité hydraulique par effet d'accumulation de glace.

1.0 INTRODUCTION

This report describes the results of a study on the performance of model flowthrough spillway structures with a view to establishing criteria for the improved design of prototype structures. In most small hydro schemes, a dam is required to create adequate head and a spillway is required to safely pass flood flows. While the dam may be comprised of earth, rockfill, or concrete, the spillway is usually a concrete structure. The traditional forms of solid spillway include the overflow ("ogee"-profile) type, the shaft (closed conduit) type, and the siphon spillway. The cost of such structures is often a major component of the total cost of civil works, particularly in remote northern environments. Also, the durability of concrete in the harsh conditions of the northern Canadian environment is adversely affected. It is believed that in many instances the provision of a "flowthrough" rockfill spillway capable of handling the design return period flood event could lead to a significant reduction in the cost of small hydro schemes. This less common form of spillway, the "flowthrough" type, is shown in Figure 1. Here flow is allowed to percolate through and sometimes over a porous section of the embankment. In this instance the "spillway" is essentially uncontrolled, however a minimum reservoir storage level can be provided by means of either an impermeable partial-height facing on the dam's upstream slope, or an impermeable internal membrane. As J.G. Beale, a former Chairman of the Australian Water Research Foundation, has noted (Parkin 1963a):

"The development of the rockfill self-spillway dam, in which excess water passes through the dam itself, thereby dispensing with the need for an expensive spillway, is an exciting promise of reduced costs of major water conservation projects under conditions favouring this method."

Since the work of Wilkins (1956, 1963) and Parkin (1963a, 1963b, 1966, 1971) little practical work has been done in the area of flowthrough rockfill dams. These studies were motivated by a search for innovative designs for cofferdams, small hydro dams, and inexpensive water supply structures. The prototype rockfill dams arising from these studies had no provision for conventional outlet works such as concrete spillways (Davey 1960). Most of the work done in the past on flowthrough dams has been related to the

construction of such structures in warm climates. However, it is perceived that rockfill structures may be particularly well suited to remote northern environments where concrete spillways are more expensive to build and to maintain.

Small-scale hydro schemes are generally located to serve small communities in relatively remote locations. In the Canadian context such works would very likely serve locations which experience severe winter conditions. It is imperative therefore that the engineering design and construction be kept as simple and as maintenance free as possible. Currently most small-scale hydro projects involve small concrete dams, spillways, and diversion structures which have three limitations:

1. Concrete works invariably require considerable site preparation before they can be constructed. A major cost is the excavation to a hard subsoil strata on which the structure can be founded. This also limits the type of terrain on which such structures can be sited.

2. Concrete structures require considerable engineering design and construction skills and these are not readily available in many northern Canadian communities. Construction skills and equipment are usually "imported" to the area, thereby increasing design and construction costs.

3. The durability of concrete in harsh winter conditions is poor, and periodic maintenance is required. This is especially true of small hydro schemes in remote locations where rigourous control of the quality of the concrete mix and of general workmanship is either lacking or non-existent.

A low-head flowthrough rockfill dam alleviates many of the problems associated with concrete dams. In particular, the low-head rockfill dam requires very little site preparation and can be placed over many soil or rock conditions where the possibility of piping does not exist. The construction work can often be carried out by utilizing the resources available within many northern Canadian communities. Also, sound rockfill is highly resistant to freeze-thaw action. The rockfill dam is deformable and accommodates

the imposed stresses and strains. In contrast to concrete, a rockfill structure is not prone to cracking.

It is of interest to note that Gordon and Noel (1986) have estimated that the civil works of hydro projects ordinarily account for 60 percent of the cost of a project. They further suggest that, for construction of such civil works in northern Canada, a factor of 1.4 be applied to the cost estimate of the civil site works, making this component responsible for 68 percent of the total cost of the project. It may therefore be expected that the use of flowthrough rockfill dams in northern Canada could reduce the high cost of civil works for small hydro developments, particularly in the north and where sufficient quantities of sound, clean rockfill are readily available.

1.1 SCOPE

This report deals with the hydraulics and stability of flow through rockfill embankments. It does not deal with issues related to rock mechanics, such as interparticle contact stresses in rockfill and the long term settlement of rockfill embankments. Information on the design of impervious membranes at the prototype scale is also not discussed. A range of options is possible for the design of such membranes, including cast-in-place or roller-compacted concrete on the upstream face, an internal impervious clay core with appropriate filter protection, and for smaller projects the possible use of geotextiles.

Topics within the scope of this report emphasize characterizing the *hydraulics* and *stability* of flowthrough rockfill embankments, particularly with regard to *flow capacity*, *erosion of the downstream face*, and the possibility of *massive deep-seated failure* of such embankments. These aspects require consideration of the pore pressures within rockfill, which has pertinence both to unravelling failure of the downstream face and to deep-seated failure. At a fundamental level the rock particles themselves were examined in regards to their surface area per unit mass and how this may affect flow capacity. This report also examines the possible effects of subzero temperatures on flow through rockfill.

1.2 BASIC NOMENCLATURE USED FOR FLOWTHROUGH ROCKFILL DAMS

Figure 1-1 shows a flowthrough rockfill dam and identifies the nomenclature used in this report for dimensioning such structures. The upstream (reservoir) water level, the phreatic surface, and the seepage surface together constitute the free surface. The tailwater depth h_{TW} may or may not be governed by a downstream control. Some of the model dams studied in this report had no upstream impermeable facing, so that the vertical height of the upstream impermeable facing, h_F, is zero.

Although SI units are generally used in this report, some empirical equations are stated with their original numerical coefficients, which are unit dependent. In some cases the original numerical coefficient(s) has been retained so the equation is not in SI units.

h = upstream depth.

h_c = depth above top of facing.

h_F = height of upstream impermeable facing.

h_e = exit height.

H = height of dam.

h_{TW} = height of tailwater.

UIF = upstream impermeable facing.

L = length of dam.

b_e = distance from upstream toe to the vertical where h_e occurs.

b_{ed} = distance from point of seepage emergence to toe of dam.

B_U = width of upstream portion.

B_C = width of crest.

B_d = width of downstream slope.

B_W = base width.

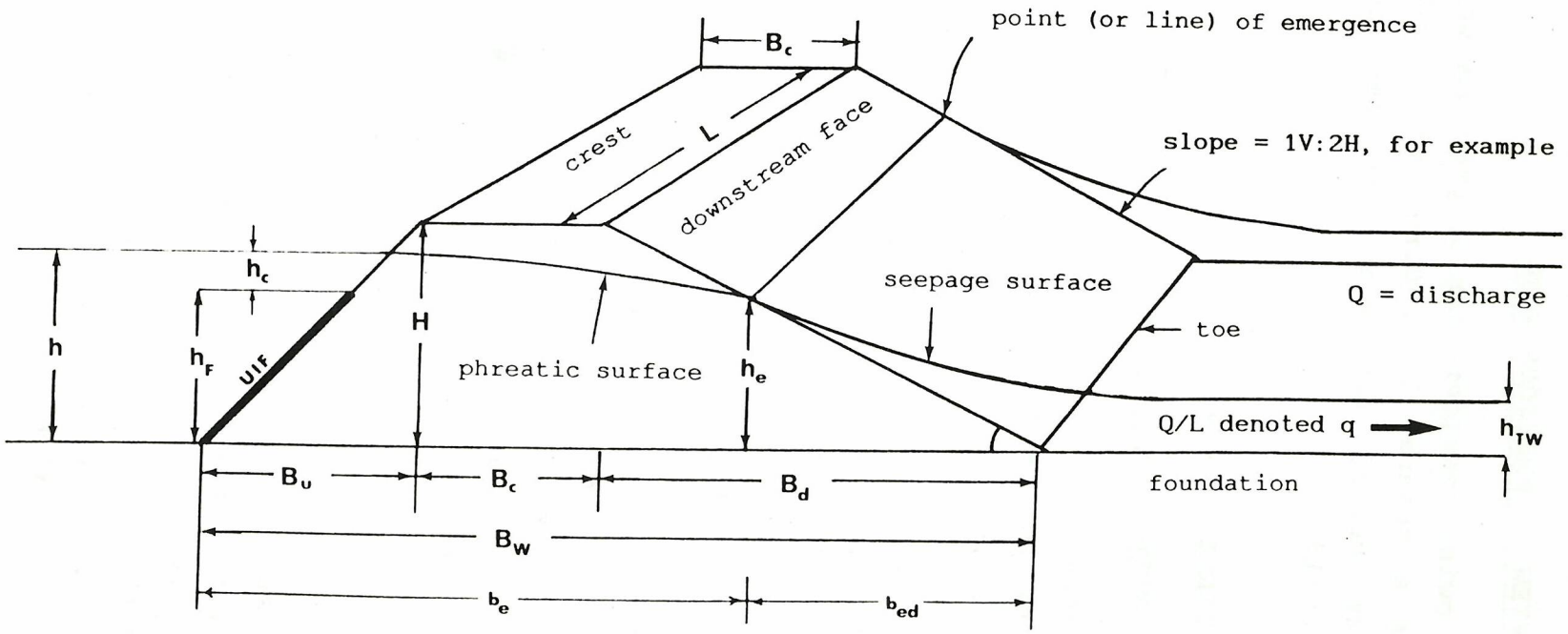


Figure 1-1. Nomenclature used in this report for a flowthrough rockfill dam.

2.0 REVIEW OF PREVIOUS WORK

The following consideration of previous work on flow through rockfill includes a general literature review and a review of some of the full-size rockfill dams which have been constructed in various parts of the world.

2.1 LITERATURE REVIEW

2.1.1 Research on non-Darcy Flow in Porous Media

The general research area of non-Darcy flow in porous media is important in the hydraulic design of flowthrough rockfill dams for two reasons:

1. Unlike conventional earth dams in which the goal is to keep the quantity of seepage relatively small, in flowthrough dams the quantity of seepage is substantial and intentional. The quantity of flow through a rockfill dam cannot be estimated without a reliable equation for non-Darcy flow.

2. In flowthrough dams the pore pressure pattern is important because downstream slope stabilization may be required if the point of emergence of the flow is relatively high on the downstream face. This point of emergence cannot be estimated without determination of the parameters in the non-Darcy seepage equation.

In this discussion non-Darcy flow refers to post-laminar non-linear flow. Two other types of non-Darcy flow exist which are not discussed in detail in this report; these are creeping flow (extremely slow movement of water) and laminar non-linear flow. There is a wealth of data and literature on the subject of non-linear flow through porous media because this subject is of interest within a number of disciplines, including civil, chemical, and mechanical engineering, as well as physics. Much attention has been focussed on the various regimes of flow (Basak 1977) and on explanations as to when and why these regimes occur (Sunada 1965,

Wright 1968). Experimental studies on non-Darcy flow are often referred to as "packed column tests" in which a constant flow permeameter is used to test relatively coarse and often angular materials, sometimes at high pressure.

The results of such studies are often summarized in dimensionless form, with a dimensionless friction factor as the ordinate and a Reynolds number as the abscissa. Unlike the definitions of friction factor and Reynolds number for pipe flow, these two dimensionless numbers do not have uniformly accepted definitions for flow through porous media. For example, porosity is sometimes included in either or both of these terms (Ergun 1952), and the Reynolds number may use either a measure of particle size or void size as the characteristic length, and may also include a shape factor or porosity. Examples of such work include that of Brownell and Katz (1947), Rose (1945a, 1945b, 1945c, 1948), Ergun (1952), Wright (1968), Ahmed and Sunada (1969), and Arbhabhirama and Dinoy (1973). McCorquodale *et al* (1978) drew together the experimental results of 1250 column tests in an effort to find a general correlation between his uniquely-defined friction factor and pore Reynolds number. A considerable amount of scatter was noted. Figure 2-1(a) and (b) present four examples of dimensionless plots for non-linear flow through porous media; other similar plots can be found in the literature.

2.1.1.1 Expressions describing one-dimensional non-Darcy Flow

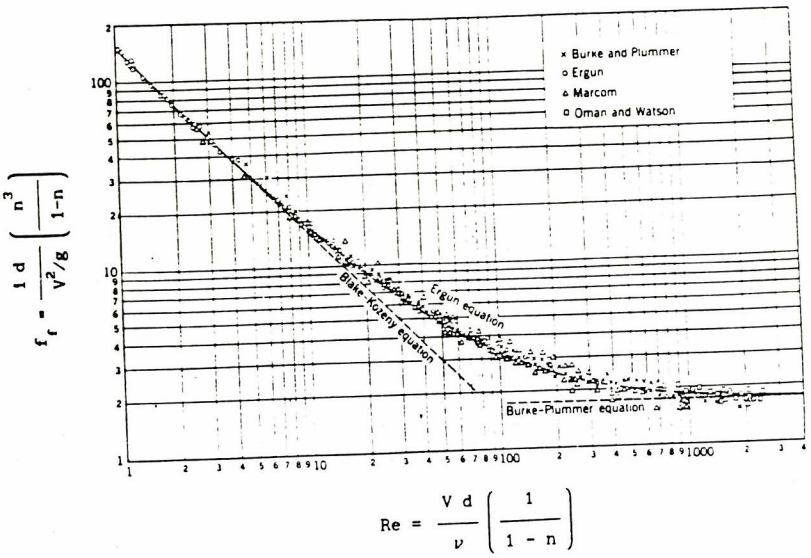
The following list presents the more well-known and widely used equations to describe non-Darcy flow through porous media:

Ergun (1952)
$$\frac{i\,d}{V^2/g}\left(\frac{n^3}{1-n}\right) = 150\left(\frac{1-n}{Re_p}\right) + 1.75 \qquad [2\text{-}1]$$

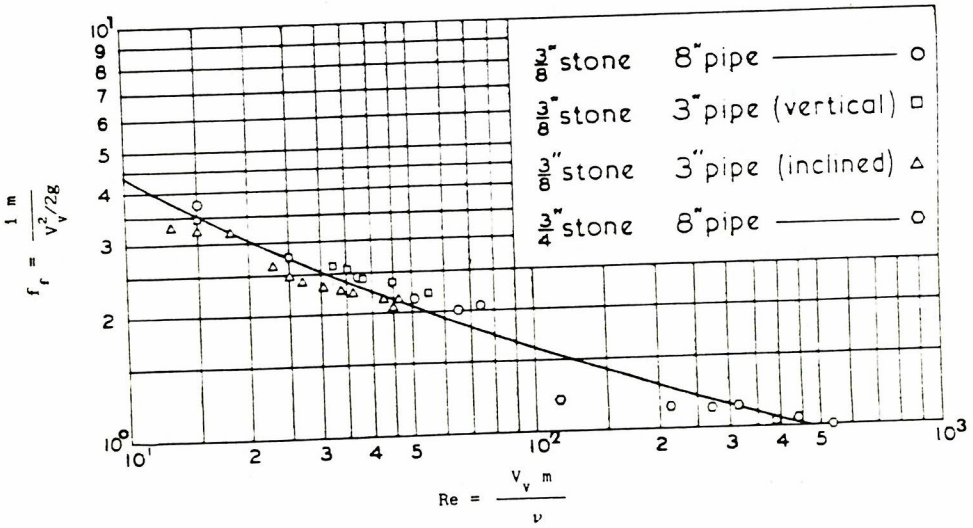
Wilkins (1956)
$$V_v = W\, m^{0.5}\, i^{0.54} \qquad [2\text{-}2]$$

General power-law form:
$$i = a\, V_v^N \qquad [2\text{-}3a]$$

or
$$V_v = a' i^{N'} \qquad [2\text{-}3b]$$

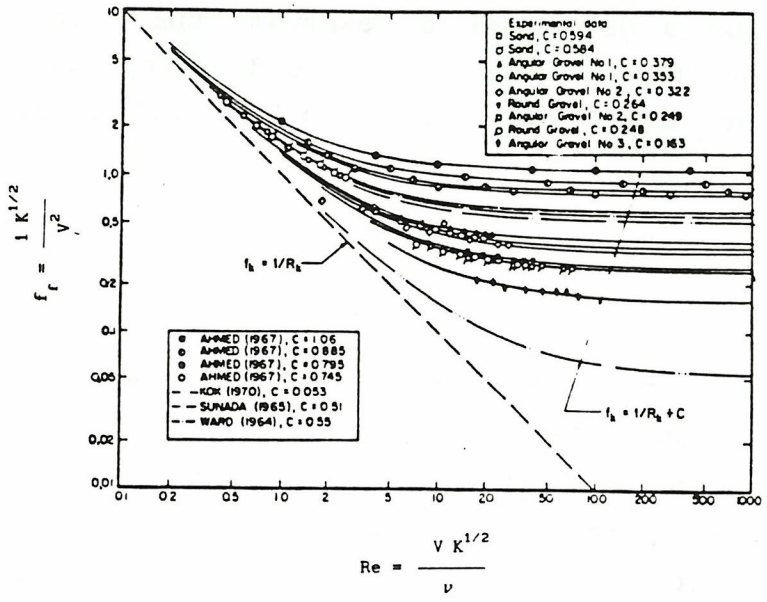


a) Ergun, 1952.

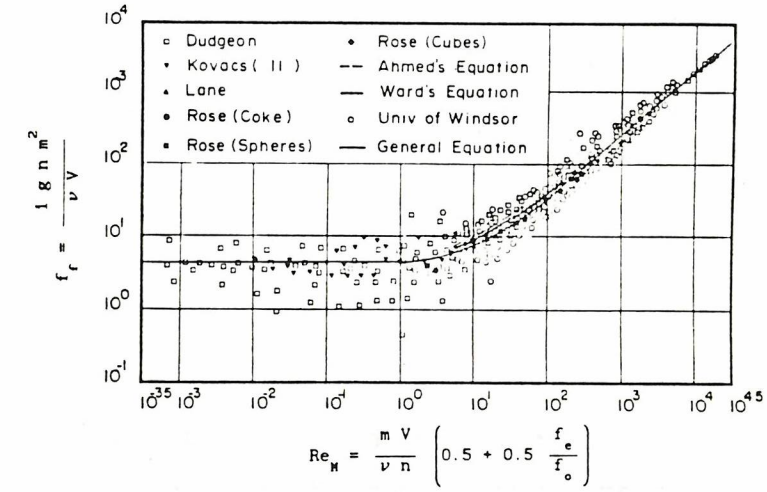


b) Parkin, 1963a.

Figure 2-1(a). Examples of friction-factor *versus* Reynolds Number plots for flow through porous media.



a) Arbhabhirama and Dinoy, 1973.



b) McCorquodale *et al*, 1978.

Figure 2-1(b). Further examples of friction-factor *versus* Reynolds Number plots for flow through porous media.

If a regression is performed on log(V) vs. log(i) rather than log(V_v) vs. log(i), for a given set of experimental data, Equations [2-3a] and [2-3b] (which are based on void velocity) are replaced by equations [2-3c] and [2-3d] (based on bulk velocity):

$$i = a\, V^N \qquad [2\text{-}3c]$$

$$\text{or} \quad V = a' i^{N'} \qquad [2\text{-}3d]$$

The role of porosity is then implicit in the empirical coefficients a and a' in equations [2-3c] and [2-3d]. However, the values of the exponents N and N' are not affected by whether bulk or void velocity is used when analysing a given set of experimental data to obtain a power-function form of the type given by [2-3]. To a given set of experimental data on non-Darcy flow, a quadratic form can usually be fitted equally well:

$$i = sV_v + tV_v^2 \qquad [2\text{-}4a]$$

$$\text{or} \quad V_v = s'i + t'i^{0.5} \qquad [2\text{-}4b]$$

In a manner analogous to the above discussion of the relationship between the pair of equations [2-3a] and [2-3b] and the pair of equations [2-3c] and [2-3d], the following equations are defined:

$$i = \alpha V + tV^2 \qquad [2\text{-}4c]$$

$$\text{or} \quad V = \alpha' i + t' i^{0.5} \qquad [2\text{-}4d]$$

Although the first mention of both the power-law and the quadratic forms to describe non-Darcy flow is that of Prony (1804) (see Jaeger 1956, p.397), the quadratic law to describe non-Darcy flow is sometimes referred to as Forchiemer's Law (Forchiemer 1901). Both the power law form and the quadratic form were later used and popularized (in the context of rockfill embankments) by Parkin (1963a, 1971, respectively).

Other equations include:

Ward (1964):

$$i = \frac{\mu}{k} V + \frac{0.55\rho}{k^{1/2}} V^2 \qquad [2\text{-}5]$$

McCorquodale *et al* (1978): $f = 70 + 0.54\ \Upsilon\ Re_M$ [2-6a]

where: $$\Upsilon = \left(0.5 + 0.5\ \frac{f_e}{f_o} \right) \qquad [2\text{-}6b]$$

and: $$f = \frac{i\ g\ n\ m^2}{\nu\ V} \qquad [2\text{-}6c]$$

$$Re_M = \frac{m\ V\ n^{0.5}}{\nu} \qquad [2\text{-}6d]$$

Dinoy (1971) rearranged (see also Arbhabhirama and Dinoy 1973):

$$i = \frac{\nu}{gk} V + \left(\frac{100\ k^{1/4}}{g\ d^{3/2} n^{3/4}} \right) V^2 \qquad [2\text{-}7]$$

Stephenson (1979) rearranged:

$$V_v = \sqrt{\frac{gdi}{K_s}} \qquad [2\text{-}8]$$

Ergun-Reichelt (see Fand & Thinakaran 1990):

$$i = 212\ \frac{M\nu}{gd^2} \cdot \frac{(1-n)^2}{n^3} V + 1.57\ \frac{M}{gd}\ \frac{(1-n)}{n^3}\ V^2 \qquad [2\text{-}9a]$$

where: $$M = 1 + \frac{2}{3} \cdot \frac{d}{D(1-n)} \qquad [2\text{-}9b]$$

for packed spheres (not rocks). However, the above equation is included because it has the advantage of incorporating a wall-effect factor, M.

Martins (1990):

$$V_v = \frac{K_M}{C_U^{\alpha}} \sqrt{2gedi} \qquad [2\text{-}10]$$

where $C_U = d_{60}/d_{10}$

The suggested form for this report (for the case of fully-developed turbulence) is:

$$V_v = K\sqrt{gedi} \qquad [2\text{-}11]$$

The following list defines the terms used in equations [2-1] through [2-11]:

i = hydraulic gradient,

W = material-dependent coefficient, reported as 32.9 when inch-sec units are used,

a, a', α, α', s, s', t, t', Δ, Δ', t, t' = empirical constants,

C_U = Martins' uniformity coefficient,

d = representative particle diameter,

d_{60}, d_{10} = particle diameter such that 60% (or 10%) is finer,

D = diameter of permeameter,

f = friction factor,

f_e = effective Darcy-Weisbach friction factor for rock and permeameter,

f_o = Darcy friction-Weisbach factor of a hydraulically smooth surface at the same Reynolds number (from a pipe-flow Moody diagram),

k = intrinsic permeability associated with non-Darcy flow,

K_M = Martins' empirical coefficient,

K_S = Stephenson's empirical coefficient,

K = empirical coefficient in [2-11], the proposed form,

m = hydraulic mean radius, a measure of pore size,

n = porosity,

N = empirical constant indicating flow regime, commonly reported to be 1.86. Note that (1/1.86) = 0.54,

N′ = 1/N,

Re_p = particle Reynolds number in [2-1], = Vd/ν,

Re_M = modified Reynolds number, as per [2-6d],

V = bulk velocity, Q/A,
V_v = void velocity, = (V/porosity),
α = empirical exponent for C_u (Martins 1990),
ρ = density of the fluid,
μ = absolute viscosity of the fluid.

Equations [2-1], [2-6] and [2-9] represent efforts to generalize large bodies of data into a single unified equation. These large data sets included the results of researchers other than those to whom the final equation is attributed. Equations [2-7] and [2-10] are the result of somewhat less extensive testing over a moderate range of materials, and include little or no data from other sources. Equations [2-2] and [2-8] represent still less general expressions in that they were developed from crushed rock of a relatively narrow size-range and of a given angularity.

Equation [2-1] can be rearranged to the form of equation [2-4c], which is more useful in the context of this report:

$$i = \left(\frac{1-n}{n^3}\right)\left[\frac{150\nu(1-n)}{g\,d^2}V + \frac{1.75}{g\,d}V^2\right] \qquad [2\text{-}12]$$

Equation [2-1], which was developed in the context of chemical engineering, has no reported restrictions (Sissom and Pitts 1972). Equation [2-6] applies only when $(Vm/n\nu) > 500$. Equation [2-6] can also be rearranged to the form of equation [2-4c]:

$$i = \left(\frac{70\,\nu}{g\,n\,m^2}\right)V + \left(\frac{0.54\,\Upsilon}{g\,n^{0.5}m}\right)V^2 \qquad [2\text{-}13]$$

According to McCorquodale (pers.com. 1990) the value of Υ is approximately 1.5 for crushed rock. McCorquodale's data was corrected for the wall effect, unlike most other analyses. Using

forms [2-3c] or [2-3d] it is possible to sketch a flow net (Wilkins 1956) or use the empirical parameters in [2-3c] or [2-4c] in conjunction with a numerical method (such as the finite differnce or finite element method) for predicting pore pressures inside a rockfill dam (Curtis and Lawson 1967, Volker 1969).

Equation [2-5], due to Ward (1964), is simple in form but of little apparent practical usefulness since no method of evaluating k from knowledge of material properties, such as the hydraulic mean radius, was suggested by Ward. The same can be said for equation [2-7].

Although Wilkins and Parkin both reported a value of about 1.86 for the exponent on V (compare [2-2] inverted to [2-3a] with Parkin's result of 1.86 for N in [2-3a]), this actually depends on the flow regime and on the nature of the porous media in the packed column (Dudgeon 1964). As full turbulence is approached, N approaches its limiting value of 2, whereas the value of N for laminar flow is 1. Therefore, in this report, equations such as Wilkins' will be referred to as "single regime" equations, in that they theoretically apply to only one level of turbulence. Accordingly, while it is mathematically possible to compute a velocity using Wilkins equation for laminar flow through sand by inserting the value of m for sand, the velocity so computed will be unreliable because Wilkins' equation cannot be applied to laminar flow conditions. This is in contrast to equations [2-1], [2-6], and [2-9], which adjust the parameters Δ and t such that the correct flow regime is automatically implied. Basak's (1977) review of non-linear flow laws indicated that the value of 1.86 for N in [2-3c] varies little, but that the coefficient a was dependent on the porous media. The value of a was not found to be clearly related to either nominal particle diameter or porosity however. In contrast, Nirandra (1973) found experimentally that:

$$t = \frac{0.28}{d^{1.41}} \qquad [2\text{-}14]$$

where:
t = empirical coefficient in [2-5] (m-sec units),
d = particle diameter (m).

Nirandra (1973) found no such simple relation between the parameter Δ in equation [2-4c] and particle diameter. If [2-14] is combined with [2-4c] using $\Delta = 0$, the resulting equation is also a single regime equation - this regime being fully-developed turbulence.

Equation [2-11], the suggested form for fully developed turbulence in this report, has the following advantages:

1) it is easy to remember.
2) it can be shown by algebraic rearrangement that the coefficient on $i^{1/2}$ corresponds to the t coefficient (equation 2-4b) for the quadratic form of such established equations as the Ergun equation [2-1], as it should.
3) it results in greater mathematical convenience within the derivation of the expression for the phreatic line when using gradually varied flow theory (GVFT), as will be seen in section 4.2.2 and in Appendix 4-1.
4) it is similar in form to two other equations for fully-developed turbulence, those of Stephenson (1979) and Martins (1990).
5) the coefficient K is independent of the system of units, unlike Wilkins' (1956) equation and certain others.
6) if the hydraulic mean radius m is to be computed, K can be readily related to m if necessary (as will be discussed in Section 4.1.1).

2.1.1.2 The Onset of Turbulence

The advantages of plotting experimental data in dimensionless form are that it helps to generalize the results and to indicate the onset of fully-developed turbulence, in the same way that for pipe flow the friction factor becomes independent of the Reynolds number when turbulence becomes fully-developed. The proliferation of diagrams of this type is probably due in part to the relatively large amount of scatter usually present and to the lack of standard definitions for the friction factor and Reynolds number. Scheidegger (1974) states that the highest reported Reynolds number

which must be exceeded before fully-developed turbulence begins is about 750, and this concurs fairly well with the data presented in Figure 2-1. The value of 10,000 reported by Jain *et al* (1988) seems to be completely unrealistic. Detailed explanations of the meaning of each dimensionless term in Figure 2-1 are not presented. Figure 2-1 illustrates that:

(a) a considerable amount of data exists relating to non-Darcy flow in porous media,

(b) established definitions of friction factor and Reynolds number do not exist, unlike the Moody diagram for pipe flow,

(c) the results can be disparate; i.e. should one curve suffice (Ergun 1952, McCorquodale *et al* 1978), or are many curves required (Arbhabhirama and Dinoy 1973, Niranjan 1973)?

McCorquodale *et al* (1978) used the pore Reynolds number to examine the onset of turbulence using data from 1250 column tests. It was found that flow could be considered fully turbulent when Re_p was greater than 500. The pore Reynolds number was defined as:

$$Re_p = \frac{V\ m}{\nu\ n} \qquad [2\text{-}15]$$

where:
V = bulk velocity,
m = effective hydraulic mean radius
("effective" implying no wall effect),
ν = kinematic viscosity, n = porosity.

Table 2-1 gives the velocities necessary to achieve fully-developed turbulence for various values of hydraulic mean radius:

Table 2-1

Velocities needed for Fully-Developed Turbulence

For $Re_{CRITICAL} = (Vd)/(\nu n) = 500$

kinematic viscosity $\nu = 1.003 \cdot 10^{-6}$ m^2/s
porosity n = 0.45

Hydraulic Mean Radius	Minimum Velocity (m/s)
1 mm	0.2260
1 cm	0.0226
10 cm	0.0023
1 m	0.0002

Table 2-1 indicates the approximate velocities needed to achieve full turbulence. Wright (1968) and Sunada (1964) sought to describe the fluid processes taking place in a porous media as the velocity of flow increases toward fully-developed turbulence. The existence of the "steady inertial" and "turbulent transition" regimes (Wright 1968) for flow in porous media do not generally exist in pipe flow. For the "steady inertial" regime the convective accelerations in the flow are important and cause the relationship between hydraulic gradient and velocity to be non-linear. These convective accelerations, caused by the tortuosity of the flow paths, suppress full turbulence in this regime. At higher velocities the "turbulent transition" regime begins, in which random micro-velocity fluctuations occur. These micro-velocity fluctuations cannot be measured directly without relatively sophisticated equipment. In this regime the hydraulic gradient is proportional to nearly the square of the velocity.

The nature of the particles making up a porous media can affect the shape of the curve describing the transition from laminar to turbulent flow. Rose (1945b) presented parallel curves on a Moody-type diagram for materials of increasing angularity. Crawford and Plumb (1986) observed a similar parallel shift in friction factor-Reynolds number curves as particles increased in angularity.

Brownell and Katz (1947) and Brownell *et al* (1950), seeking as others have done to find a suitable redefinition of the Reynolds number which could be universally applied to porous media, found that porosity was the most important parameter affecting resistance to flow, with particle sphericity and angularity of secondary importance.

2.1.1.3 The Wall Effect

The term "wall effect" refers to the fact that the flow in a packed column test tends to be more rapid in the annular zone immediately adjacent to the wall of the permeameter than in the porous media itself. Most investigators do not account for the wall effect in the analysis of their results. The wall effect refers to the fact that higher velocities exist near the wall because the porosity is higher adjacent to the wall (Dudgeon 1967). This higher porosity is due to the absence of interlocking particles at the face of the container. The result is unrealistically high bulk velocities. Table 2-2 summarizes various published estimates of the error introduced by the confinement of a cylindrical container:

Table 2-2

Estimates of the Wall Effect

Rose (1945)	D/d = 10	about 6% error
Franzini (1956)	D/d > 40	negligible error
Dudgeon (1967)	D/d = 35	about 7% error
Somerton and Wood (1988)	D/d = 200	negligible error
Fand and Thinakaran (1990)	D/d > 40	negligible error

D = diameter of the container,

d = representative particle diameter.

2.1.2 Characterization of the Porous Media

Careful characterization of the porous media is important because the nature of the media greatly affects the hydraulic properties of the media. Beard and Weyl (1973) investigated the effects of

texture on the porosity and hydraulic conductivity of beach sands for the laminar flow regime. They demonstrated that well-graded sands had lower porosities and lower hydraulic conductivities than uniformly-sized sands. Hydraulic conductivity was found to decrease with a decrease in the median grain size of the sand. Both of these observations are intuitively correct. However, little quantitative information could be found in the literature directly relating gradation and hydraulic behaviour for flow beyond the laminar regime.

The hydraulic mean radius is a measure of the diameter of an average pore within a porous media. This parameter has been found to be useful in the study of seepage characteristics of granular materials (Wilkins 1956, Olivier 1967, McCorquodale *et al* 1978, Jain *et al* 1988). Since the fluid flows through these pores the hydraulic mean radius would appear to be the most rational choice for the characteristic length in the Reynolds number, as is done by McCorquodale *et al* (1978). Since gradation implies filling of the voids with smaller rock, and angularity affects the mass-specific surface area, the hydraulic mean radius can be expected to have built into it such factors as particle gradation and angularity. Taylor (1948) defined the hydraulic mean radius, m, as:

$$m = \frac{\mathcal{V}_v}{S_A}; \qquad \text{units: L} \qquad [2\text{-}16]$$

where:

$\mathcal{V}_v$ = volume of voids within a control volume containing a porous media,

S_A = surface area of voids having total volume $\mathcal{V}_v$.

The value of the intrinsic permeability k of a given porous media is unaffected by the fluid passing through the media and is a media-dependent property. The parameter k may be defined as:

$$k = \frac{\nu}{g} K \qquad [2\text{-}17]$$

where:

ν = kinematic viscosity, $[L^2/T]$,

g = gravitational constant, $[L/T^2]$,

K = hydraulic conductivity, $[L/T]$.

The intrinsic permeability k of a porous media has units of L^2. It is interesting to note that the Ward Reynolds number (McCorquodale *et al* 1978, Ward 1964) for flow through porous media uses the square root of the intrinsic permeability for the characteristic length, implying that hydraulic mean radius (with units L) is a key physical parameter in characterizing such flows. The value of m can also be calculated from:

$$m = \frac{\mathcal{V}_B\, n}{A_{MS} M_R} \qquad [2\text{-}18]$$

or:

$$m = \frac{e}{A_{VS}} \qquad [2\text{-}19]$$

where:

$\mathcal{V}_B$ = control volume (bulk volume), containing porous media,

n = porosity,

e = void ratio,

A_{MS} = mass-specific surface area, (surface area per unit rock mass),

A_{VS} = volume-specific surface area, (the surface area per unit volume of rock),

M_R = mass of rock.

The mass-specific and volume-specific surface areas are related as follows:

$$A_{VS} = \rho\, A_{MS} \qquad [2\text{-}20]$$

where ρ is the density of rock.

It is evident therefore that a means of determining the surface area of irregularly-shaped rock particles is required. The determination of surface area would enable the evaluation of the hydraulic mean

radius, m. It should be noted however that equations [2-18], [2-19] and [2-20] assume that the surface area of the pores within a given volume of porous media is the same as the surface area of the particles in that media. This will be a poor assumption for plate-like rocks such as shales because of the relatively large amount of surface area lost to interparticle contact. For porous media made up of such rocks a significant amount of the particle area would not contribute to the fluid shear perimeter within the voids.

Relatively little published information is available on the measurement of the surface area of crushed rock particles. Most methods cited in the literature refer to those developed for use in powder technology (such as gas adsorption, quantitative stereology, and indirect evaluation by measurement of air permeability; Scheidegger 1974, Bessy and Soul 1954, Dullien 1979). Hedlin and Collins (1961) sought to quantify the surface area of grain seeds and coated the seeds first with ordinary varnish and then with powdered nickel. The difference in weight before and after coating was then a measure of the surface area. Other investigators have attempted using plasticene (Sandie 1962) and dye (Alger and Simons 1968), with varying degrees of success.

2.1.3 EMPIRICAL RESEARCH ON MODEL FLOWTHROUGH ROCKFILL DAMS

Table 2-3 presents a brief history of research on flow through rockfill. In the following sections those contributions of a general nature pertaining to hydraulic capacity and the phreatic surface (based on research on model dams) will be discussed.

2.1.3.1 The Research of Wilkins and Parkin

Prior to the work of Wilkins (1956), engineers designing flowthrough rockfill dams apparently did so without any hydraulic design methodology. The unavailability of hydraulic design methods was due to the non-Darcy nature of flow in coarse rockfill. The proposal to

Table 2-3

Historical Summary of Research on Flow Through Rockfill

Researcher	Description of Work
Weiss 1951	Documented construction and performance of rockfill spillways in Mexico.
Escande 1953	Tests on rectangular model dams, 3.5 cm rock. Equation for "a" knowing phreatic surface and assuming N = 2.
Cohen de Lara 1956 (in french)	Tailwater effects on quantity of discharge and stability.
Wilkins 1956	Developed widely accepted equation [2-2] using hydraulic mean radius. Non-Darcy flow net.
Wilkins 1963	Stability analysis using Bishop's method. Suggestions for reinforcement.
Parkin 1963a	A partial differential equation for non-Darcy; flow zones of flow when inbuilt spillway present.
Sharp & James 1962	Analysis of spatially varied flow.
Curtis & Lawson 1967	Finite difference modelling of pore pressures.
Dudgeon 1964, 67	Column tests on 15 cm rock; estimated wall effect.
Olivier 1967	Overflow equation for threshold discharge for gradual slopes. Very similar to Schoklitsch eqn.
Sarkaria 1968	Tests on reinforced model dam at Froude scale.
Volker 1969 McCorquodale 1970	Concurrently developed FEM coding for computing discharge, free surface, and pore pressures.
Parkin 1971	Used FEM pore pressures with Bishop's method to estimate location of reinforcement.
Stephenson 1978,79	Dimensionless phreatic surfaces, textbook on Rockfill in Hydraulic Engineering.
Gerodetti 1981	Model dam tests with full-height central impermeable core. Gabions on downstream face found to be inadequate.
Jain *et al* 1988	Model tests to determine total head loss when no impermeable facing present; "variable gradient method" for computing phreatic surface and approximate flow net.
Martins 1990	Packed column tests on a variety of materials; investigated effect of gradation of the media.

construct the Laughing Jack and Wayatina B rockfill dams in Tasmania initiated Wilkins' research under the auspices of the Tasmanian Hydroelectric Authourity. Experiments were performed in packed columns and on a 0.61 m (2 feet) high model dam in a flume. For most of the experiments crushed dolerite was used as the porous media. Ordinary glass marbles were also used in a packed column test to examine in a limited manner the effect of angularity on head loss. Three equations resulted:

$$V_v = 32.9\ m^{0.5} i^{0.54} \quad \text{(for crushed stone in a packed column)} \qquad [2\text{-}21]$$

$$V_v = 46.5\ m^{0.5} i^{0.54} \quad \text{(for marbles in a packed column)} \qquad [2\text{-}22]$$

$$V_v = 42.0\ m^{0.5} i^{0.54} \quad \text{(for crushed stone in a flume)} \qquad [2\text{-}23]$$

where:

V_v = void velocity, $Q/(A \cdot n)$, in the porous media (inches/sec),

i = hydraulic gradient,

m = hydraulic mean radius (inches).

Wilkins' main contributions can be considered to be as follows:

1. Use of a simplified form of equation [2-2] to construct "turbulent" flow nets. This contribution was later applied by Gerodetti (1981) to model rockfill embankments.

2. The modes of failure of rockfill dams, also confirmed by Sandie (1962). For relatively steep downstream slopes the primary mode of failure was found to be progressive sloughing of the downstream face. If the downstream face was anchored and a sufficient head was applied, a secondary mode of failure was found to be a massive deep-seated circular slippage or sliding, near the foundation.

3. Based on his qualitative observations on types of failure, Wilkins suggested means of anchoring large rockfill dams to ensure their stability and, in later research (1963), presented anchor schemes based on slip-circle stability analyses.

Parkin's early research (1963a, 1963b) at the University of

Melbourne in Australia was generally in good agreement with Wilkins' results. His experiments were done both with packed columns and with a model dam in a flume 1.2 m wide. The various model dams tested had a sloping internal impervious wall set parallel to the upstream face, but not reaching the crest. Parkin stated his non-Darcy flow equation (for nominal 3/4 inch aggregate) as:

$$i = 0.0351\ V_v^{1.86} \qquad [2\text{-}24]$$

where V is in ft/sec (see p.77 of Parkin 1963a).

The exponent 1.86 in the above equation compares well with that found by other investigators (see Basak 1977).

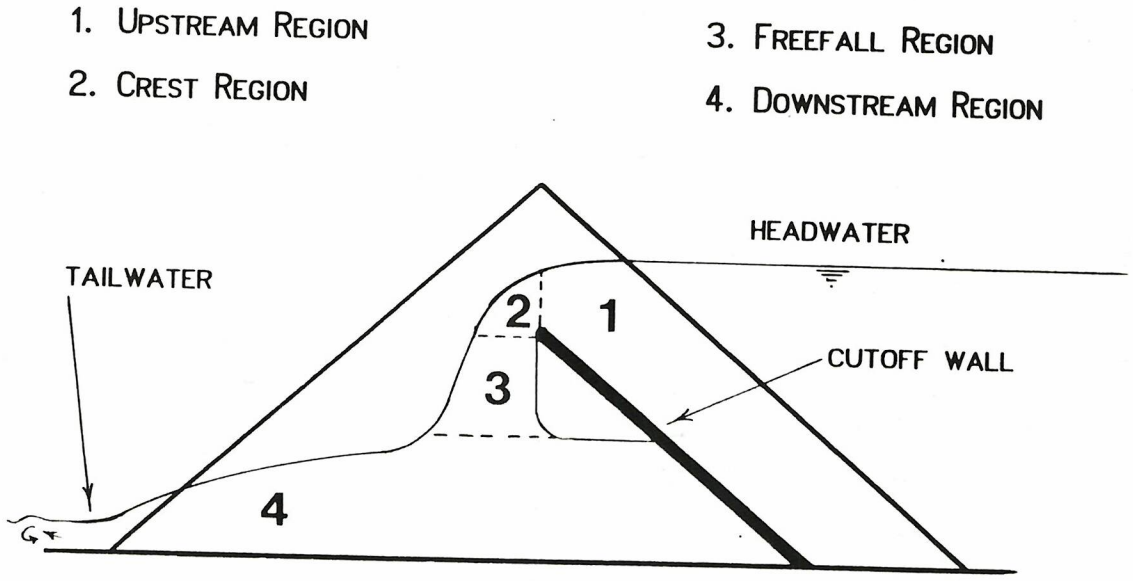
Parkin's main contributions are as follows:

1. The delineation of four zones of flow within rockfill dams having inbuilt spillways of the type described above. These four zones are shown schematically in Figure 2-2.

2. The identification of the two key points of hydraulic control in a rockfill dam with an inbuilt spillway. These are the depth over the inbuilt spillway, h_F, and the height above tailwater of the highest point of emergence of seepage on the downstream face, h_e. Parkin (1963a) also found that if the height of the inbuilt spillway is low relative to the height of the dam, the height of the point of emergence on the downstream face begins to be affected by the depth of water over the crest of the inbuilt spillway.

3. The presentation of a method of directly calculating the discharge through the dam.

4. The incorporation of equation [2-24], in vectorial form, into the Laplacian continuity equation which resulted in a partial differential equation for "turbulent" flow in porous media. This equation would later be successfully used by Curtis and Lawson (1967) to arrive at numerical solutions to describe 'turbulent' flow in porous media.



REGIONS OF FLOW IN A SELF-SPILLWAY DAM

Figure 2-2. Zones of flow within a self-spillway flowthrough rockfill dam (after Parkin, 1963a).

SIAST, PALLISER CAMPUS
LIBRARY
MOOSE JAW, SASK.

Parkin's two reports for the Water Research Foundation of Australia (1963a, 1963b) are significant in that they most closely approach a design manual for flowthrough rockfill dams. Parkin's (1963) work can be summarized as being largely an extension and verification of the work of Wilkins, again for rock of nearly uniform gradation and of a particular angularity and size.

Parkin identified two quantities of particular importance in design. These are h_c, the height of water over the upstream impermeable facing resulting from a given discharge, and h_e, the exit depth. The following is a description of Parkin's (1963a) method for computing these two quantities.

Parkin *et al* (1966) found that the discharge through the rockfill occurring over an internal impervious element was linearly proportional to the head. Thus, the stage-discharge curve for the model flowthrough rockfill dams he studied showed no curvature, unlike the stage-discharge curves of rivers or weirs. The stage-discharge curve establishes the relationship between the upstream water level and the quantity of flow passing through and over the dam. This curve is important because the designer needs to know the discharge which can be expected to pass through and over the dam for a given upstream head. The stage-discharge curve also significantly alters the outflow hydrograph (Findikakis and Tu 1985) because the dam represents a hydraulic control section in the river.

Parkin (1963a) found that the hydraulic gradient over the crest of an inbuilt spillway was 0.82 for 3/4 inch crushed rock, and felt that this would also be a good first approximation for prototypes. This gradient is then substituted in the governing flow equation:

$$0.82 = a\, V_v^N \qquad [2\text{-}25]$$

For a given porosity the bulk velocity, V, can be determined from [2-25], knowing *a* and N. The crest head h_c can then be determined

LIBRARY

from:

$$Q = V\ h_c\ L \qquad [2\text{-}26]$$

where:

Q = desired flood capacity,

L = width of the spillway (see Figure 1-1),

h_c = crest head; the height of water above the impermeable element.

Equations [2-25] and [2-26] may apply only when an impermeable facing is present, and seem to represent a simplistic approach because V is assumed to be a single-valued material-dependent quantity which does not change with depth. The computed discharge depends on the values of *a* and N. The value of *a* will depend on the material used. Parkin *et al* (1966) presented a nomogram to assist in estimating the value of *a* from porosity and the mean surface area per unit volume of the particles, but suggested that the values of *a* and N should be determined experimentally when approaching a design problem. In view of the fact that the variability of *a* is far greater than the variability of N, it would appear that, for design purposes, it is relatively more important to determine *a*.

Parkin (1963a) concluded that if the tailwater level is below the point of emergence on the seepage face it had practically no effect on the height of the point of emergence, which was determined using the following formula:

$$h_e = \frac{q}{n}\left[\frac{a}{\sin\theta}\right]^{(1/N)} \qquad [2\text{-}27]$$

where:

q = unit-width discharge, Q/L,

θ = angle of downstream toe,

a & N from equation [2-3a],

h_e = exit height on downstream face, relative to the foundation.

Equation [2-27] can be obtained by applying either equation [2-3a] or [2-3b] at the vertical cross section where flow emerges, knowing that

$q = V_v \cdot n \cdot h_e$ for a rectangular section. It applies whether or not an impervious facing is present and assumes that the hydraulic gradient through h_e is $\sin\theta$. Equation [2-27] can be restated in the form of a rating curve (without using Parkin's approximation that $\sin\theta = \tan\theta$):

$$Q = h_e L\, a' (\tan\theta)^{1/N} \qquad [2\text{-}28]$$

This in effect makes the simplistic assumption that the bulk velocity moving through the dam is single-valued, so that the discharge varies solely because h_e varies. The development of equation [2-28] also assumes that the slope of the water surface profile on the downstream face is equal to the slope of the downstream face of the dam.

Cohen de Lara (1956) examined the effect of tailwater on the quantity of flow passing through a model dam. He developed relationships for computing the discharge for trapezoidal sections and for rectangular sections, and used a limited range of particle sizes.

2.1.3.2 Location of the Phreatic Surface

The profile of the phreatic surface in a rockfill dam is of interest for two reasons:

1. The exit height indicates the amount of the downstream face that will be submerged at a given discharge. If, for the maximum discharge of interest, the computed value of h_e is small, this implies a short seepage face and hence less potential for erosion.

2. The shape of the phreatic surface provides one of the boundary conditions needed to model internal pore pressures. Knowing the position of the phreatic surface simplifies the computation of pore pressures. For most numerical methods used to compute pore pressures it is more efficient to know beforehand the location of the phreatic surface than to use a trial and error procedure within the finite difference or finite element coding. Knowledge of pore

pressures also permits calculation of the hydraulic gradients, which are needed to compute seepage forces acting on the downstream face.

Although gradually varied flow theory (GVFT) is normally applied to flow in open channels, it seems to have been first proposed by Wilkins (1956) as a means of modelling the profile of the phreatic surface within a rockfill embankment. This method was later tested by Parkin (1963a) to calculate the position of the phreatic surface within several model rockfill embankments. Stephenson (1979) presented the result of an analytical integration of the governing ordinary differential equation for GVFT in a rectangular channel, and presented a comparison between observed and computed phreatic surfaces for rectangular embankments in a flume. Stephenson's (1979) analytical equation only applies to fully-developed turbulence and proposes that at critical depth (which was redefined for porous media), the flow emerges from the embankment on the downstream face (h_e in Figure 1-1).

The method of application of the theory of gradually varied flow depends to some extent on the geometry of the channel; that is, whether prismatic or irregular in cross section. For prismatic channels the direct step method is usually applied, for non-prismatic channels the standard step method is applied. These methods of numerically integrating the governing differential equation (to be stated below) are described in many texts on open channel flow (for example see chapters 9 to 11 of Chow 1959). Many of the assumptions associated with the theoretical development behind gradually varied flow theory also apply to flow through porous media. It is assumed, for example, that the pressure distribution at a given vertical is hydrostatic. To the extent that this is not true, the water levels computed by GVFT will be erroneous. An example where the pressure distribution is not hydrostatic is the case of flow near a brink (classical M2 profile). Directly above and adjacent to a brink the streamlines are curved enough that the pressure at the bed is less than hydrostatic. This M2 "drawdown" profile is the profile of interest for flow through

rockfill embankments, and the same computational difficulty may be expected for steep exit gradients. Another assumption inherent in GVFT is that in order to compute the friction slope (rate of change of depth plus velocity head) a rearranged form of the equation for *uniform* flow (for which friction slope *equals* bed slope) in open channels is considered valid, even though it is known that the friction slope differs from the bed slope. The most commonly uniform flow equation (in North America) is Manning's equation.

In applying GVFT to rockfill dams, Wilkins (1956) used equation [2-3a] instead of Manning's equation when computing the friction slope. For drawdown curves of the type seen within flowthrough rockfill embankments (or near a brink for open channel flow) direct step method computations proceed in an upstream direction, and the upstream distance associated with each increment of depth is computed. The starting depth h_e must be known beforehand.

The ordinary differential equation for steady gradually varied flow in open channels is:

$$\frac{dy}{dx} = \frac{S_o - S_f}{1 + \alpha \frac{d}{dy}\left(\frac{V^2}{2g}\right)} \qquad [2\text{-}29]$$

where:

dy/dx = rate of change in local vertical depth with distance along the bed,

S_o = bed slope, equal to zero for the glass flume tests,

S_f = friction slope,

α = energy correction coefficient, typically 1.1 to 1.2 for turbulent flow,

$V^2/2g$ = velocity head, based on the average velocity, V = Q/A.

In order to determine the water surface profile for gradually varied

flow in an open channel, equation [2-29] can be numerically integrated. The expression used in the direct step method (after Chow 1959) is:

$$\Delta x = \frac{\left(y_2 + \alpha_2 \frac{V_{v2}^2}{2g} \right) - \left(y_1 + \alpha_1 \frac{V_{v1}^2}{2g} \right)}{S_o - S_f} \qquad [2\text{-}30]$$

Equation [2-30] only applies to prismatic channels, in which the cross sectional shape is the same at all cross sections.

Under the direct step method, a difference in depth Δy between two cross sections (denoted by subscripts 1 and 2) is assumed. The distance between the two sections, Δx, is unknown and is computed from equation [2-30]. This is done iteratively for a number of sections upstream (or downstream) of the section of where the depth and velocity are known *a priori*. It is noted that if an impervious facing is present, the procedure ceases to apply when the freefall zone is encountered. It is also very important to note that V_v is being used to compute the velocity head $V_v^2/2g$. This is intuitively correct since V_v (which is V/n) is *representative* of the velocity of the flow in the pores (Freeze and Cherry 1979), and will yield a higher velocity head than $V^2/2g$ (where V is the bulk velocity) since $V_v > V$.

Parkin (1963a) tested the GVF method and found fair agreement between observed and computed phreatic surfaces for three cases. The only modification suggested by Wilkins (1956) and Parkin (1963a) was the replacement of the expression for friction slope in an open channel with the expression for the "friction slope" for flow through a porous media. Stephenson (1979) also found good agreement between observed and computed phreatic surfaces using his analytical expression (no numerical integration required).

The friction slope in the context of open channel flow is generally found from rearranging either the Manning or Chézy equation. In the context of non-Darcy flow through porous media, Stephenson (1979) has

suggested using a power-law (a rearranged form of equation 2-8) to evaluate the friction slope. This assumption can be written as:

$$S_f = i = aV_v^N \qquad [2\text{-}31]$$

where:

i = hydraulic gradient (dimensionless),

a = empirically determined coefficient,

N = empirically determined exponent, equal to 2 for fully-developed turbulence.

Equation [2-31] (and equations of this form) are for unidirectional flow and are generally determined in an apparatus having no phreatic surface. If the rate of change of piezometric head with distance at the phreatic surface (at a given point along that surface) is used to approximate i, this is known as the Dupuit assumption, and is known to be a good approximation of the true hydraulic gradient (at a given vertical) as long as the phreatic surface is not steep (Harr 1962).

Basak (1976) applied to Dupuit assumption and simply integrated a non-Darcy flow equation of the following form:

$$i = \alpha V + t V^2 \qquad [2\text{-}4c]$$

The kinetic energy of the flow was not considered (unlike application of GVFT). In spite of this Basak obtained good agreement between the resulting equation and Volker's (1975) phreatic surface data (which was obtained from studies on a rectangular embankment made up of small diameter angular gravel).

The "variable gradient method" of Jain et al (1988) is a computational procedure based on Wilkins' equation [2-2], and it proceeds in an upstream direction. It can also be used to generate a rough flow net consisting of a series of straight lines. Unfortunately it requires *a priori* knowledge of the upstream water level, greatly reducing its usefulness.

Solvik (1966) has suggested the following equation:

$$x = L\left[1 - \frac{1 - \left(\frac{y}{H}\right)^3}{(1+0.36P^2)^2}\right] \qquad [2\text{-}32]$$

where:

x = distance upstream from the downstream toe,

P = (H/L) cotanθ,

L = total distance from toe to upstream entry point,

H = height of upstream entry point above foundation,

θ = angle of toe (Figure 1-1).

It is difficult to see how this equation can be of practical use when no terms are included to account for the hydraulic characteristics of the porous media, as contained in Wilkins', Stephenson's, Jain's, and Basak's methods. In addition, the value of L in [2-32] is generally not known beforehand. Solvik's equation assumes full turbulence and, like the Escande (1953) equation for rectangular embankments, contains a third order polynomial in y. It is interesting to note that equations to predict the phreatic surface for laminar flow (Casagrande 1932) are second-order polynomials.

Escande (1953) examined the phreatic surface using 3.5 cm rocks and developed an empirical equation for rectangular embankments subject to fully turbulent flow. Other techniques exist for predicting the phreatic surface for non-Darcy flow, many of them associated with the influx into a vertical drilled well or a horizontal drain (Volker 1975, Basak 1976, Sên 1989, Mustafa and Rafindadi, 1989). Stephenson (1978) has given dimensionless phreatic surface plots, but only for rectangular embankments. Kleiner (1985) presented a trial and error technique which can be used in the context of finite difference modelling on a cell-by-cell basis, but this method is very laborious and is therefore not tractable for the design engineer.

2.1.3.3 Pore Pressure Modelling

Pore pressures and the associated hydraulic gradients have been the subject of considerable study because high exit gradients contribute to slope instability and because knowledge of pore pressures permits the investigator to perform classical rotational failure analysis. Methods for computing pore pressures can be categorized into three approaches:

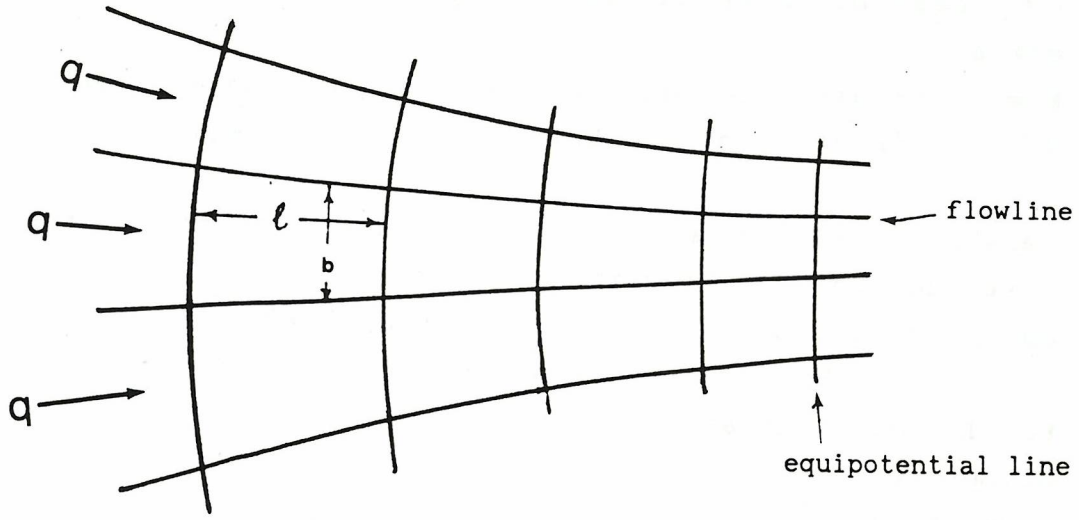
(i) sketching a non-Darcy flow net.

As with laminar flow nets, much can be learned quantitatively and qualitatively from the two-dimensional flow net of a dam. First, the quantity of seepage can be estimated if the parameters in the governing flow equation (such as equation [2-3]) are known. Second, the pore pressures within the dam can be estimated for any location. This is particularly important when considering the stability of the downstream slope of the structure. Third, an approximation can be made as to the location of the highest point where water emerges from the downstream face. This indicates the region on the downstream face for which anchorage is most important.

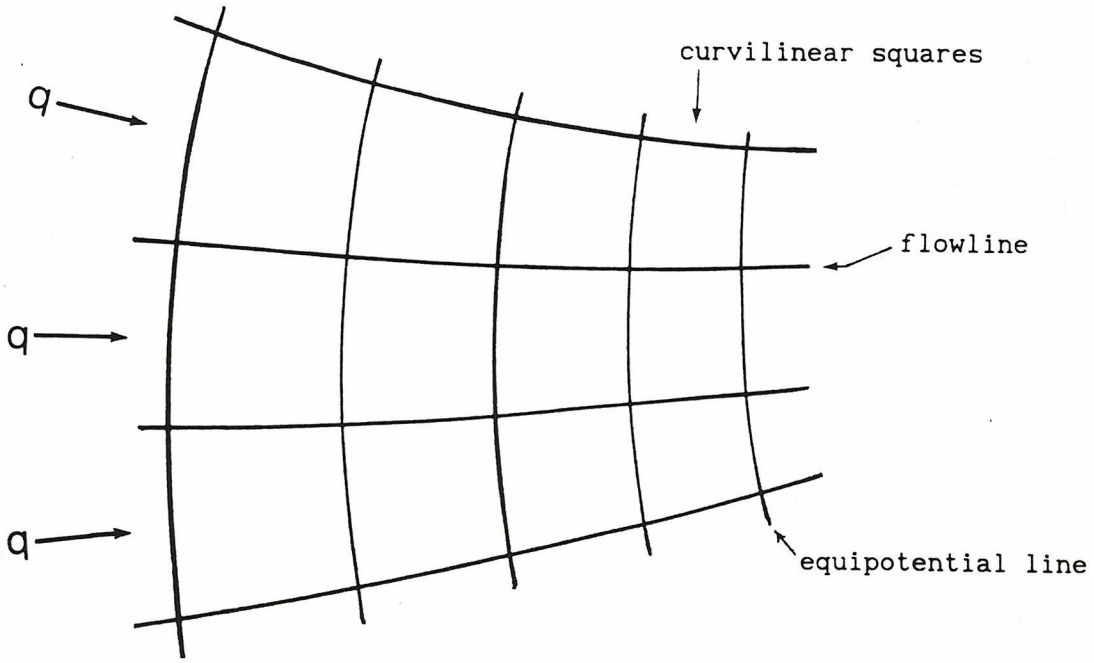
Figure 2-3 illustrates, for a homogeneous isotropic porous media, the difference between an ordinary Darcy flow net and a "turbulent" flow net. A well-known characteristic of ordinary laminar flownets is that each panel or element in the mesh is square-like, with the mean distance between flowlines (denoted b in equation [2-33] following) being equal to the mean distance between equipotential lines (denoted ℓ in equation [2-33]) for a given individual element. This is not the case for non-laminar flow. For Darcy (laminar) flownets it is known that N=1, whereas N>1 for flow beyond the laminar regime.

According to Wilkins (1956) and Parkin (1963a) a non-Darcy flow net can be sketched using the relation:

$$\ell = b^N \qquad [2\text{-}33]$$



a) non-Darcy flow net for isotropic homogeneous porous media.



b) Darcy flow net for isotropic homogeneous porous media.

Figure 2-3. Comparison of Darcy and non-Darcy flow nets (after Wilkins, 1956).

where:

ℓ = mean distance between equipotential lines within a given mesh element,

b = mean distance between flow lines within a given mesh element,

N = empirical exponent defined in eqn [2-3a].

Relation [2-33] means that for a given hydraulic gradient the mean distance between flowlines is less than the mean distance between equipotential lines for any individual element in a non Darcy flow net mesh. Decreasing the mean distance between flowlines relative to the mean distance between equipotential lines implies a greater number of flow paths. The greater number of flow paths is consistent with a greater total quantity of seepage for the semi-turbulent nature of the flow. Since N is typically 1.85, it would appear that the value of b in equation [2-33] cannot be less than unity, otherwise the above principle regarding the distances between flowlines and equipotential lines will not hold.

According to Parkin (1971), the elements in a turbulent flow net ..."change their geometry with increasing velocity while maintaining orthogonality". This would make sketching difficult. However, a flow net, once obtained, can be used to determine the pore pressure at any point in the dam using the standard interpolation technique (Cedergren 1977).

(ii) finite difference methods.

It is well known that when Darcy's law is valid, the elliptic partial differential equation known as the Laplacian is the governing equation which describes the variation in piezometric head for a given set of steady-state boundary conditions. In two -dimensional Cartesian coordinates, and for a homogeneous isotropic media, the Laplacian is:

$$\frac{\partial^2 h}{\partial x^2} + \frac{\partial^2 h}{\partial y^2} = 0 \qquad [2\text{-}34]$$

where h denotes piezometric head.

It can be readily shown (Freeze and Cherry 1979) that for a homogeneous isotropic porous media, the following five-point finite difference (FD) expression is valid for an internal node if Darcy's law applies:

$$h_c = (h_1 + h_3 + h_5 + h_7)/4 \qquad [2\text{-}35]$$

where:

h_c denotes the central node,

h_n denotes surrounding nodes (see Figure 2-4).

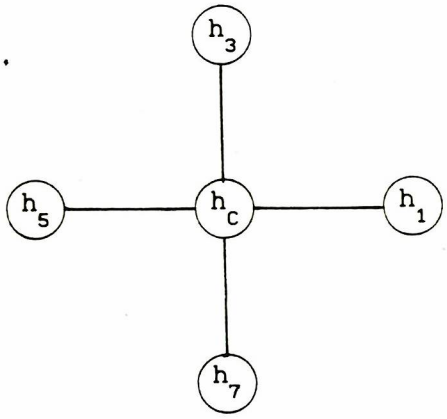
If a more refined FD scheme is desired, the corresponding nine-point case for an internal node is given by (Southwell 1946):

$$h_c = \left(4h_1 + h_2 + 4h_3 + h_4 + 4h_5 + h_6 + 4h_7 + h_8\right)/ 20 \qquad [2\text{-}36a]$$

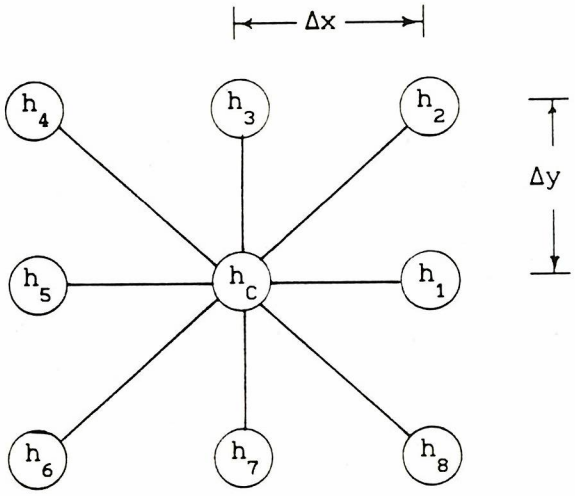
The FD diagrams in Figure 2-4 may be referred to as a "finite difference stars" (Freeze and Cherry 1979). The technique of applying these FD expressions came to be known as relaxation methods (Southwell 1946, Allen 1954), and various refinements are available for special boundaries. These include the phreatic surface, regular and irregular impermeable boundaries, and boundaries residing at an angle and having an applied piezometric head. As an example, the expression for a node next to an impermeable boundary is:

$$h_c = \left(4h_1 + 2h_2 + 8h_3 + 2h_4 + 4h_5\right)/ 20 \qquad [2\text{-}36b]$$

Two finite difference methods for non-Darcy flow are known to the authors, that of Curtis and Lawson (1967) and that of Kirkham (1967). The following partial differential equation, developed by Parkin (1963a) for non-Darcy flow, was obtained by substituting the vector form of equation [2-3b] into the continuity equation:



$$h_c = \frac{1}{4}\left[h_1 + h_3 + h_5 + h_7 \right]$$



$$h_c = \frac{1}{20}\left[4h_1 + h_2 + 4h_3 + h_4 + 4h_5 + h_6 + 4h_7 + h_8 \right]$$

Figure 2-4. Finite difference stars for 5 point and 9 point schemes.

$$\left[\frac{\partial^2\phi}{\partial x^2}+\frac{\partial^2\phi}{\partial y^2}\right]\cdot\left[\left(\frac{\partial\phi}{\partial x}\right)^2+\left(\frac{\partial\phi}{\partial y}\right)^2\right]+$$

$$(N'-1)\left[\left(\frac{\partial\phi}{\partial x}\right)^2\frac{\partial^2\phi}{\partial x^2}-2\frac{\partial\phi}{\partial x}\frac{\partial\phi}{\partial y}\frac{\partial\phi}{\partial x\partial y}+\left(\frac{\partial\phi}{\partial y}\right)^2\frac{\partial^2\phi}{\partial y^2}\right]=0 \qquad [2\text{-}37]$$

where ϕ is the scalar potential (equal to the piezometric head for an isotropic homogeneous rockfill) and N′ is defined in equation [2-3b].

Curtis and Lawson (1967) developed a finite difference form of equation [2-37] in which a nine-point FD star was used as the basis for approximating the hydraulic gradients in various directions. The mathematics involved is described by the above-named authors, and will not be repeated here. The resulting FD expression is:

$$h_c = T1\cdot(h_1 + h_3 + h_5 + h_7) + T2\cdot T3 \qquad [2\text{-}38a]$$

where:

$$T1 = \frac{1}{2(N'+1)} \qquad [2\text{-}38b]$$

$$T2 = \frac{(N'-1)}{2(N'+1)} \qquad [2\text{-}38c]$$

$$T3=\left[\frac{(h_1+h_5)(h_1-h_5)^2+0.5(h_1-h_5)(h_3-h_7)(h_2+h_6-h_4-h_8)+(h_3+h_7)(h_3-h_7)^2}{(h_1-h_5)^2+(h_3-h_7)^2}\right] \qquad [2\text{-}38d]$$

where:

h_n = piezometric head at a nodal point n,

N′ = empirical exponent from [2-3b] or [2-3d].

Since the value of N (equation 2-3a or 2-3c) is between 1 and 2 (2 indicating complete turbulence), the value of N′ (equation 2-3b or 2-3d) is between 1 and 0.5. Equation [2-38] has the expected property that, as N′ approaches its upper bound of unity, it becomes identical to the case of Darcy flow given by equation [2-35]. Term

T3 in equation [2-37d] generally represents a positive quantity. As N increases from unity to 2, the value of T2 decreases from zero to -1/6. This is consistent with the fact that as N approaches 2, turbulent head losses occur. It can therefore be inferred that changing the value of N will change the shape of a flow net for a given configuration of dam under given boundary conditions. This is in contrast to flow nets associated with Darcy's law in which the shape of the flow net is always the same for a given configuration of dam and set of boundary conditions.

No expressions have appeared in the literature for non-internal nodes associated with the non-Darcy flow case given by equation [2-38]. There are three other categories of nodal expressions used in the modelling of piezometric pressure heads in a homogeneous isotropic rockfill embankment. These are:

Case 1. nodes next to an impermeable boundary.
Case 2. nodes next to the phreatic surface.
Case 3. nodes on a non-45° slope next to an applied head.

An important application of the partial differential equation developed by Parkin (1963a) was demonstrated by Curtis and Lawson (1967). In their study equation [2-38] was used to predict lines of equal pressure within a low rockfill bank having no inbuilt spillway. This rockfill bank of 3/8 inch basalt particles was built in a glass-sided flume which was instrumented with piezometer tapping points at regular intervals on the floor beneath the model embankment. The horizontal profile of water over the bank was measured with a carriage-mounted vernier point gauge. The turbulent flowlines within the structure were observed by injecting flourescein dye at various points on the upstream face. In this way the flow net predicted using the numerical solution to the partial differential equation for "turbulent" flow could be compared with an observed flow net in the rockfill.

Unfortunately three factors limit the wider applicability of the

results of the study by Curtis and Lawson to the analysis of predominantly flowthrough rockfill dams. First, an unusual geometry for the embankment was used. The model embankment in this case was 25 cm high, 1.8 m long, 1.2 m wide, and had vertical upstream and downstream faces. Second, flowthrough was only 5 to 10 percent of the total flow, making this more of a specialized overflow study. Third, no phreatic surface existed within the model dam used. The pressure of the overflowing water was used as a boundary condition for the numerical solution of the partial differential equation. Nonetheless, this study presents a viable experimental and analytical methodology for the study of flowthrough rockfill dams, and could be duplicated using flow conditions and a dam geometry more suitable to consideration of small hydro schemes.

Unfortunately Curtis and Lawson (1967) did not present a quantitative comparison of observed and computed pore pressures for their experimental work but stated that conditions satisfying equation [2-38] had been achieved for a rectangular embankment. In a very brief discussion of Curtis and Lawson (1967), Kirkham (1968) argued that N does not have a fixed value for the entire flow field. This appears to be a debatable point. In his doctoral thesis Kirkham (1967) presented an alternative equation to [2-38] but these have apparently not been published. Volker (1969) considered Kirkham's method an "unwarranted refinement" of the method of Curtis and Lawson (1967).

(iii) the finite element method.

This method is probably the most computational intensive, yet it is difficult to find a comparison of results between the various numerical methods which might indicate whether the additional computational effort of the finite element method is justified by an improvement in accuracy. In this method the quadratic form of the non-linear flow law is normally used (equation [2-4] rather than equation [2-3]).

Volker (1969), McCorquodale (1970), and Parkin (1971) all developed and tested separate coding for the finite element method to compute pore pressures in a non-linear flow field. In an apparent departure from his previous work, Parkin (1971) suggested the use of the Forcheimer (1901) form of a non-Darcy flow law to describe turbulent flow in porous media:

$$i = \alpha V + \beta V^2 \qquad [2\text{-}4c]$$

Parkin used this equation with an integral form of the equation for "turbulent" flow in porous media to arrive at solutions using the finite element method. The flow net from this study confirmed Wilkins' (1956) previous results; namely, that the non-Darcy nature of the flow resulted in higher hydraulic gradients at the toe, in a higher phreatic surface, in a larger seepage face, and in higher pore pressures within the structure. Based on these considerations and some slope stability analyses using Bishop's method, Parkin presented a useful rule of thumb for the extent of stabilization needed for the downstream face of a rockfill dam.

Using pore pressures computed from the finite element method together with Bishop's (1956) method for slope stability, Parkin (1971) inferred the fraction of the downstream face normally requiring anchorage. No comparison of observed and computed pore pressures was presented by Parkin (1971). McCorquodale (1970) found that the finite element method gave results within about 5% of observed pore pressures, and sought to extend this methodology to the analysis to transient flow conditions.

Volker (1969) concentrated on prediction of the free surface profile and the quantity of discharge in his finite element method study, partly because he found little difference between piezometric pressures predicted by Darcy's law and the observed pressures in his model. This may have been because 19 mm gravel was used. In this study the downstream slope of the model embankment was constrained by a vertical wire mesh, an unrealistic prototype configuration.

Good agreement between theoretical and observed discharges and phreatic surfaces was obtained. Volker (1975) commented that although the finite element method was advantageous when irregular boundaries were present, it was more computationally intensive than the finite difference method.

Volker (1969) performed a study similar to that of Curtis and Lawson (1967) except that the geometry of the model dam more closely approximated the geometry of a typical prototype-sized rockfill dam, and flow through the dam was emphasised as opposed to overflow. In accordance with Parkin's (1971) findings, Volker found that equations of the form of [2-4] performed more satisfactorily than equations of the from of [2-3] in conjunction with the finite element method. Using the finite element technique Volker (1969) was able to accurately estimate the location of the free surface and was also able to estimate the discharge within 10 percent of experimental observations. Volker noted however that the existence of a mathematical 'singularity' at the top of the impermeable element reduced the accuracy of computed discharges for this numerical method when an impermeable element was present. He also noted that the freefall zone described by Parkin (1963a) could not be accurately simulated due to its somewhat erratic behaviour. Fortunately, the precise configuration of the freefall zone is of little consequence in design (Parkin 1963a).

Parkin's comments on the merits of finite difference and finite element methods in the study of turbulent flow in porous media are worthy of mention. The finite element method was considered to be computationally faster but more complex. Moreover it was also considered to be more suitable for the study of flow where a curved free surface exists because a series of triangular elements can closely approximate a curved boundary. The finite difference method was considered to be slower but computationally simpler. Parkin preferred equations of the form of [2-3] for finite difference solutions and equations of the form of [2-4] for finite element solutions.

2.1.4 Erosion of the Downstream Face

A choice of emphasis is apparent in the literature regarding the type of hydraulic design for rockfill dams not having traditional concrete spillways. A number of engineers have opted for a design which emphasises overflow. That is, the dam is designed to pass the probable maximum flood with most if not all of the excess water passing over the crest and downstream face of the dam. Others have designed and built rockfill dams with the intention that the overflow condition should not occur, so that the the probable maximum flood passes through the dam. In any case, as Leps (1973) has noted in commenting on the work of Parkin ... "it will seldom be prudent to permit flow through a rockfill without reinforcing or buttressing the downstream face." This statement seems to give recognition to the fact that even when true overflow does not occur, all the flow which passes through the dam will pass over the toe of the dam in overflow. The distinction between overflow and "throughflow" is therefore somewhat artificial.

When a rockfill dam is overtopped the water flowing down the downstream face may cause stones on this slope to dislodge. If a sufficient number of stones dislodge this effect may become self inducing; the stones rolling down the face tend to set other stones in motion which are already in a state of incipient motion under the turbulent flowing water. This is known as "unravelling" failure (Gerodetti 1981). Unravelling failure usually leads to a sloughing-off of material on a larger scale, and the dam is often breached not long afterward (Wilkins 1963).

The usual method of protecting against unravelling failure is to place wire mesh on the downstream face of the dam and anchor this mesh at a number of locations with tie-back bars projecting back into the body of the dam. For this type of design the integrity of the mesh is crucial, and the mesh openings must be smaller than the smallest rock on the downstream face of the dam. The failure of the partially completed Cethana dam on November 15, 1968 in Tasmania was due to damage to the mesh during an overtopping flood (H-E.C.

Tasmania 1969). Stones rolling down the face damaged the mesh, finally resulting in the washing away of 15,300 cubic meters of material. Similarly, the failure of Paloona dam in Portugal on February 24, 1969 was due to the wire mesh being badly torn by a log carried by the flood (H-E.C. Tasmania 1969).

Incidents like these have generated interest in the design of stable rockfill slopes which can be submerged, without appreciable unravelling, by high velocity turbulent flow. Guskov and Pravdivets (1987) and Hartung and Scheuerlein (1970) have presented equations for determining the stable rock size required for flow in steep open channels with a view to improving rockfill dam design. Ulrich (1987) has more recently presented a similar equation in which the angle of repose is replaced by the so-called "bearing angle" of the rock. Unfortunately the above methods do not consider the destabilising effect of the seepage forces acting on the external rock face. This outward seepage force must be considered if such flow of water can occur (Stephenson 1979), and has been included in investigations by Sparks (1967) and Gerodetti (1981). This is an important point because even a rockfill dam with an impervious wall extending to the crest has significant seepage through the downstream shell and out of the downstream face, as illustrated in Figure 2-5. Because of this phenomenon the term "overflow" is to some degree a misnomer for rockfill dams undergoing seepage through the downstream shell. Figure 2-6 illustrates the forces acting on a particle on the downstream face of a dam undergoing both overflow and flowthrough.

The key factors affecting the relative merits of overflow versus flowthrough design for small hydro development are economics and safety. The starting point for such a discussion pertains to two important parameters: the design flood, Q_{PMF}, which is essentially imposed, and the amount of head, H, desired for the small hydro scheme. The cost of any embankment dam of a given configuration is proportional to the height of the dam. For a strictly flowthrough dam, part of the total height must be used for passing the design flood, namely, that fraction of the total height above the upstream

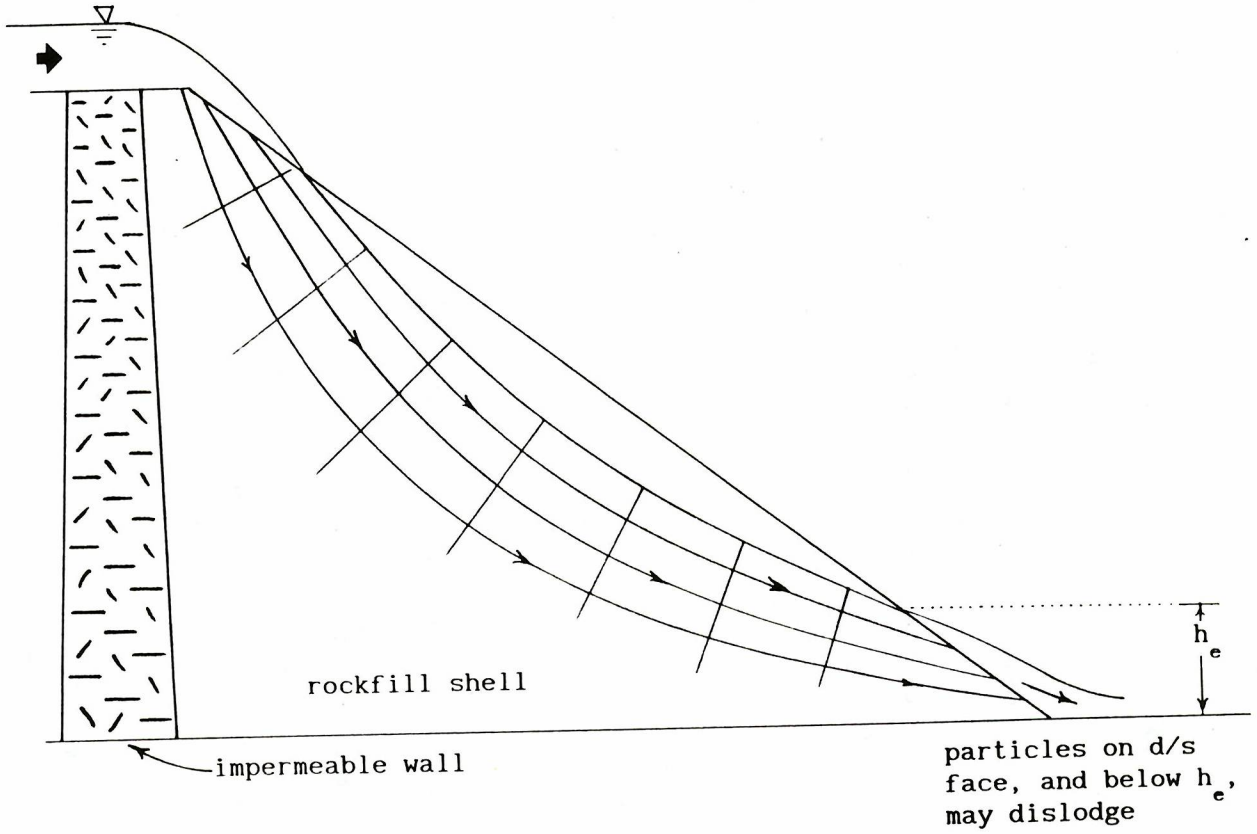


Figure 2-5. Illustration of flowthrough occurring in a dam primarily designed for overflow.

impermeable facing. The remainder of the height is available for storing water behind the impermeable facing. For a dam which emphasises overflow, the entire height of the embankment is available for storing water. It is therefore evident that the relative 'spillway' capacities of these two types of dam, keeping in mind the relative heights of the dams, is of critical importance. This is because part of the cost of the fill for a flowthrough dam is associated with providing for flowthrough capacity above the upstream impermeable facing. If the impermeable facing extends to the crest, as in overflow design, the storage is maximized for a given height of dam. However, two factors tend to mitigate against the choice of overflow design:

1. In the absence of a protective mesh on the downstream face, relatively flat slopes are needed to ensure the hydraulic stability of the rock on this face (Olivier 1967). This tends to increase the cost of the dam because its volume becomes great.

2. If steeper slopes are used to reduce the volume of fill, a protective mesh covering the downstream face is essential. Such mesh has a limited life span, and as has been indicated earlier, failure of the mesh can mean failure of the dam.

3. For flowthrough dams only extreme events need pass over the dam. Flowthrough dams normally operate with the flow passing through the dam. This design, having relatively low velocities of flow in the voids as compared to the high velocities associated with the overflow condition, is inherently safer.

2.1.4.1 The Initiation of Motion Approach

The failure mode most frequently encountered is "unravelling" failure (Wilkins 1956 & 1963, Parkin *et al* 1966, Gerodetti 1981), in which the flow on the seepage face causes rocks to dislodge and move down the face.

It might be expected that the discharge which an unreinforced dam

can sustain without major damage is strongly related to the slope of the downstream face of the dam. In the early 1960's the British Hydromechanics Research Association performed studies on the threshold discharge which could be sustained by various sizes of rock placed on various inclines. These results were first reported by Linford and Saunders (1967) and later by Olivier (1967). Olivier (1967) emphasised so-called overflow design, with flowthrough behaviour occurring only in the downstream shell. In order to avoid destabilisation of the downstream slope Olivier proposed very flat downstream slopes of the order of 1V:5H, particularly at the toe of the dam, so as to help ensure submergence by the tailwater of the point of emergence of the seepage. If some dislodgement of material occurred, Olivier observed that at these gradual slopes the stones simply rearranged themselves into a series of steps which were more stable than the original slope. The disadvantage of Olivier's approach is that the volume of rock in the dam becomes very large for such gradual downstream slopes, thereby reducing the economic advantage of the rockfill dam. The steepness of the downstream slope can be safely reduced by using larger rock for this surface (Sparks 1967). This may be an economical solution if large rock is abundantly available and can be placed cheaply.

Olivier (1967) presented the following formula for the threshold discharge of a rockfill slope experiencing overflow:

$$q_{OT} = 0.423\ d_s^{3/2}\ [G_s-1]^{5/3}\ (\tan\theta)^{-7/6} \qquad [2\text{-}39]$$

where:
q_{OT}: observed threshold flow (cfs per ft of width),
d_s : equivalent spherical diameter of the rock (inches),
G_s: specific gravity of the stone particle(s) (dimensionless),
$\tan\theta$: slope of downstream face; for a slope of 1V:2H, $\tan\theta = 0.5$.

1. The slopes used in the BHRA tests were all flatter than those used in this study.

2. In most of the BHRA tests seepage through the fill was not

permitted and equation [2-39] was derived from the results of tests in which water flowed only over the rock slope. This is in contrast to the tests undertaken in this study where a more realistic simulation of flow, both through the fill and over it, was undertaken.

3. No upstream impermeable facing was used in the BHRA tests.

4. The base layer of rocks was "keyed in" to a metal mesh, which was placed at a slope.

It is interesting to note that the Olivier's equation bears striking resemblance to the Schoklitsch expression for the initiation of bed-load movement along a river-bed (see Shulits 1935, and Goulter 1986):

$$q_{CR} = 0.2\ d_s^{3/2}[G_s-1]^{5/3}(\tan\theta)^{-7/6} \qquad [2\text{-}40]$$

where:

q_{CR} = critical unit-width water discharge at which bed-load movement begins.

Olivier's formula presumes that there is no motion of rock up to the threshold discharge and that failure of the structure occurs once the threshold discharge has been exceeded. Due to the stochastic nature of sediment transport and erosion processes (Neill and Yalin 1969, Farhoudi and Smith 1982, Smith 1986) it might be expected that a single threshold discharge would be difficult to clearly identify for a rockfill structure. The total amount of erosion might be expected to be a function of time. Typically, erosion occurs quite early in most tests; Cohen de Lara (1956) noted that initiation of surface movement occurred when the seepage face extended only three stone diameters upstream of the toe.

It might be expected, therefore, that the progressive nature of failure precludes the development of a clear relationship between threshold discharge and the angle of the downstream toe for unreinforced flowthrough rockfill dams made up of a given size of

rock. The slight trend that does exist for the set of tests done in each flume is probably due to the fact that the model dams with flatter slopes incorporated a larger volume of material. Once this larger amount of rockfill adjusted itself to a more gradual slope by partially moving downstream, its bulk helped to prevent erosion from progressing upstream to the impermeable facing.

Erosion of the downstream face versus consideration of a potential slip surface within the dam represent different emphases in designing a safe flowthrough rockfill dam. Erosion of the downstream face is different from classical initiation of motion studies for two reasons. First, the velocity distribution over the downstream face does not have a "no-slip" condition at the boundary. This is because of the emerging seepage (see Figure 2-6). The local boundary shear stress can therefore not be computed from a logarithmic-type velocity distribution. Second, the emerging seepage tends to lift the rocks resting on the downstream face, further contributing to local instability.

Normally, knowledge of the velocity distribution next to a boundary can be used to determine the local boundary shear stress. For example, in the tractive force - velocity distribution method, described by Reese (1984), the entrainment function (Shields 1936) is equated to the shear stress computed from the mean velocity in a logarithmic velocity distribution:

$$\frac{\rho\ V^2}{(\gamma_s-\gamma)d_{50}} = K_T\left[5.75\ \log_{10}\left(12.2\ R/k_s\right)\right]^2 \qquad [2\text{-}41]$$

where:

V=mean velocity

γ_s=specific weight of rock, γ=specific weight of water,

ρ=density of water, K_T=Shields constant, about 0.06,

R=hydraulic radius, k_s=equivalent sand grain roughness.

Any consistent set of units can be used with [2-41]. This method

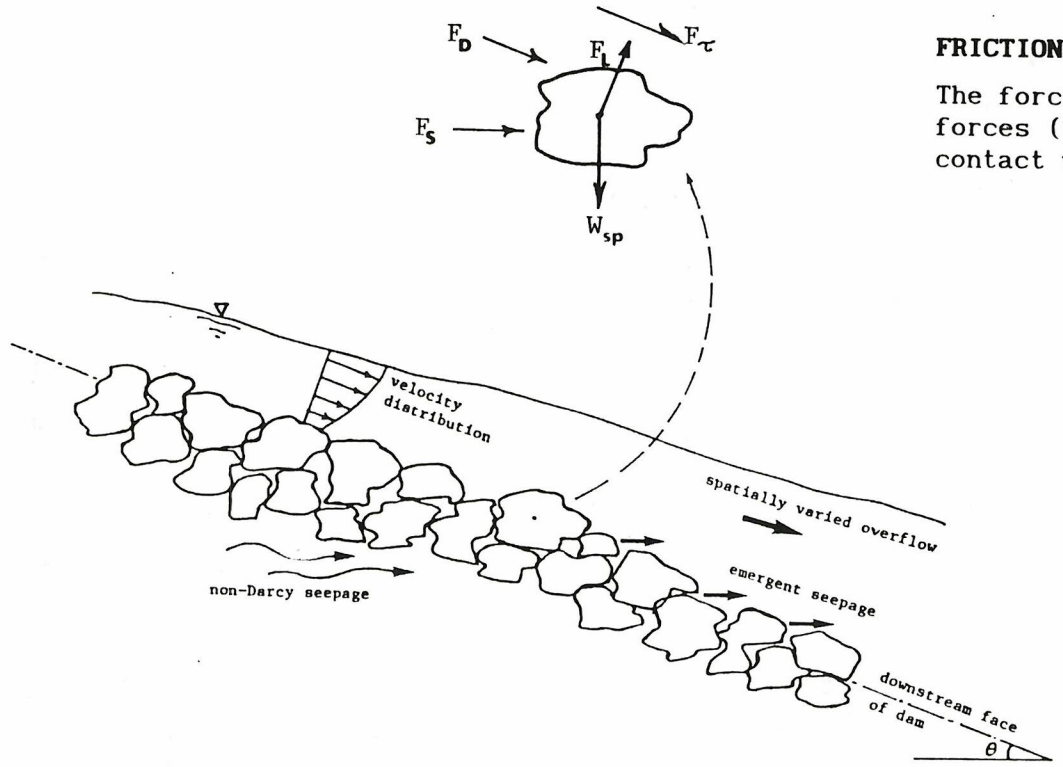
HYDRAULIC FORCES:

1. F_τ = shear force due to overflow,
2. F_S = seepage force,
3. F_D = drag force,
4. W_{SP} = submerged weight of particle,
5. F_L = hydrodynamic lift.

FRICTIONAL FORCES (not shown):

The force opposing the resultant of the above forces (for a particle at rest) is provided by contact with neighbouring particles:

6. frictional resistance beneath particle,
7. constraint provided by particles in the same plane.



θ = angle at toe of dam

Figure 2-6. Forces acting on a single particle located on the downstream face.

uses the Shields' K_T, which should not be applied to a seepage face. It also assumes a no-slip condition at the face, a condition not met in this case. However, if the velocity distribution in the seepage face zone were known, the local boundary shear stress could be estimated and the destabilizing force due only to overflow also estimated.

2.1.4.2 Quantifying Shear Stresses in Spatially Varied Flow

In considering whether to design a structure based on overflow conditions or on classical slope stability analyses using non-Darcy pore pressures, it should be remembered that the total quantity of flow passing through the structure will be completely in overflow at the toe of the dam. Spatially varied flow occurs on the seepage face, beginning at the point of flow emergence. This category of flow occurs when discharge increases (or decreases) with distance along a relatively short channel under steady-state conditions. Sharp and James (1963) presented the following equation describing this phenomenon for the seepage face of a flowthrough rockfill dam. Their development assumes:

1. a hydrostatic pressure distribution exists within the rock mass which is adjacent to the downstream face.
2. only atmospheric pressure acts on the downstream face.
3. equation [2-3a] applies. Then:

$$\frac{dQ}{dx} = n \left(\frac{\tan\theta}{a} \right)^N \qquad [2\text{-}42]$$

where:
dQ/dx = rate of change of discharge along the downstream face,
θ = angle of downstream toe,
n = porosity,
a, N from [2-3a].

Thus, according to the development of Sharp and James (1963), which

also assumed a hydrostatic pressure distribution in the vicinity of the downstream slope, dQ/dx is constant for a given material at a given slope. Equation [2-42] may have usefulness in the following alternate approach to estimating shear stress.

Sharp and James (1963) began their theoretical analysis with the following well-known expression (Chow 1956, King and Brater 1963):

$$\frac{dy}{dx} = \frac{S_o - S_f - (2\alpha Q q_*)/(gA^2)}{1 - (\alpha Q^2)/(A^2 D)} \qquad [2\text{-}43]$$

where:
dy/dx = rate of change of water surface elevation,
S_o = bed slope,
S_f = friction slope,
α = energy correction coefficient,
Q = discharge,
q_* = rate of change of discharge with distance = dQ/dx,
A = cross-sectional area of flow,
D = hydraulic radius.

If it were possible to estimate dy/dx and dQ/dx for design purposes, the friction slope could be solved for and used in the following equation:

$$\tau_o = \gamma_w R S_f \qquad [2\text{-}44]$$

where:
τ_o = boundary shear stress,
R = hydraulic radius,
S_f = friction slope.

In this way it may be possible to estimate the shear stress due to the overflow component of the discharge moving through a rockfill dam.

2.1.4.3 Quantifying Seepage Forces

Perhaps more important than the choice of which numerical technique to use to compute pore pressures is how to use the computed pore pressure results. Seepage emerging from the downstream face has a certain hydraulic gradient associated with it, and the destabilizing effect of this seepage must be considered in addition to that of overflow erosion. For laminar flow in soils the "quick" condition, which occurs when intergranular contact forces become zero, is:

$$i_C = (\rho_{MEDIA} - \rho_{WATER}) / \rho_{WATER} \qquad [2\text{-}45]$$

where:
i_C = critical hydraulic gradient,
ρ_{MEDIA} = bulk density of the porous media.

It is not clear what the critical hydraulic gradient is when the flow is non-Darcy. Wilkins (1956) stated that if the critical hydraulic gradient is unity and a factor of safety of 2 is used, then from his own equation [2-2]:

$$V_P = 16\ m^{1/2} \qquad [2\text{-}46]$$

where:
m = hydraulic mean radius (inches),
V_P = "piping velocity", inches/sec.

Wilkins (1956) cited no experimental evidence for [2-46] and stated that it should be "treated with reserve". In general, the force per unit volume of material due to seepage is (Holtz and Kovacs 1982):

$$F/\mathcal{V} = \gamma_W\ i \qquad [2\text{-}47]$$

where:
F = seepage force,
$\mathcal{V}$ = bulk volume,
γ_W = weight density of water,
i = hydraulic gradient.

Equation [2-47] is an analytic non-empirical expression. Using it the seepage force can be computed knowing the hydraulic gradient, which can be readily obtained from the results of pore pressure modelling.

Estimates are needed of the local boundary shear stress exerted on particles resting on the downstream face due to the effect of seepage flowing over the downstream face of the dam. To estimate the shear stress any data on the velocity distribution would be useful. Information on the hydraulic gradient acting on the layer of rock making up the downstream face would be useful in estimating seepage forces.

2.1.5 Classical Slope Stability Analysis

Classical slope stability methods require pore pressure information. However, the work of Wilkins (1956, 1963) and Parkin (1963b) indicate that analyses based on an assumed slip surface are more applicable when the downstream face has been anchored. Classical slope stability analysis, such as described by Bishop (1956), yields a single dimensionless number: the factor of safety F. This is the ratio of the mobilized shear strength to the applied shear stress along a potential slip surface. The expression for F is obtained by considering the forces acting on each thin vertical slice within a slope. This slope is assumed to become mobile over a slip surface of an assumed shape. The forces involved in this analysis exist because of three factors:

1. the self weight of the granular media.
2. internal friction in the granular media.
3. hydraulic pressure.

The internal angle of friction affects the computed factor of safety when using classical methods for evaluating slope stability. Marachi *et al* (1969) found that the internal angle of friction is dependent on particle size and on confining pressure. Table 2-4 summarizes Marachi's findings for crushed basalt.

Table 2-4

Influence of Particle Diameter and Confining Pressure σ_3 on the Angle of Internal Friction.

σ_3 = 267 kPa

maximum particle size d	approx. ϕ°
150 mm	51.7
50 mm	48.3
10 mm	47.3

d = 5 cm

confining pressure (kPa)	approx. ϕ°
267	48.3
965	42.2
2896	38.2

In this study it was possible to use particles 13 cm in diameter for some tests. Particles in prototype rockfill dams can be as large as 1 m in diameter. In addition, the confining pressures near the foundation of a model rockfill dam will be considerably less than the confining pressure in a prototype structure. It will therefore not be possible for $\phi_M/\phi_P = 1$. However, if standard methods for evaluating internal slope stability, such as Bishop's method, are used for analysing the results of experiments on model dams, the role of ϕ in these analytical methods is well known. If pore pressures are successfully modelled results can be extended to a prototype by adjusting ϕ along the lines of the results of Marachi *et al* (1969).

At a given site there may be constraints as to the quantity and size of rock available. If it is concluded that some form of reinforcing mesh is necessary at a particular site, two questions arise. First, what is the magnitude and direction of forces acting on the reinforcing mesh? Second, since the mesh must be anchored somewhere, how deeply into the body of the dam should the anchors extend? With regard to the first question, to date no references to actual measurements were found in the literature regarding the magnitude and direction of bursting forces on the reinforcing mesh of flowthrough rockfill dams. As to anchoring strategies, it is clear that anchor bars, to which the mesh is attached at intervals,

must extend into the body of the dam to a location where the rock will not be mobilized by excessive hydraulic gradients. Parkin (1971) has suggested an "unsafe" zone requiring reinforcement if a conservative design is desired (see Figure 2-7(a)). This zone of possible instability lies between two parallel lines. The first is the downstream face itself. The second is a line parallel to this which extends between a point on the crest set back two-thirds of the height of the dam, and the corresponding point at the foundation of the dam. This is a considerable fraction of the total volume of fill even though no upstream impermeable facing was considered. The zone proposed by Shand and Pells (1970), for the case when an upstream impermeable facing is employed, appears to be larger still.

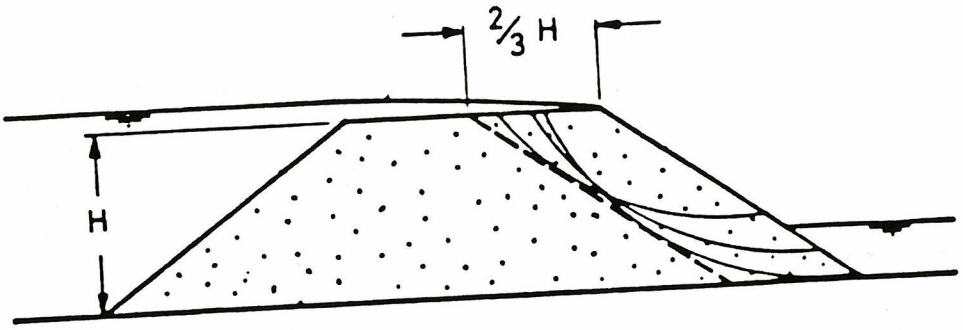
It is widely recognized that a flowthrough rockfill dam with no reinforcement will usually undergo some degree of failure even for modest flows. Wilkins (1963) has indicated that, given the relative amounts of flow that can pass over the dam versus through the dam, overflow will often govern the design. Olivier (1967) suggests that the toe of the dam be covered with heavier material at a slope of perhaps 1V:10H, and this would appear to be the simplest and cheapest way of preventing failure if such rock is available. The other approach is to reinforce the downstream face of the structure with wire mesh and tie rods, as illustrated in Figure 2-7(b).

In order to determine the amount of reinforcement some investigators have used Bishop's (1956) method together with non-Darcy pore pressure information. Shand and Pells (1970) suggested that Bishop's equation be modified to account for the restraint introduced by the reinforcing bars:

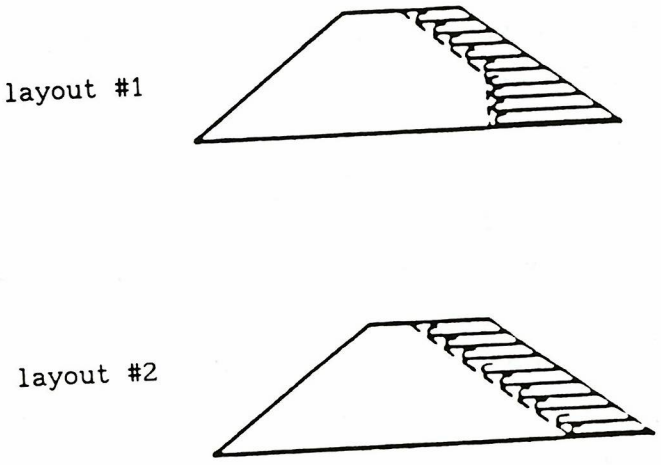
$$FOS = \frac{\Sigma W(1-r)\ \tan\phi/M}{\Sigma(W-pb)\sin\theta} \qquad [2\text{-}48a]$$

where:

$$M = \left[1 + \frac{\tan\alpha\ \tan\phi}{F}\right] \qquad [2\text{-}48b]$$



a) zone requiring reinforcement to prevent rotational failure (after Parkin, 1971).



b) layout of tie-back rods suggested by Wilkins (1963).

Figure 2-7. Considerations in preventing failure.

and where:

FOS = factor of safety, r= pore pressure ratio,

W = weight of a slice, ϕ= internal angle of friction,

p = force provided by tie-bars in a given slice,

b = width of a slice,

θ = angle of downstream slope, Σ= summation, over the # of slices.

Based on Bishop's method and finite element pore pressure computations, Parkin (1971) presented a design guideline for the amount of reinforcement needed (see Figure 2-7(b)). However, it may be that prevention of erosion of the downstream slope is the primary function of a reinforcing mesh; an internal potential slip surface does not usually occur unless the dam is already reinforced (Guidici 1967). Parkin (1963b) observed that it is possible to compute a factor of safety of unity and have no circular failure in a model dam.

These questions have led some investigators to perform model tests to examine the effects of reinforcement. The model tests of Sarkaria and Dworsky (1968) at a 1:40 Froude scale indicated that mesh tied back into the body of the dam had a very significant effect on stability. However, as noted by Shand and Pells (1970), the experiments of Sarkaria imply an unrealistically large amount of reinforcing at the prototype scale. Clearly, the restraining force exerted by metal rods used in model dams is completely out of scale relative to the slope failure forces in a model (Guidici 1967).

Gerodetti's (1981) model tests used a full-height impervious core so that no flowthrough occurred upstream of the center of the crest. The downstream face of his model employed a thin layer of horizontally-laid gabion baskets, each with a sloping face, and was therefore relatively smooth. He concluded that seepage forces were responsible for shifting the gabions out of place during overflow. This shows that the erosive forces of overflow combine with significant seepage forces to cause unravelling of the face.

2.1.6 Behaviour of Flowthrough Rockfill in Subzero Temperatures

There appears to be little in the literature on how flowthrough rockfill dams behave hydraulically under severe winter conditions. However, certain inferences can be made based on existing knowledge of river ice processes and of the operation of non-rockfill hydroelectric dams in winter.

Three forms of ice may be pertinent to this study. First, ordinary sheet ice will probably cover much of the upstream reservoir. This may have a small effect on the "flowthrough" behaviour of the dam because the velocity distribution under such conditions is known to be different from that encountered in open water (Uzuner 1975). Second, it is known that ice called "shorefast" ice is the first ice to appear in natural rivers due to the higher rate of heat loss by conduction from the river banks. This type of ice is particularly prevalent where there are rock outcrops from the river banks. This phenomenon raises the question of whether heat loss from the exposed rock at the water surface will hasten the formation of a surface layer of ice.

Third, under certain upstream conditions "frazil" ice can form in the water and move downstream, attaching firmly to anything it comes in contact with (Tsang 1982). This floss-like ice of neutral buoyancy forms when there is no sheet ice cover, when the rate of heat loss at the surface is sufficiently high, and if sufficient ions are in the water to enable nucleation (Osterkamp 1978). This type of ice has caused difficulties for hydro-electric plants during winter operation because it can very quickly block intake structures by adhering to the trash racks (USACE 1982). Very few laboratories have the capability to generate known mass flow rates of frazil since specific conditions of the atmosphere, water quality, and fluid turbulence must be correctly simulated (Osterkamp 1978). Further, no accepted method exists to measure the mass flux of frazil, although attempts have been made (NWRI 1982).

If ice growth should occur in the voids of a flowthrough rockfill

dam due to anchor ice growth on the rocks or due to frazil accumulation, the dam would overtop because flowthrough operation would cease. As water flows through a rockfill embankment three heat exchange phenomena occur:

1. If the rock particles are at a different temperature than the water, heat transfer will occur.

2. The water/rock matrix making up the embankment may exchange heat with the air and the underlying ground.

3. As water moves between the voids in a turbulent fashion some of its hydraulic energy is converted to heat by viscous dissipation.

Phenomenon 1 is probably the least important since the thermal inertia of the rock would only come into play if the ambient temperature changed very suddenly.

For phenomenon 2 it is expected that the phreatic surface will be subject to freezing for the same reasons that a reservoir is subject to freezing in winter: it is a water surface exposed to the atmosphere. The following factors affect the net heat exchange between a water surface and the environment (Tsang 1982):

1. Shortwave insolation (a heat gain mainly via sunshine),
2. Net long wave radiation (which is affected by air temperature, cloud cover, cloud elevation, and albedo),
3. Evaporative heat loss (affected by relative humidity),
4. Convective heat loss (affected by wind speed),
5. Snowfall (a heat loss).

Evaporative heat losses are frequently computed as part of convective heat losses and this combination is then referred to as sensible heat loss. Of the five above-mentioned factors affecting heat exchange, convective heat loss is usually the most important in determining the net heat loss coefficient. Prowse (unpublished)

states that net heat loss coefficients of between 25 and 50 $W/(m^2C^\circ)$ apply to rivers in Canada, with the latter associated with "extremely cold windy conditions".

Phenomena 3, viscous dissipation, is a quantity of heat which can be directly computed (Tsang 1982) from:

$$q = \Gamma \, Q \, \Delta h \qquad [2\text{-}49]$$

where:
q = heat generated (kcal/sec),
Γ = 2.342 kgf-m per kcal, a conversion factor which includes the mechanical equivalent of heat,
Q = discharge (m^3/s),
Δh= drop in water surface elevation (m).

The height of a flowthrough rockfill dam therefore determines the rise in temperature. Viscous dissipation will mitigate against the formation of frazil ice in the voids within a flowthrough rockfill dam. This is because:

1. Water below the sheet ice cover in the upstream reservoir must be at or above 0 °C.

2. The phreatic surface is directly exposed to the air. Therefore sheet-like ice can be expected to form first at the phreatic surface. This then prevents convective and evaporative heat losses, which are the largest mechanisms for heat loss (Tsang 1982).

3. The passage of water through the voids causes a slight temperature rise in the water, bringing it above 0°C.

4. The formation of frazil requires a slightly negative water temperature (of the order of -0.05 °C, (Osterkamp 1978)).

Ice can therefore be expected to form first at or near the phreatic surface if conditions are sufficiently severe. This will probably be due in part to the intermittent wetting of rocks which occurs

because of turbulent fluctuations in those void spaces adjacent to the phreatic surface. The growth of ice on the surface of a river or lake can be estimated (Zarling 1978) from the equation:

$$I_T = \vartheta\sqrt{\Psi} \qquad [2\text{-}50a]$$

where:

$$\Psi = \sum_{i=1}^{n} (0 - T_{air}) \qquad [2\text{-}50b]$$

and where:

I_T = ice thickness (mm),

ϑ = an empirical coefficient varying from 7 to a theoretical maximum of 34,

Ψ = a freezing index (Celcius degree days).

It may be possible to adapt [2-50] to the problem of ice formation at the phreatic surface of a flowthrough rockfill dam.

Little mention in the literature could found on the behaviour of prototype flowthrough rockfill dams in subzero conditions. In a study of mine waste containment at two mines near Yellowknife N.W.T. freezing did occur within the body of the tailings dams (Berubé *et al* 1972). These dams were not constructed as flowthrough dams however; any water moving through the dikes was considered to be undesirable seepage having poor water quality characteristics. At Giant Mine (dike #3, 20 m high) the maximum seepage was less than 0.25 cfs per 100 ft of width, and this occurred in August 1971. During the winter the storage reservoir apparently froze to the bottom, so that ice also formed within the tailings dam because fluid motion ceased.

MacIntosh (1985) investigated temperature distributions within a rubble mound breakwater in Lake Nipissing during the winter of 1984-85 and found that no major ice inclusions formed within the berm. Locations below the low water level never froze, but subzero temperatures did occur at points subject to intermittent wetting.

2.2 CASE HISTORIES

Table 2-5 summarizes the basic information available for four notable rockfill structures to be discussed in the ensuing paragraphs.

Some of the earliest examples of rockfill dams having no conventional spillway were constructed in Mexico between 1939 and 1945 and are documented by Weiss (1951). These dams were constructed in remote areas where skilled labor and special construction equipment were difficult to procure and where the frequency of flooding made it difficult to construct conventional concrete spillways. The first of these dams, the San Ildefonso, was 62 m high and used a concrete facing on the upstream side of the embankment to maintain a pool level. A reproduction of a photo of the spillway section is shown in Figure 2-8(a). The downstream face was at a 1V:1.4H slope and was covered with a rebar mesh tied back into the body of the dam. A schematic of the reinforcing system is shown in Figure 2-8(b). The rockfill spillway was designed for a depth of flow of 3.0 m, but the details of the hydraulic design are not mentioned by Weiss. The dam sustained a flow of 142 m^3/s with no erosion or breaching of the mesh. Some bulging of the mesh was observed at the toe, however. Subsequent to this flood it was decided to use the mesh for another purpose and it was removed. A flood then occurred and this caused 7000 m^3 of material to be washed downstream.

Due to the need for a larger water supply for the city of Osceola, Iowa, it was decided to raise the height of an existing dam using rockfill. The toe of the rockfill spillway was built such that it ended at the top of the old concrete spillway (see Figure 2-9(a)). Figure 2-9(b) shows the crest of the rockfill spillway, which was designed to sustain a flow of 76.5 m^3/sec at a mean velocity of 5.2 m/s. It was estimated by Barr and Rosene (1958) that a concrete spillway would have cost 3 to 6 times as much as the rockfill spillway, made from 3720 tonnes (4100 tons) of quarried limestone. The rockfill making up the spillway was graded such that 40% of the

Table 2-5

Some Prototype Flowthrough Rockfill Dams/Spillways

Name of Dam & Documentor(s)	Descriptive Notes
San Ildefonso, Weiss (1951)	Completed 1939 in Mexico. H = 62 m, B_c = 5 m d/s slope: 1V:4H; rebar lattice + tiebacks. Undamaged by 142 m^3/s flood, but subsequently damaged by another flood after mesh removed. Present status unknown.
Osceola, Barr & Rosene (1958)	Completion date unknown; Iowa, USA. H = 3.6 m, B_c = 2.4 m, L_c = 30.5 m d/s slope: 1V:5H; concrete apron over the toe. Design discharge = 76.5 m^3/s Present status unknown.
Hellhole, Johnson (1971)	Partly completed in 1964; California, USA. H = 67 m, B_c = 18.3 m d/s slope: 1V:1.3H, no reinforcement. Failed by flow of about 56.6 m^3/s. Present status unknown.
Cethana, H.-E.C. (1969) Varty *et al* (1985)	Completed 1971 in State of Tasmania, Australia. H = 110 m, B_c small, L_c = 215 m d/s slope: 1V:1.3H; gabion lattice + tiebacks. Damaged before completion, repaired. Subsequently undamaged by "massive" flood. Functioning as of 1985.

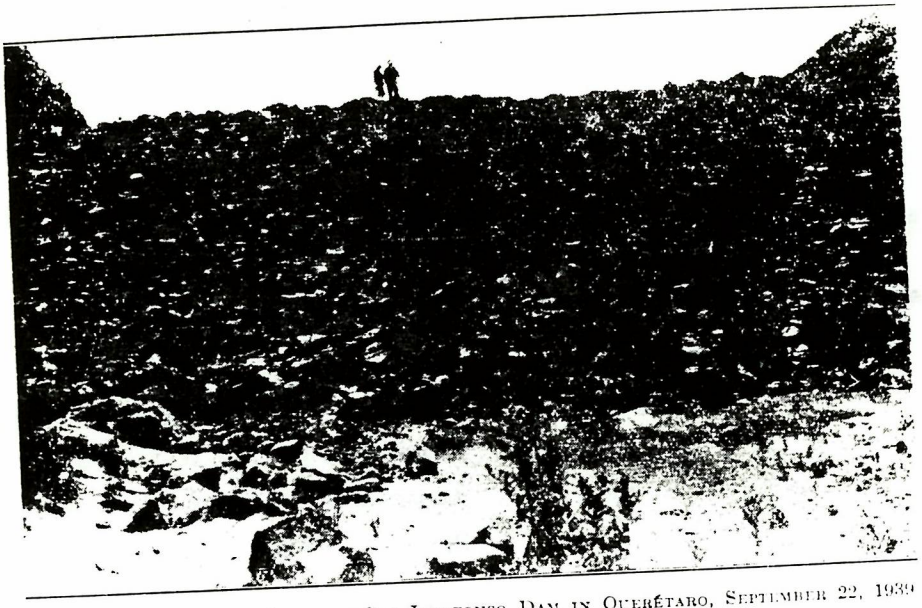
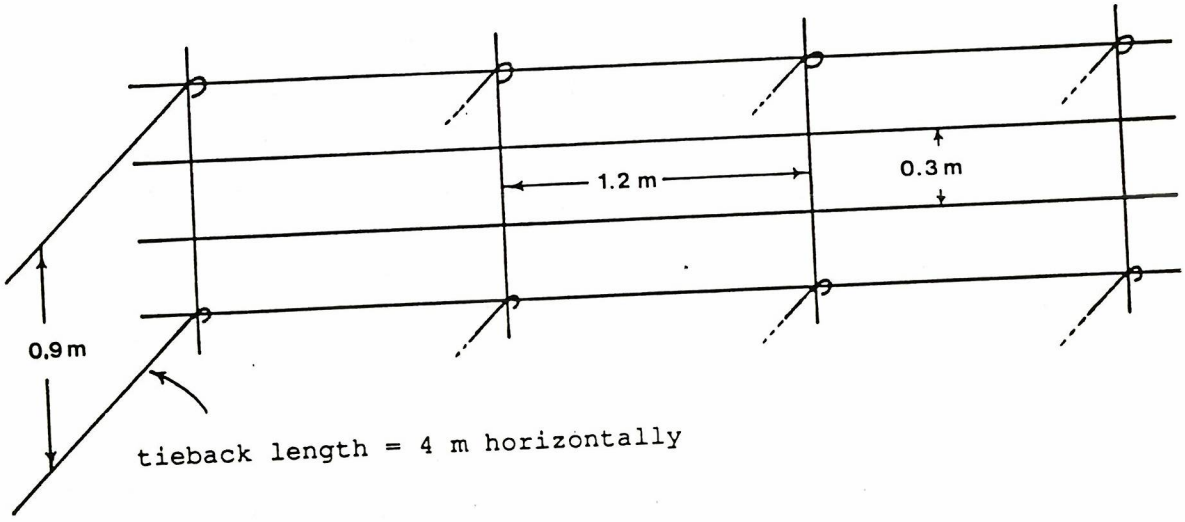


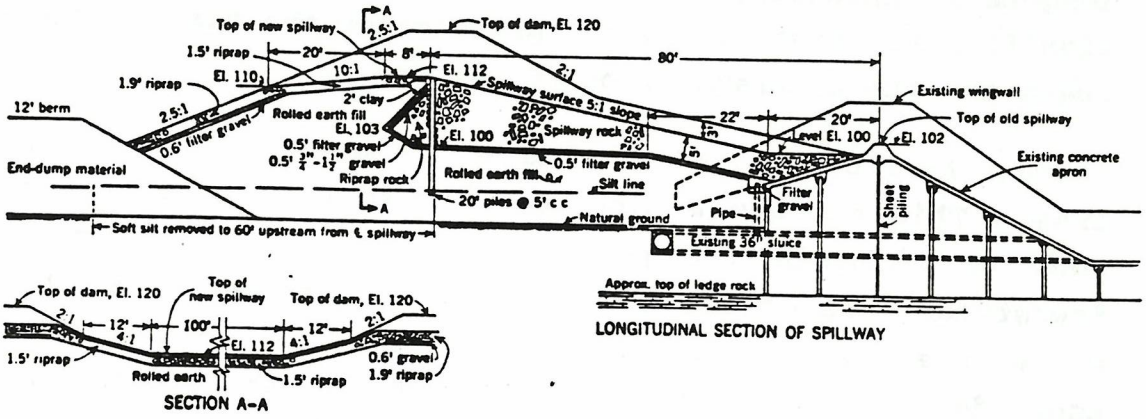
FIG. 2.—DOWNSTREAM SLOPE OF SAN ILDEFONSO DAM IN QUERÉTARO, SEPTEMBER 22, 1939

a) spillway section.

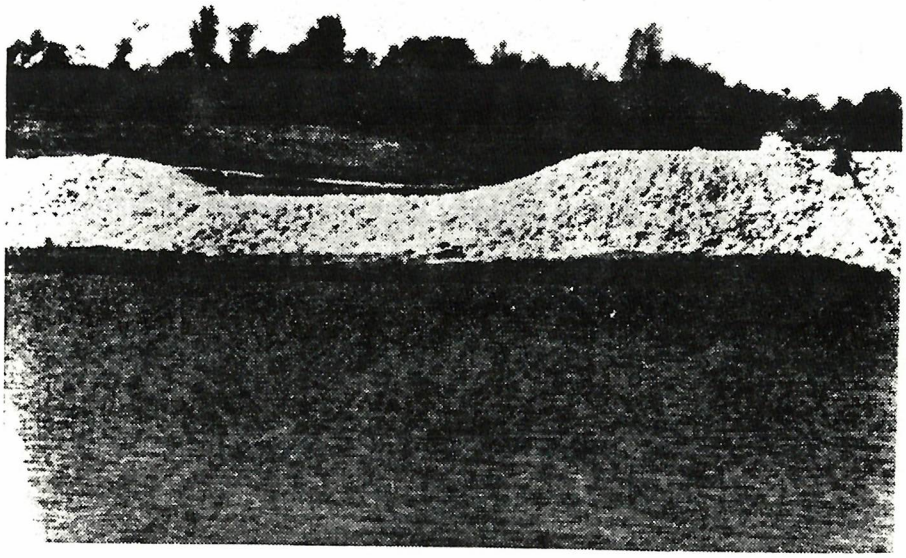


b) spacing of horizontal and vertical mesh restraint on downstream face.

Figure 2-8. The San Ildefonso Dam in Mexico, described by Weiss (1951).



a) cross section.



b) spillway opening.

Figure 2-9. Osceola rockfill spillway in Iowa, (Barr and Rosene 1958).

rock was larger the 610 mm (2 ft) in nominal diameter. The long-term integrity of this rockfill spillway was no doubt significantly enhanced by the presence of the timber bulkhead in the crest and the concrete apron at the toe.

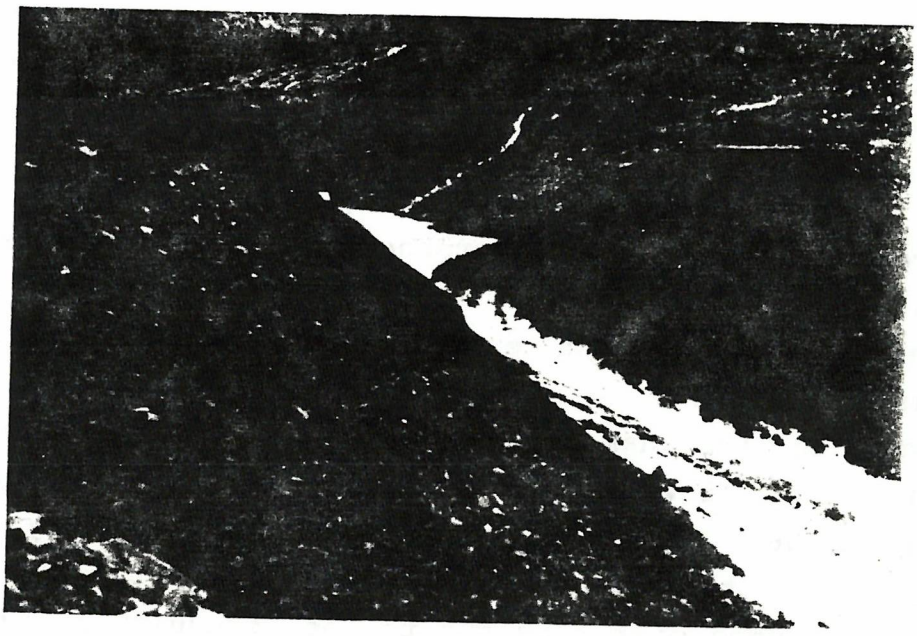
Another American example is the Hellhole dam in California, built in 1964. This dam had a sloping upstream core of compacted soil and rock to maintain the pool elevation and was 67 m high. The downstream face of the structure, which was set at a 1V:1.3H slope, was apparently not reinforced. Johnson (1971) did not have detailed knowledge of the nature the rockfill other than that it was "end-dumped and homogeneous". Johnson was fortunate to have access to fairly comprehensive data on the conditions which brought about failure of the dam and used this data to evaluate some of the work of Parkin. Using independent hydrologic and hydraulic estimates Johnson developed a rating curve for the dam. Based on photographs of water emerging from the seepage face he estimated h_e and computed the coefficient a in [2-3c] as 0.57 (ft-sec units with V as V_v).

However, the value of a which resulted was in fact in poor agreement with Parkin's value of 1.86. The reason for this appears to be confusion over the definition of "seepage velocity" (which is bulk velocity divided by porosity). Figure 2-10(a) shows the dam before failure; Figure 2-10(b) shows the dam after failure. It would appear from Figure 2-10(b) that the material making up Hellhole Dam had a great deal of fines, making it possible for the nearly vertical slope angle to exist at the side of the breach after failure (see vertical white line).

Formal investigations into the hydraulic behaviour of coarse rockfill began in the late 1950's with the work of Wilkins (1956) under the sponsorship of the Hydro-Electric Commission (H-E.C.) of Tasmania, Australia. These studies were motivated by a search for innovative designs for cofferdams, small hydro dams, and inexpensive water supply structures. The prototype rockfill dams arising from these studies had no provision for conventional outlet works such as concrete spillways (Varty *et al* 1985). It was considered feasible



a) before failure.



b) after failure. Note steep face within breach.

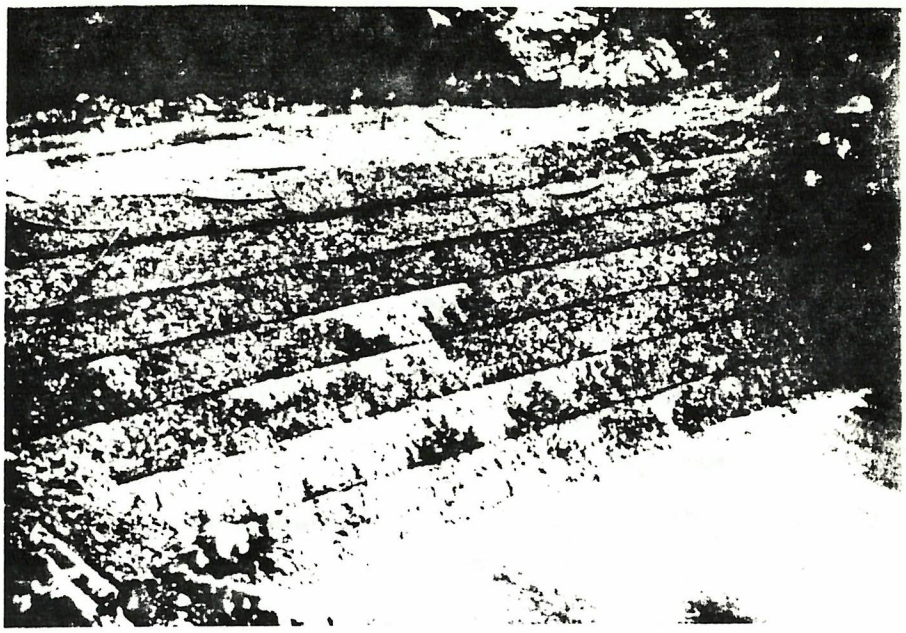
Figure 2-10. Hellhole Dam in California before and after failure (after Leps 1973).

that a flood could pass over the impermeable upstream facing of the dam, through the rockfill, and then over the rock making up the downstream face. Cethana Dam, completed in 1971, is the most frequently cited example of such a dam.

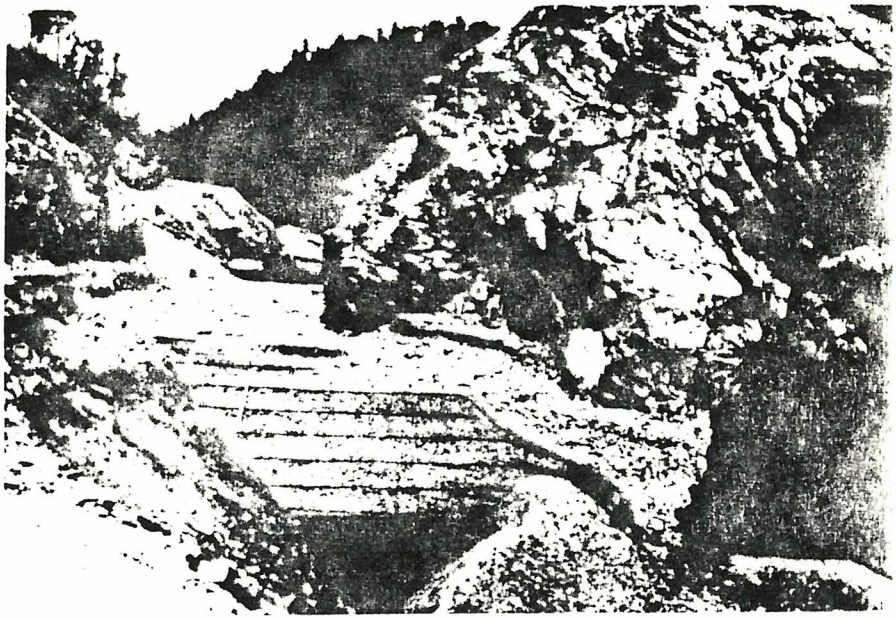
Cethana Dam is 109 m high and has a downstream slope of 1V:1.3H. The upstream face consists of a series of concrete slabs connected by copper water-stop joints. The downstream face was reinforced using chain link wire mesh and rebar tiebacks which were hooked at both ends. The dam failed before being completed as a result of an overflow of 170 m^3/s. This occured due to tearing of the protective mesh by dislodged stones and debris (H-E.C. Tasmania 1969). The dam was repaired and completed to its full height. As of 1985 it was reported as still functioning (Varty *et al* 1985). Figure 2-11(a) and (b) show the dam before and after the 1969 failure, respectively. According to Varty *et al* (1985) the dam sustained an even larger flood (termed "massive overtopping") after completion, with no damage to the dam. Figure 2-12(a) gives a sectional detail of this type of dam used in Tasmania, of which Cethana Dam is representative.

In a recent personal correspondence, Mr. M.D. Fitzpatrick, Assistant General Manager Engineering, Hydro-electric Commission (H-E.C.) of Tasmania, described the experience of H-E.C. Tasmania with the Laughing Jack Marsh Dam, completed in 1957 (see Figure 2-12(b)). This was the first dam to be built based on Wilkins' research on the hydraulics of flow through rockfill, and is briefly described in Wilkins (1956). The design discharge for Laughing Jack Marsh Dam was 28 m^3/s. It is interesting to note, however, that this capacity has been reduced over time due to the accumulation of debris on the upstream face to 9 m^3/s. Fitzpatrick further reports that the quantity of debris remains approximately constant "due to a cycle of build-up during floods and decomposition of debris between these floods." Burning of the debris was found to be only partially successful.

Canadian examples of flowthrough structures are more common in the

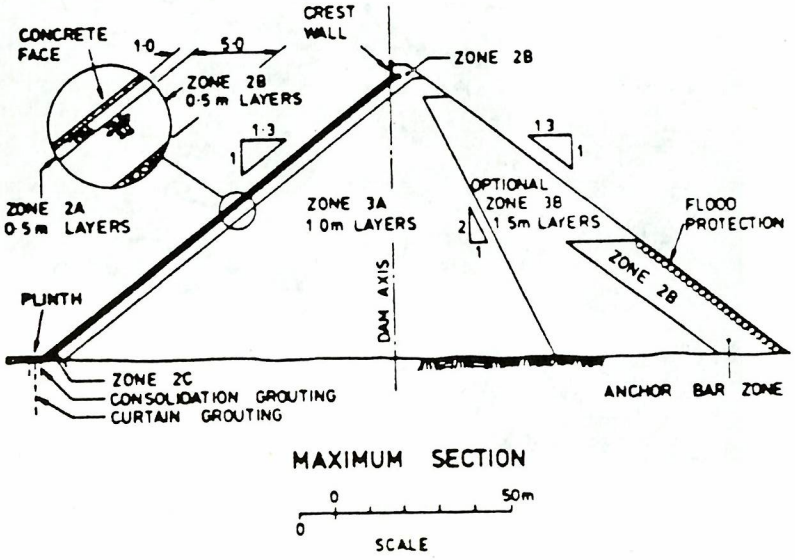


a) partially-completed dam, before failure.

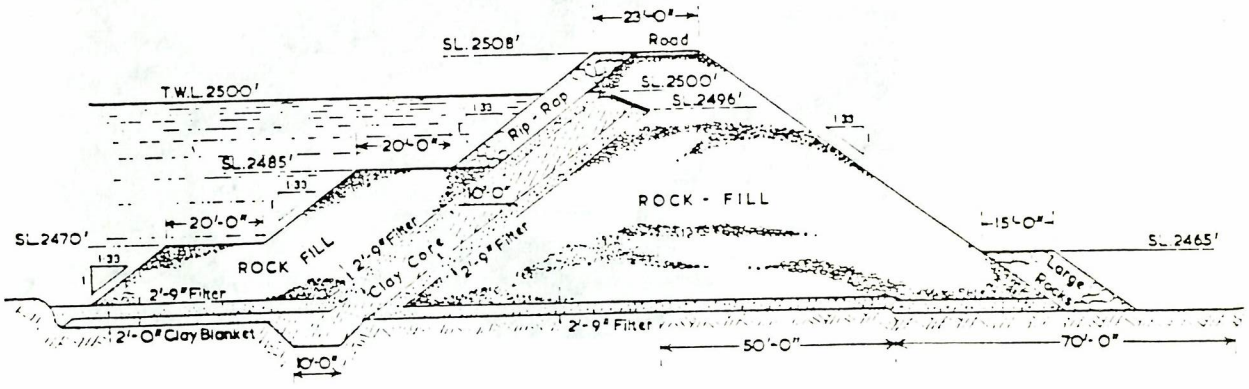


b) after failure. Mesh torn open by debris and possibly rocks rolling down from above. Mass movement followed.

Figure 2-11. Cethana Dam in Tasmania, 1969.



a) for dams typical of Cethana Dam (after Fitzpatrick, 1985).



b) for Laughing Jack Marsh Dam (after Wilkins, 1956).

Figure 2-12. Cross-sections of rockfill dams constructed in Tasmania.

mining industry, e.g. the Swift Creek flowthrough rockfill drain, near Elkford, British Columbia, which is described by Lane et al (1986). In this instance flow passes through the base of the mine waste dump. Because waste dumps are usually formed by end-dumping, rocks of the order of 1 m in diameter make up the base of such dams, while the crests are usually comprised of much finer material. Accordingly, due to the large voids at the base of tailings dams, it is possible to pass small streams through them relatively unimpeded. Velocities as high as 20 cm/s have been estimated to have occurred within the Swift Creek drain during a particular flood event. At this velocity 100 m^2 of flowthrough area could accommodate 20 m^3/s, which is a relatively small flow compared to that generated by the same flow area at the crest of a standard overflow spillway. Nevertheless, in cases where sufficient quantities of large rock are available, a flowthrough design may still be more economical than a traditional concrete structure. An innovative design of flowthrough structure for the abandonment of acid-generating metal tailings in the Yukon has been described by Garga *et al* (1983).

2.2.1 RELATED REFERENCES

The following five references make mention of other rockfill dams or spillways in various parts of the world. These were not described in detail herein because the information contained in the material was either untranslated, considered too minimal to include, or emphasized topics not within the scope of this report:

1. Airapetyan R.A., 1968. Modern rockfill dams. Israel Program for Scientific Translations, Jerusalem 1970.
- emphasises geotechnical concerns; a number of cross-sections for various rockfill dams around the world.

2. Davey G.I., 1960. Rock fill dams at Mary Kathleen and Mount Isa. Journal of the Institution of Engineers (Australia),December, p.291-302.

(regarding Davey 1960)
- describes Corella River and Leichardt River dams in Western Queensland, Australia. Gunite upstream facings, report emphasizes hydrologic design. Built to supply remote mining operation with electricity.

3. Fitzpatrick M.D., Cole B.A., Kinstler F.L., Knoop B.P., 1985. Design of concrete-faced rockfill dams. ASCE Convention on Concrete-Faced Rockfill Dams - Design, Construction and Performance, Edited by J.B. Cooke and J.L. Sherard, Detroit Michigan, p.410-434.
- details of the amount of settlement of Cethana dam. Mentions 9 other dams constructed along the lines of Cethana Dam, all reported as still functioning. Article emphasizes details. Same volume as Varty *et al* (1985).

4. Gorchakov M.P., 1953. The design of a spillway dam of rockfill construction. Hydrotechnical Construction, no.4, USSR.

5. Sherard J.L., 1959. A steel-faced rockfill dam. ASCE Civil Engineering Magazine, October, p.42-45.
- describes Rio Lagatijo water supply dam in Venezuela. Steel facings are no longer in use.

3.0 EXPERIMENTAL PROGRAM

3.1 PACKED COLUMN TESTS

3.1.1 Apparatus

For this study a specially designed acrylic column was constructed. This column is shown in Figure 3-1. The physical specifications of the column were as follows:

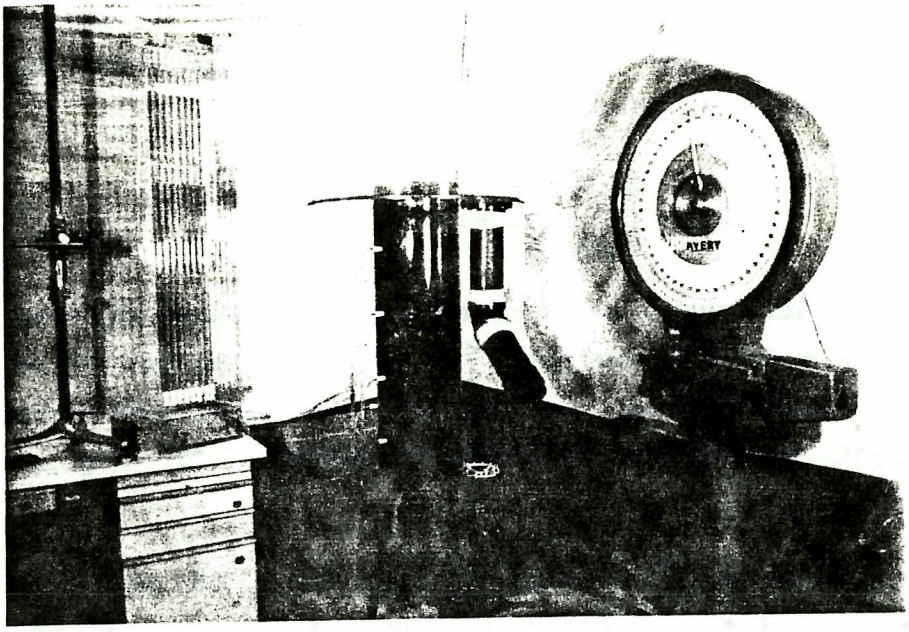
Length:	1000 mm
Inside diameter:	285 mm
Volume:	67 L

The hydrostatic head available from the constant head tank was 2.9 m at the base of the column. This head proved to be sufficient to provide for non-Darcy flow for all the materials tested, but was not sufficient to induce a quick condition in the material in the column.

Flow occurred upwards through the rock in the column and passed unrestricted into a weighing tank. Flow was controlled by a valve near the base of the column. Piezometric pressures were obtained using brass tubes at eight equally-spaced locations in the centre of the column, and the piezometric head readings were precisely measured with a cathetometer at each flow setting. The tips of these piezotaps pointed upward to avoid the influence of the kinetic head and to facilitate determining the exact location of each tap in the column after each test. Maximum bulk velocities using this apparatus were of the order of 10 cm/s.

3.1.2 Methodology

The first step in preparing for a column test was the preparation of the rock material by sieving it to achieve the desired size fraction, and washing it to remove excess fines. This rock was then placed in small quantities (lifts) in the column. After each lift the material was compacted if any compaction was required for the test. Compaction consisted of dropping a tamper of known weight a known height a predetermined number of times. The piezotaps were inserted at intervals of approximately 11 cm during the process of adding lifts. There were eight piezotaps in total, as shown by the



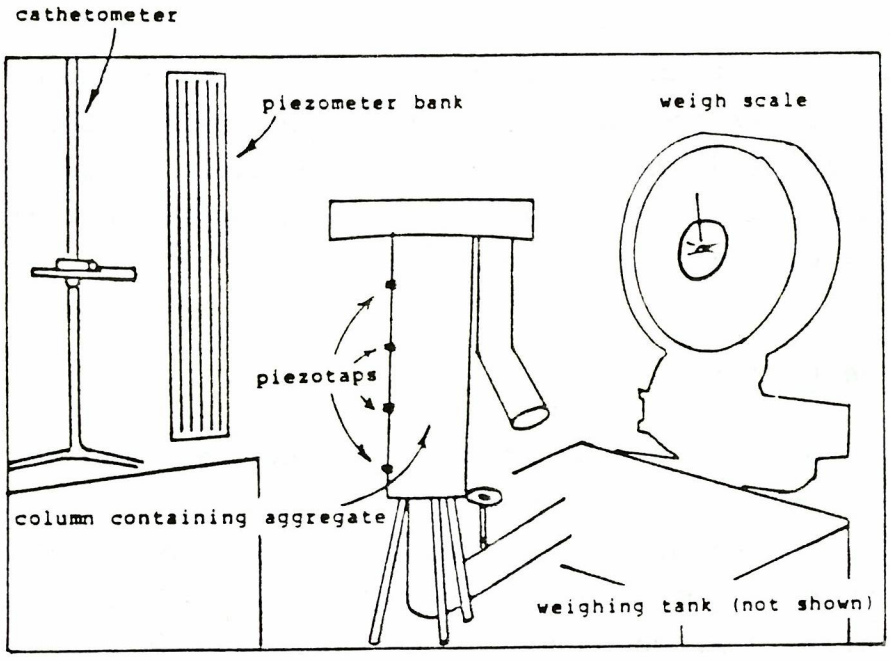


Figure 3-1. Packed column apparatus.

tubes protruding from the wall of the column in Figure 3-1. Once the column was full the piezotubes were connected to a piezobank and the pumping of water could begin.

After filling the constant head reservoir, the discharge control valve was opened and the piezotubes were primed by suction. The control valve was then opened to its highest flow setting. This showed whether the position of the piezobank was high enough. It also indicated whether the water supply rate was sufficient to maintain the level in the constant head tank.

At this point the test commenced. To begin with the flow was reduced to a low flow setting. The eight piezolevels were read and recorded with a cathetometer, a precision instrument for measuring height differences. For a given flow setting the time required to collect 100 kg (or more) of water was measured three times with a stopwatch accurate to 0.2 seconds. The water temperature was recorded to permit accurate determination of the density of the water. In this manner a bulk velocity was determined by computing the volume of water that passed through the column of known diameter in a known time.

After each set of eight readings, the flow was increased so that the maximum piezometric height increased by about 4 cm. The settings of the system were left unchanged for a short time to allow it to reach a new equilibrium state. The spirit level on the cathetometer was then releveled if required, and the next readings were recorded. This procedure was repeated until the maximum possible flow was reached. At this point the control valves were shut off and the pump was shut down. The material in the column was then removed by hand and was spread out on a large board to air dry for a few days. The final data set for a single test consisted of 10 (or more) values of the bulk velocity and of the average hydraulic gradient (dimensionless) associated with each bulk velocity.

3.1.3 Characterization of the Porous Media

In this study three different types of material were used in the column tests:

1. crushed limestone of different sizes, as supplied by a local

quarry,
2. a graded subrounded gravel of glacial origin,
3. round glass marbles.

Samples of the materials used in selected column tests are shown in Figure 3-2. All material used in the flume tests was crushed limestone. Tables A-1(i) to A-1(iii) in Appendix 1 list the properties of the various porous media used in the column tests.

3.1.3.1 Characterizing individual particles

Table A-1(i) (Appendix 1) presents the particle sizes for the material used in each column test. The representative particle size was determined by measuring with calipers the intermediate axis of 25 to 200 particles for each test. Figure 3-3(a) shows the definition of the "a", "b", and "c" axes of a particle, and Figure 3-3(b) is an example Zingg diagram indicating the variability in shape for the material used in column test 7. Table A-1(ii) (Appendix 1) indicates the proportion of the most common particle for the media used in each test. In Table A-1(iii) (Appendix 1) the computed sphericities, the mean shape factors, and an approximate value of roundness for each material (Krumbein and Pettijohn 1938) are presented. The sphericities were computed using the following equation:

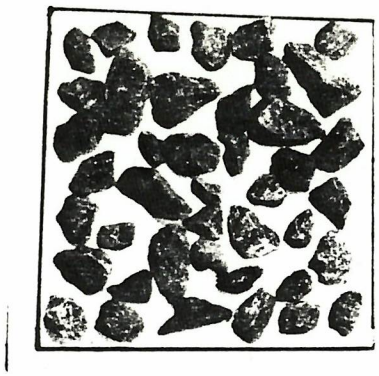
$$\text{Sphericity} = \left[\frac{V_P}{V_{SP}}\right]^{1/3} \qquad [3\text{-}1]$$

where:

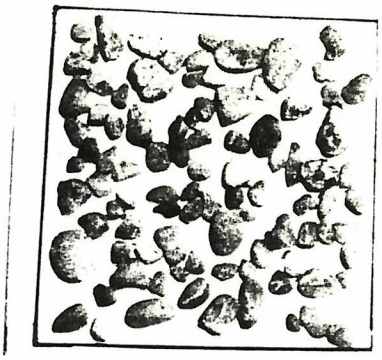
V_P = volume of particle, determined as mass/density,
V_{SP} = volume of circumscribing sphere.

Sphericity is a measure of the shape of the particle in that it indicates how closely the major axes of the particle approximate a sphere. The shape factor, SF, is a measure of the oblateness of the particle; expressed as:

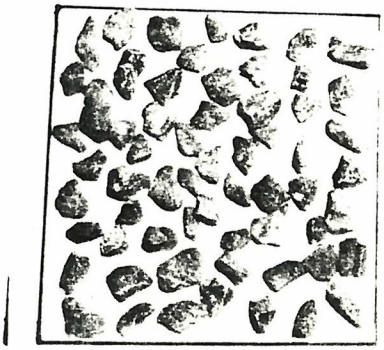
$$SF = \frac{c}{\sqrt{a\ b}} \qquad [3\text{-}2]$$



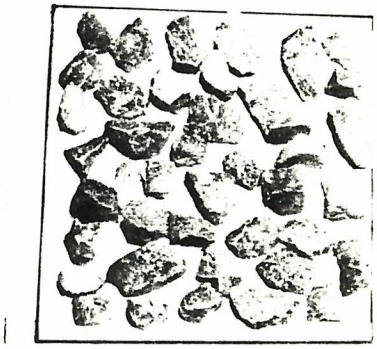
column tests 1 to 4



column test 5



column tests 6, 11 and 12



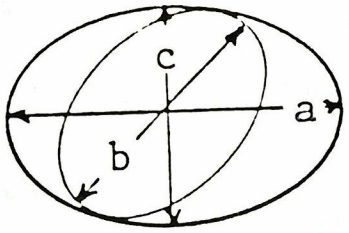
column test 7



column test 8

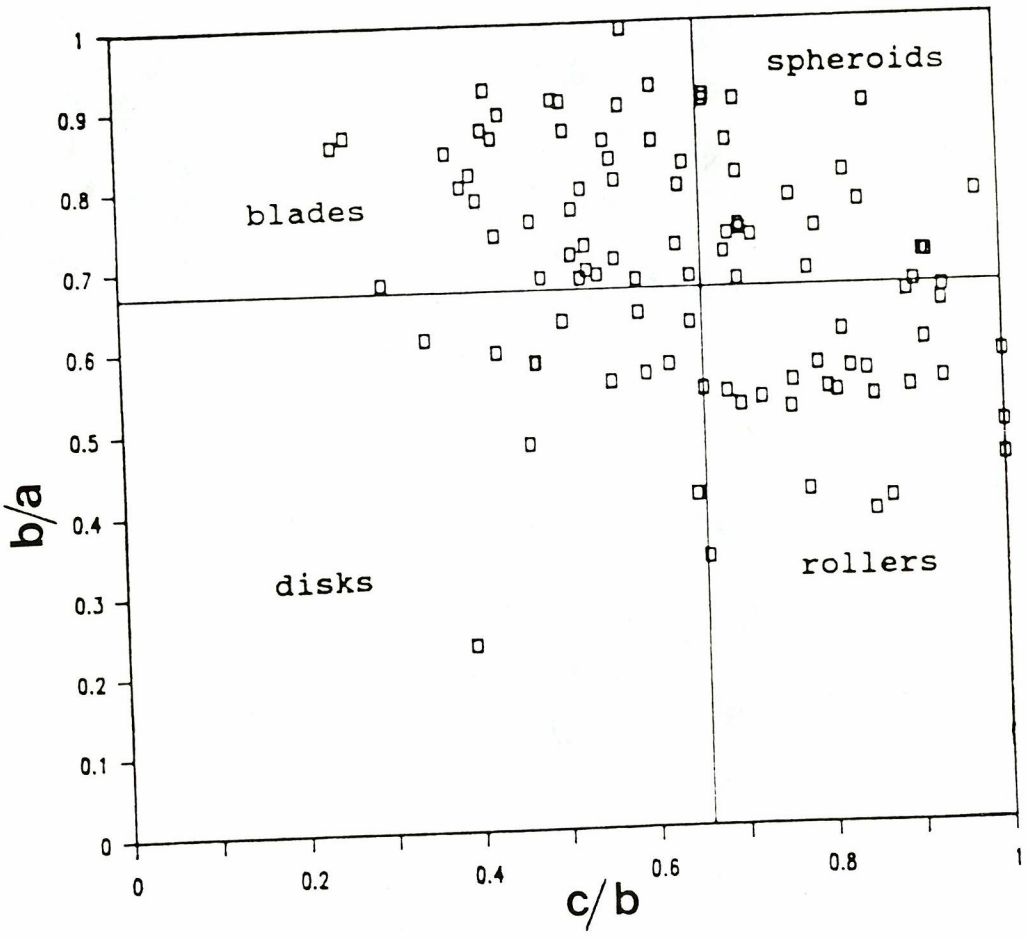
10 cm

Figure 3-2. Material used in selected column tests.



a > b > c

a) definition of the axes of a particle.



b) typical Zingg diagram (sample of particles used in column test 7).

Figure 3-3. Characterization of particle shape.

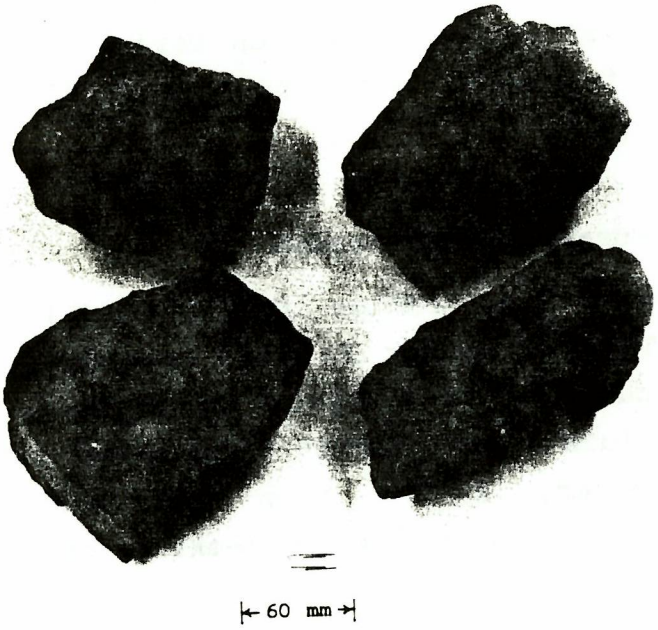
It appeared that the angularity of the crushed limestone was quite independent of size. However, it was found that the relative proportions of shapes of stones varied from size to size. As the stone size increased, more and more of the particles were found to be disk-shaped.

3.1.3.2 Hydraulic mean radius

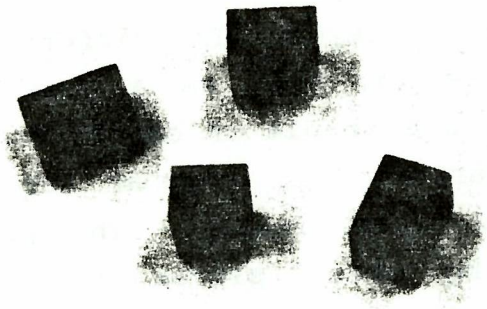
The hydraulic mean radius (Taylor 1948) is defined by equation [2-16]. This parameter is more appropriate for use in hydraulic studies because it is a measure of the pore size in the packed bed. Since the fluid flows through these pores it is more rational to use this parameter, rather than the nominal particle size, to characterize the media when seeking correlations with hydraulic behaviour.

In order to compute this parameter a means of measuring the surface area of the particles was needed. Based on similar work done by Hedlin and Collins (1961) stones were coated with varnish and then coated with powdered nickel. The technique to determine surface area consisted of coating individual rock particles with a thin layer of varnish. Before the varnish was dry, powdered nickel (-48 mesh to +100 mesh) was sprinkled on the rock, which then adhered to the rock in a uniform layer. The difference in mass between coated and uncoated rocks was used as a measure of the surface area. Figure 3-4(a) shows a sample of coated rocks. Calibrations of the technique were performed on regular surfaces for which the area could be computed geometrically. The first such calibration was obtained by coating cubical pieces of limestone, cut specially for this purpose (see Figure 3-4(b)). The second involved the coating of machined alumiunum shapes of precisely known surface area.

The third consisted of applying the nickel coating technique to flat regular rock surfaces. Under this method eleven rocks of 130 mm nominal size with one relatively flat surface with natural texture were selected. A cut parallel to the flat surface was made at a depth of approximately 20 mm in order to separate this surface from the rest of the rock. These pieces were then masked-off and the nickel coating technique was applied to the rectangular area having a natural texture. The coefficient of variation for coverage was



a) rocks coated with powdered nickel (average diameter 130 mm).



b) coated geometrically regular surfaces used for calibration.

Figure 3-4. Nickel coating technique applied to crushed rock.

only about seven percent, indicating that this coating technique was also quite reproducible. It is therefore concluded that whether limestone "cubes" or flat limestone surfaces having natural roughness were used had little effect on reproducibility. The fact that the rates of coverage for limestone "cubes" and for the aluminum objects were higher than for the specially-cut limestone slices can be partly attributed to differences in operator technique. Also, in general, a thicker layer of varnish was unavoidable when it was necessary to coat all the exposed surfaces.

The rate of coverage C_o (expressed as cm^2 per gram), selected for the calculation of the surface areas of the smaller rocks was the mean value associated with the "limestone cube" calibration (method 1). This coating rate was chosen because the thickness of the nickel coating on the cut limestone cubes appeared to be about the same as the coating on the smaller rocks. The surface area (S_A) for each rock was computed as:

$$S_A = C_o M_N \qquad [3-3]$$

where:

C_o = coating rate (cm^2 per gram of nickel);

M_N = mass of nickel only, (equal to mass of object after nickel coating minus mass of object before nickel coating (g)).

Results were found to be reproducible within about 10 percent of true areas, as given in Table A-1(iv) (Appendix 1). The surface area of the material in the column was estimated on the basis of average surface area per unit mass for 25 to 200 particles. Having the surface area for a sample of known porosity permitted calculation of the hydraulic mean radius according to equation [2-16]. The total surface area was computed from a pro-rating based on mass. Table A-1(iii) (Appendix 1) gives the hydraulic mean radius estimated for each column test.

3.2 STUDIES IN THE GLASS-WALLED FLUME

Figure 3-5 shows an example of a model dam in the glass-walled flume, located in the hydraulics laboratory, University of Ottawa. A coordinate grid on the glass permitted the observer to record the

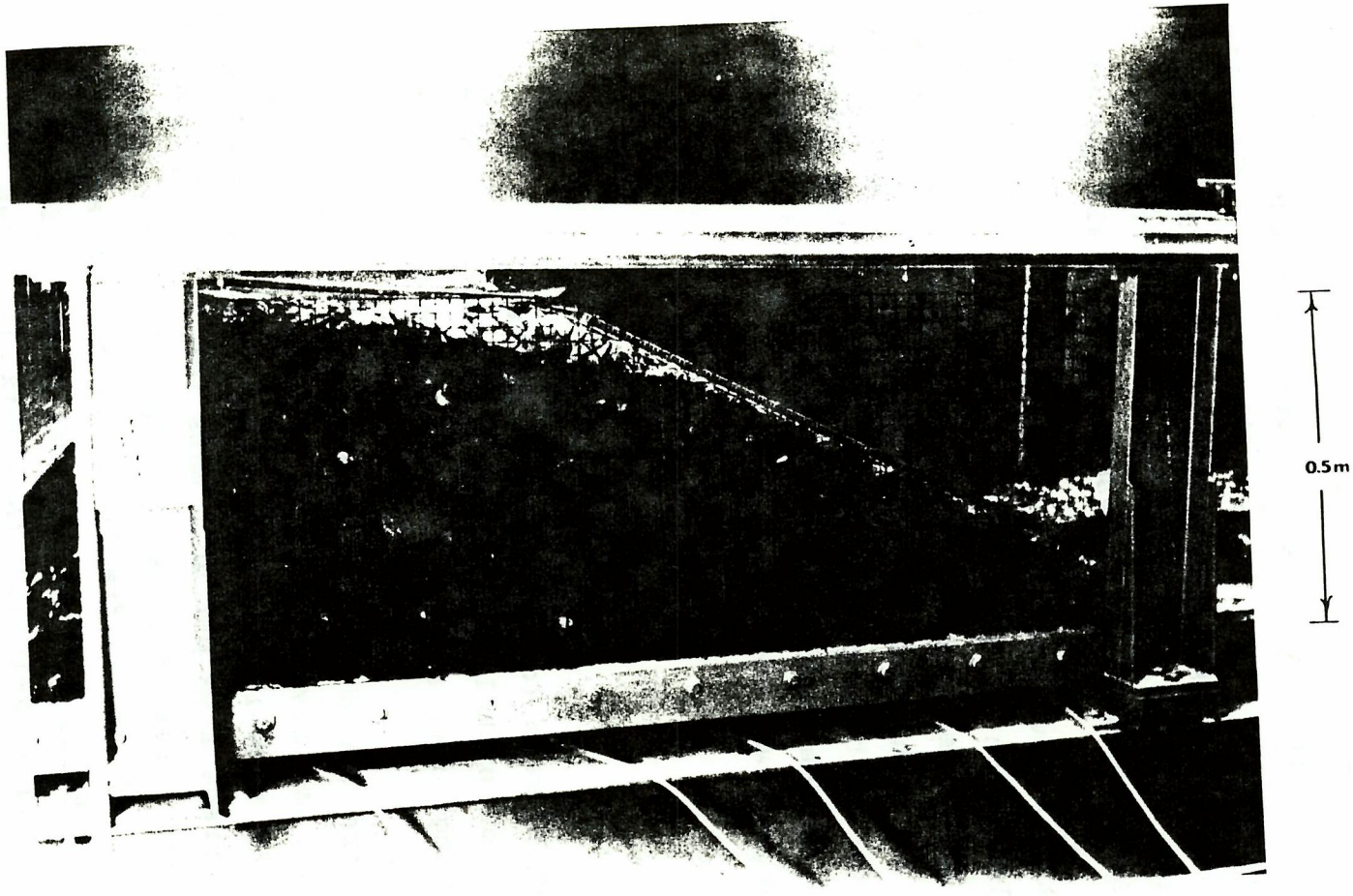


Figure 3-5. Typical model dam in glass-walled flume.

position of the phreatic surface, the location of the point of emergence, and the seepage surface. An example of the rise in the phreatic surface with increasing discharge is shown in Figure 3-6. Discharge was measured with a 90° V-notch weir installed in the collection tank. Upstream and downstream water levels were measured with a point gauge or with a measuring tape on the glass. The tailwater level downstream of the dam was adjusted by a variable-height control gate at the downstream end of the flume. The stage-discharge curve was obtained by increasing the discharge in steps and recording the upstream water level and discharge at each step, after equilibrium conditions were attained. The flume was 38.5 cm wide and could accomodate a model dam about 0.5 m high, depending on the amount of overflow desired. For this width of flume particle diameters of about 35 mm nominal diameter can be accommodated. For the safety of the glass and because of greater availability, 25 mm (nominal -1 1/2" to +3/4") crushed gravel was used. This was the same material as was used for column test 7 and has the associated geometric properties listed in Tables A-1(i) to A-1(iii) (Appendix 1).

Preliminary tests were directed at investigating the threshold discharge (minimum discharge causing complete failure) for various downstream slopes, as well as performing general investigations into the effects of tailwater and crest width. These tests were performed with no restraint on the downstream face of the dam. Consequently, as the experiment progressed from low to high discharge, more and more material eroded away from the downstream face. Thus, the shape of the dam changed as the experiment progressed. It was therefore concluded that systematic study of any parameter, except threshold discharge, could not be done without restraining the downstream face. With this in mind a systematic parametric study was planned.

This systematic study considered the following four parameters (refer to Figure 1-1):

i) the relative crest width B_c/B_w,
ii) the downstream slope θ,
iii) the presence or absence of an upstream impermeable facing,
iv) the relative tailwater level h_{TW}/H.

The effect of the above four parameters on the following two hydraulic characteristics of the dam were investigated:

(i) the stage-discharge curve, and
(ii) the location of the free surface (including the height of the point of exit, h_e).

Table 3-1 summarizes the experiments associated with the parametric study undertaken in the glass-walled flume (tests GF27 to GF35 in Table A-1(v), Appendix 1):

Table 3-1
Tests in Glass-walled Flume

All upstream slopes at 45°, downstream slopes as indicated.
Material: 25 mm crushed limestone.
TW = effect of increased tailwater examined.
F = measurements of force needed to prevent failure.
B_c = width of crest, B_w = base width

crest	$B_c = 0$	$B_c = 0.25 \cdot B_w$	$B_c = 0.33 \cdot B_w$
slope:	1V:1H	1V:1H,+TW, +F	1V:1H
slope:	1V:2H	1V:2H,+TW, +F	1V:2H
slope:	1V:3H	1V:3H,+TW	1V:3H

In this study the exit height was estimated by recording each complete free surface (which is comprised of the seepage surface and the phreatic surface) at the experimental stage and by then plotting this surface on the two-dimensional cross section of the model dam. The value of h_e at each level of discharge was then measured graphically. This was felt to be a more objective way of determining the exit height, especially for slopes of 1V:3H for which the exact location of the exit point was difficult to assess in the laboratory.

All the above tests were performed with and without an upstream impermeable facing (UIF), resulting in the development of 21 separate rating curves. For those tests with a UIF, the crest of the facing was at 80% of the height of the dam. Some piezometric pressure measurements were taken at the base of the dam where predrilled tapping points were already in place. In some tests prior to the above parametric study the piezometric pressures were

also obtained within the body of the dam through the use of tubular probes. Also, in some cases, the velocity in the seepage face zone was measured either with a propellor-type Nixon velocity probe (propellor diameter 1 cm) or with a pitot tube (diameter 3 mm). Figure 3-7 shows the probe within the seepage surface. Given the small depth of flow on the seepage face which normally occurs when the dam functions in a flowthrough mode, it was found to be difficult to define more than two or three points in a given vertical.

3.3 STUDIES IN THE LARGE FLUME

Figure 3-8 shows a model flowthrough embankment in the large masonry flume in the University of Ottawa hydraulics laboratory. Table A-1(vi), Appendix 1 summarizes the tests carried out in the large flume. This flume is 1.38 m wide and 0.75 m deep. Discharge was adjusted via a butterfly valve on the 33 cm (13 inch) supply line. Discharge was measured by measuring the pressure drop across a calibrated orifice plate having a 17.8 cm (7 inch) orifice opening. Hydraulic measurements in the glass walled flume were more convenient than in the large flume since floor taps already exist in the glass walled flume and the glass permits viewing of the free surface. A description of the features which allow hydraulic measurements in the large flume follows.

On the right side of Figure 3-8(b), against the wall of the channel, can be seen a narrow acrylic box with rectangular openings at the top. This transparent box has a grid inscribed on it, and this permitted the observer to record the coordinates of the free surface by using a mirror to view its path. In addition, piezometer taps inserted in the body of the dam from above were connected to a piezometer bank, and this system permitted the measurement of pore pressures in a model dam. In this way it was hoped that any non-Darcy flow model giving pore pressures at regular intervals could be evaluated by comparison with the data collected in the manner described above.

The large masonry flume was used for three purposes:

1. To obtain measurements of the threshold discharge for comparison

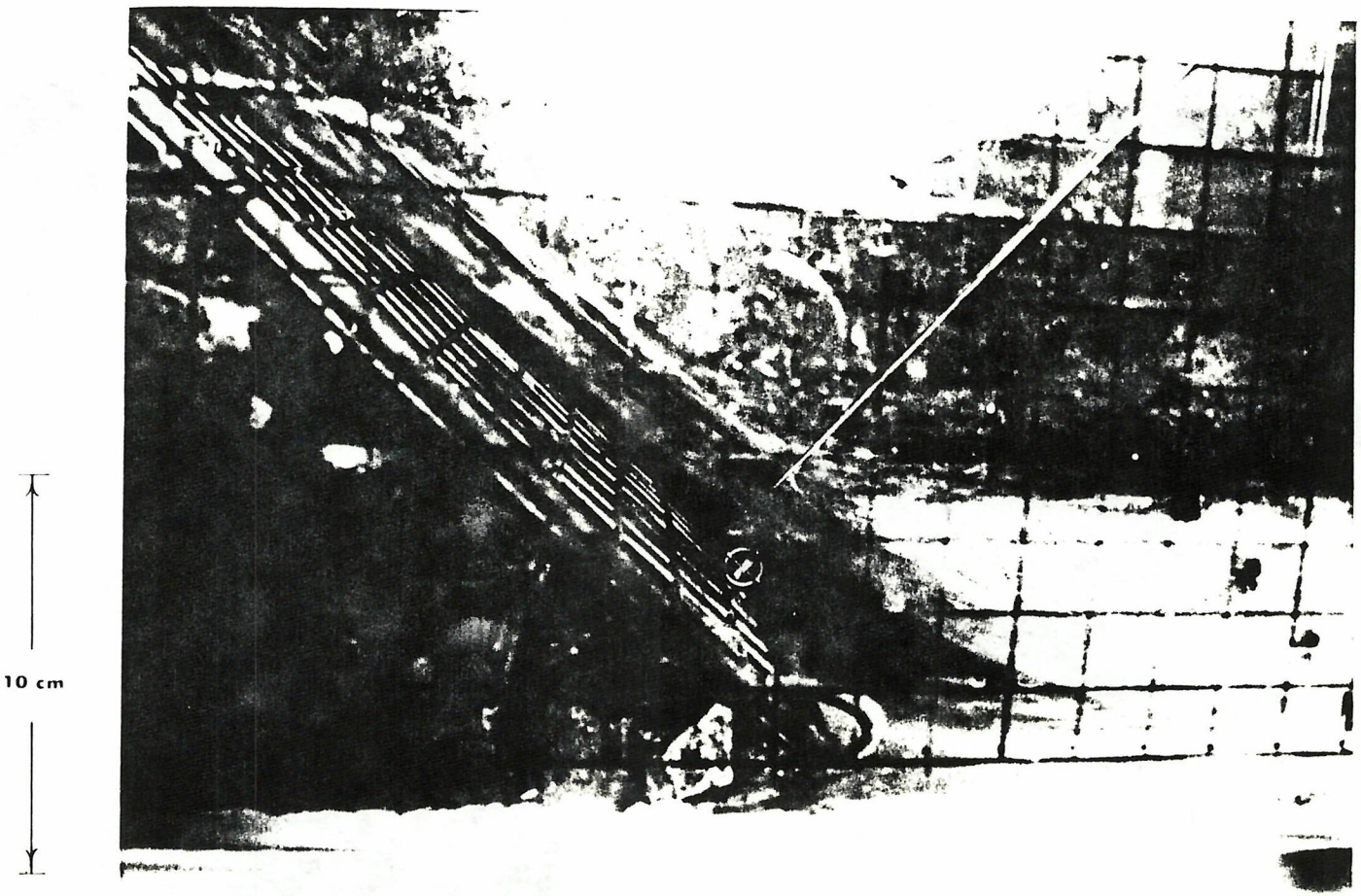
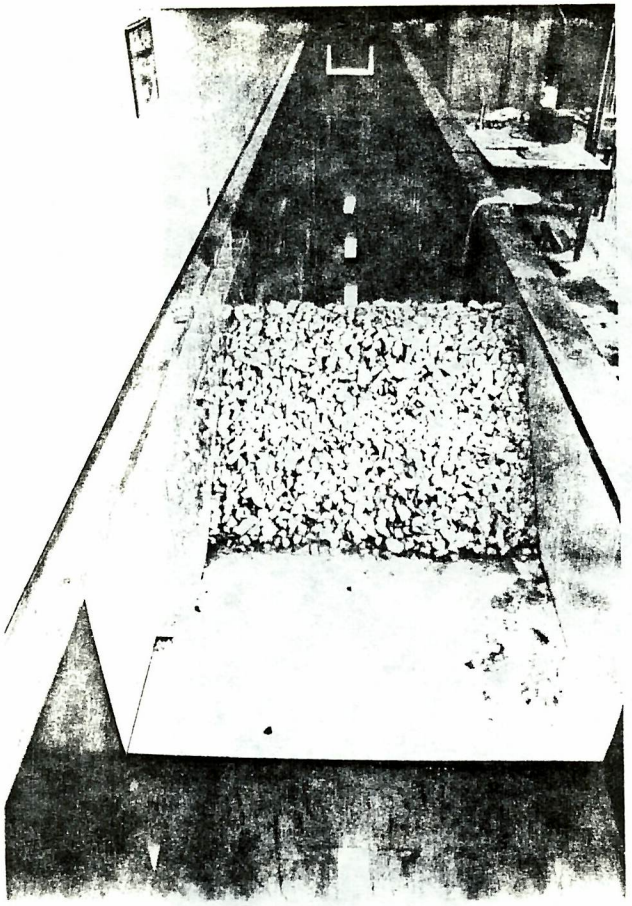
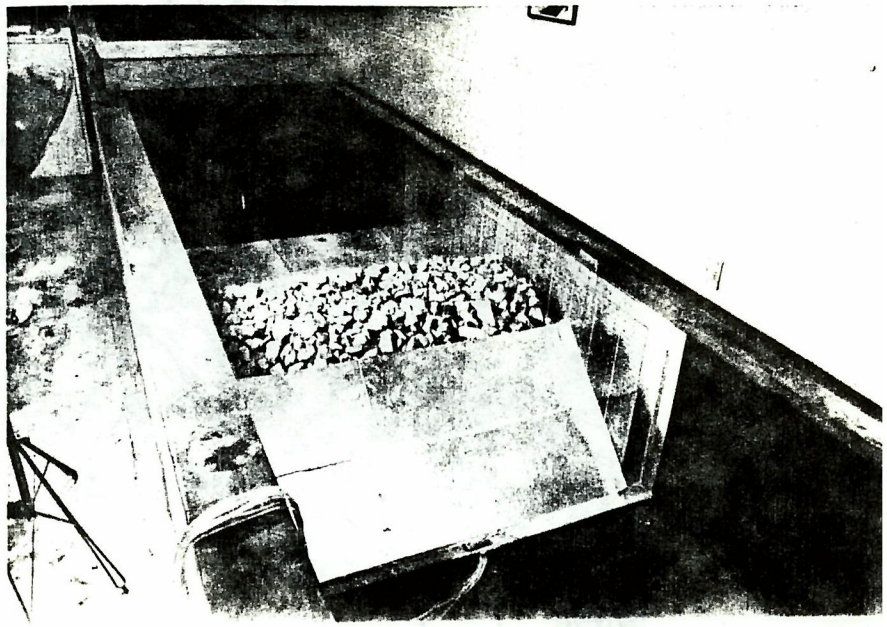


Figure 3-7. Nixon probe used for measuring velocity within the flow making up the seepage surface.

flume width ≅ 1.4 m



a) looking upstream.



b) looking downstream.

Figure 3-8. Model flowthrough rockfill dam in large flume.

with similar measurements in the glass-walled flume.

2. To observe how, for the same two-dimensional shape, the increase in particle size (from the 25 mm size used in the glass-walled flume) altered the general hydraulic behaviour. It was hoped that this would provide valuable information of scale effects on work done in the glass flume. Due to the labour-intensive nature of changing dam configurations in the large flume (involving many hundreds of kilograms of rock) a limited number of two-dimensional dam shapes were considered.

3. To measure the free surface and the internal piezometric pressures under conditions of fully-developed turbulence.

4. To perform experiments to measure the force required to restrain the downstream face under various discharge conditions.

Figure 3-9 shows the arrangement of the force-measuring apparatus for the large flume. Plan and side-view schematic diagrams of this apparatus are shown in Figure 3-10. Preliminary experiments on force measurement in the glass-walled flume showed that the mobilization of material near the crest invalidated the assumption of a overall triangular force distribution acting on a restraining frame covering the downstream face. By dividing the downstream face into four sections, it was hoped that some information of the variation of the bursting force over the length of the face would be obtained.

3.4 LOW TEMPERATURE FLUME EXPERIMENTS

The cold room at the National Research Council of Canada has the capacity to sustain temperatures in the vicinity of -16°C. A 1.2 m wide flume was constructed out of plywood in the cold room in late 1988, and a model rockfill dam was constructed in the flume using 130 mm rock. The interior of the dam was instrumented with 22 piezotaps and 32 thermocouples. A pump recirculated water through the flume, with provision for temperature modification using flow from a large reservoir of water at 0°C. Figure 3-11 gives the overall layout of the experimental set-up. Initial concerns about rapid cooling of the recirculated water to the point of frazil generation proved to be unfounded, and a fan was added to cool the

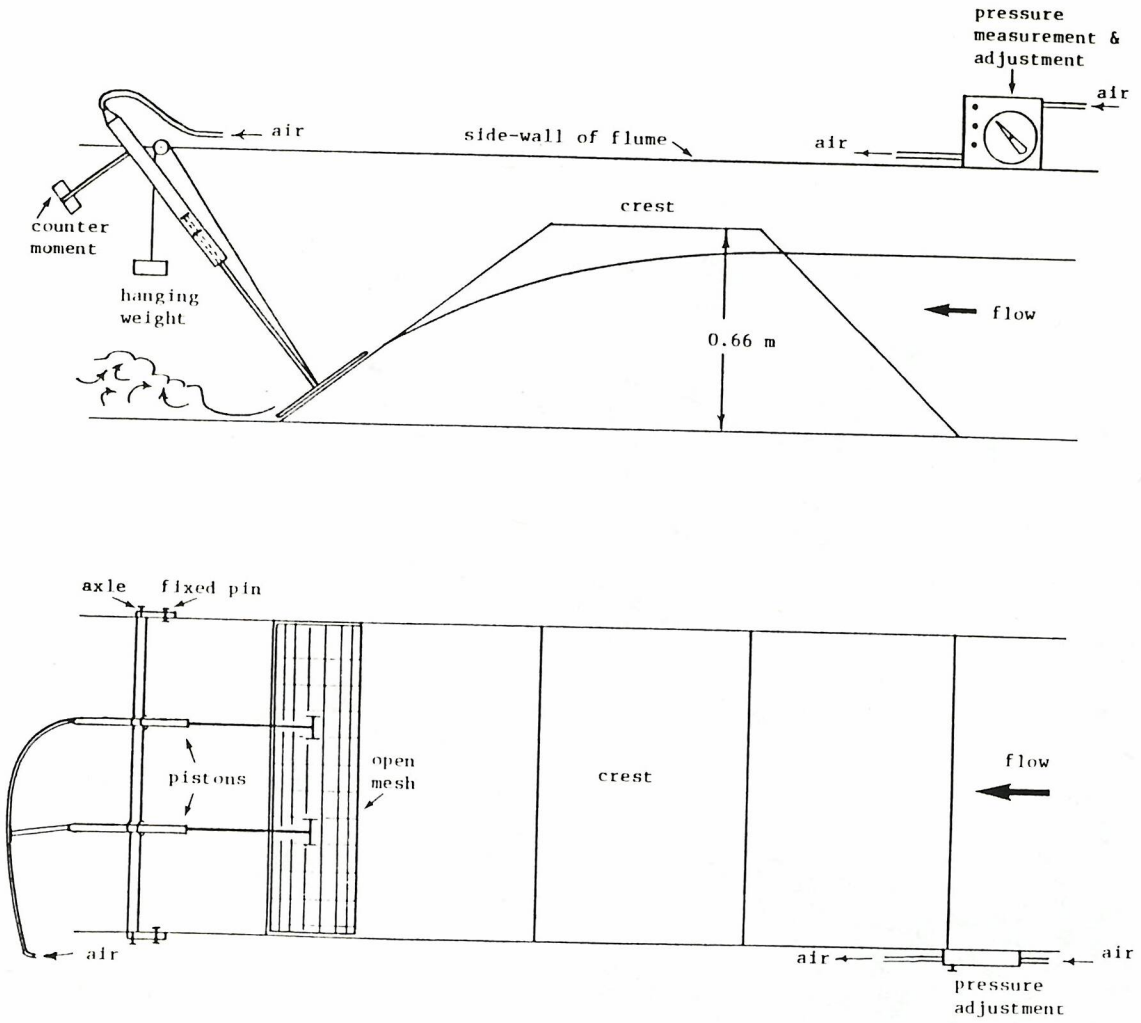


Figure 3-10. Arrangement of model dam and force-measurement system in large flume.

flume width ≅ 1.2 m
average particle size ≅ 130 mm

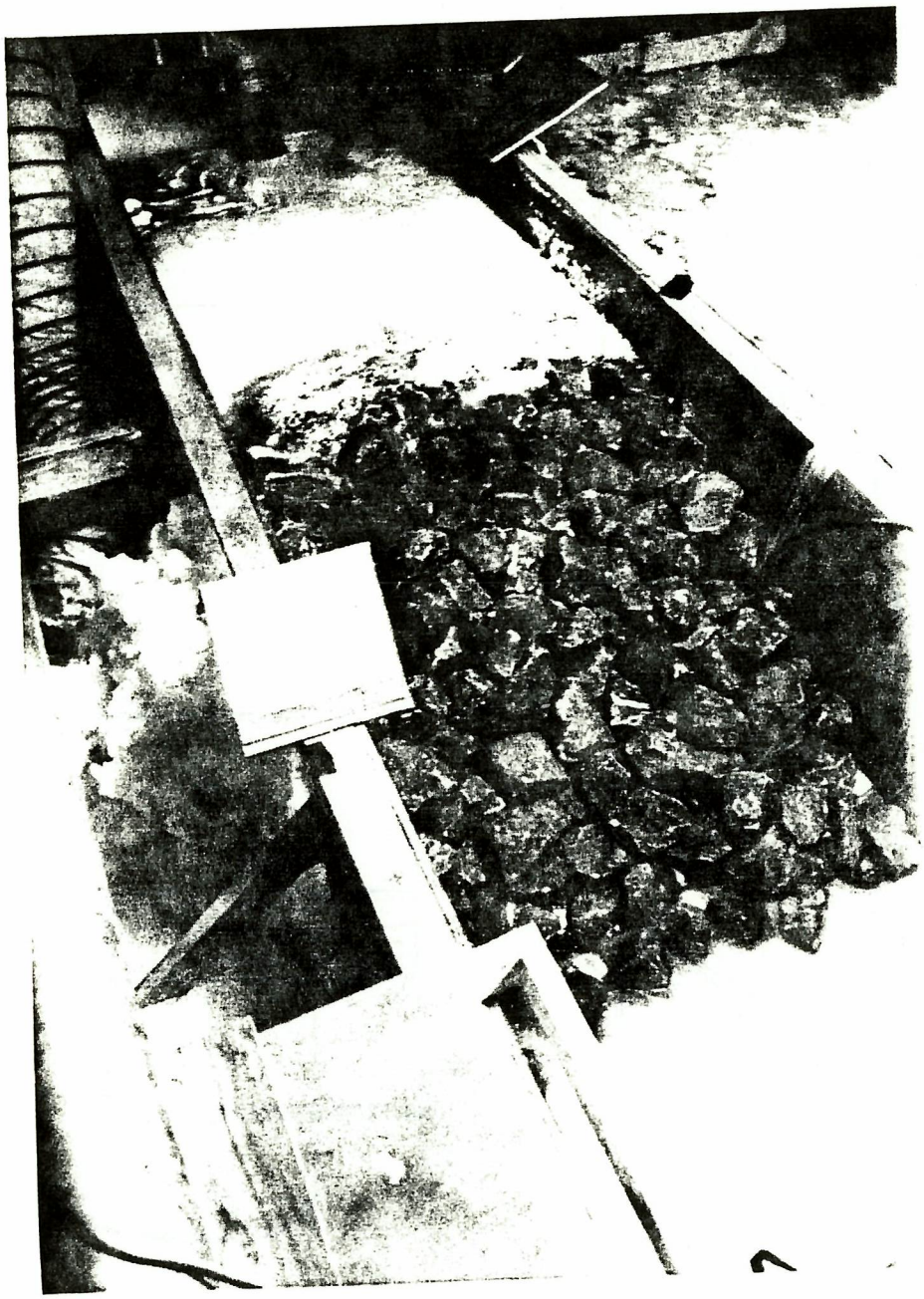


Figure 3-11. Layout of flume experiment in the NRCC low temperature laboratory.

upstream water surface.

Three experiments were performed, each lasting about 3 days. The experiments examined the following scenarios:

i) maximum flow (about 69 L/s) with no impermeable facing,
ii) same maximum flow, but with an impermeable facing,
iii) a low flow (about 20 L/s) with an impermeable facing.

Even though the water in the piezometer lines was mixed with an equal part of ethylene glycol, some difficulties were encountered making the piezotaps function.

The main heat sink for the water moving through the dam was by convection to the surrounding air. The heat sources were from the recirculating pump and a small amount of heat from viscous dissipation of hydraulic energy within the dam.

4.0 DESIGN CONSIDERATIONS I: INTERNAL FLOWS

4.1 DEVELOPMENT OF THE STAGE-DISCHARGE CURVE

The stage-discharge curve of a flowthrough rockfill dam is a curve relating the upstream water level to the discharge which passes through, and possibly over, the structure. Before this relationship can be estimated, the non-Darcy flow parameters, such as a and N in equation [2-3c], must be determined. These parameters in turn depend on the physical characteristics of the porous media, such as hydraulic mean radius and porosity. The determination of a stage-discharge curve solely from the properties of the media and from the shape of the dam is a fundamental task facing the designer possessing only this basic information. A satisfactory method for generating the stage-discharge curve has been developedbased on the hydraulic tests performed in this study and on laboratory estimates of the hydraulic mean radius. The description of the method developed begins with the determination of the hydraulic mean radius of the porous media making up the dam.

4.1.1 Estimating the Hydraulic Mean Radius

A convenient expression for computing the hydraulic mean radius is:

$$m = \frac{e}{A_{vs}} \qquad [4\text{-}1]$$

For a media made up of perfect spheres the following expression applies:

$$A_{vs} = \frac{\pi d^2}{\frac{1}{6}\pi d^3} = \frac{6}{d} \qquad [4\text{-}2]$$

Combining [4-1] and [4-2]: $m = \frac{e\,d}{6}$ [4-3]

where:

m = hydraulic mean radius,

e = void ratio,

A_{vs} = volume-specific surface area, d = particle diameter.

The sphere is the geometric shape which has the least surface area per unit volume. Highly angular rocks with many sharp and jutting edges are relatively inefficient with respect to surface area per unit volume and will have higher values of A_{VS}. The inefficiency is due to the shape of the rock as well as to its roughness. A smooth but oblate ellipsoid will also have poorer surface area efficiency than a sphere. Plate-like rocks such as shale will also have relatively high values of A_{VS}. Noted that equation [4-1] should not be used with porous media made up of plate-like rocks because a significant amount of particle area is lost to inter-particle contact. When the amount of interparticle contact is large the assumption that the surface area of the voids is equal to the surface area of the rocks is not valid. Smoother and rounder rocks will approach the value of A_{VS} for spheres.

Equation [4-2] can be restated as:

$$A_{VS} = \frac{J}{d} \qquad [4\text{-}4]$$

where the constant J is 6 for spheres. The extent to which the value J for a particle exceeds the value of J for spheres indicates the degree of surface area efficiency of the particle. The relative surface area efficiency, r_E, can be stated as:

$$r_E = \frac{J_{ROCK}}{J_{SPHERE}} \qquad [4\text{-}5]$$

Hence, [4-4] becomes:

$$A_{VS} = \frac{r_E \, J_{SPHERE}}{d} \qquad [4\text{-}6]$$

Therefore:

$$m = \frac{e \, d}{6 \, r_E} \qquad [4\text{-}7]$$

The method used in this study to measure the surface area of crushed limestone rocks for a range of sizes was describe in section 3.1.3.2. A comparison between Wilkins' (1956) estimates for the

surface area of crushed dolerite with the surface area determinations made in this study can be made. The points for mass-specific surface area were obtained from Wilkins' work by abstracting the points of inflection from "Figure 2" presented in Wilkins (1956). Mass-specific surface area is related to volume-specific surface area by equation [2-20]. Figure 4-1(a) gives the values of A_{MS} determined in this study, Figure 4-1(b) gives the points determined by Wilkins (1956).

Table 4-1 presents a comparison between Wilkins' estimates of r_E and those of the present study:

Table 4-1

Comparison of Particle Surface Area Efficiencies

Wilkins (1956)			Present Study		
diameter (cm)	J_{ROCK}	r_E	diameter* (cm)	J_{ROCK}	r_E
2.29	9.33	1.56	1.94**	9.11	1.52
4.45	7.26	1.21	2.46	9.44	1.57
7.62	9.33	1.56	3.59	11.00	1.83
10.20	7.47	1.24	13.00	8.12	1.35
	mean:	1.39		mean:	1.57

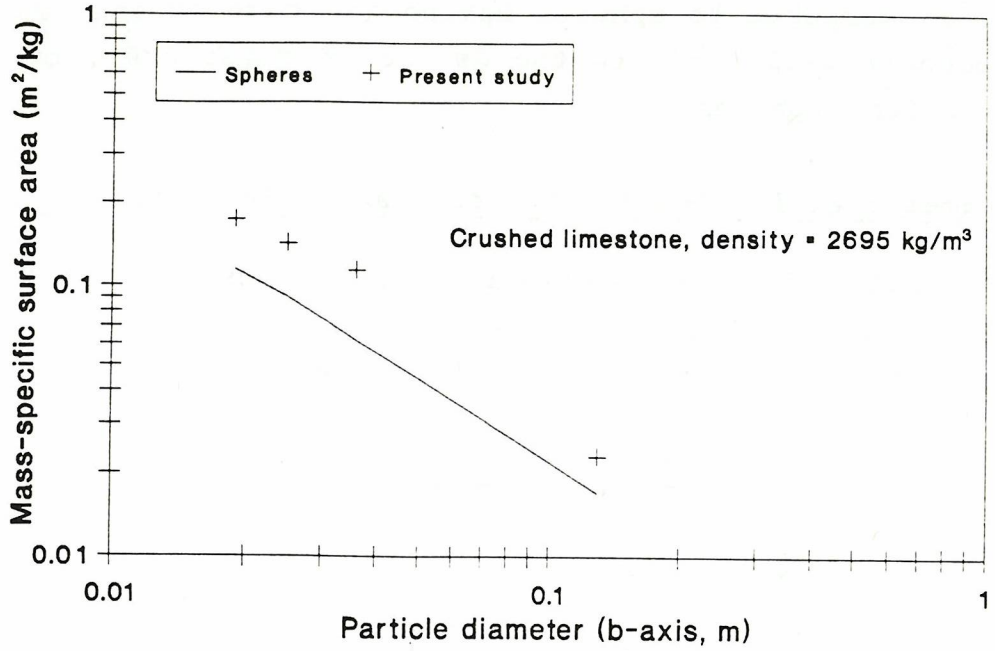
* mean value for a sample numbering from 49 to 75 particles.

** this aggregate depicted in Figure 3-2.

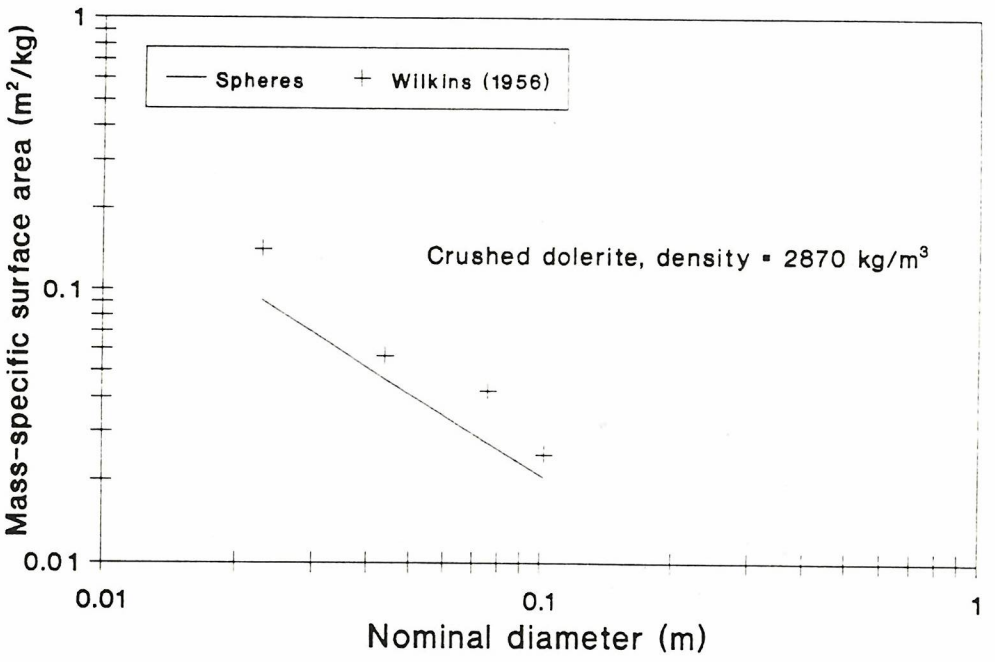
For the case of a graded rockfill, the following steps are suggested for determining m:

1. Obtain the grain size distribution by weight in the form of a histogram.
2. Estimate r_E for each size class and apply equation [4-7] to each class.
3. The value of the hydraulic mean radius may then be computed as a weighted mean.

Campbell (1989) suggests a value of J of 7.5 (implying an $r_E = 1.25$) as an inherent part of Wilkins' equation, and that the mean stone size be used for d. This Report does not recommend this because the r_E of each size class of rock should be evaluated using engineering judgment regarding the relative shape and angularity of the rock in



a) present study, using crushed limestone.



b) Wilkins' (1956) estimates for crushed dolerite.

Figure 4-1. Comparison of mass-specific surface area results for crushed rock.

each class as compared to spheres having the same nominal diameter. Such a procedure will indicate the degree of departure from the A_{MS} curve for perfect spheres.

4.1.2 Parameter Estimation for the non-Darcy Flow Equation

In section 2.1.1.1 five well-established equations were presented in which the non-Darcy flow parameters could be estimated without performing a hydraulic experiment. These are restated below:

Ergun $$i = \left(\frac{1-n}{n^3}\right)\left[\frac{150\nu(1-n)}{g\,d^2}V + \frac{1.75}{g\,d}V^2\right] \qquad [2\text{-}12]$$

Wilkins $$V = 5.243\ n\ m^{0.5}\ i^{0.54} \qquad [2\text{-}2]$$

or $$i = \left(\frac{0.0465}{n^{1.85}\ m^{0.93}}\right) V^{1.85} \qquad [4\text{-}8]$$

McCorquodale *et al* $$i = \left(\frac{70\ \nu}{g\ n\ m^2}\right) V + \left(\frac{0.81}{g\ n^{0.5} m}\right) V^2 \qquad [2\text{-}13]$$

Stephenson $$V_v = \sqrt{\frac{gdi}{K_s}} \qquad [2\text{-}8]$$

Martins $$V_v = \frac{K_M}{C_U^{\alpha}}\sqrt{2gedi} \qquad [2\text{-}10]$$

where all terms have been previously defined. Metre-sec units apply to equations [2-2] and [4-8], while the other equations are dimensionally homogeneous. In equations [2-12] and [2-13] the coefficient of V decreases in importance relative to the coefficient of V^2 as the level of turbulence approaches fully-developed turbulence. Equation [4-8] applies only to nearly fully-developed turbulence. It is noted that there is disagreement regarding the role of porosity in the above equations. Wilkins and Ergun use approximately the same power for n of 2, but McCorquodale uses $n^{0.5}$.

The following table illustrates a range of values possible for the coefficient a' preceding i, when using the above equations:

Table 4-2

Computed Coefficient a' in non-Darcy Flow Equations

Form: $V = a' i^{N'}$ eqn [2-3d]

Assume porosity = 39%, r_E = 1.6, and a uniform particle size.

b-axis particle diameter (cm):	30	15	3
Ergun* (1952)	0.40	0.29	0.13
Wilkins (1956)	0.29	0.20	0.09
McCorquodale* *et al* (1978)	0.40	0.27	0.09
Stephenson (1979)	0.33	0.24	0.11
Martins (1990)	0.42	0.30	0.13
Mean	0.37	0.26	0.11
Sample standard deviation	0.06	0.04	0.02
Coeff. of Variation	15.1%	15.6%	18.2%

* by regression analysis to obtain a power function form, over the range V = 0 to 25 cm/s. Note: N becomes less than 2 as d decreases.

It is evident that, for design purposes, the equations by Wilkins (1956) and by Ergun (1952) give comparable results a' for the above range of particle sizes. The lowest values of a' are consistently from Wilkins' equation, the highest from Martins' equation. An average value could be used for design purposes, as is done for the worked example in Appendix 6.

As was described in section 3.1, twenty one column tests were performed in this study to examine the relationship between the coefficient a, in equations of the form of [2-3c], and the characteristics of the media. Figure 4-2 summarizes how the results of this research compare with estimates of a given by Wilkins' (1956) equation. For Wilkins' equation the value of a was computed using the expression given by [4-8]. The experimentally determined values of a were those obtained directly from the hydraulic tests CT3 through CT21, the results of which are summarized in Table A-1 (vii) (Appendix 1). It appears that Wilkins' equation agrees reasonably well with observed values of a, especially for crushed rock.

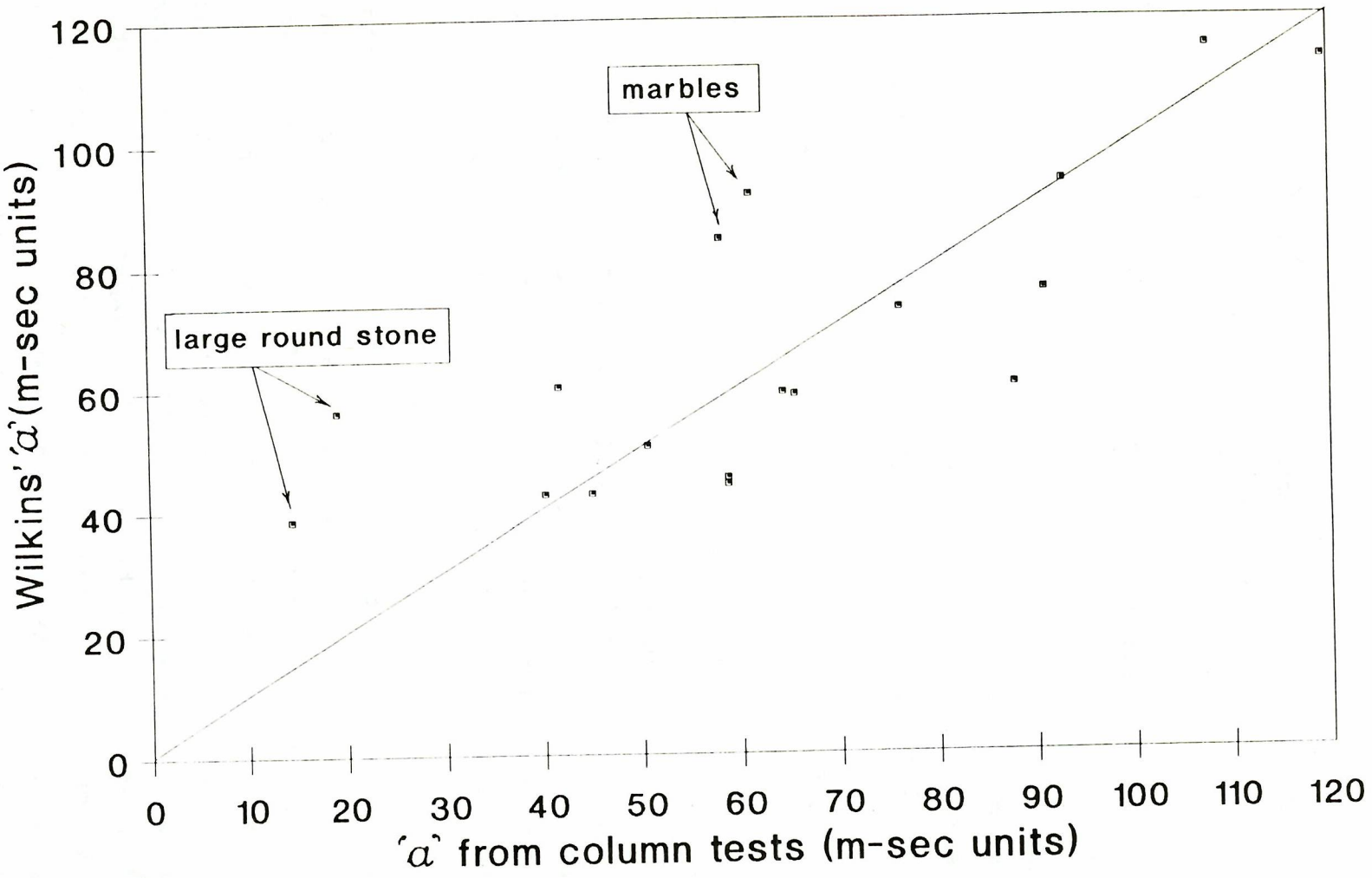


Figure 4-2. Comparison of observed values of a in equation [2-3c] with values computed using Wilkins' (1956) equation.

Departures from the straight line in Figure 4-2 can be attributed to the following four factors:

(a) For each column test a sample of rocks comprised of 25 to 200 particles was examined with respect to surface area. The total estimated surface area of the rocks in the packed column would have been somewhat different had the surface area of every particle in the column been estimated.
(b) The imprecision in the nickel-coating technique used to measure surface area of rocks in the sample.
(c) Differences in the value of r_E for the rocks used in this study and the rocks used in Wilkins' study. Expression [4-8] does not contain the parameter r_E, and this explains the sharp departure for round particles seen in Figure 4-2.
(d) The wall-effect. Using the wall-effect factor M from the Ergun-Reichelt equation [2-9b] for particles 25 mm in diameter within a column 285 mm in diameter gives an overestimation of the bulk velocity of about 7%. This error varied from one column test to the next, depending on particle size. Further, more detailed, estimates of the wall-effect were not justified since the Ergun-Reichelt equation was developed for spherical particles, and as such only gives an approximation of the severity of the wall effect in this case.

It is therefore concluded that:
(a) the effect of gradation is included in Wilkins' formulation for *a*. Graded media have lower porosities and also have lower values of m. There was reasonable agreement between Wilkins' *a* and experimental determinations (by column test) of *a* for crushed rock, whether graded or uni-sized.
(b) The parameter r_E has a significant effect on hydraulic behaviour. If the equation being used employs the particle diameter d rather than the hydraulic mean radius m, the effect of changing r_E can be considered simply by rearranging equation [4-8].
(c) Wilkins' hypothesis that *a* is inversely proportional to approximately the square of the porosity is reasonable. This assumption is also supported by the Ergun equation, which is a well-accepted equation in chemical engineering. However, based on

Table 4-2 it is evident that Wilkins' equation predicts the lowest velocities for a given hydraulic gradient. Other equations, based on far more experimental data, tend to predict higher velocities for a given gradient i.

4.1.3 Computing the Stage-Discharge Curve

Two cases are of interest when considering flowthrough rockfill structures. The first is when no impermeable upstream facing is present. This is of interest when the structure is used as a "leaky weir" for regulation of flow. The second is when an impermeable facing is present in order to increase the head in the reservoir. The former case will be discussed first.

4.1.3.1 The Case of No Impermeable Facing and No Tailwater

It was hypothesized that the hydraulic gradient for flow entering the upstream face of the dam is dependent upon the upstream water level and on the width of the dam, B_w. However, an expression was needed to describe the *effective* width of the dam. Clearly, a dam with a small crest width and a gradually sloping downstream face will not represent the same hydraulic barrier as a rectangular embankment of the same total width. The latter will cause a greater total head loss, and observations in the laboratory during the parametric study described in section 3.2 confirmed this. The effective width of the dam is defined as (refer to Figure 1-1 for definition of terms):

$$B_{eff} = \left(B_U + B_C + \frac{0.5\ H}{\tan\theta} \right) \qquad [4\text{-}9]$$

This effective width was made dimensionless by defining the aspect ratio of the structure as:

$$A_R = B_{eff}/H \qquad [4\text{-}10]$$

By performing a multiple non-linear regression analysis on data obtained from the parametric study in the glass-walled flume, the following equation was obtained:

$$i = 0.8\ A_R^{-3/2} \cdot (h/H)^{1.4} \qquad r^2 = 0.98 \qquad [4\text{-}11]$$

Note that the above value of hydraulic gradient is representative of the entire structure and has been derived from consideration of the hydraulic gradient in effect for flow entering the upstream face of the dam. This permits computation of the horizontal bulk velocity approaching the dam, using the following previously stated equation:

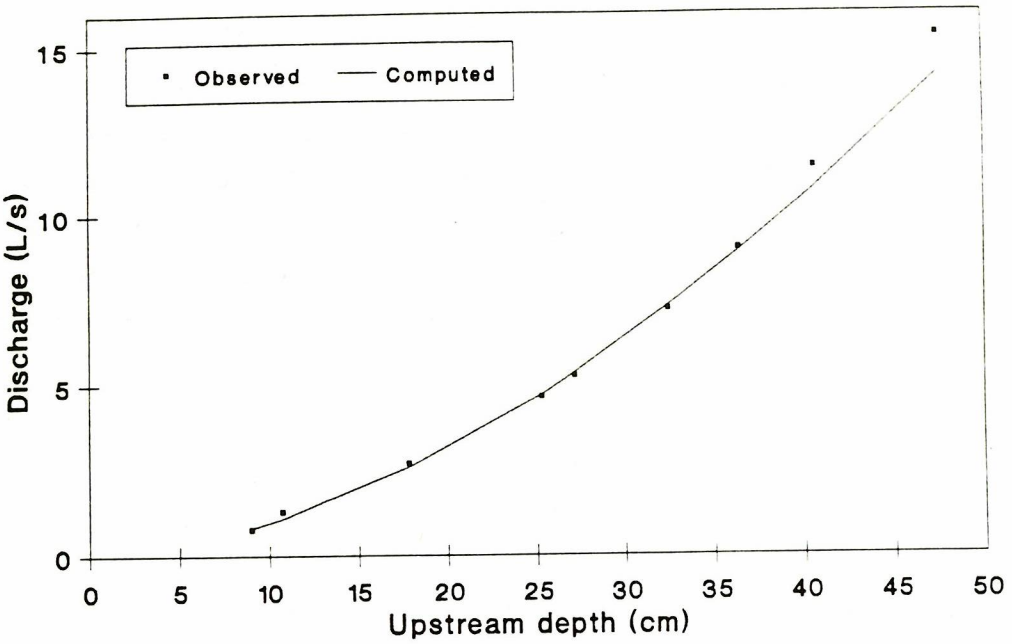
$$V = a' i^{N'} \qquad [2\text{-}3d]$$

Therefore:
$$Q = V\ A = \left(a' i^{N'}\right) h\ L \qquad [4\text{-}12]$$

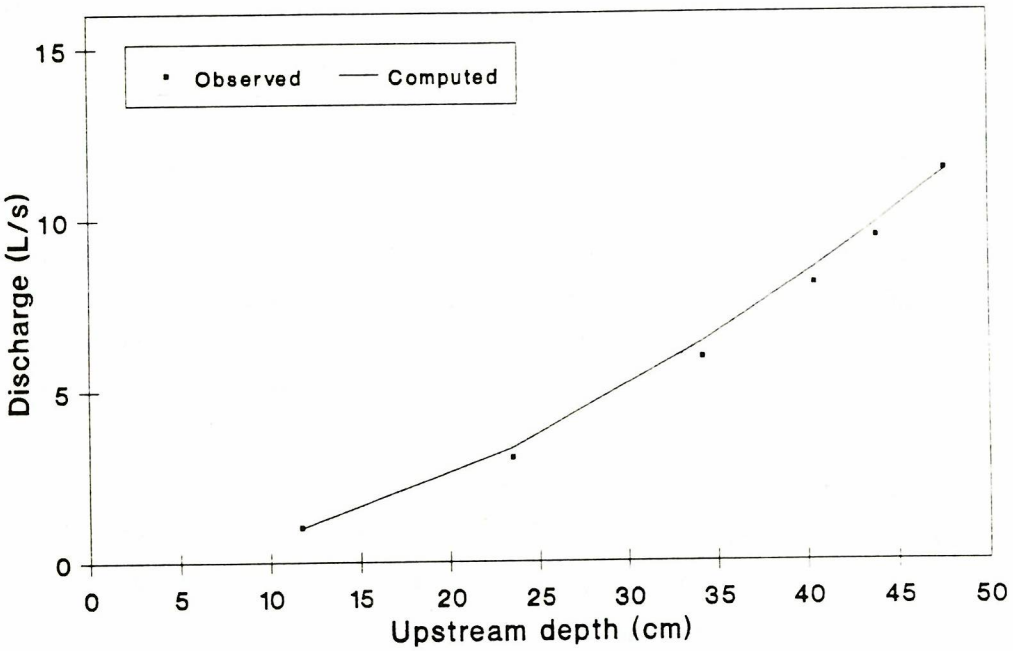
(For Wilkins' equation $a' = 5.243\ n\ m^{1/2}$, m/s units).

It should be noted that while equation [4-11] can be used with any consistent set of units, equation [4-12] must use those units associated with the units of a'. The rating curve equation [4-12] is valid in the range of $h < H$ for flowthrough model embankments with no upstream facing and no imposed tailwater level. For $h > H$ the rating curves changed slope markedly as the overflow condition was approached.

Figures 4-3 through 4-5 show a comparison of [4-12] against observed points for some model flowthrough rockfill embankments. The average absolute error in computed discharges was approximately 5%. It should be noted that H was not varied in the development of equation [4-11]. The equation was therefore tested on a model dam with different characteristics. The model dam used in this evaluation was that in the large flume, made up of 130 mm rock, and with a height of 0.7 m (40% higher than the dams tested in the glass flume). The parameter *a* was estimated using Wilkins' (1956) equation and the value of r_E was that determined using the nickel coating technique described in section 3.1.3.2. Figure 4-6 shows how the computed rating curve compares with observations of stage and discharge measured in the laboratory. This result is comparable to the results obtained for the model dams in the glass flume, even though these dams were of lesser height, different aspect ratio, and

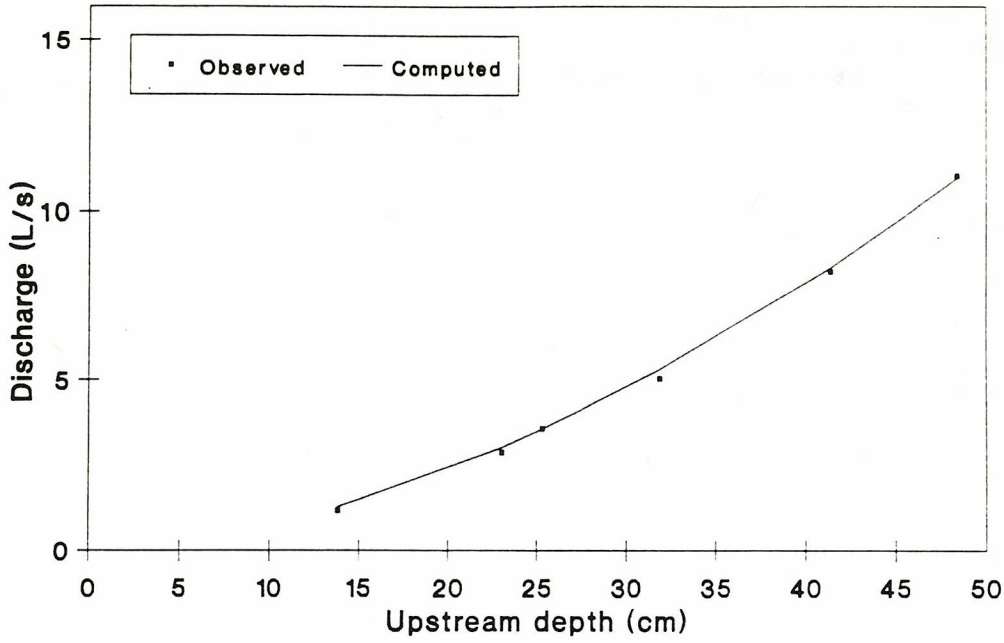


a) model test GF27a.

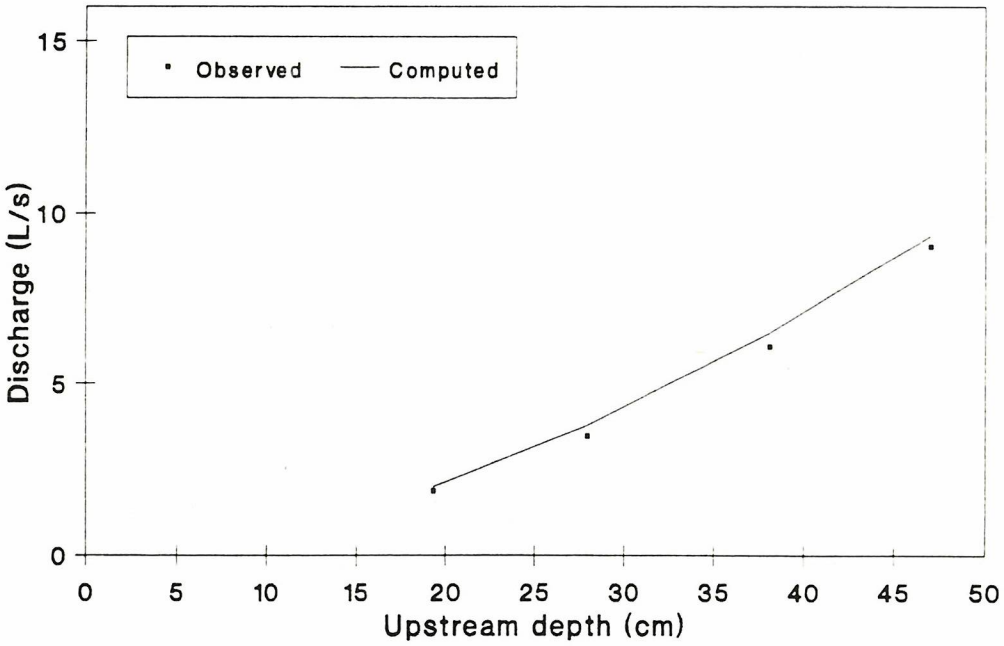


b) model test GF28a.

Figure 4-3. Comparison of observed and computed rating curves for tests GF27a and GF28a.

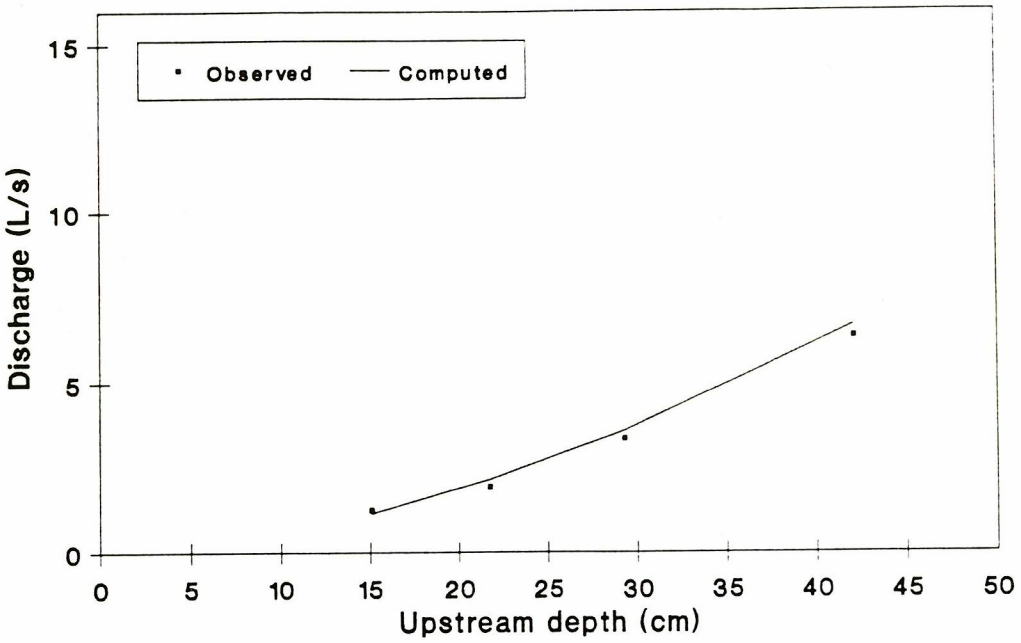


a) model test GF29d.

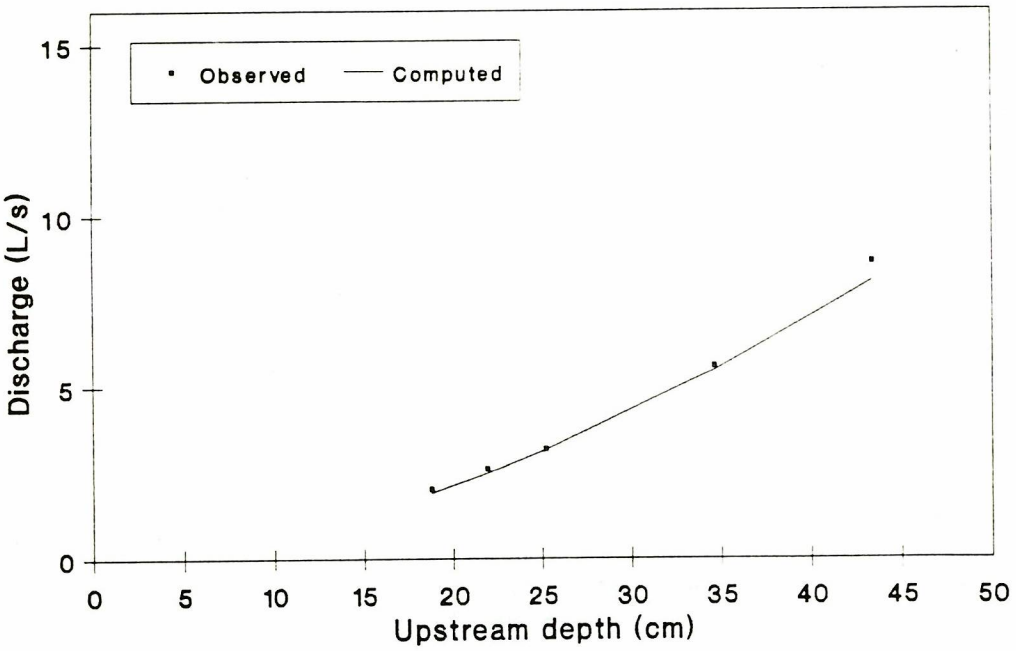


b) model test GF30a.

Figure 4-4. Comparison of observed and computed rating curves for tests GF29d and GF30a.



a) model test GF31c.



b) model test GF32a.

Figure 4-5. Comparison of observed and computed rating curves for tests GF31c and GF32a.

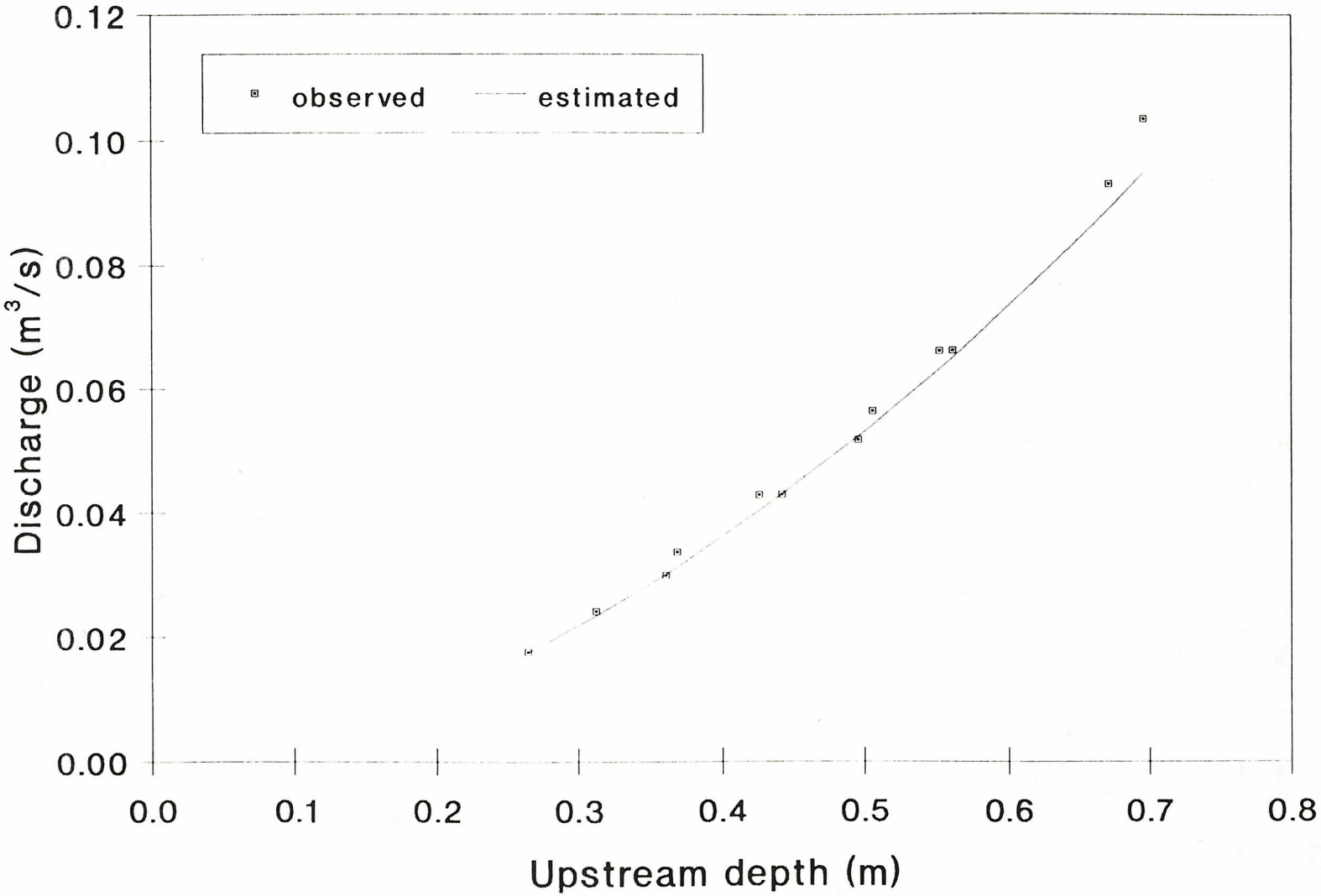


Figure 4-6. Comparison of observed and computed rating curves for test FF17.

had much smaller average particle size. It is also noted that B_U in equation [4-11] was not varied in the set of experiments used to obtain equation [4-11]. Generally, B_U would be made as small as possible in order to reduce the volume of fill. Further research is needed to examine the effect of relatively large values of B_U.

4.1.3.2 Rating Curve when Impermeable Facing is Present

For the parametric study performed in the glass-walled flume, the height of impermeable facing investigated was 40 cm, which was equal to 0.8 of the height of the dam. According to Parkin (1963a), the section through h_c is a section of hydraulic control, and the discharge over the facing is directly proportional to the head h_F (Figure 1-1) in a linear fashion. These observations were also found to be valid in this study, as is evident from Figure 4-7. The equation of the solid line in Figure 4-7 was found to be:

$$Q = h_c - 0.7 \qquad [4\text{-}13]$$

where:
Q = discharge (L/s),
h_c= depth above the impermeable facing (cm) (see Figure 1-1).

The upward curvature for higher discharges occurred when the upstream water level h exceeded the height of the dam H, so that an entry point existed somewhere along the crest of the dam. Clearly, since the vertical section through h_c is a section of hydraulic control, the shape of the stage discharge curve at this section is unrelated to the downstream geometry of the dam.

Figure 4-7 shows the three approaches taken to analyze the stage-discharge curve data for all model dams having an upstream impermeable facing (UIF). Parkin (1963a) suggested that the hydraulic gradient i associated with the flow over the UIF was constant and equal to 0.82. The curve resulting from this assumption is the lowest curve shown in Figure 4-7. The solid line above the curve for Parkin's method is given by equation [4-13], stated above. The uppermost curve in Figure 4-7 was generated using the following expression:

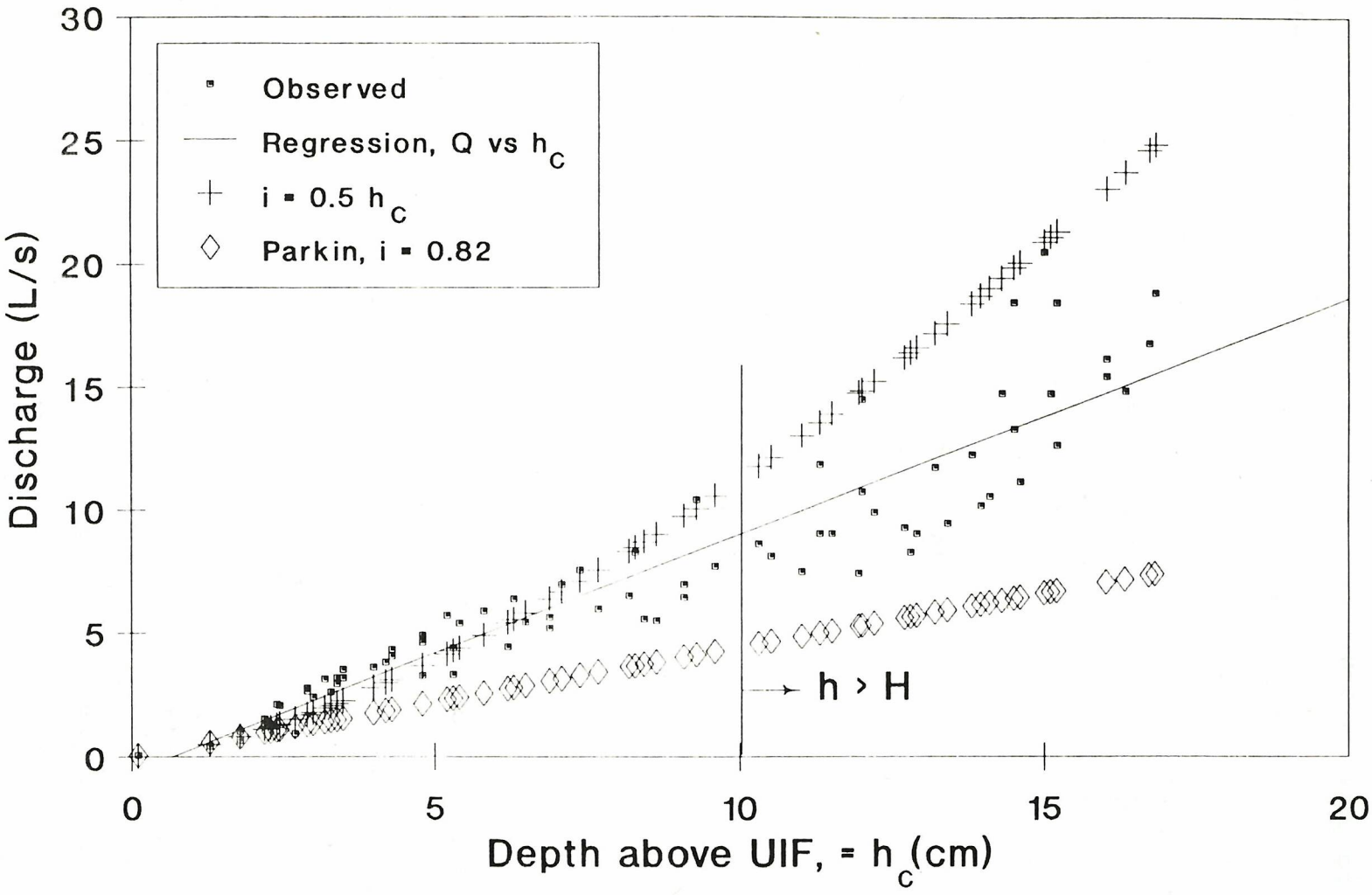


Figure 4-7. Comparison of techniques for estimating the stage-discharge rating curve when an upstream impermeable facing (UIF) is present.

$$i = 0.5\ h_c \qquad [4\text{-}14]$$

For Parkin's assumption of i = 0.82 and with equation [4-14], the discharge was computed using:

$$Q = V\ L\ h_c \qquad [4\text{-}15]$$

where $V = a' i^{N'}$.

It is evident from Figure 4-7 that for the zone of primary importance (h < H), equation [4-14] underestimated the flow for small h_c and overestimated the flow when h_c approaches $H-h_F$. Parkin's assumption of i = 0.82 consistently underestimated the discharge.

Unfortunately, equations [4-13] and [4-14] are empirical relations for model dams and are not of general applicability. Based on the results presented thus far, the designer possesses the following information:

(a) Parkin's assumption of i = 0.82 tends to underestimate the discharge.
(b) The stage-discharge relation at the vertical section through h_c is approximately linear.
(c) The hydraulic gradient at the section through h_c can be expected to be linearly proportional to h_c.

In comparing stage-discharge rating curves for model dams with and without impermeable facings, it was found that at relatively high discharges, when the flow entered the dam at a position roughly one third of the way along the crest, the upstream water level was unaffected by the presence of an impermeable facing. This was confirmed experimentally by removing the facing at such a discharge and noting that the upstream water level did not decrease. This behaviour can be explained by noting that the entrance hydraulic gradient is high when a facing is present, but acts over a small area. When the facing is removed, the average entrance hydraulic gradient decreases sharply, but this gradient acts over the upstream face of the dam, which is a much larger area.

4.1.3.3 Effect of Tailwater on Rating Curves

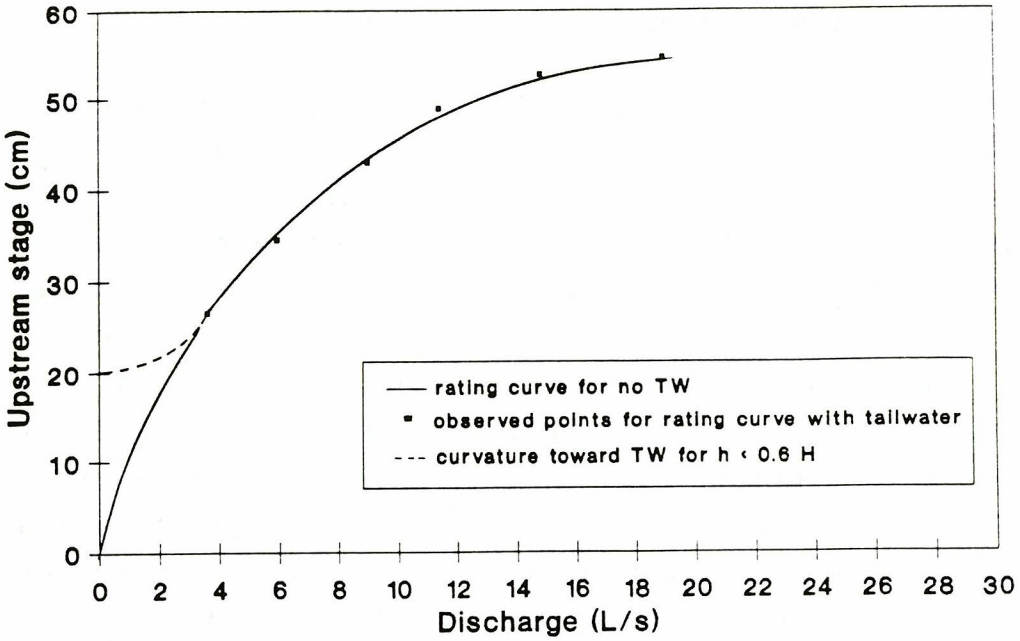
Figures 4-8 shows that, as expected, a tailwater level equal to 25% of the height of the dam caused zero discharge at $h = h_{TW}$ when h_F was zero. When a tailwater level is present, the shape of the stage-discharge curve (for $h_F = 0$) can be approximated by computing the stage-discharge from equations [4-11] and [4-12], and using this as a guide in drawing a smooth curve toward the known tailwater level. It was observed that, at $h > 0.6H$,, the rating curves with and without tailwater were virtually identical. Therefore, when estimating the location of the stage-discharge curve when a tailwater level is present, the rating should begin to curve toward the tailwater level at approximately $h < 0.6H$ (rather than toward $h = 0$ for $Q = 0$), for a tailwater level equal to 0.25H. It is expected that the value of 0.6 will be somewhat higher for higher tailwater levels, and lower for tailwater levels less than 0.25H. Nonetheless, knowledge of the stage-discharge curve for the case of no tailwater, and knowledge of the tailwater level itself, should provide an adequate guide for estimating the rating curve when a tailwater level exists. An illustration of the use of this approximation is shown in Figure 4-8. When an impermeable facing was present an increase in h_{TW} had no apparent effect on the stage-discharge curve. This is consistent with the fact that when an upstream impervious facing is present, the section of hydraulic control passes through h_c.

4.2 POSITION OF THE PHREATIC SURFACE

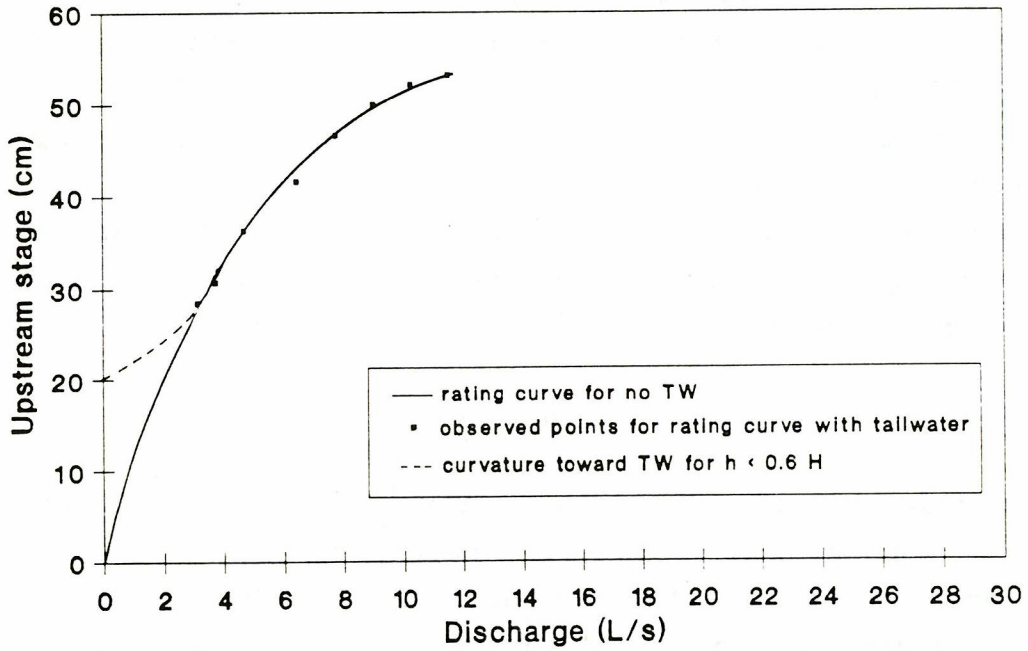
The computation of the phreatic surface will be considered in two parts: (i) computation of the exit height h_e, and (ii) calculation of the location of the phreatic surface. Using the method to be described herein for the calculation of the phreatic surface, the calculation of the exit height h_e is a necessary first step.

4.2.1 Computing the Exit Height h_e

The following section presents a rapid and direct means of computing h_e. A more rigorous, but more involved method, will be discussed in section 4.2.2, which deals with computing the phreatic surface.



a) model test GF29c.



b) model test GF31d.

Figure 4-8. Illustration of the technique for estimating rating curve when tailwater present, tests GF29c and GF31d.

For flowthrough rockfill dams the exit height h_e (where calculation of the phreatic surface begins) indicates the extent of the downstream face which will be submerged by the emergent seepage. This fraction of the downstream slope beneath the seepage surface is the area which may fail by erosion. It is therefore of interest to to compute h_e corresponding to the design discharge. Parkin (1963a) concluded that if the tailwater level, h_{TW}, is below the point of emergence of the seepage surface, h_e, it had practically no effect on the height of the point of emergence, which he determined as follows:

$$h_e = \frac{q}{n}\left[\frac{a}{\sin\theta}\right]^{(1/N)} \qquad [2\text{-}27]$$

where:
q = unit-width discharge, Q/L,
n = porosity,
θ = angle of downstream toe,
a & N from equation [2-3a],
h_e = exit height on downstream face, relative to the foundation.

Equation [2-27] was obtained by applying equation [2-3a] at the vertical cross section where flow emerged, and is valid whether or not an impervious facing is present. Equation [2-27] can be restated in the form of a rating curve:

$$Q = n\, h_e\, L\, a'(\tan\theta)^{1/N} \qquad [2\text{-}28]$$

where a' is defined in equation 2-3(b) & L is defined in Figure 1-1.

As was noted in section 2.1.3.1, equation [2-28] assumes that the gradient of the flow exiting the downstream face is equal to $\tan\theta$, the slope of the downstream face. Equation [2-28] was not found to compare well with the observed values of discharge versus h_e obtained from the parametric study in the glass-walled flume. It was hypothesized that the emergent flow field on the downstream face has a hydraulic gradient which is different from $\tan\theta$ and dependent on h_e/H. At low discharges (small h_e/H), the phreatic line was

almost flat as it approached the downstream face, indicating that the hydraulic gradient for the exiting flow was smaller than tanθ. At high discharges (larger h_e/H), the exit gradient was steeper, approaching tanθ.

Figure 4-9 illustrates the concept of the angle of the emergent flow field θ_{ff}, and that it can be expected to be different from the angle of the toe of the dam θ. As the exit height h_e increases it can be expected that θ_{ff} will increase. The following equation was developed to determine the angle θ_{ff}:

$$\frac{\theta_{ff}}{\theta} = 1.41 \frac{h_e}{H} + 0.17; \qquad r^2=0.79 \qquad [4\text{-}16]$$

Equation [4-16] can be used with equation [2-28] (ie. by setting θ in equation [2-28] equal to the θ_{ff} computed from equation [4-16]) to determine the discharge associated with a given h_e. Often the discharge, Q, is known and the exit height, h_e, is required. In this case the exit height associated with the discharge Q of interest can be obtained by successive trials. Alternatively, equations [2-28] and [4-16] can be used to generate and plot a stage-discharge curve, and h_e may be obtained from this curve at the desired Q.

The performance of equation [4-16] is illustrated in Figures 4-10 and 4-11. In general the equation worked reasonably well, but in some cases poorly represented experimentally observed curves of discharge versus the exit height. This was due to the difficulty in accurately assessing the exit height. Slight differences in the slope of the downstream face or in the angle of inclination of the phreatic surface approaching the downstream face made for potentially significant differences in h_e. Assessing h_e experimentally is even more difficult for dams composed of large rock. Regarding a series of experiments on model dams composed of 300 mm rock, Jain *et al* (1988) have notedthat h_e could not be accurately assessed when tailwater conditions were low, and therefore did not report h_e. It was found that equation [4-16] worked best for $h_e < 0.5$ H. For h_e greater than approximately 0.6

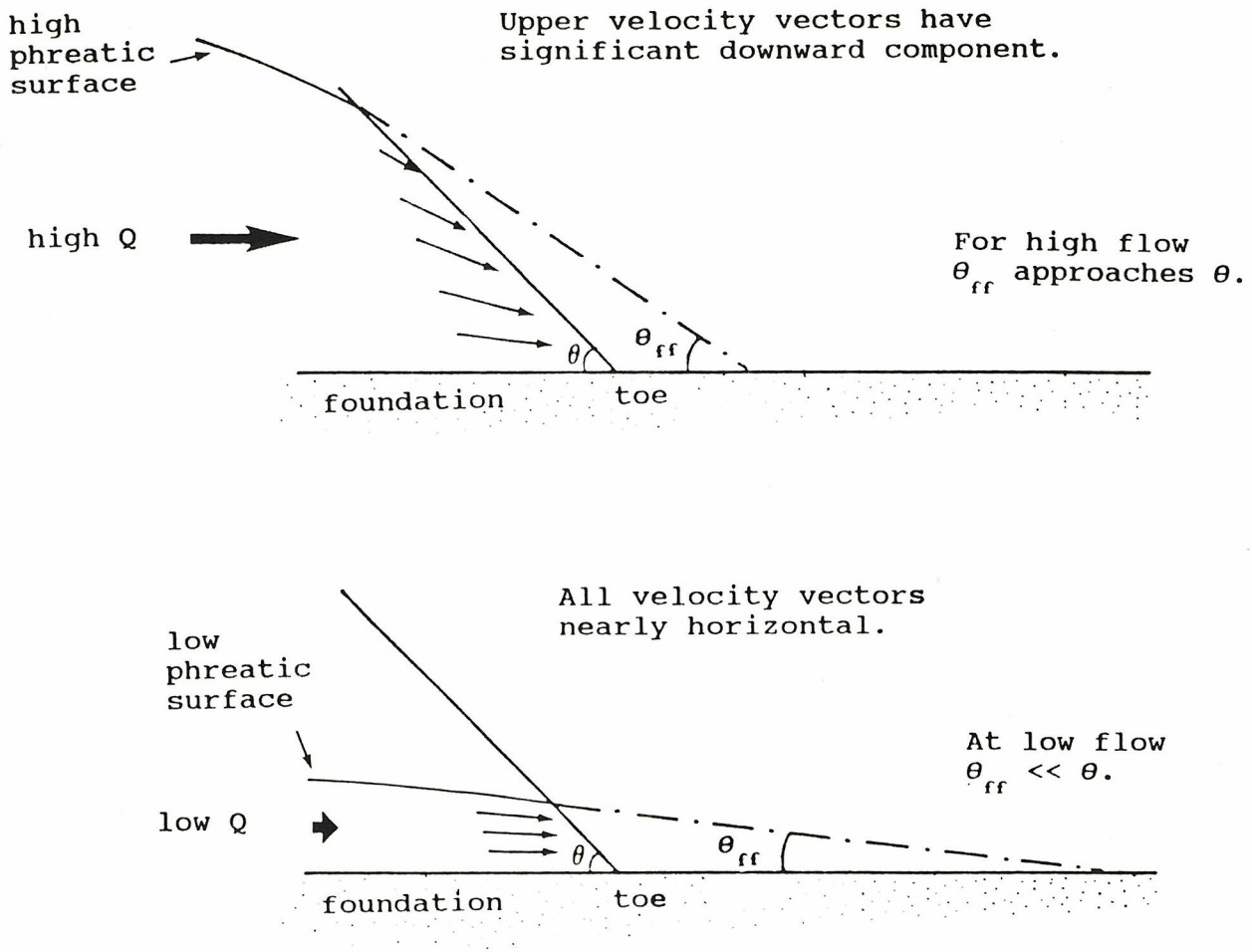
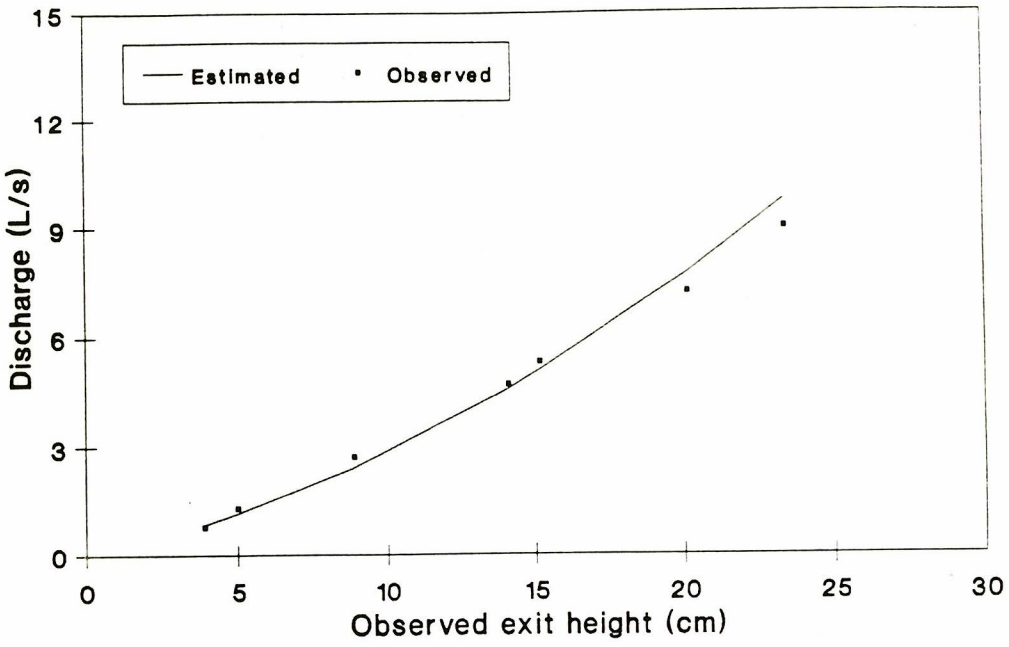
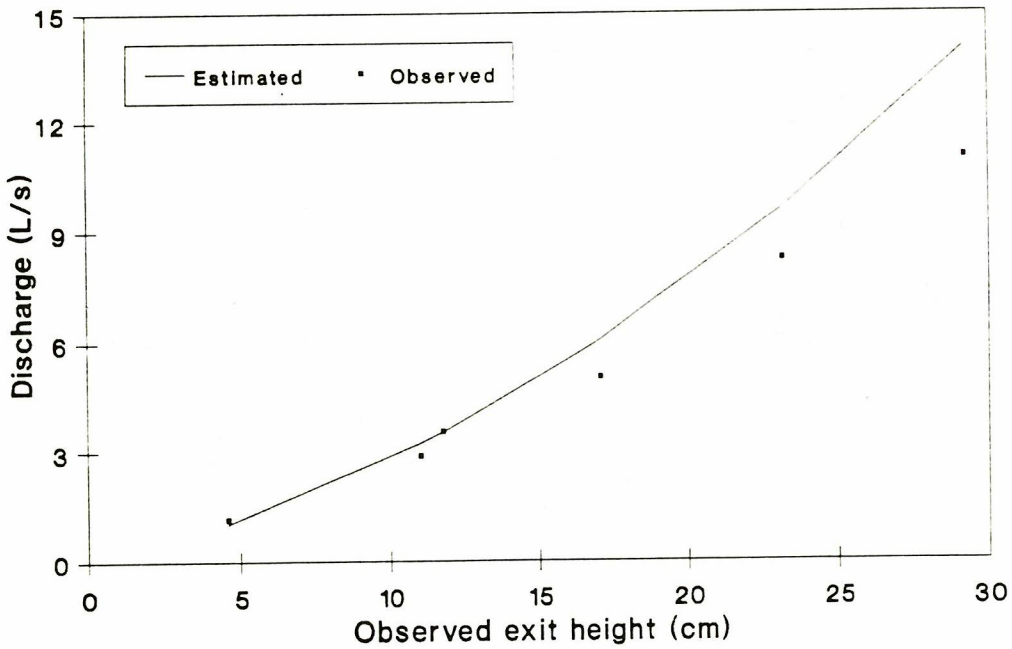


Figure 4-9. Illustration of the concept of the angle of the emergent flow field.

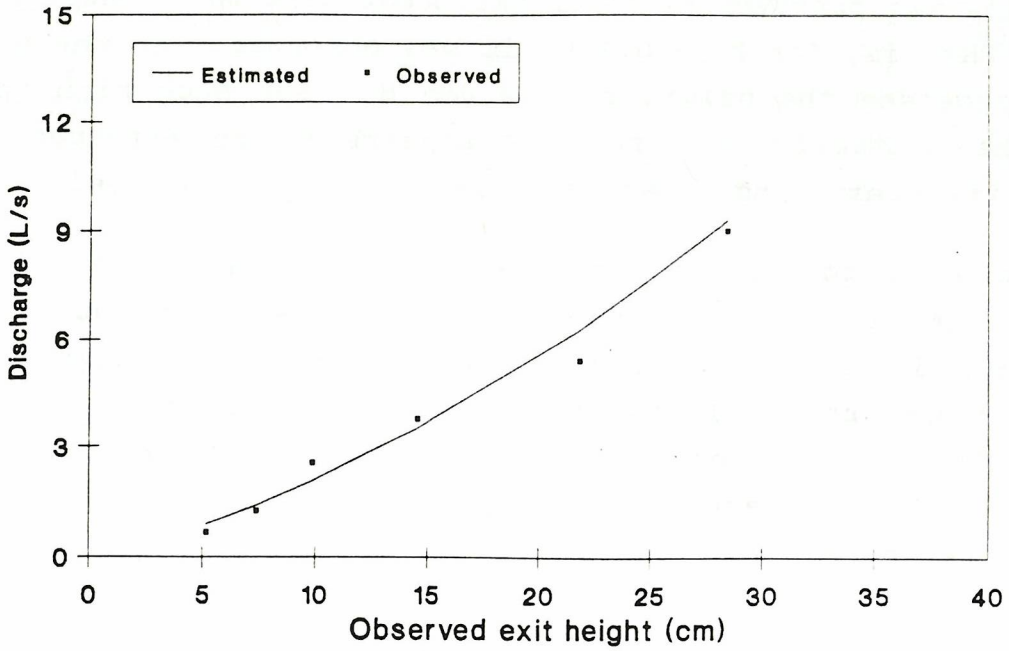


a) model test GF27a; slope 1V:1H, $B_c = 0 \cdot B_w$.

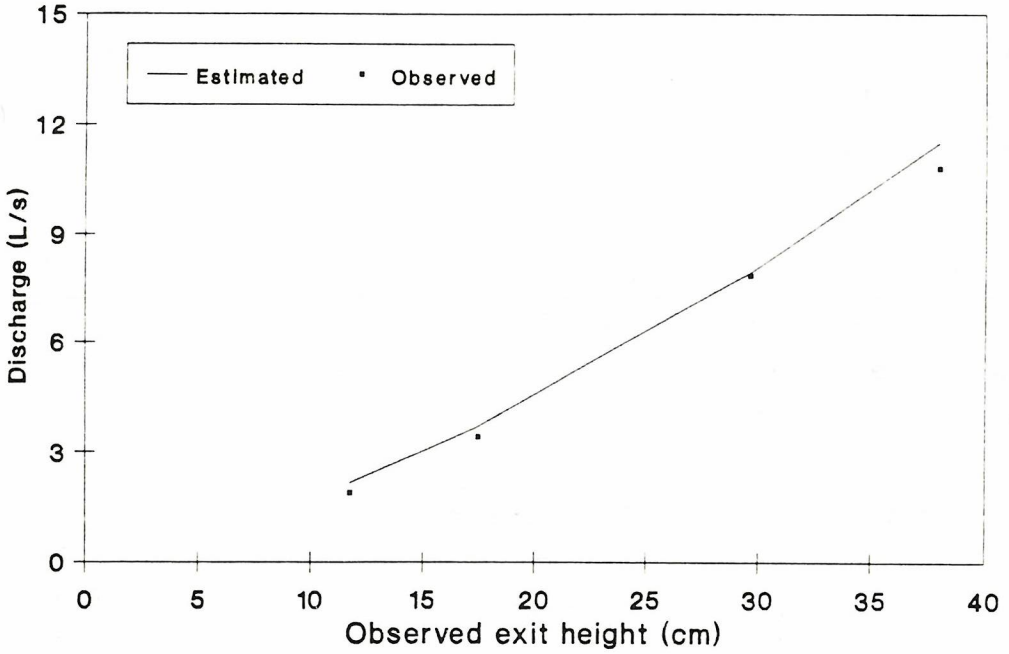


b) model test GF29d; slope 1V:1H, $B_c = 0.25B_w$

Figure 4-10. Comparison of observed and computed rating curves for the downstream face.



a) model test GF33a; slope 1V:2H, $B_C = 0.33B_W$.



b) model test GF34a; slope 1V:3H, $B_C = 0.25B_W$

Figure 4-11. Comparison of observed and computed rating curves for the downstream face.

H, the flow was observed to enter the crest part way along the crest length. That is, for h_e > 0.6 H, it was observed that the upstream depth h exceeded the height of the dam H. For such high upstream stages the hydraulics of the flow appears to be affected by the width of the crest, and equation [4-16] no longer applies.

The question of the general applicability of equation [4-16] is now examined. An attempt was made to deduce a similar equation from experiments in the large flume, and it was found that equation [4-16] did not apply. It is noted however that there appears to be a scale defect when the ratio of the height of the dam to the diameter of the average particle is small. Table 4-3 lists the ratio H/d ratio, for four cases:

Table 4-3

Four Cases of the Ratio H/d

Dam	Particle Diameter d (m)	Height H (m)	H/d
Glass flume	0.025	0.5	20
Large flume	0.130	0.7	5
Jain *et al* (1988)	0.305	1.2	4
Possible prototype	0.30	25	83

When H/d is small the seepage surface is, in general, difficult to identify because the flow must travel some distance along the downstream face of the structure before it has sufficient depth to fully submerge outcropping particles. Consequently, for small H/d, the exit gradient should be relatively constant. This was observed to be the case for the large flume studies undertaken using 130 mm rock. It is suggested that as H/d approaches the ratio for a typical prototype, the exit gradient becomes more dependent on h_e/H, and this dependence will be along the lines of equation [4-16]. The next section presents a more rigorous and general method for computing h_e, again as part of the determination of the entire phreatic surface.

4.2.2 Computing the Phreatic Surface

In this section the accuracy of three analytical methods for calculating the position of the phreatic surface is compared. The first method considered (Stephenson 1979) is based on the assumptions that fully-developed turbulence exists and that the flow emerges on the downstream face at critical depth. It includes consideration of the kinetic energy of the flow. The second method, due to Basak (1976), permits any single level of turbulence, but does not consider the kinetic energy of the flow, nor does not it explicitly assume that the flow emerges at critical depth. The third method (developed in the present study) is the most general. For this method any single level of turbulence is permissible, the kinetic energy of the flow may be included, and it is not required within the derivation that the flow emerge at critical depth. All of the three methods to be described make the Dupuit assumption (see Harr 1962), which is:

$$\frac{dh}{dx} = -i \qquad [4\text{-}17]$$

This means that at any point on a given vertical section within the embankment (where a phreatic surface exists) the hydraulic gradient driving the flow is dh/dx, where dh/dx is the slope of the phreatic line at that vertical. This is analogous to the assumption within the development of the equation for gradually varied flow in open channels that there is negligible curvature in the streamlines, yet the friction slope has a non-zero value. This existence of this strong analogy is not surprising when it is considered that A.J. Dupuit did his pioneering research on gradually varied open-channel flow before he began studying flow through porous media, although the latter contribution is much more well-known (see Rouse and Ince 1957, p.167). It is known (Harr 1962) that the Dupuit assumption is only applicable (that is, gives good results for the computed flow and height of the phreatic line at a given location) when dh/dx is not large. When dh/dx is large (ie. approaching unity) at a given vertical dh/dx is no longer representative of the overall hydraulic gradient at that vertical. The breakdown of the Dupuit assumption for steep phreatic surfaces is analogous to the case of the water

surface profile near a brink in an open channel. It is well-known that gradually varied flow theory will not predict the correct water level near a brink. This is due to significant curvature of the streamlines and to the existence of a non-hydrostatic pressure distribution. The water surface profile known as M2 in gradually varied open-channel flow is analogous to the case of the phreatic line through an embankment with a low tailwater level.

Another common feature of the three methods to be discussed is that the equations for the phreatic surface all give distance as a function of an assumed height of the phreatic surface. Although we would actually prefer the height (as the dependent variable) at some distance of interest (as the independent variable), this is mathematically awkward to develop, and does not appear in the literature. A comparison of computed and observed phreatic surfaces will be presented for all three methods after they have been individually described. The derivation of the equation associated with each method is given in Appendix 4.

Stephenson (1979, p.26) presented the following equation for analytically computing the height h of the phreatic surface at some point x relative to the upstream toe:

$$\frac{3K_s}{d}(b_e - x) = \left(\frac{h}{h_e}\right)^3 - \ln\left(\frac{h}{h_e}\right) - 1 \qquad [4\text{-}18]$$

where:

K_s = Stephenson's empirical non-Darcy flow coefficient in eqn [2-8],
b_e = the distance from the upstream toe to a point directly below the point of flow emergence on the downstream face (see Figure 1-1).
h = height of phreatic line at x.
h_e = the height of the point of emergence of the downstream face, which in Stephenson's development requires that this take place at the critical depth, as defined for flow through a porous media.
x = computed distance for a given value of the height of the phreatic surface h.

The development of Stephenson's equation assumed that:

1) Flow takes place in a channel whose cross-section is rectangular.

2) Flow emerges at critical depth, *as defined for porous media flow*.
3) Turbulence is fully-developed for the flow in the porous media.
4) The configuration of the embankment (side view looking normal to the direction of flow) is a rectangle of width b.

In order to be consistent with accepted terminology in dam engineering, the flow takes place in the direction of the *width* of a dam. The length L of a dam is the span of the channel cross-section normal to the flow direction; see Figure 1-1. The formula for the critical depth for the case of free-surface flow in a porous media is:

$$y_c^3 = \frac{q^2}{g\ n^2} \qquad [4\text{-}19]$$

where:
y_c = critical depth for free surface flow in a porous media,
q = discharge per unit length of the dam, Q/L (see Figure 1-1 for L),
g = gravity,
n = porosity.

Note that if no assumption is made about the width of the embankment in equation [4-19], the resulting values of x are negative. This is a consequence of defining the hydraulic gradient as:

$$\frac{dE}{dx} = -\ i \qquad [4\text{-}20]$$

in the development of equation [4-18]. The negative values computed for x indicate that we are moving in a direction opposite to the decline in the water level for each positive increment of h. In this case (M2 profile, see Chow 1959) negative computed x means upstream of h_e for flow occurring from left to right.

In Appendix 4 it is shown that if the form of the non-Darcy flow equation for fully-developed turbulence is [2-11], the equation for the phreatic surface is:

$$\frac{3}{K^2 ed}\ x = \left(\frac{h}{h_e}\right)^3 - 3\ \ln\left(\frac{h}{h_e}\right) - 1 \qquad [4\text{-}21]$$

Any consistent set of units can be used in equation [4-21] since K is from a dimensionally homogeneous equation. This equation does not directly require the discharge per unit width. The value of 3 in front of the 'ln' term is also needed in equation [4-18], and was apparently omitted in error in Stephenson's 1979 text. However, the value of this term is small compared to $(h/h_e)^3$, and this may explain why Stephenson still obtained good results. For equation [4-21] the computed values of x will be positive but it will be understood that the distance *upstream* of h_e is meant. This is done for the sake of consistency with Basak's equation, to be described below.

Basak's (1976) method was originally presented in dimensionless form, but a dimensional form was derived and checked for this study (see Appendix 4) because it is easier to use. Basak's dimensionless form is:

$$X = \frac{H}{L}\left[\frac{y^2 - y_o^2}{2} - c\,(y - y_o) + q_* c^2 \ln\left(\frac{y + c\,q_*}{y + c\,q}\right)\right] \qquad [4\text{-}22]$$

where X, H, L, q_* etc. are defined in Basak (1976).
The above equation in dimensional form is:

$$x = \frac{1}{\Delta}\left[\frac{h^2 - h_e^2}{2q} - \frac{t}{\Delta}(h - h_e) + \frac{t^2 q}{\Delta^2}\ln\left(\frac{\Delta h + tq}{\Delta h_e + tq}\right)\right] \qquad [4\text{-}23]$$

where:
Δ, t = empirical parameters from $i = \Delta V + tV^2$, [2-4c],
q = discharge per unit width,
h_e = height at point of emergence, but not necessarily critical depth.

The units of q and h in [4-23] must be consistent with the units associated with the equation $i = \Delta V + tV^2$. Equation [4-23] is obtained by simply integrating $i = \Delta V + tV^2$, knowing that $V = q/h$ and setting $i = dh/dx$ (the Dupuit assumption). The velocity head is not considered.

It was thought that it may be of interest to combine some of the features of both methods. This method would be able to handle the

case of turbulence which is not fully-developed, include the velocity head (denoted as KE for kinetic energy) and require no assumption about the value of h_e within the derivation. The derivation of the following expression which results from this approach is given in Appendix 4.

$$x = \frac{t}{s^2}\cdot(h-h_e) - \frac{n}{2sq}(h^2 - h_e^2) + \frac{t\,q^2}{s^3 n}\ln\left(\frac{snh + tq}{snh_e + tq}\right) + \ldots$$

$$+\frac{1}{tg}\cdot\ln\left[\left(\frac{h}{h_e}\right)\frac{snh + tq}{snh_e + tq}\right] \qquad [4\text{-}24]$$

where:
s, t = empirical parameters from $i = sV_v + tV_v^2$, [2-4a],
g = gravity
n = porosity, (other terms as for equation [4-23])

Note that the resulting expression is similar to equation [4-23] except for the addition of an additional term (the term involving gravity). It turns out that the value of this term was small for the cases considered in the laboratory. Figures 4-12 to 4-16 present a comparison of observed and computed phreatic surfaces for the small and large flumes used in this study. Appendix 4-2 presents similar results for flume test GF34. The values of the empirical parameters used were as follows:

Table 4-4

Values of Empirical Non-Darcy Flow Parameters used in Phreatic Surface Calculations

		s	t	K in eqn [2-11]
Modified Stephenson	GF	N/A	N/A	0.655 †
	FF	N/A	N/A	0.757 ††
Dimensional Basak and Basak with KE	GF	0.41	63.87	N/A
	FF	0.01	15.00 ††	N/A

† found by equating a' from CT7 to $nK(ged)^{1/2}$, see eqn [2-11].

†† from Dudgeon's data (1964).

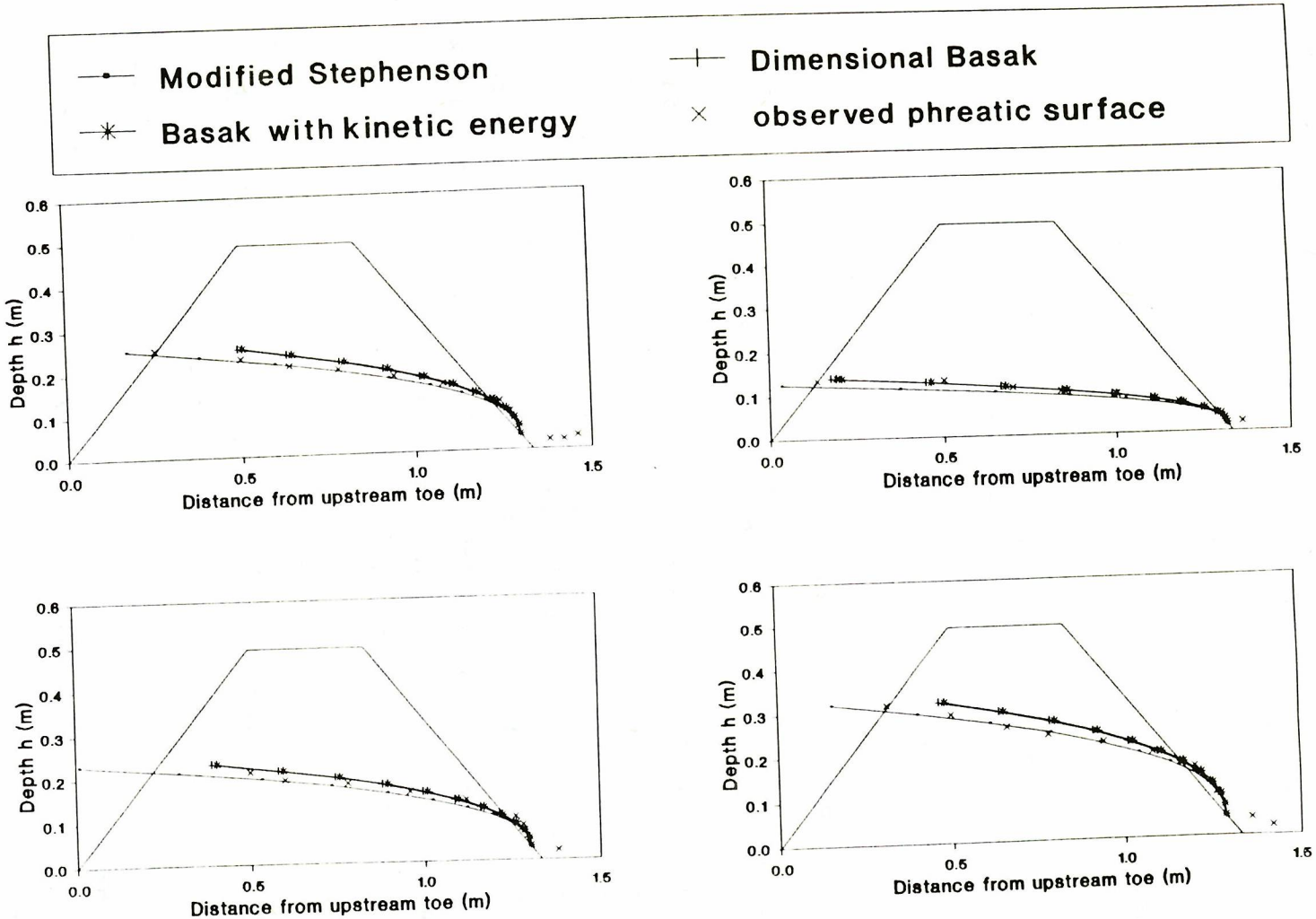


Figure 4-12. Observed and computed phreatic surfaces for GF29d.

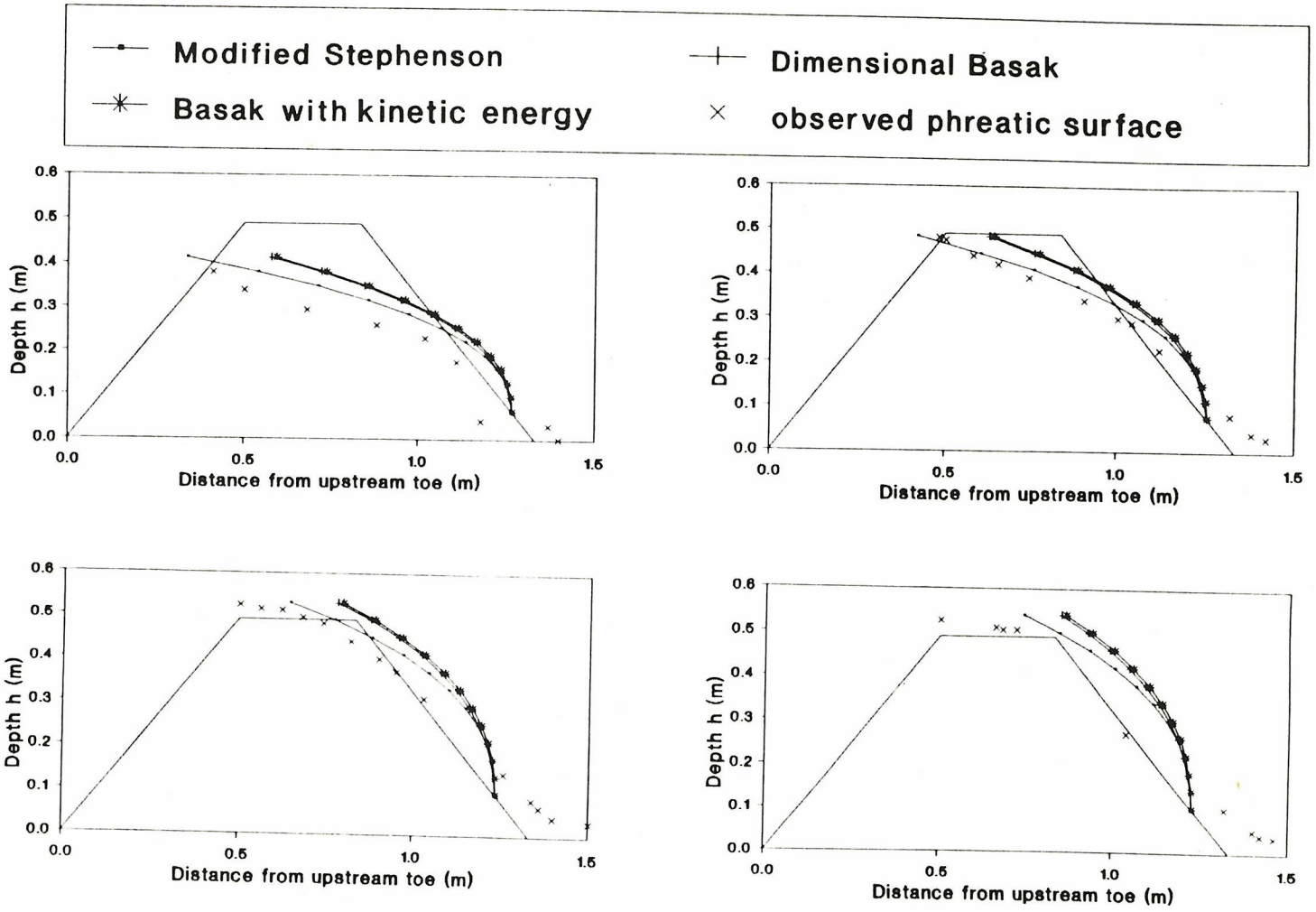


Figure 4-13. More observed and computed phreatic surfaces for GF29d.

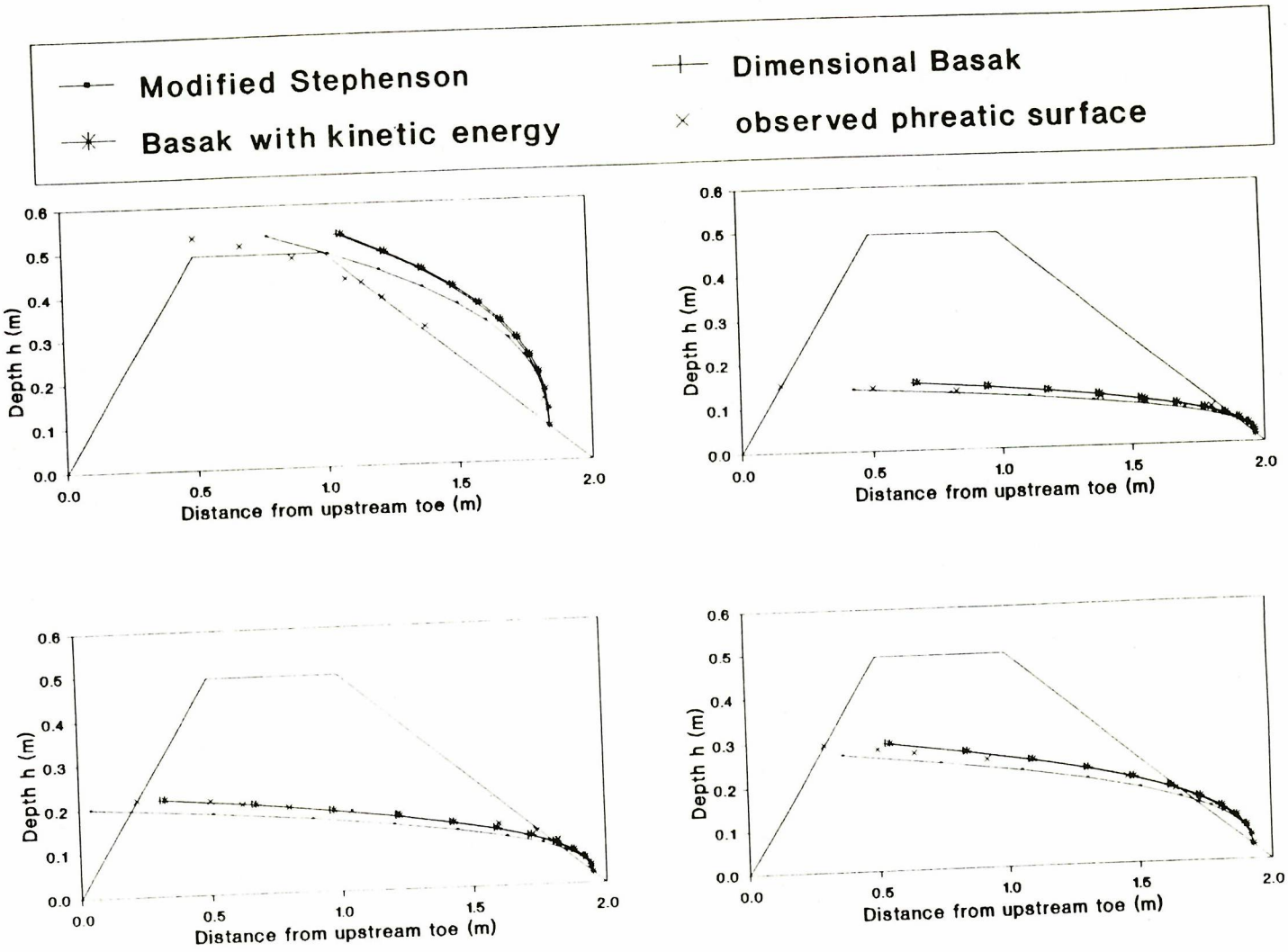


Figure 4-14. Observed and computed phreatic surfaces for GF31c.

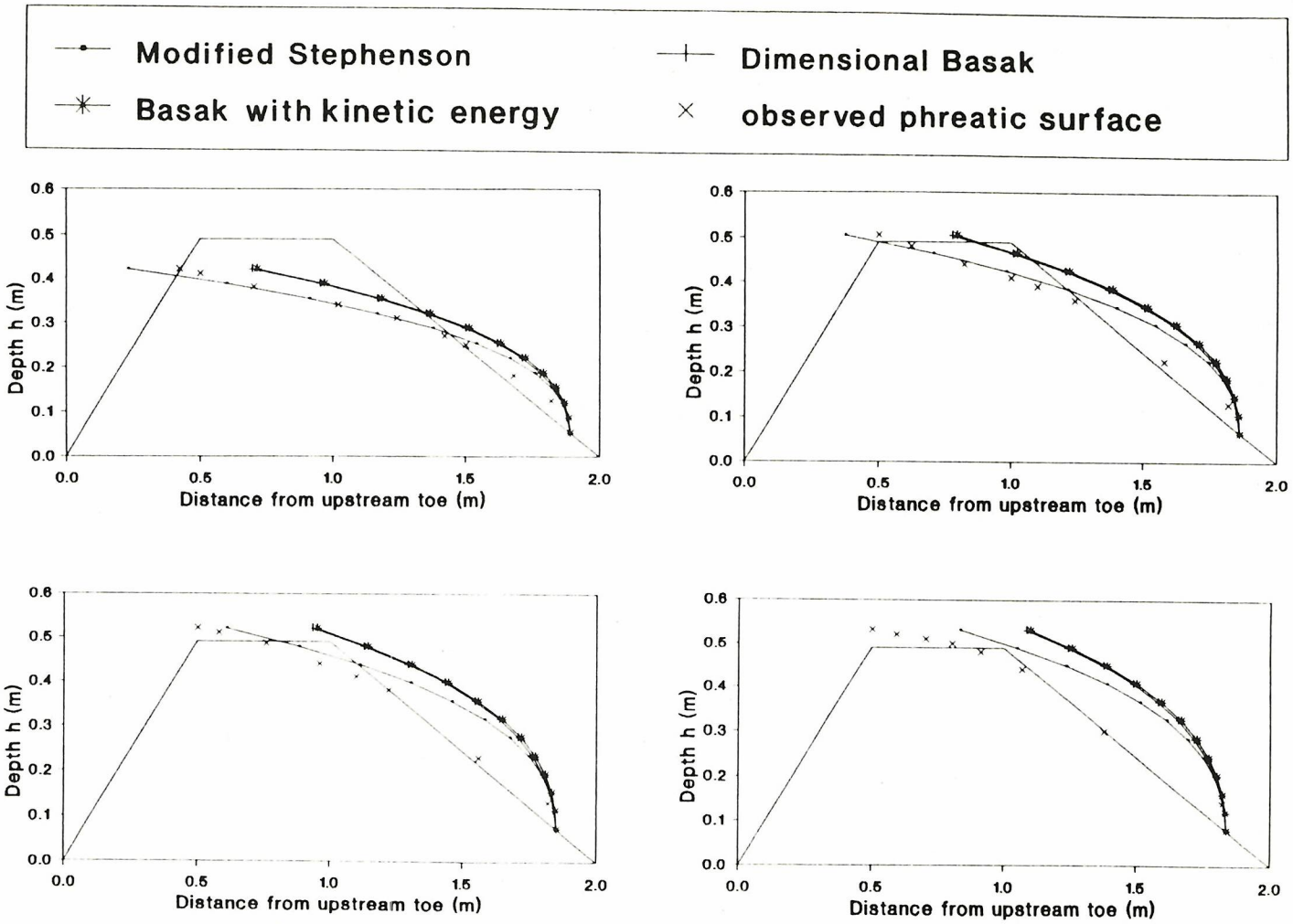


Figure 4-15. More observed and computed phreatic surfaces for GF31c.

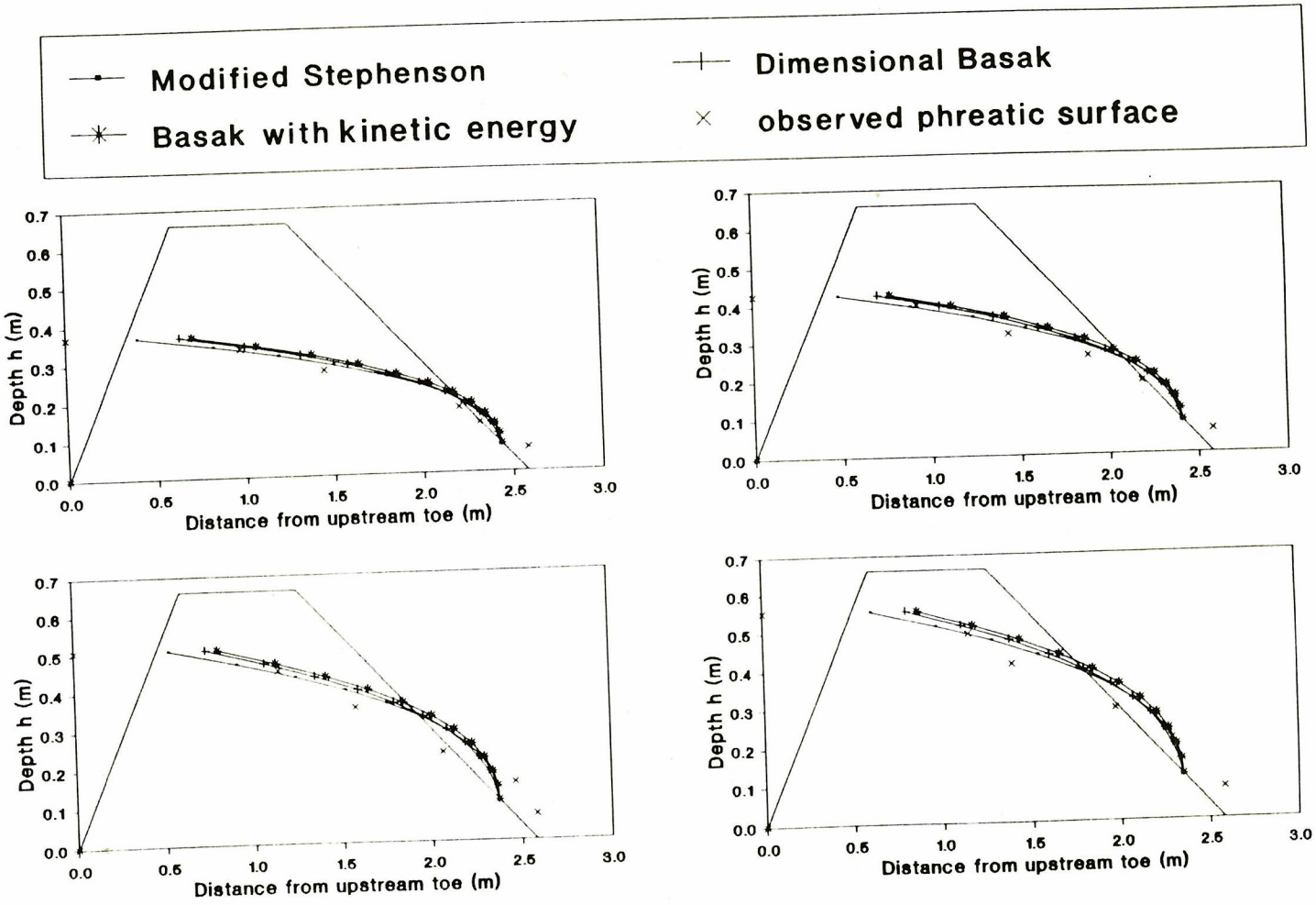


Figure 4-16. Observed and computed phreatic surfaces for FF17d.

In order to use equation [4-24] the empirical parameters a and t (based on bulk velocity, [2-4c]) must be converted to s and t (based in void velocity, [2-4a]). This conversion is discussed in Appendix 4-1. The values for a and t for the GF series of tests were taken directly from regression analysis (using column test 7 data) for 0.0247 m rock, which was the same rock used in the glass-walled (GF) flume. The values of s and t for floor flume tests (FF) were adapted from the author's regression of Dudgeon's (1964) original data for large column tests on river gravel of nominal diameter 0.152 m (6 inches). Actual particle diameter (defined as mean b-axis) for rock used in the floor flume was 0.13 m.

Note that for a regression yielding $i = aV^N$, it can be readily shown that:

$$\frac{3}{K^2 ed} = 3\, a\, n^2\, g \qquad [4\text{-}25]$$

Equation [4-25] makes it convenient to use equation [4-21] if the form in hand is $i = aV^N$, where V is bulk velocity. The method of determining s and t was discussed in section 4.1.2. The value of K for fully-developed turbulence in coarse rockfill is about 0.76, as can also be inferred from Stephenson's data (1979).

In order to use the "Dimensional Basak" and "Basak with KE" methods, a starting depth is required for the downstream face. This depth was estimated using equation [4-19], even though turbulence was not fully-developed in the glass-walled flume experiments. Based on an examination of Figures 4-12 through 4-16, the following observations can be made:

1) The exit height, as computed by the critical depth formula for porous media flow, only compared well with the observed exit heights at relatively low flows. It compared very poorly with observed exit heights at high flows. Therefore, equation [4-19] should not be used blindly to compute the exit height h_e.

2) The accuracy of all three methods decreased with increasing discharge.

3) All methods predicted too high a phreatic surface at high discharges.

4) The point of *intersection* of the computed phreatic lines with the downstream face of the embankment was closer to the actual exit height than the exit height computed using the critical depth formula, equation [4-19]. This means that it is still useful to *begin* computation of the phreatic line at the exit height computed using the critical depth formula. That part of the phreatic line outside the embankment can then be ignored. It is not surprising that part of the computed phreatic lines were outside the slope of the model embankments tested here since the three formulae were developed for rectangular, rather than trapezoidal, embankments. The above finding is consistent with Youngs' (1990, p.202) comments that it appears that the undesirable effects of the Dupuit assumption are to some degree compensated for by the non-rectangularity of the embankment; namely, a longer seepage face.

5) All methods gave reasonably good results when the actual h_e was less than or equal to about 60% of the height of the dam.

6) The modified Stephenson method gave the best results of the three methods considered. The other two methods tended to overestimate the height of the phreatic line at a given vertical. The two methods using the quadratic form were almost identical, meaning that the inclusion of the velocity head (kinetic energy of the flow) was not significant. Even in nearly turbulent non-Darcy flow, the velocities are in general too low (as compared to the depth) to warrant inclusion in an analytical method for finding the phreatic line. In some applications, however, such as rockfill drains flowing at small depth over steep slopes, the velocity head may be significant enough to warrant inclusion.

It is somewhat surprising that the modified Stephenson method, which assumes full turbulence, gave the best results, even though N was slightly less than 2 for flow in the glass-walled flume. This may be due in part to the consequences of the Dupuit assumption. It may also be that the two forms $i = \alpha V + tV^2$ and $i = aV^N$ (which were obtained from data for V up to 0.1 m/sec) perform differently for

the somewhat lower range of velocities encountered in the glass-walled flume. Other errors included differences in the relative effect of the wall between the column and the flume, and to the flow possibly not reaching complete equilibrium in one or two cases. It is noted that the appropriate empirical parameters could have been adjusted to give a best-fit between observed and computed phreatic surfaces. This was deliberately not done so as to get a better indication of the consequences of using a one-dimensional non-Darcy flow equation (obtained from a column test) in a problem in which the flow was two-dimensional.

In practice the cross-sectional shape of a river is usually not rectangular. Moreover, the shape of the channel usually changes as one moves upstream; that is, it is not prismatic. In such cases a numerical method known as the standard step method may be employed to integrate the dynamic equation for gradually varied flow:

$$\frac{dy}{dx} = \frac{S_o - S_f}{1 + \alpha \frac{d}{dy}\left(\frac{V^2}{2g}\right)} \qquad [4\text{-}26a]$$

where:

S_o = the bed slope beneath the dam,

S_f = the friction slope.

The standard step method is well-known because it is used in HEC-2, a computer program developed by the US Army Corps of Engineers, and is the industry standard method of performing gradually varied flow calculations in open channels (HEC undated). The standard step method is described in most texts dealing with open-channel flow, and is described in some detail in Chow (1959).

If the standard step method were to be employed, the required modifications to the method would be to estimate the friction slope using a non-Darcy flow equation rather than a Manning or Chezy equation, and to use V_v rather than V for evaluation of the velocity head. Such an approach would be aided by the foregoing analysis of the application of gradually varied flow theory to free-surface porous media flow, in which it was shown that:

1) The flow emerges at critical depth only at low flows. At high flows, in which the value of dh/dx is large, the flow will not emerge at critical depth, but at some greater depth, for sloping embankments. This larger depth is reasonably approximated by the intersection of the computed phreatic line with the downstream slope.

2) The standard step method includes the velocity head, but this can be expected to have minimal effect on the computed height of the phreatic line at a given vertical.

3) Due to the well-known breakdown of the Dupuit assumption (which is analogous to some assumptions made in gradually varied flow theory) at steep gradients, the computed phreatic line will be a poorer representation of the actual phreatic line for high flows with steep phreatic surfaces than for low flows with gradually sloping phreatic surfaces.

4) For exit heights greater than about 60% of the total height of the dam, the flow generally enters the dam at a point somewhere along the crest (that is, $h > H$). Gradually varied flow theory will probably represent the phreatic line very poorly at flows exceeding this level of h_e. It was observed that when the upstream depth was equal to the height of the dam ($h = H$), the exit height was about 60% of the height of the dam, and a straight line joining these two points would be an adequate approximation of the phreatic line, lessening the need to perform any calculations when $h = H$.

5.0 DESIGN CONSIDERATIONS II: SLOPE STABILITY

5.1 EVALUATION OF POSSIBLE UNRAVELLING FAILURE

As described in section 2.1.4, unravelling failure is failure of the downstream face by erosion. This type of failure occurs beneath the seepage surface (Figure 1-1) and progresses up the downstream face of the dam, beginning at the toe. Olivier (1967) assumed that erosion leading to failure occurred spontaneously at a given discharge. Such an approach can be categorized as an "initiation of motion" approach. It was found, however, for the slopes investigated in this study, that some motion began at the onset of flow. The number of particles set in motion increased gradually with each increment of discharge. The discharge at which complete failure of the dam occurred was not related to the threshold discharge given by Olivier's equation [2-39], as shown in Figure 5-1. The failure discharge for the model dams tested in the present study was defined as the discharge at which the dam eroded to the upstream limit of the crest. Figure 5-2 shows a failed model dam in the large flume. The amount of erosion was observed to increase progressively with each increment of discharge. Use of Olivier's equation for the stability of rockfill slopes is therefore not recommended for steep slopes if the intention is to compute the discharge associated with a substantial amount of erosion.

In the following sections a detailed framework for quantifying the erosion potential of the downstream face is presented and discussed.

5.1.1 Erosion Potential of the Downstream Face

As indicated in Figure 2-6, there can be up to seven forces acting on a single rock residing on the downstream face of a flowthrough rockfill dam. These are:

1. Shear due to overflow (in this case spatially varied flow).
2. The force due to emergent seepage.
3. Drag force due to overflow.

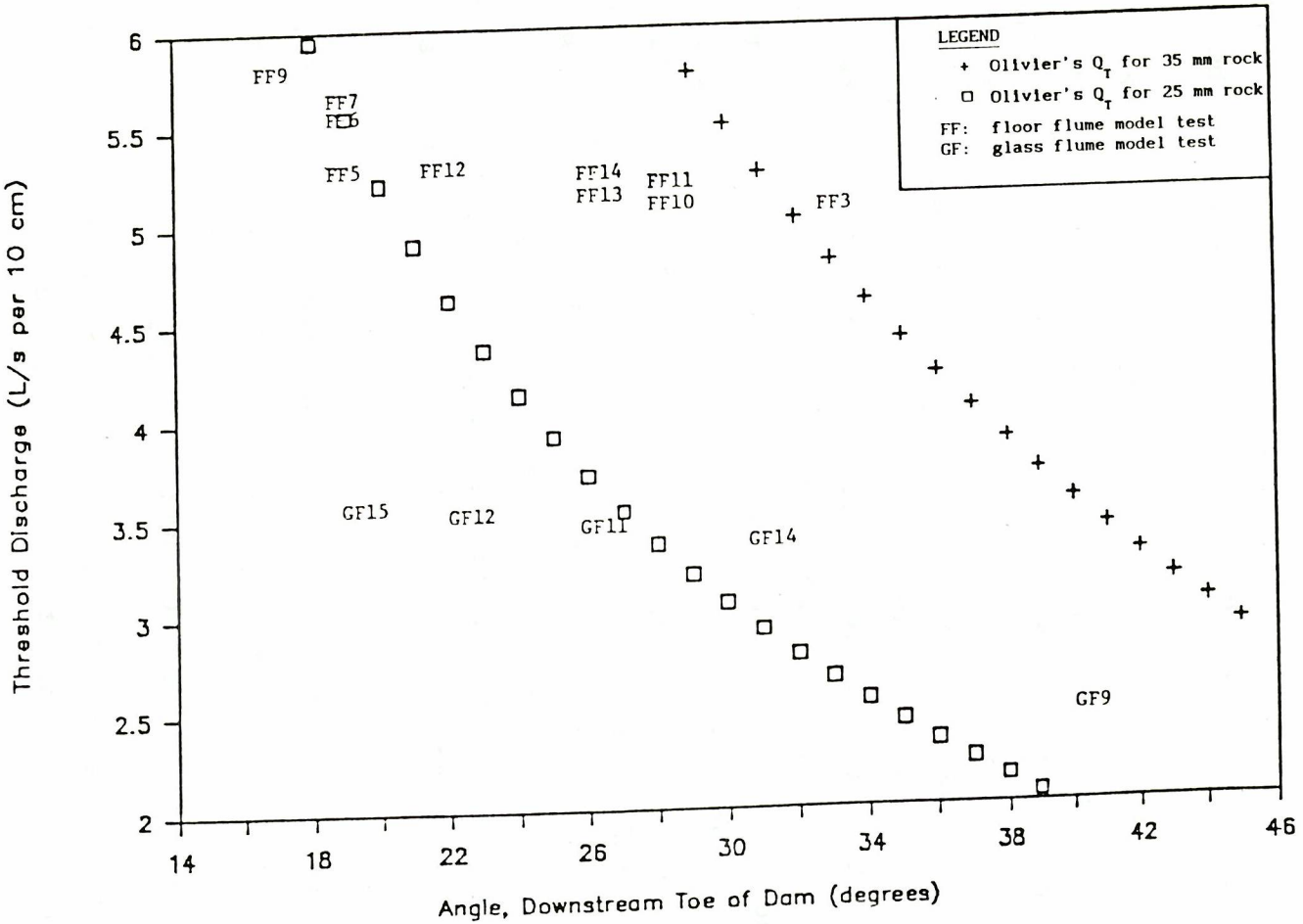


Figure 5-1. Threshold discharge Q_T *versus* angle of the downstream toe θ; a test of Olivier's equation.

flume width ≅ 1.4m

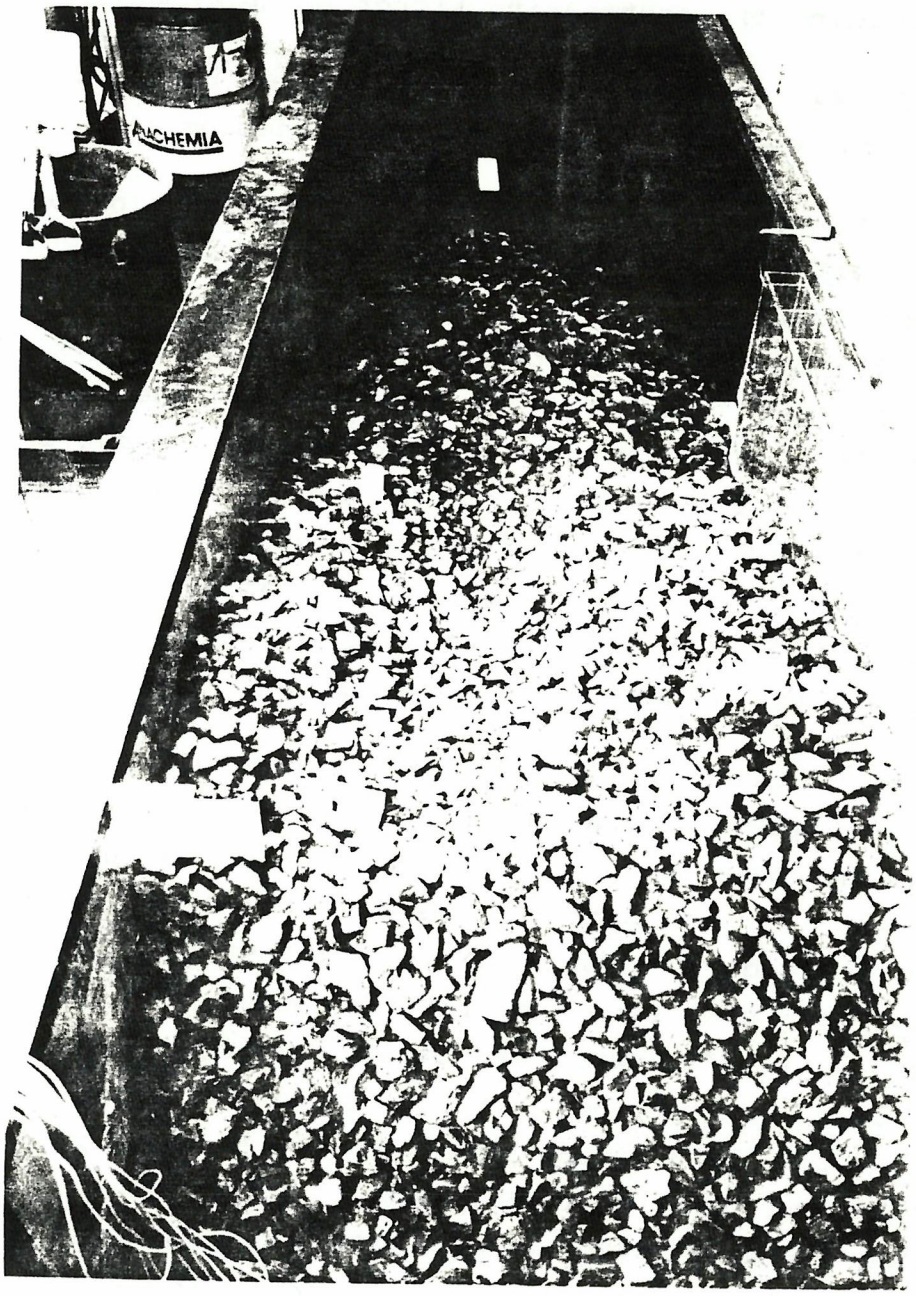


Figure 5-2. Failed model dam in large flume.

4. The buoyant weight of the particle.
5. The hydrodynamic lift.
6. The frictional resistance underneath the particle.
7. The pinching or constraining effect of neighbouring particles.

An attempt was made to quantify only the first four of the above seven phenomena, for the following four reasons:

1. Only semi-quantitative experimental information on the position of first particle motion was collected. During the course of the parametric model dam study conducted in the small flume, it was noted that quite often particles unprotected by the mesh over the toe of the dam moved out of position as the flow reached the discharge level of interest. The position of first particle motion was not highly consistent; it was merely noted that for the 45° slopes, some of the particles approximately two-thirds of the distance up the wetted face 'turned out' of position and rolled down the slope. For the 26° slopes this occurred much closer to the protective mesh, at about the one-third point up the wetted face.

2. Force number 5 was omitted because guidance in the literature implied too broad a range of lift coefficients, from negative values (Watters and Rao 1967) to values as high as unity (Stevens and Simons 1971). Force number 6 was omitted since, under the proposed conceptualization of initiation of motion, particles do not slide down the face, they turn out, rotating around the contact point with the next adjacent downstream rock. Force number 7 was omitted because it was considered to be conservative to do so, and because it was noted that there were always a few rocks which were "unpinched" on the downstream face. Such unconstrained rocks, if mobilized, could displace other rocks while rolling down the slope. This would likely damage a mesh covering lower elevations of the downstream face. Since a mesh covering the downstream face adds to the cost of the structure, the minimum required elevation for coverage is of interest. This is consistent with the conceptual model for initiation of motion used here; namely that the next-most downstream particle cannot turn out of position because of the mesh

protection.

3. Since the goal of the analysis was to provide a rationale, based on sound assumptions, for the maximum elevation at which protection of the downstream face was required, exactitude was not required. A given minimum predicted elevation from the analysis would probably not be strictly adhered to in design; a somewhat higher elevation would be used so as to provide for a factor of safety.

4. It was of interest to examine the *relative* importance of the dominating forces, amongst the seven listed above. For example, Gerodetti (1981) found that the emergent seepage was very important for the case of wedge-shaped gabion baskets. A crucial question is just how important the emergent seepage is relative to the other phenomena.

The following discussion will examine each of the first four components in turn. The most difficult of these to estimate was found to be the first, namely, the shear stress due to overflow.

1. *Shear due to overflow.*

As noted in section 2.1.4, the basic approach used to estimate the shear stress under spatially varied flow was to solve for the friction slope in the the differential equation for spatially varied flow. Chow (1959) notes that the standard form of this equation (equation [2-43]) must be modified if it is to be made applicable to steep slopes ("steep" normally implying a bed slope of greater than about 4°, Bray 1987). Chow (1959) does not present the needed modification, however. Appendix 5-1 gives the derivation of the required expression for steep slopes. The expression is:

$$\frac{dd}{dx} = \frac{\dfrac{S_o - S_f}{\cos\theta} - \alpha \dfrac{2q^* Q}{gA^2\cos\theta}}{\left[1 - \alpha \dfrac{Q^2}{A^2 D\, g\cos\theta}\right]} \qquad [5\text{-}1]$$

where:

d = local depth perpendicular to the bed (see Figure 5-3),

dd/dx = rate of change of local depth with distance along the bed,

S_o = bed slope, = $\sin\theta$ (see Chow 1959, pgs.32 & 218),

S_f = friction slope, which in this case is not equal to the absolute value of the rate of change of total head with distance along the bed,

α = velocity head correction coefficient,

θ = angle of toe of dam (Figure 1-1),

Q = discharge,

g = gravitational constant,

q_* = local rate of change of discharge with distance = dQ/dx,

A = cross-sectional area of the flow,

D = called the hydraulic depth by Chow (1959), meaning the cross-sectional area of flow divided by the top width; can be taken as the flow depth for wide channels.

Note that for the purposes of discussions regarding the seepage face, that is, the spatially varied flow occurring on the downstream slope, the "bed" will refer to the downstream face of the dam and not the foundation of the dam, which may have been a river bed before construction of the dam.

The only unknown in equation [5-1] is the friction slope S_f. If S_f can be determined this will enable the local shear stress due to the overflow of the seepage surface to be approximated using:

$$\tau = \gamma_w R\, S_f \qquad [2\text{-}44]$$

so that:

$$F_\tau = \tau\, A_p \qquad [5\text{-}2]$$

where:

τ = shear stress,

S_f = friction slope,

γ_w = specific weight of water,

F_τ = force due to overflow shear stress,

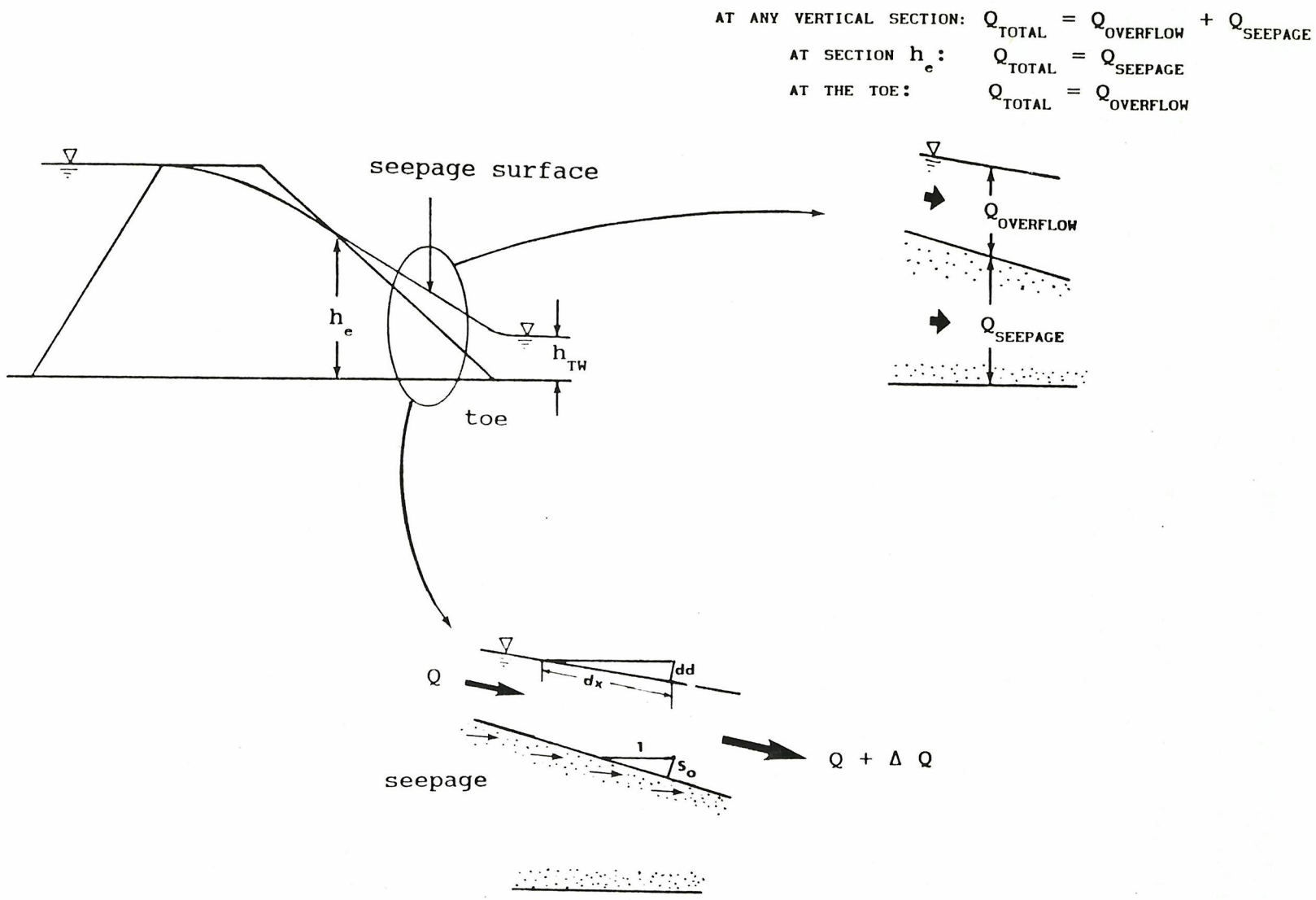


Figure 5-3. Schematic for seepage-surface definitions.

A_p= representative particle area, parallel to the flow and over which τ acts.

Three methods for determining S_f were considered. The first method will be described in some detail even though it was not successful. This description is given because the assumptions involved appear reasonable and greatly simplified the hydraulic calculations, and may therefore appear attractive (at first sight) to a designer who does not have detailed information. This first method was based on two assumptions:

(i) linear variation in depth from the seepage breakout point at elevation h_e to an independent estimate of the depth at the toe.

(ii) calculating q_* as:

$$q_* = \frac{(Q_{TOE} - Q_{he})}{b_{ed}/\cos\theta} \qquad [5\text{-}3]$$

where $b_{ed}/\cos\theta$ represents the total distance, along the bed, from the seepage breakout point at elevation h_e, to the toe of the dam. Q_{he}, the discharge at h_e, is zero. Equation [5-3] implies a linear variation of discharge with distance, a common assumption used in the analysis of spatially-varied flow in side-channel spillways (Henderson 1966, p.271).

The independent estimate of the depth at the toe of the dam was estimated from the following two equations, the first of which is a completely empirical result from the parametric study performed in the glass-walled flume, and the second of which is a definition (for any rectangular cross section of flow):

$$Fr_o = \frac{1}{4}\left\{ 11 \log_{10}\left(\frac{h_e}{H}\right) + 12 \right\} \qquad [5\text{-}4]$$

$$y_o = \left(\frac{q^2}{Fr^2 g}\right)^{1/3} \qquad [5\text{-}5]$$

where:

Fr_o = Froude number at the toe of the dam, associated with the vertical depth y,

h_e/H = elevation of seepage breakout point relative to the height of the dam,

q = discharge per unit length L of dam,

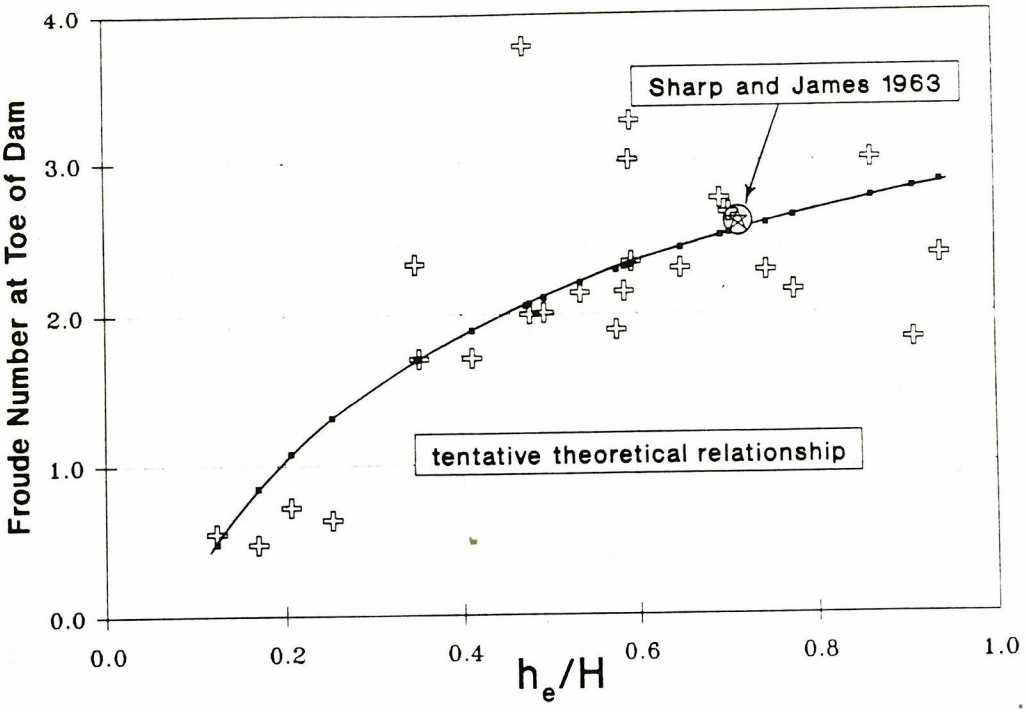
y_o = depth at toe of dam.

Strictly speaking, the depth y_o (measured vertically) in equation [5-5] should be d_o (measured normal to the bed). However, in collecting the experimental data for equation [5-4] the depth y_o was measured, not d_o. The relationship between the local depth perpendicular to the bed, denoted d, and the depth measured perpendicular to the horizontal, denoted y, can be geometrically shown to be as follows:

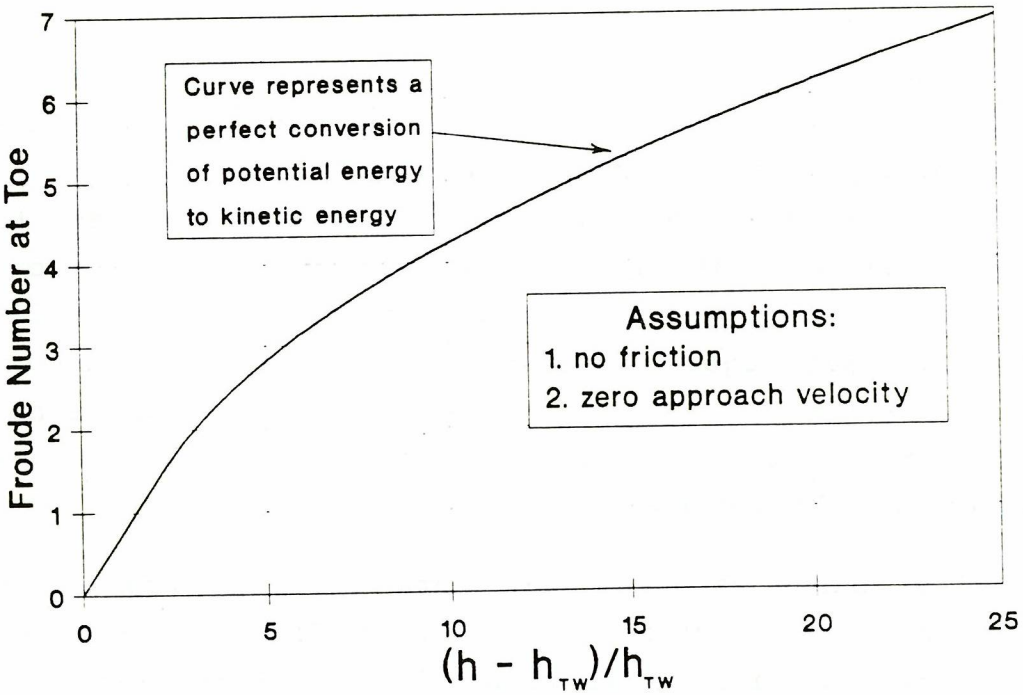
$$d = y \cos\theta \left[1 + \frac{dy}{dx} \sin\theta \right] \qquad [5\text{-}6]$$

Normally, such a correction is not taken into account in the analysis of gradually varied or spatially varied flow (Chow 1959), probably because in rivers the angle θ is rarely more than 4°. The writer is not aware of the above relationship having been presented elsewhere. The fact that dy/dx can be determined exactly only *after* the flow profile has been generated means that this relationship is difficult to apply rigorously, and could usually only be used in a tedious iterative fashion. Since the downstream slope of a flowthrough rockfill dam will always be greater than 4°, equation [5-6] should not be ignored.

Figure 5-4(a) shows equation [5-4] and the data from which it was derived. The similarity of the curves in Figures 5-4(a) and 5-4(b) is noted here and will be discussed later. Some observations were omitted from the regression analysis used to obtain equation [5-4] because a number of different methods were used to measure depth, and these methods were not equally precise. It was not always possible to use the depth at the toe inferred from a piezometric tapping point



a) tentative empirical relation.



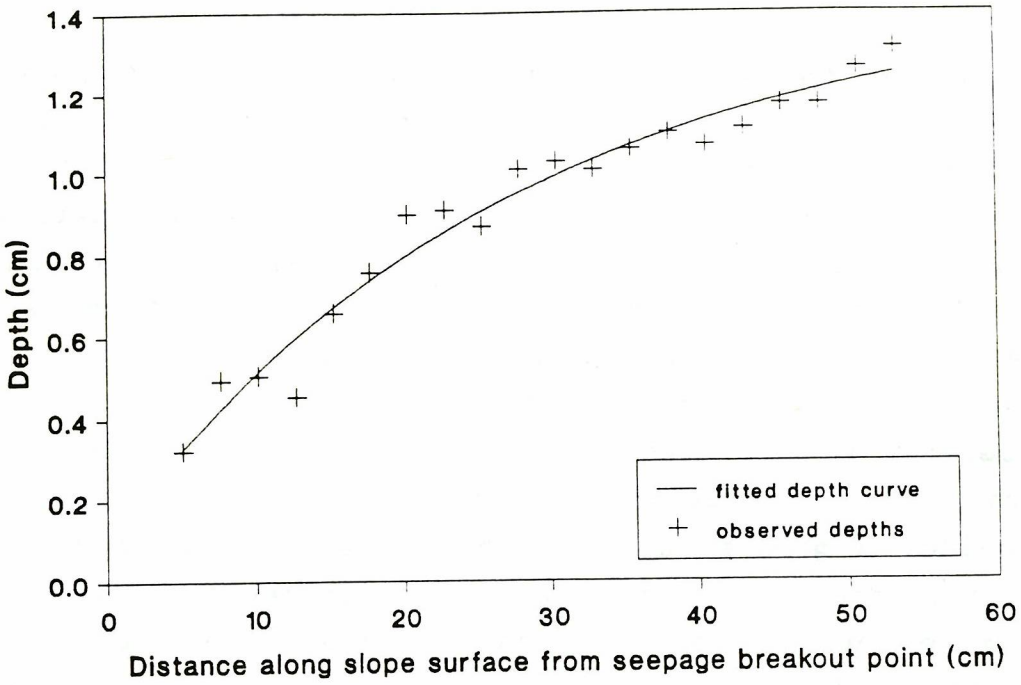
b) theoretical variation, no frictional effects.

Figure 5-4. Consideration of the Froude Number at the toe of the dam.

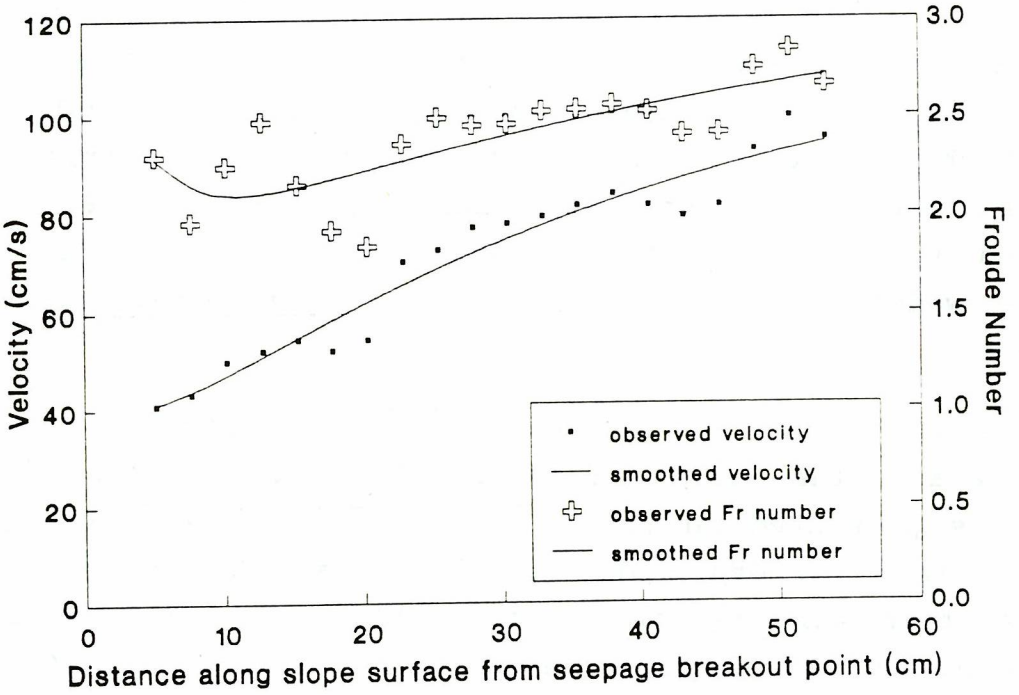
in the floor of the flume because a tapping point did not always coincide closely enough with the toe of the dam. The accuracy of measurements made using a ruler, an overhead point gauge, and the scale on the glass side-wall all suffered from the fluctuating nature of the flow, which in this case was a substantial fraction of the depth (as long as no tailwater was imposed). Equation [5-4] must therefore be taken as a tentative relation. It is somewhat surprising that the Froude number at the toe was not found to be clearly related to the downstream slope θ, as well as to the ratio h_e/H. This may be due to the fact that for a given h_e/H, a gradual slope provides a greater *distance* over which the flow velocity may increase, than does a steeper slope. This increased distance appears to compensate the lack of steepness for this particular example of spatially varied flow.

In order to evaluate method 1, as well as the next two methods attempted, data was needed at a level of detail not available in this study. This unavailability was partly due to the fact that it was not realized that this level of detail would be required, and partly due to the fact that it was found to be difficult to obtain data which adequately described the hydraulic characteristics of the seepage wedge. Fortunately, Sharp and James (1963) performed detailed measurements of both depth and velocity for a single seepage wedge on the downstream side of a flowthrough rockfill embankment.

Figure 5-5(a) shows the variation in local depth for the Sharp and James data. The variation in the local velocity and the Froude number is presented in Figure 5-5(b), where the Froude number was inferred from the depth and velocity data. The measurements under consideration were performed in a flume 30.5 cm wide on a model embankment with a slope angle of 25.2°, made up of 19 mm crushed basalt at a void ratio of 0.73. Velocity measurements were made with a pitot tube. It is immediately evident from Figure 5-5 that a considerable amount of scatter was observed, in spite of the fact that each point represented the average of five observations. A



a) depth *versus* distance.



b) velocity and Froude Number *versus* distance.

Figure 5-5. Data of Sharp and James (1963) for a seepage wedge.

second notable fact evident from the data is that the flow was supercritical throughout the length over which measurements were made. Since no tailwater was imposed on the model studied by Sharp and James, a mild hydraulic jump would have formed near the toe of the structure. This places this class of flow profile in Chow's (1959) "category D" for spatially varied flow: most of the length of flow supercritical with a hydraulic jump forming beyond the outlet, and not part way up the slope.

As a first attempt to compute shear stress, equation [5-1] was simply rearranged to give:

$$S_f = S_o - \left[\mathfrak{A} + (1-\mathfrak{B}) \frac{dd}{dx} \right] \qquad [5-7]$$

where:

$\mathfrak{A} = (2\alpha Q q_*)/(gA^2\cos\theta)$,

$\mathfrak{B} = (\alpha Q^2)/(A^2 D\cos\theta)$.

permitting the shear stress to be estimated using equation [2-44]. The lowest curves in Figure 5-6(a) and (b) show this simplification. It is evident that this simplification, together with $q_* = (Q_{TOE}\cos\theta)/b_{ed}$, gave completely unsatisfactory results for the shear stress so computed, with negative shear stresses resulting over nearly half the seepage face. Accordingly, this first simplification for estimating S_f, and thereby τ, was rejected.

A second method was therefore attempted. This method was based on the idea, suggested by Sharp and James (1963), that friction was of little importance near the seepage breakout point. Sharp and James (1963) demonstrated that the critical depth (Fr = 1) was reached very quickly within the seepage wedge, both experimentally and theoretically. Figure 5-5(b) shows that after a short distance down the seepage face, the Froude number was easily in excess of unity. They further showed that, if friction can be neglected for the very short subcritical zone, the distance at which the flow becomes critical is given by:

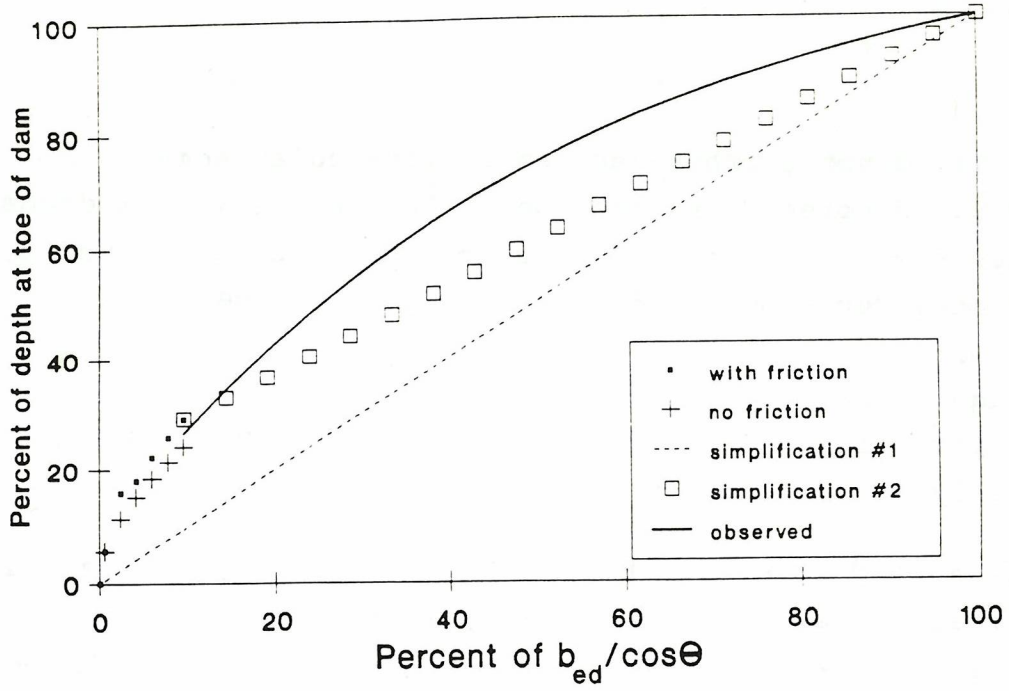
$$x = \frac{8 \cos^2\theta \, q_*^2}{g \, L^2 \sin^3\theta} \qquad [5\text{-}8]$$

where $q_* = dQ/dx$ and L and θ are defined in Figure 1-1. For the Sharp and James experiment the above equation gave x = 4.3 mm, which was easily upstream of the most upstream measurement made by James. Figures 5-6(a) shows that whether or not friction was included (as a non-zero value for Manning's n) in the analysis of the zone leading up to the first observation reported by Sharp and James made very little difference; the resulting depth at about 10% of $b_{ed}/\cos\theta$ was nearly the same. The following approximation was therefore attempted. A straight line was drawn between the depth occurring at 10% of $b_{ed}/\cos\theta$ and the depth at the toe, and q_* was given a single value, also based on a linear rate of change (of discharge) between these two points. Figure 5-6(b) shows that simplification #2 also gave unrealistic results (refer to the second lowest curve in Figure 5-6b). This is probably due not only to the fact that dd/dx was not single-valued (see slope of curve in Figure 5-5a), but also to the fact that q_* was not quite single-valued along the seepage face.

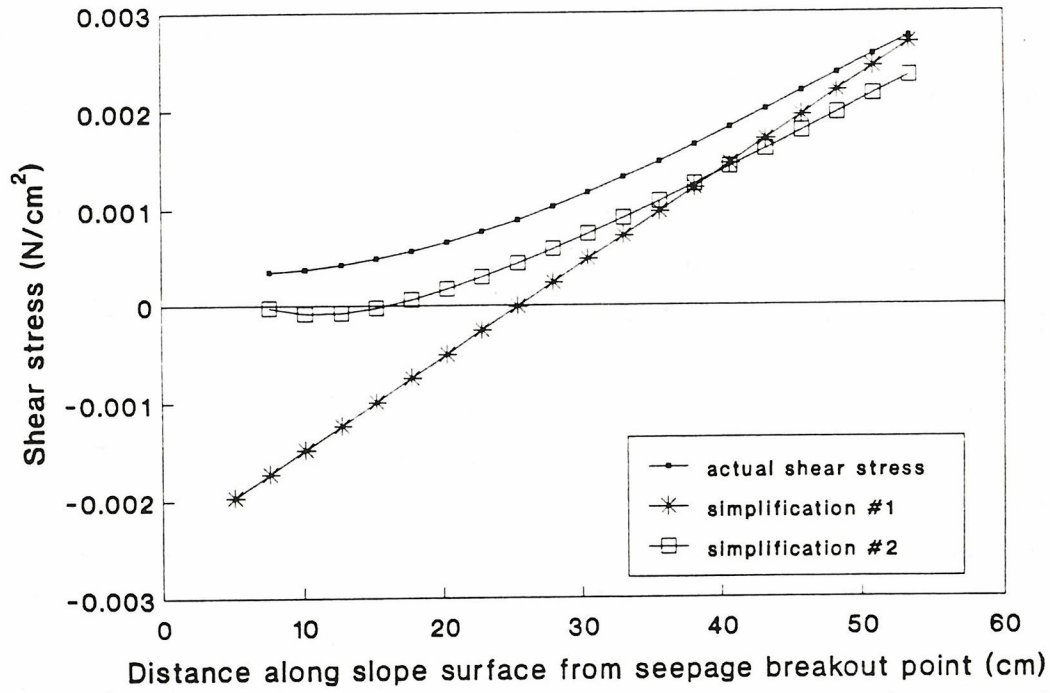
The above negative results led to the last alternative for computing the friction slope, and to thereby obtain an estimate of the shear stress. Unfortunately, this method is the most computationally intensive and is also the least general, which was why it was deemed worthwhile to first carefully examine the simpler options described previously.

Chow (1959) presents a means of numerically handling equation [5-1], and this method is clearly described both in a step-by-step and in a tabular form in Chow. Only a resumé of this standard (if little used) method will be given here (see also Appendix 6). The following equation can be used to compute the change in local depth

$$\Delta d(\cos\theta) = \underbrace{-\frac{Q_1(V_1 + V_2)}{g\,(Q_1 + Q_2)}\left(\Delta V + \frac{V_2}{Q_1}\Delta Q\right)}_{\text{"impact" loss}} \underbrace{- S_f \Delta x}_{\text{pure friction loss}} \qquad [5\text{-}9]$$



a) percent depth *versus* percent distance along the slope surface.



b) shear stress *versus* distance.

Figure 5-6. Attempted simplifications in modelling the seepage wedge.

where:

Subscript 1: denotes cross-section 1, located at some x,

Subscript 2: denotes cross-section 2, located at x + Δx downstream,

Δ: denotes the change in a quantity between sections 1 and 2,

$d\cos\theta$ = (local depth measured normal to bed) $\cdot$ $\cos\theta$,

Q = discharge,

V = average velocity (Q/A),

S_f = that part of the loss in total energy ($Z + P/\gamma_w + V^2/2g$) due *only* to friction at the bed,

Under this method (see also B part of Appendix 5-2), as applied to a supercritical regime, a drop in local depth between sections 1 and 2 (which are separated by a predetermined arbitrary distance) is assumed. This drop then implies a certain cross-sectional area of flow at section 2, as well as values for Q_2 and V_2, since q_* (= dQ/dx) is known. The assumed depth change also permits calculation of the so-called impact loss, which is the change in depth due to the interchange of emerging flow having little momentum, and the overflow, having much greater momentum.

As an aside, it is noted that the adjective "impact" is commonly used because the most commonly described scenario for spatially varied flow (with positive q_*) is a rectangular weir from which water falls into a side channel whose length is parallel to the plane of the weir. It is in this side channel, into which waters "impacts" as it falls in a sheet-like fashion from above, that the classical case of spatially varied flow takes place. It should be made clear that the term "impact" loss does not directly refer to losses caused by the considerable turbulence generated in the interchange; it does refer to the effect of adding some incremental flow to an existing flow, wherein the incremental flow has no component of momentum in the direction of the existing flow. A more precise term might be the "momentum interchange" energy loss. The term "impact" loss is a particularly manifest misnomer for the example of spatially varied flow under discussion, in which the incrementally added water does not fall from any height, but rather

emerges from beneath the main body of the flow as seepage. However, in the interests of consistency with existing terminology, the term impact loss will be used here.

Having evaluated the impact loss, the friction slope can be separately calculated using:

$$S_f = \left(\frac{n \overline{V}}{R^{2/3}} \right)^2 \qquad [5\text{-}10]$$

which is simply a rearrangement of the of Manning's equation for uniform flow (SI version). S_f can be calculated because R is consequential to the assumed change in local depth, as is $\overline{V}$, and a value for n is assumed. By adding the various terms causing a net change in the water surface elevation, the assumed change in local depth is compared with the computed change, and the assumed depth is adjusted until it matches the computed change. The calculation is then reperformed for the next contiguous Δx increment on the slope. This is done in a downstream direction for supercritical flow.

Sharp and James (1963) intimated the difficulty with the above method as applied to the seepage wedge when they stated:

"It is apparent that for the case of spatially varied flow at the toe of a rockfill slope the incoming fluid alters the boundary layer flow conditions."

Sharp and James (1963) suggested no values for Manning's n and did not attempt to numerically regenerate a depth curve such as the smoothed depth curve in Figure 5-5(a), based on some inferred variation in Manning's n value. However, by careful analysis of the smoothed Sharp and James data, back calculation of the appropriate value of Manning's n was performed, using equation [5-10] to determine S_f, and knowing the observed local values of d, Q, V, and q_*. Figure 5-7 shows how Manning's n varied along the seepage face. Unfortunately, the variation in n is considerable, almost linear with distance. The existence of some variation in n is not surprising, however, because the relative roughness varied along the the seepage

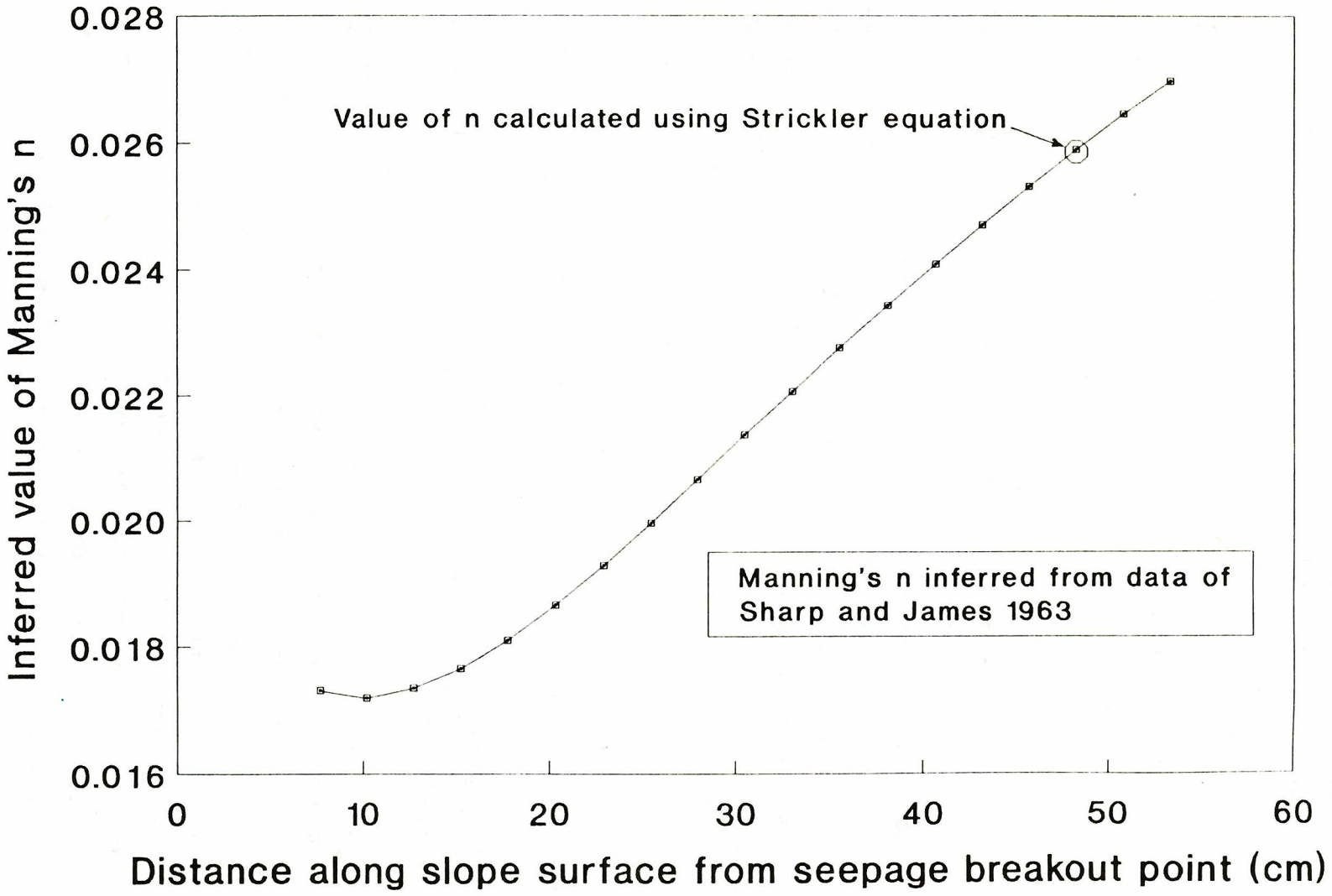


Figure 5-7. Inferred variation in Manning's n for Sharp and James data.

face. Relative roughness can be defined as (Schlichting 1955):

$$\Xi = \frac{u_* k_s}{\nu} \qquad [5\text{-}11]$$

where:

Ξ = relative roughness,

u_* = the friction velocity (a fictitious boundary velocity used to quantify boundary shear stress), $u_* = \sqrt{gRS}$ for uniform flow,

k_s = the roughness height, which characterizes the vertical size, arrangement, and spacing of roughness elements,

ν = kinematic viscosity.

Using k_s equal to the particle diameter implied that Ξ varied from about 1000 to about 4000 for the Sharp and James experiment (using the approximation that $u_* = \sqrt{gRS}$). These are extremely high values, indicating a very hydrodynamically rough boundary. The question of how to select Manning's n in general, for this class of problem, therefore arises. This is even more problematic when it is realized that the variation in relative roughness within the seepage face of a prototype dam may well be different from that of a model.

In spite of these observations the following comments can be made:

1. It is doubtful that a prototype would exhibit a different flow regime over most of the seepage face. Fully-developed turbulence existed within the seepage face of all models functioning at $h_e/H \geq 0.6$ (Re was greater than 1300 for the Sharp and James test, for example), so that viscous effects were minimal. The variation in Froude number would therefore still be expected to be primarily in the supercritical flow range for a prototype, just as they were in the models. The fact that ogee-type spillways can still be meaningfully modelled at about the same scale as that used in this study, for flowthrough rockfill embankments, tends to support the contention that a supercritical flow regime should also be expected to exist over most of the seepage face of a prototype.

2. Froude numbers computed in the range of 2.5 to 3.5, as calculated

from equation [5-4], would appear to be reasonable for a slope with considerable frictional effects, as is the case here. Consideration of Figure 5-4(b) shows that a frictionless spillway could only give a Froude number equal to approximately 5 for the maximum ratio of upstream depth to tailwater depth of 12 to 15 found in this study. Figure 5-4(b) is based on the following readily derived theoretical relationship for a hydraulic structure with no friction, and effecting a perfect conversion of potential energy (on the upstream side) to kinetic energy (at the toe):

$$Fr_{TOE} = \left[\frac{2(h-h_{TW})}{h_{TW}} \right]^{1/2} \qquad [5\text{-}12]$$

where:
Fr_{TOE} = the Froude number at the toe of the dam,
h = upstream depth, h_{TW} = tailwater depth at the toe (Figure 1-1).

3. It will always be possible to assume a variation in Manning's n along the seepage face such that the final computed depth at the toe (using numerical spatially-varied flow calculations; equation [5-9]) gives a reasonable match to the Froude number computed independently, using equations [5-4] and [5-5]. The numerical integration method used to model the spatially varied flow already involved using successive trials to find every local value of d along the slope. Consequently an attempt to arrive at the depth at the toe which precisely matched the depth found using equations [5-4] and [5-5] would be computationally intensive and not warranted, since equation [5-4] is itself an empirical result, with considerable scatter in the data.

4. Figure 5-7 shows how a value of n, computed using Strickler's equation, plotted as a point on the curve of the inferred variation in Manning's n, for the Sharp and James data. Strickler's equation is as follows (Bray and Davar 1987):

$$n = 0.047 \left(d_{50}\right)^{1/6} \qquad [5\text{-}13]$$

where:

n = Manning's friction coefficient,

d_{50} = median bed material size in m.

The above equation did not arise from an experimental study of the resistance of channel beds to spatially varied flow, for various sizes of bed material. Nor does equation [5-13] ostensibly apply, in general, to supercritical flow conditions. As such, it may be fortuitous that the value of n so computed occurred near the toe of the dam studied by Sharp and James. However, it will be possible to use item number 3 above to advantage to determine whether or not the use of the Strickler equation tends to give reasonable results for the depth computed at the toe of the dam.

The following table shows that for an assumed variation in Manning's n, the depth computed using equations [5-4] and [5-5] and the depth computed using the numerical form of equation [5-1] (that is, equation [5-9] applied using the method described in Chow, 1959) compared reasonably well:

Table 5-1

Comparison of Depth-at-Toe Computed Using Numerical Method (Equation 5-9), and using Equations [5-4] and [5-5]

Designation	Rock Size (mm)	n from Strickler	assumed n at toe	Numerically Computed *d* Depth (Eqn 5-9)	Depth y from Eqns [5-4] and [5-5]
Sharp&James	19.0	0.026	0.027†	1.25 cm‡	1.50 cm §
GF29d*	24.6	0.026	0.028	3.36 cm	2.82 cm
GF31c**	24.6	0.026	0.028	2.41 cm	2.23 cm
Prot1-N2***	300	0.038	0.038	0.60 m	0.67 m §§

† indirectly observed (inferred).

‡ directly observed.

* model in glass flume, downstream slope 1V:1H,

** model in glass flume, downstream slope 1V:2H,

*** fictitious prototype, downstream slope 1V:1.5H. See Appendix 6.

§ the observed value of *d* from the smoothed data was 1.33 cm.

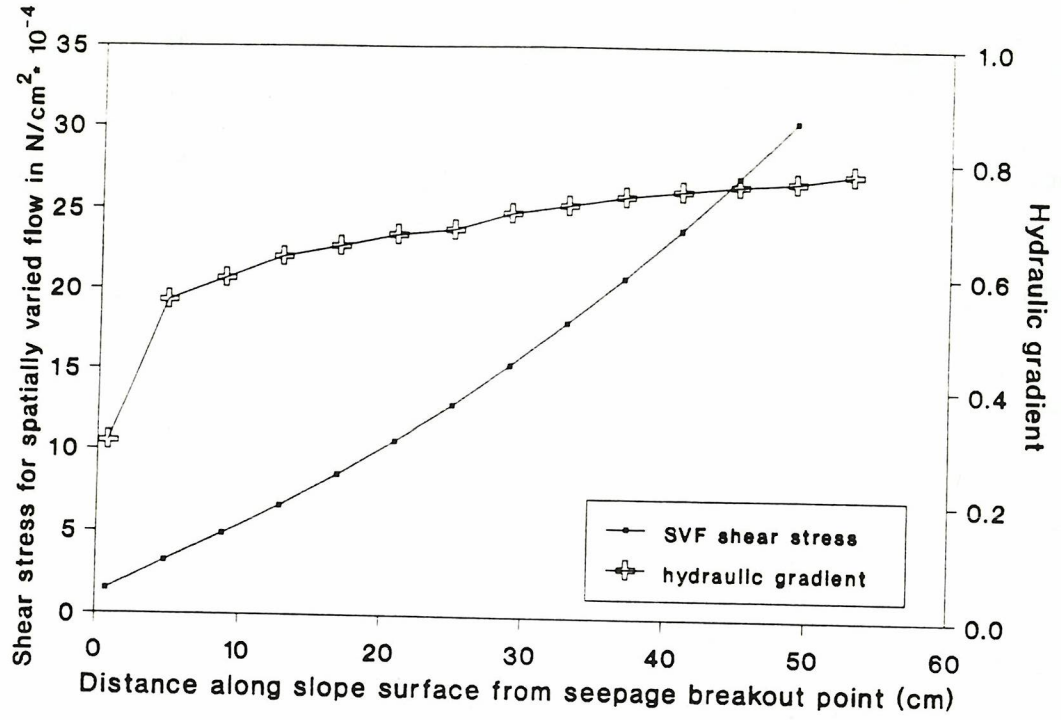
§§ if equation [5-6] is applied to convert y to *d*, *d* is 0.57 m.

None of the above cases had an imposed tailwater level, nor did any have an upstream impervious facing. Due to the tentative nature of equation [5-4] it was not considered meaningful to apply the refinement implied by equation [5-6] to the depths y, at the toe, computed for the two models in the glass flume.

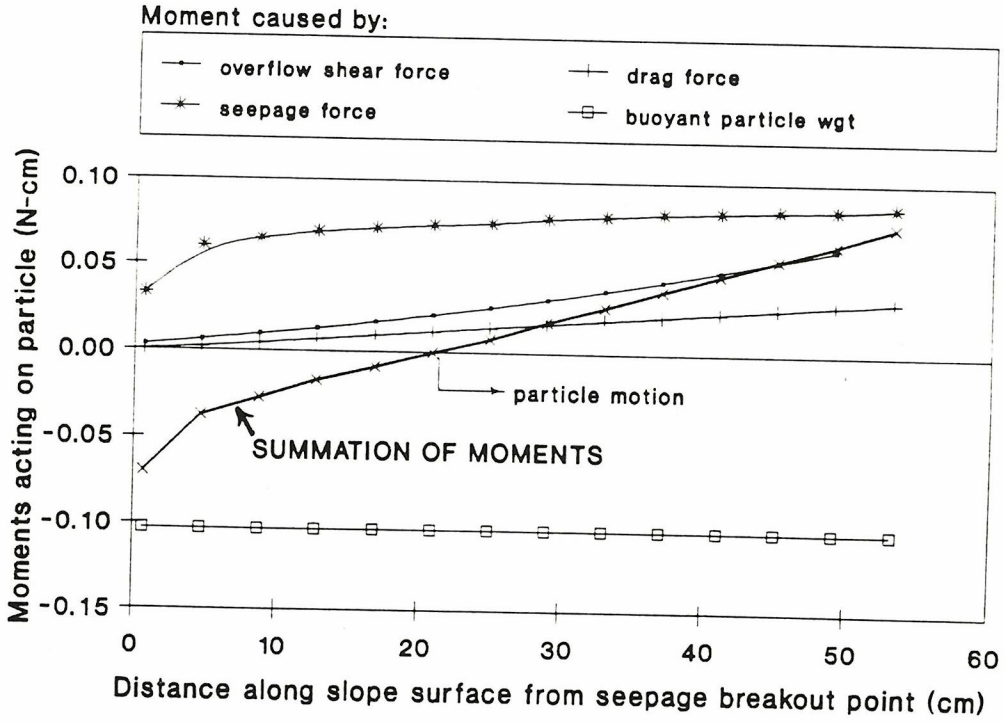
It might be argued that the depths (with the exception of the depth for the fictitious prototype) in Table 5-1 are very small, and that efforts to accurately compute them are therefore questionable. However, physical modelling must necessarily be done within the confines of laboratory-sized flumes, and the data reflect this constraint. Moreover, these small differences in depth correspond to real and important differences when seeking to make estimates for a prototype dam using the same computational techniques.

In each case the value of n at about 10% of $b_{ed}/\cos\theta$ was taken as a relatively low value (about 0.017) and increased linearly along the seepage face to the toe, where the value of n was taken as approximately that found from the Strickler equation. In the case of the two models (GF29d and GF31c), a slightly higher n at the toe was used. This is in keeping with the the fact that a slightly higher n than that calculated from the Strickler equation was inferred for n at the toe from the Sharp and James (1963) data. For the fictitious prototype this small refinement was not warranted.

Based on the above discussion and the ensuing results, it was concluded that a feasible method for estimating the shear stress due to spatially varied overflow had been developed. Unfortunately, the only workable method of the three methods considered required that the role of friction varies in an increasing manner along the seepage face. This method also required the most computational effort. Figures 5-8(a), 5-9(a), and 5-10(a) show how the shear stress due to spatially varied overflow varied along the seepage face (length = $b_{ed}/\cos\theta$) for the two models and the one prototype mentioned in Table 5-1.

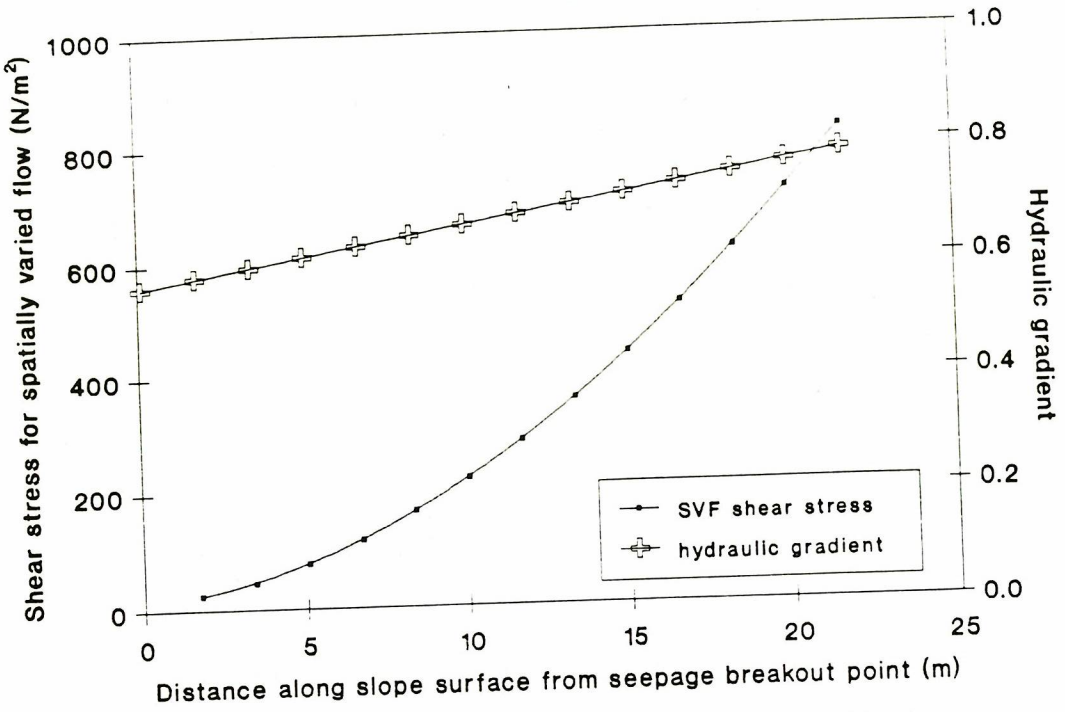


a) variation in shear and hydraulic gradient.

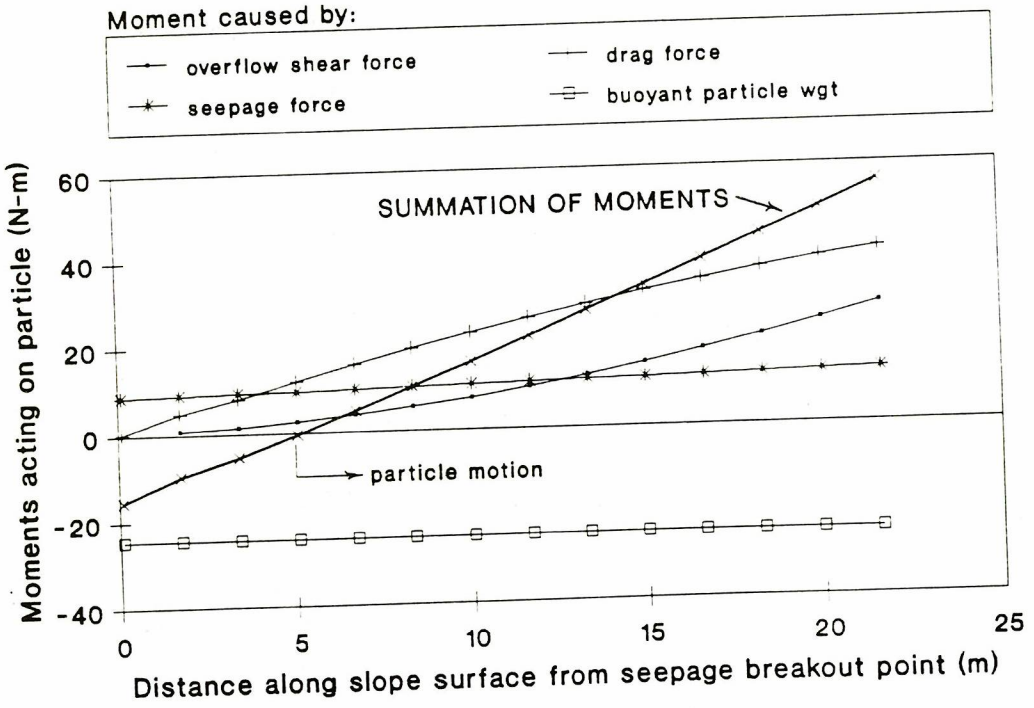


b) variation in particle moment.

Figure 5-8. Variation in shear, emergent hydraulic gradient, and particle moment, beneath the seepage surface for GF29d.

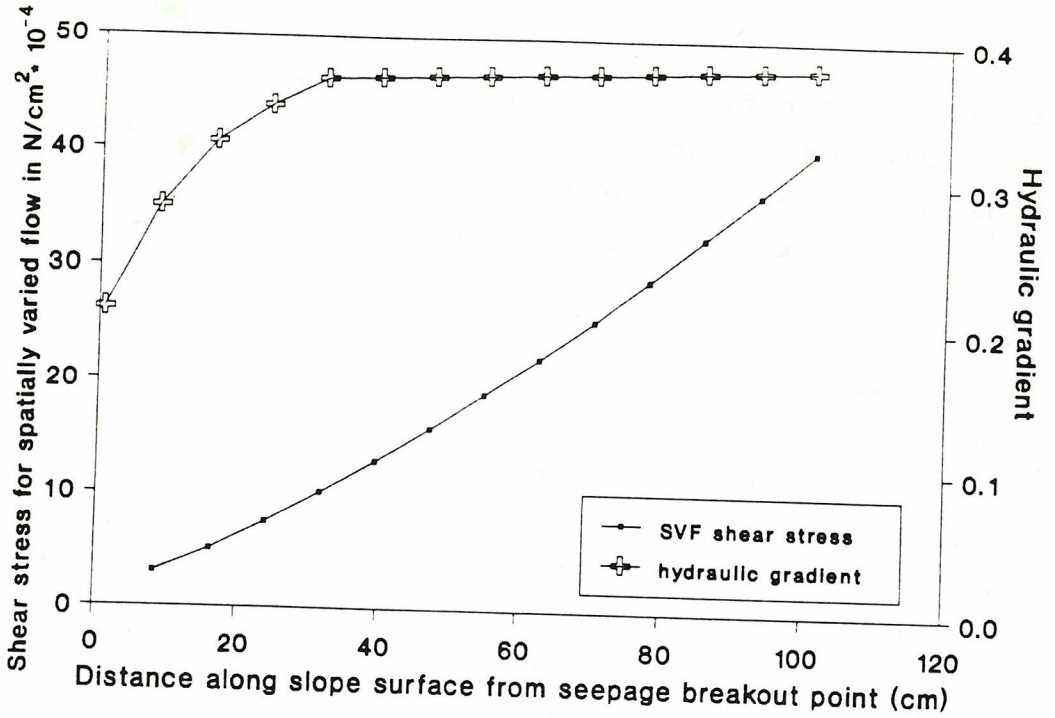


a) variation in shear and hydraulic gradient.

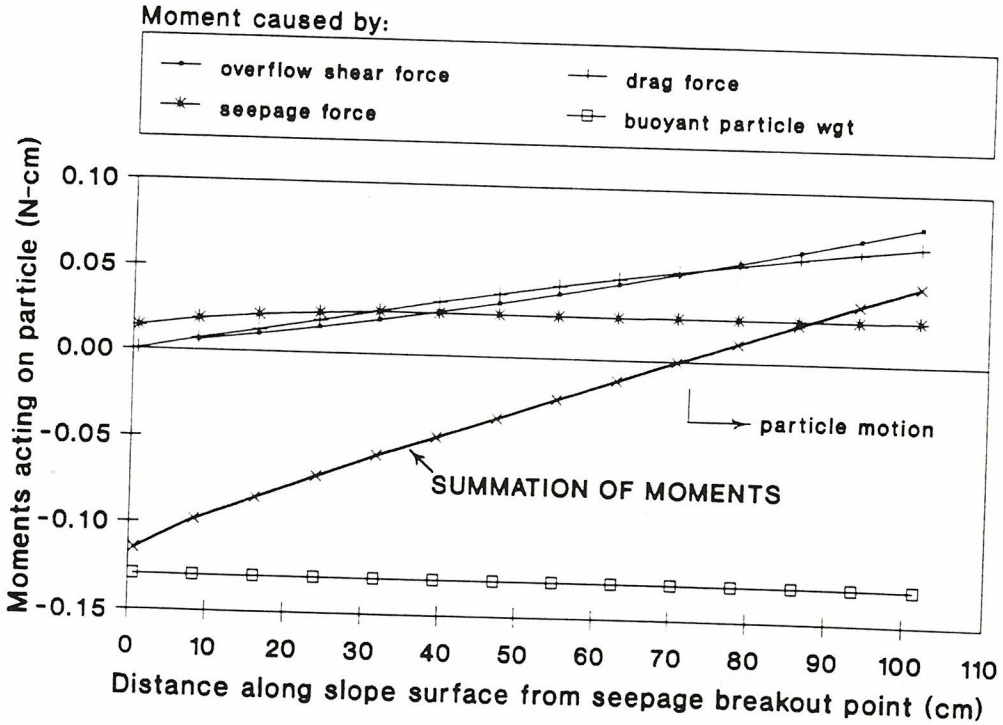


b) variation in particle moment.

Figure 5-9. Variation in shear, emergent hydraulic gradient, and particle moment, beneath the seepage surface for a prototype.



a) variation in shear and hydraulic gradient.



b) variation in particle moment.

Figure 5-10. Variation in shear, emergent hydraulic gradient, and particle moment, beneath the seepage surface for GF31c.

In addition to the overflow shear stress,two other quantities are needed to estimate the moment causing a rock particle to turn out of position because of overflow shear. These are: (1) the appropriate particle surface area exposed to the shear, and (2) the appropriate moment arm about which particle turning takes place. For the two models GF29d and GF31c, the surface area on which shear was assumed to act was taken as one-half the average *measured* rock surface area, as determined from the nickel coating technique described in section 3.1.3.2. For the fictitious prototype, having a nominal particle diameter of 0.30 m, this area was assumed to be 0.446 m^2, which is an approximation based on the surface area of an ellipsoid with axes in the ratio b/a = c/b = 2/3 from the Zingg diagram (Sabin pers.com., 1991). The length of the moment arm about which particle turning was assumed to take place was taken to be b/2, where b is the length of the intermediate axis. Appendices 5-3 and 5-4 summarize the areas and moment arms which were assumed in order to compute the various particle moments due to phenomena 1 through 4, stated at the beginning of this section. The particle radius r was taken as b/2.

The variation in the computed particle moment due to the computed overflow shear stresses, for the two models and the one fictitious prototype in Table 5-1, are shown in Figures 5-8(b) to 5-10(b). These results will be discussed in the context of a comparison of the relative magnitude of all particle moments.

2. *The seepage force* F_s per unit bulk volume $\mathcal{V}$ of porous media is:

$$\frac{F_s}{\mathcal{V}} = \gamma_w \, i \qquad [2\text{-}47]$$

Since a rock particle is under consideration, as opposed to a small bulk volume, an expression is needed for the seepage force per particle. If a porous media is conceived of as a continuum, any given bulk volume within that continuum contains both void space and solid rock. Clearly, the minimum bulk volume which could contain a single particle of volume $\mathcal{V}_p$ for a porous media having void ratio e,

is (Craig 1987):

$$\mathcal{V}_{min} = e\mathcal{V}_p + \mathcal{V}_p \qquad [5\text{-}14]$$

where:

$\mathcal{V}_p$ = representative particle volume,
(Can be computed from average rock mass/rock density),

$\mathcal{V}_{min}$ = minimum bulk volume which could contain a particle of volume $\mathcal{V}_p$,

e = void ratio, (volume of voids)/(volume of solids).

Combining equations [2-47] and [4-40] yields the expression for the seepage force per particle:

$$F_{sp} = (e\mathcal{V}_p + \mathcal{V}_p)\ \gamma_W\ i \qquad [5\text{-}15]$$

where:

F_{sp} = seepage force per particle,

γ_W = unit weight of water.

Equation [5-15] is an analytical result and can be used with any consistent set of units.

The hydraulic gradient i along the downstream face was obtained from non-Darcy pore pressure modelling, described in section 4.3.2.1. Although the gradient i is in fact a vector which can be resolved into vertical and horizontal components, in virtually all instances the considerably larger component was the horizontal one, at any given point along $b_{ed}/\cos\theta$ (that is, along the surface of the downstream face). The seepage force per particle causing the particle to turn out of position was therefore computed using the horizontal component of the hydraulic gradient. Although the magnitude of the true vector acting on each particle was somewhat larger than only its horizontal component, use of this larger value of i for the local hydraulic gradient would have been compensated for by the necessity of using a slightly shorter moment arm, since the angle of the particle moment arm above the horizontal is fixed at the value θ (the slope of the downstream face), and the length of the particle moment arm for this case is $(b/2)\sin\theta$ (see Appendix 5-4).

Figures 5-8(a) to 5-10(a) show how the value of the horizontal component of the hydraulic gradient varied along the downstream face, for the three dams considered. The local values of the horizontal component of i were computed using:

$$i_h = (h_5 - h_1)/(2\Delta x) \qquad [5\text{-}16]$$

where Δx and piezometric heads h_1 and h_5 are defined in Figure 2-4.

Knowledge of the variation in the hydraulic gradient i, together with equation [5-16], permitted estimation of how the moment tending to turn particles out of position varied along the distance $b_{ed}/\cos\theta$. Unlike the shear force previously discussed, and the drag force to be discussed next, there is no need to assign a value for the particle area associated with the seepage force; it is already computed on a per-particle basis.

3. *The drag force* due to overflow.

A drag force occurs when the overflowing water impinges on the exposed frontal surface of a given rock particle. This is because the rock juts out somewhat from the plane of the downstream face. The fluid thus loses some momentum as it passes over and around the rock. This change in momentum imparts a force against the front of the rock. The classical expression for the drag force imparted to an object within an infinite flow field is:

$$F_D = C_D \rho A \frac{V^2}{2} \qquad [5\text{-}17]$$

where:
F_D = force due to fluid drag,
C_D = shape-dependent empirical coefficient,
ρ = density of the fluid impinging on the object,
A = area presented to the flow (that is, a forward projection),
V = velocity of the flow.

If the velocity V can be approximated by the local mean velocity of the spatially varied overflow, the two main unknowns needed to

evaluate the drag force are then the coefficient C_D and the area A. In order to convert the force computed using equation [5-17] into a moment which tends to turn a given particle out of position, an approximation will also be needed for the length of the moment arm involved.

With regard to the area and the moment arm, it was assumed that the projected area against which the flow impinged was equal to one half πr^2, where the radius r was taken as the b axis (as defined in Figure 3-3a) divided by two. The moment arm was also taken as b/2. It is known that for the case of hydrostatic pressure against a plane that the line of action occurs at b/3 above the point of maximum depth, b/2 was taken since this is more conservative. In addition, for an irregular shape such as a rock it is very difficult to infer where the line of action of the drag force would actually act.

Unfortunately, information on the drag coefficient C_D for a roughened half-sphere was not readily available in the literature. Therefore, as a further approximation, the average of the values of C_D for a circular plate and that of a sphere was used. It was considered that a rock was neither as hydrodynamically smooth as a sphere nor as hydrodynamically blunt as a circular plate, but somewhere in between. The drag coefficient for a circular disk is 1.12, and is independent of the Reynolds number. In the interests of computational efficiency, the following approximation was developed to compute the drag coefficient of a sphere, and gives reasonable results for Reynolds numbers in the range 10 to 10000:

$$C_D = 0.38 + 0.32\,\mathfrak{p} + 0.13\,\mathfrak{p}^2 - 0.20\,\mathfrak{p}^3 \qquad r^2=0.9966 \qquad [5\text{-}18]$$

where:

C_D = drag coefficient for a sphere (points for regression were taken from an accepted curve, example is diagram F, Giles 1962),

$\mathfrak{p} = \log_{10}Re - \log_{10}5000$

$Re = VD/\nu$, D = diameter of sphere, ν = kinematic viscosity.

The velocity used to compute the Reynolds number and the drag force

using equation [5-18] was taken as the local mean velocity. For the case of the numerically determined depth of overflow in the prototype (test code Prot1-N2),it was found that the Reynolds number exceeded 10000. A high Reynolds number was not surprising since the boundary was hydrodynamically rough and the flow was supercritical. For this case only the drag coefficient C_D was therefore obtained by reading diagram F found in Giles (1962) (included in Appendix 6). Beyond **Re** = 10000 the drag coefficient for a sphere is known to have an erratic behaviour, to which a single curve could not be fitted to aid in computer computations.

The variation in the computed particle moment due to the fluid drag force for the two models and for the fictitious prototype mentioned in Table 5-1, are shown in Figures 5-8(b) through 5-10(b). These results will be discussed in the context of a comparison of the relative magnitude of all particle moments.

4. *The buoyant weight* force of the particle itself is the one force which results in a stabilizing moment acting in a direction opposite to the three moments previously described, and tends to keep the particle in place. For the two models GF29d and GF31c, the buoyant weight of the representative rock particle was computed knowing the mean of the measured mass for 75 particles, which was determined as part of the investigation on particle characterization (results summarized in Appendix 1). This mean value was 19 grams. The submerged weight was therefore:

$$W' = (19 \cdot 10^{-3}) \cdot (g) - \left(\frac{19 \cdot 10^{-3}}{\rho_{rock}} \; 9789 \; N/m^3 \right) = 0.12 \; N \qquad [5\text{-}19]$$

g = gravitational constant, 9.81 m/s^2,
ρ_{rock} = measured density of the limestone rock, 2695 kg/m^3.

The moment arm in this case was b/2, as shown in Appendix 5-4.

For the particles in the fictitious prototype, the particle mass was

computed from the following information:

(i) b axis assumed to be equal to 0.30 m,

(ii) the ratios b/a and c/b were taken to be the same as the average values for the rock particles used in the model embankments, that is, about 2/3 for both ratios,

(iii) by computing the ellipsoidal volume as $(\pi/6)\cdot a\cdot b\cdot c$,

(iv) taking the rock density to be 2695 kg/m^3, the density of the limestone used in the model studies.

As before, having this information permitted calculation of the submerged weight and the associated stabilizing moment for a representative prototype-sized particle (see also worked example in Appendix 6).

5.1.2 Discussion of the Summation of Particle Moments

The following table summarizes the estimated location of the position of first particle turn-out on the seepage face, for the three cases considered:

Table 5-2(a)
Summary of Estimated Positions of First Particle Turn-out

Test Code	Relative location of first particle turn-out*	Relative location of first particle turn-out†
GF29d	(13.85 cm)/(53.18 cm)= 26%	74%
Prot1-N2	(10.36 m)/(21.6 m)= 48%	52%
GF31c	(57.66 cm)/(101.22 cm)= 57%	43%

* as % of $b_{ed}/\cos\theta$ (see Figure 1-1); origin = seepage breakout pt.

† as % of $b_{ed}/\cos\theta$; origin at toe of dam.

Table 5-2(b)
Summary of Estimated Positions of First Particle Turn-out

Slope	Test Code	$B_d/\cos\theta$	Relative location of first particle turn-out‡
1V:1H	GF29d	70.72 cm	56 %
1V:1.5H	Prot1-N2	36.06 m	31 %
1V:2H	GF31c	112.5 cm	39 %

‡ as a % of $B_d/\cos\theta$ (see Figure 1-1); origin at toe of dam.

It was previously noted that particles unprotected by the mesh over the toe of the dam sometimes moved out of position at or near the discharge level of interest. The position of first particle motion was not a single highly repetitive position. However, it was observed that for the 45° slopes, some of the particles about two-thirds of the distance *up* the wetted face (relative to the toe) 'turned out' of position and rolled down the slope. For the 26° slopes this occurred much closer to the protective mesh, at about the one-third point *up* the wetted face. Based on the results for the model tests given in Table 5-2, it would therefore appear that the foregoing procedure for estimating the net particle moment, and therefore the position of first particle movement, is reasonable. It is also inherently somewhat conservative from a design point of view.

It is again emphasized that the foregoing analysis presumes that the particle downstream of the particle of interest is prevented from turning out of position by some form of restraint, such as a protective mesh. The analysis therefore indicates the required elevation of protection on the downstream face. The following sections will discuss these results on the basis of test-code designation, in order of increasing steepness of the downstream slope.

GF29d ($\theta \cong 45^{\circ}$)

Figure 5-8(b) shows the variation in estimated particle moments for the model test GF29d. It shows both the variation in the individual components due to overflow shear, emergent seepage, hydrodynamic drag, and buoyant particle weight; as well as the summation of these components. It is evident from Figure 5-8(b) that the particle moment due to seepage exceeded that of the drag force, and that both of these exceeded the moment due to overflow shear. It is evident that the particle moment due to seepage approximately offset the moment due to the submerged weight of the particle. Consequently, the sum of the moments due to overflow shear and drag acted on a particle which was in a meta-stable condition. (An example of a

meta-stable object is a sphere resting on a plane). In absolute terms, the effect of seepage is therefore seen as extremely important for this case (downstream slope $\theta = 45^{\circ}$). It is noted that, in terms of the *rate of change* in the particle moment, the moment due to drag changed most rapidly, followed by the moment due to overflow shear, followed by the moment due to the seepage force.

Prot1-N2 ($\theta \cong 34^{\circ}$)

Figure 5-9(b) shows the variation in estimated particle moments for the fictitious prototype PROT1-N2. It also shows both the variation in the individual components due to overflow shear, emergent seepage, hydrodynamic drag, and buoyant particle weight; as well as the summation of these four components. It is evident from Figure 5-9(b) that for the first two-thirds of the seepage face, as measured from the seepage breakout point, the particle moment due to seepage exceeded that of the drag force, and that both of these again exceeded the moment due to overflow shear. However, in moving further down the seepage face, the moments due to drag and shear increased in importance, whereas the moment due to seepage became less important relative to the other two moments. At the toe of the dam the largest moment was that due to drag, followed by that due to overflow shear, followed by that due to seepage. Although the the particle moment due to seepage did not completely offset the moment due to the submerged weight of the particle, as in the previously described case, it was still fairly important, allowing drag and shear to act on a particle which was considerably less stable than if seepage had not occurred at all. It is further noted that, in terms of the *rate of change* in the particle moment, the moment due to drag changed most rapidly, followed by the moment due to overflow shear, followed by the rate of change in the moment due to the seepage force, which had a small rate of change.

It can also be concluded from Figures 5-9(b) that mesh protection, to guard against unravelling failure, would be required over about three-quarters of the the wetted downstream face of this prototype flowthrough rockfill dam. This prototype was assumed to be

constructed out of rock of nominal size 0.30 m residing at a downstream slope of 1(V) on 1.5 (H). This dam was assumed to be functioning in flowthrough mode only, and for the conditions h = H and $h_e/H \cong 0.6$ (see Figure 1-1 for definitions).

GF31c ($\theta \cong 26^\circ$)

Figure 5-10(b) shows the variation in estimated net particle moment for model test GF31c. It also shows both the variation in the individual moments due to overflow shear, emergent seepage, hydrodynamic drag, and buoyant particle weight. It is evident from Figure 5-10(b) that, unlike the previous two cases, the particle moment due to drag exceeded that induced by the overflow shear, and that both of these exceeded the particle moment due to seepage, over most of the length of the seepage face. It is evident that the particle moment due to seepage did *not*, in this case, offset the moment due to the submerged weight of the particle. It is believed that this occurred for two reasons. First, the hydraulic gradient of the emergent seepage was not as high to begin with, compared to the previous two cases. Second, the slope of the downstream face was relatively flat, meaning that the moment arm over which the seepage force acted was short. Consequently, the moments due to overflow shear and drag were acting on a much more stable particle. The effect of the relatively flat downstream slope is therefore seen as very important in this case (downstream slope angle $\theta = 26^\circ$). Although the flat slope greatly reduced the destabilizing effect of seepage, it did not greatly affect the particle moments due to drag and overflow shear, since these are working on the same amount of exposed particle, and have moment arms which are unchanged by the flatness of the slope. Finally, it is noted that, in terms of the *rate of change* in the particle moment, the moments due to drag exceeded that of the overflow shear, and that these exceeded the rate of change of the seepage force.

5.2 EVALUATION OF POSSIBLE MASSIVE DEEP-SEATED FAILURE

5.2.1 Modelling of Pore Pressures for Non-Darcy Flow

An important issue in the design of flowthrough rockfill structures is the pore pressure distribution and the associated hydraulic gradients, neither of which are associated with Darcy's law. For such determinations the finite difference scheme of Curtis and Lawson (1967) (see equation 2-37), which is based on the partial differential equation presented by Parkin et al (1963a) (see equation 2-36), was tested and verified as a useful tool for non-Darcy flow pore pressure modelling. Equations [2-37] and [2-38] are derived in Appendix 2. The finite difference method of Curtis and Lawson (1967) was applied to model dams GF25, GF26, GF29d, GF31c, GF34a, FF17d, FF18a, and FF19b (refer to Tables A-1(v) and A-1(vi), Appendix 1, for a description of these model dams). It was also applied to a fictitious prototype designated PROT1-N2. The pore pressures computed using the finite difference method described in this section were used in the erosion and/or rotational failure analyses of configurations GF29d, GF31c, FF17d, FF18a, FF19b, and PROT1-N2. The following table gives the Reynolds number through the vertical section at h_e for some of these configurations, as well as for the two tests (GF25 and GF26) described in detail in this section:

Table 5-3

Reynolds Numbers at h_e for Selected Dam Configurations

Test	d (cm)	Porosity	Hydraulic Mean Radius (cm)	V_{he} (cm/s)	Re_p
GF25	2.5	~ 0.44	0.3	8.0	484
GF26	2.5	~ 0.44	0.3	7.1	433
GF29d	2.5	~ 0.44	0.3	10.4	635
GF31c	2.5	~ 0.44	0.3	6.6	401
PROT1-N2	30	0.39	2.0	29.4	15000

where:
d = nominal particle diameter,
V_{he} = horizontal bulk velocity through vertical section at h_e,
Re_p = pore Reynolds number (equation [2-15]).

Based on the above Reynolds numbers it can be expected that undesirable scale effects in modelling pore pressures will not be large. Since the particle diameter for tests in the floor flume ("FF" tests) was 13 cm, the Reynolds number for these tests would be larger than for the GF tests (and any undesirable scale effect even smaller). It should also be noted that a value of N = 1.88 in equation [2-3a] implies that the flow is characterized by nearly fully-developed turbulence. Such a value of N was used in the pore pressure modelling for glass-flume (GF) tests, as will be discussed in this section.

This section will only present details of the testing of this method for flume experiments GF25 and GF26. More information was collected regarding *internal* pore pressures for these experiments than for the experiments conducted as part of the parametric study described in Table 3-1. It was felt that if both the pore pressures and the discharges predicted by the finite difference model for these two tests were in reasonable agreement with observations, and if the discharges predicted by the model for tests GF29d, GF31c and GF34a were in reasonable agreement with discharges measured using the weir in the laboratory, this finite difference method could be considered generally useful in this study.

The emphasis in the following discussion will be on the application and verification of the finite difference method for determining pore pressures given by equation [2-38] to model tests GF25 and GF26. It is noted that no expressions have appeared in the literature for non-internal nodes associated with the non-Darcy flow case given by equation [2-38]. Such expressions are helpful if pore pressure modelling is to be attempted for the configuration of a typical embankment. If such expressions for boundary nodes are not used, the edge nodes must also be given by equation [2-38]. This

can be done but will necessitate a somewhat coarse description of the boundary in a step-wise fashion in which no adjustments are made to account for the true location of the local piezometric head relative to the edge of the numerical model of the dam. Other than the definition for an internal node, there are three nodal expressions which are useful in the modelling of piezometric pressure heads within a homogeneous isotropic rockfill embankment. These are:

1. *The case of a node adjacent to an impermeable boundary.*
It is known that equipotential lines lie perpendicular to impermeable boundaries. By performing a number of numerical tests it was found that equation [2-36a] gave the same result as equation [2-38] if piezometric heads were symmetrical about a vertical axis. It might therefore be expected that the impermeable boundary case for equation [2-36b] would give acceptable results even for non-Darcy flow. The standard expression used is:

$$h_c = \left(4h_1 + 2h_2 + 8h_3 + 2h_4 + 4h_5\right) / \ 20 \qquad [2\text{-}36b]$$

2. *The case of a node adjacent to the entrance or discharge (seepage) face of the dam.*
For this case two expressions are useful. The first is (see Figure 5-11(a)):

$$\left[\ 2 + \frac{1}{x'} + \frac{1}{y'}\ \right] h_c = \frac{1}{x'}h_1 + \frac{1}{y'}h_3 + h_5 + h_7 \qquad [5\text{-}20]$$

The second is (Figure 5-11(b)):

$$\left[\ 3 + \frac{1}{y'}\ \right] h_c = h_1 + \frac{1}{y'}h_3 + h_5 + h_7 \qquad [5\text{-}21]$$

If, for example, the upstream slope of the dam is at an angle other than 45 degrees, the line describing the entrance face of the dam will pass through the connections between many nodes. If two such connections are intersected at a given location, equation [5-20] is needed; if one connection is intersected then equation [5-21] is applied. Equation [5-20] is used more frequently on gradual slopes than equation [5-21]. Both are generally needed for inclinations of other than 45 degrees.

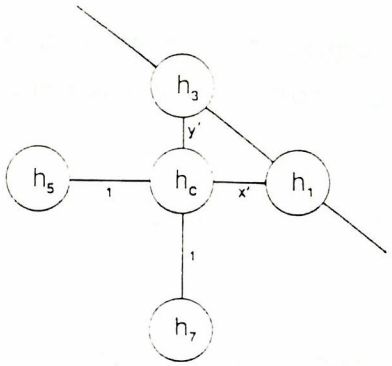
3. *The case of a node adjacent to the phreatic surface.*
If the location of the phreatic surface is known *a priori*, equations [5-20] and/or [5-21] can be used. If the phreatic surface is not known it can be determined by trial and error. Although the following pair of equations (Kleiner 1985) were not used in the analysis described herein, they are given here for completeness (Figure 5-11(c)):

$$\left[3 + \frac{1}{y'} \right] h_c = h_1 + \frac{1}{y'} h_3 + h_5 + h_7 \qquad [5\text{-}22a]$$

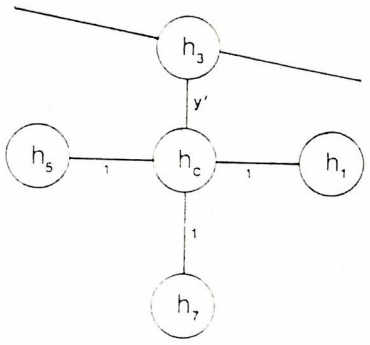
$$h_Q = h_3 - y'(1 - \cos^2\theta) \qquad [5\text{-}22b]$$

Figure 5-11 defines each variable and node location for equations [5-20], [5-21], and [5-22].

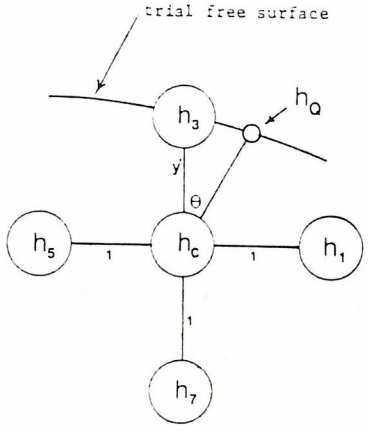
It is assumed, when using equation [5-22], that h_Q and h_c lie on an equipotential. Since all points along an equipotential line have the same piezometric head, the final value computed for h_Q must equal h_c. According to Kleiner (1985) the assumed position for the phreatic surface is changed until the difference between h_Q and h_c is zero. This would also appear to require adjustment of the values of y and θ, making this technique computationally cumbersome. Note that equations [5-20], [5-21] and [5-22] are based on a five-point rather than a nine-point finite difference scheme (see Figure 2-4).



a) finite difference star for equation [5-20].



b) finite difference star for equation [5-21].



c) finite difference star for equation [5-22].

Figure 5-11. Finite difference stars for non-internal nodes.

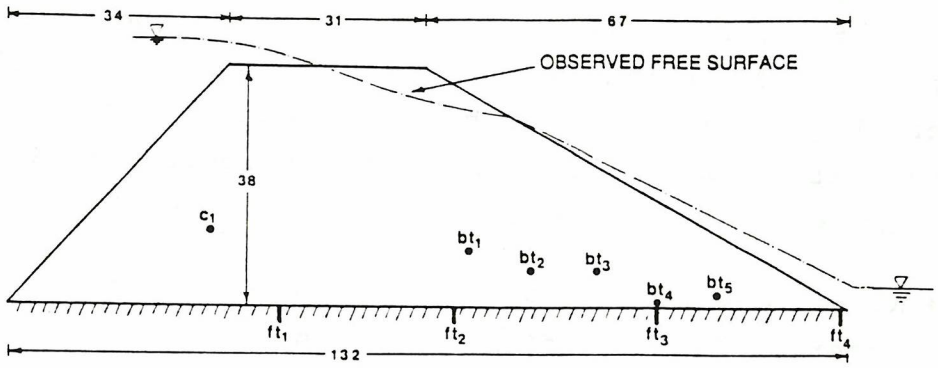
However, for the sake of consistency of nomenclature, the subscripts indicating nodal points for the nine-point scheme have been retained.

The prediction of the phreatic surface is best approached without recourse to a trial and error procedure. The method developed for computing the location of the phreatic surface was described in section 4.2. Once the location of the phreatic surface has been directly computed, equations [5-20] and [5-21] can be used for the nodes adjacent to the phreatic surface.

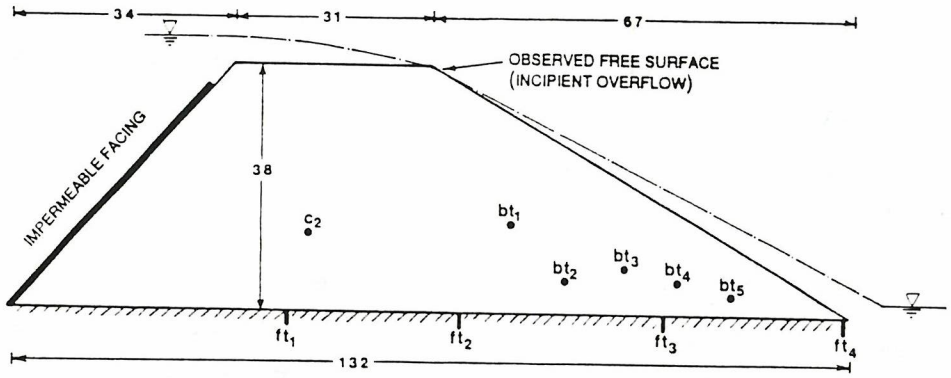
For an entrance (or exit) face inclined at exactly 45 degrees, equation [2-38] can be used directly, as long as care is taken to ensure that node h_4 (or h_2) in Figure 2-4 is also assigned the applied head. Non-linear finite difference expressions for entrance and exit faces inclined at other than 45 degrees do not exist. Also, a non-linear finite difference expression is not available for nodes next to an impermeable boundary. In order to circumvent this difficulty equations [2-36b], [5-20] and [5-21] were used. These finite difference expressions are associated with Darcian linear flow, for which N = 1 in equation [2-38] . However, only a single layer of such nodes was needed along the boundary of the embankment. These nodal definitions transmitted applied heads to the inner nodes, which were defined by equation [2-38] for non-linear flow. It was expected that if a reasonably large number of finite difference nodes was used, this single layer of Darcian nodes around the boundary would not result in significant errors.

The finite difference equations can be conveniently solved using a commercially available electronic spreadsheet operating on a desktop microcomputer. Some comments pertaining to practical aspects of the use of a spreadsheet for solving this type of numerical problem are presented in Appendix 8.

Figure 5-12 shows the configuration of the model rockfill dam and the location of the piezometric tapping points for the two tests to be discussed. For model test GF25, shown in Figure 5-12(a), no upstream



a) test GF25, without upstream impermeable facing.



bt: BODY TAP FOR MONITORING PIEZOMETRIC PRESSURE

ft: FLOOR TAP FOR MONITORING PIEZOMETRIC PRESSURE

C1 AND C2: POINTS USED FOR CHECKING NUMERICAL CONVERGENCE

DIMENSIONS IN CENTIMETERS

b) test GF26, with upstream impermeable facing.

Figure 5-12. Configurations of model dams GF25 and GF26, showing piezometric tapping points.

impermeable facing was present. For model test GF26, shown in Figure 5-12(b), an impermeable facing was provided on the upstream face. In order to prevent erosion of the downstream face, a metal mesh was tensioned around a rebar frame and this assembly was anchored onto the downstream face of the dam. The width of the glass-walled flume was 38.5 cm, and a coordinate grid on the glass wall made it possible to record the position of the phreatic surface. Rock of diameter 25 mm (3/4") was placed in the flume at a porosity of about 44%. This is the same material as was used for column test 7.

A distance of one centimeter between any two nodal points was used for all interior finite difference stars, for GF tests. It was found that if the distance between nodal points was made larger than this for the numerical simulations (resulting in a smaller total number of finite difference stars), unrealistic piezometric heads were computed for the downstream toe. Equations [5-20] and [5-21] were used for the entrance and exit faces and equation [2-36b] for the layer next to the floor of the flume. Equation [2-38] was used for all other (internal) nodes. It was necessary to select a value of N (see equation 2-3) in equation [2-38]. For these tests N was set equal to 1.88, a value previously determined from column test 7 performed on a sample of the same rockfill.

Table 5-4 presents a comparison of the observed discharges with the discharges computed from the results of finite difference modelling. The common vertical cross-section used to compute the discharge was that through h_e. The local velocity within each such vertical section was computed using the following empirical equation, determined from column test 7:

$$V = 12.39\ i^{0.53} \qquad [5\text{-}23]$$

where:
i = hydraulic gradient,
V = local bulk velocity, cm/s.

The local horizontal hydraulic gradient used to compute the local velocity in equation [5-23] was obtained from equation [5-16].

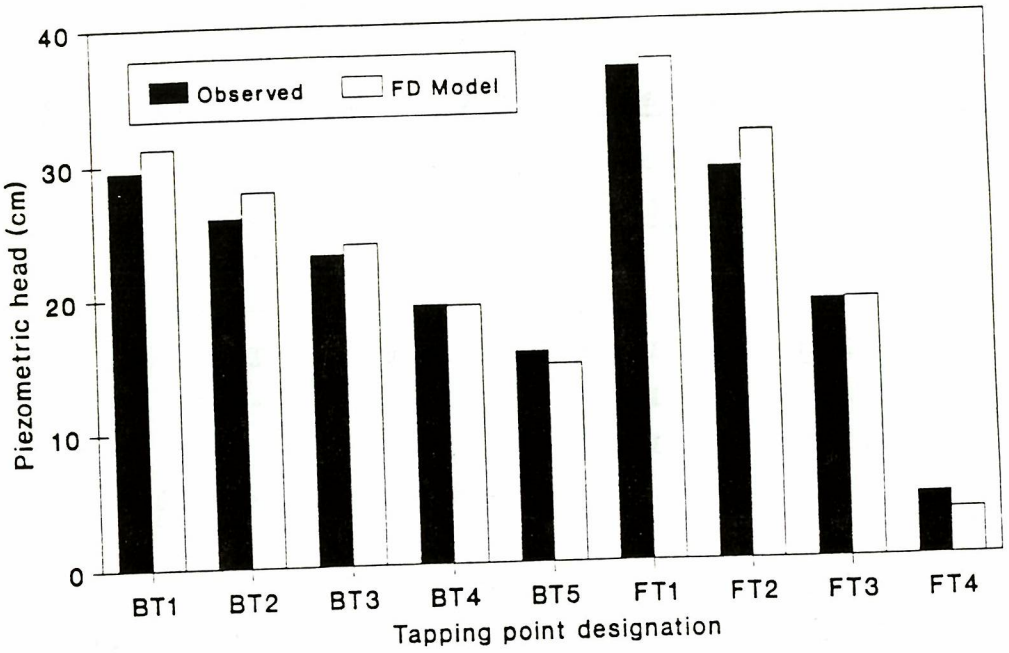
Table 5-4

Comparison of Observed Discharges with FD Modelling Results

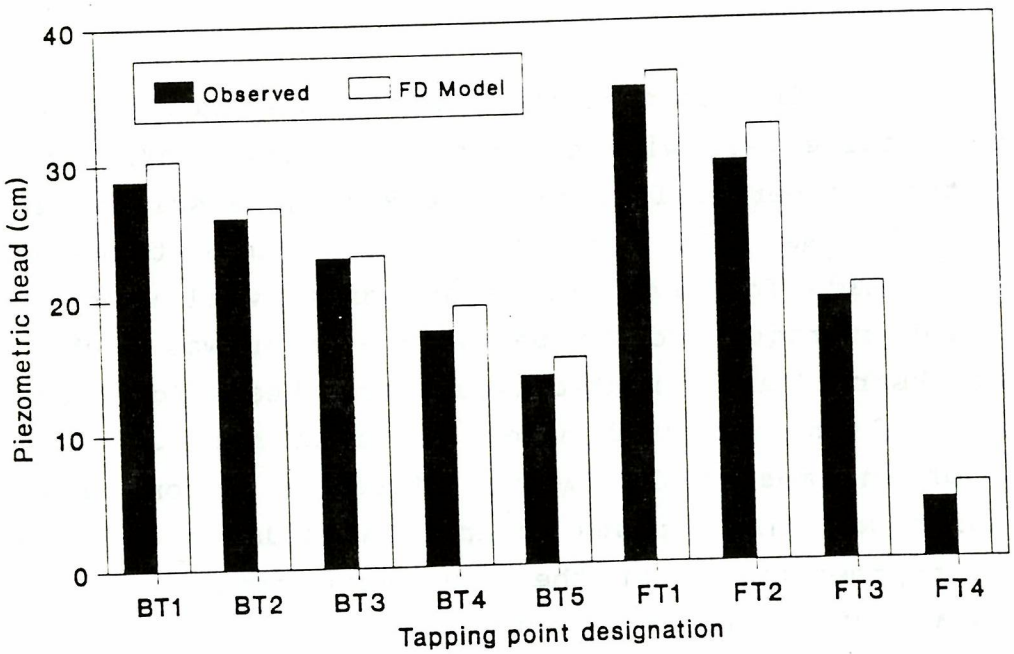
	Actual (L/s)	predicted (L/s)	% error
GF25	9.35	8.12	-13.2%
GF26	9.18	8.27	-9.9%
GF29d	14.96	12.68	-15.2%
GF31c	11.31	10.71	-5.3%
GF34a	10.82	10.82	0.1%
		average	-8.70%

Table 5-4 indicates that the discharges inferred from finite difference modelling of pore pressures tended to underestimate the actual discharges, but that the predicted discharges were reasonably close to observed values. Part of the error may be due to overestimation of the actual flow using the available empirical equation for the weir.

Figure 5-13(a) indicates that the computed piezometric heads for test GF25 agreed quite well with observed piezometric heads for the case of no upstream impermeable face. The average absolute percent error for test GF25 was 6.7%. Figure 5-13(b) shows that the computed piezometric heads for test GF26 also agreed well with the observed values. The average absolute percentage error was 8.0%. Table 5-5 gives the observed and computed piezometric heads for Figure 5-13 and the errors of the computed heads for both tests. Note that the presence of an impermeable facing introduced a zone underneath the facing which was only exposed to applied heads on one side. For the numerical representation of the embankment used for test GF26, the applied heads of the boundary conditions had to move inward from the crest and from the downstream face of the dam (that is, from upper right to lower left). Computationally this was a very slow process, necessitating many more relaxations of the grid than were used for the numerical simulation of GF25. The last part of the numerical representation of the embankment to be affected by the boundary



a) test GF25, without upstream impermeable facing.



b) test GF26, with upstream impermeable facing.

Figure 5-13. Comparison of computed and observed piezometric heads for model tests GF25 and GF26.

Table 5-5

Comparison of Observed and Computed Piezometric Heads

TEST: GF25	Tap:	BT1 (cm)	BT2 (cm)	BT3 (cm)	BT4 (cm)	BT5 (cm)
Observed		29.48	25.88	23.06	19.14	15.50
FD Model		31.16	27.82	23.79	19.08	14.55
% error		5.69%	7.50%	3.17%	-0.31%	-6.15%

	Tap:	FT1 (cm)	FT2 (cm)	FT3 (cm)	FT4 (cm)
Observed		36.54	28.94	18.98	4.54
FD Model		37.05	31.58	19.08	3.34
% error		1.40%	9.12%	0.53%	-26.42%

average percent error	-0.61%
average absolute percent error	6.70%

TEST: GF26	Tap:	BT1 (cm)	BT2 (cm)	BT3 (cm)	BT4 (cm)	BT5 (cm)
Observed		28.80	25.99	22.93	17.43	13.95
FD Model		30.23	26.73	23.09	19.25	15.23
% error		4.95%	2.85%	0.71%	10.40%	9.17%

	Tap:	FT1 (cm)	FT2 (cm)	FT3 (cm)	FT4 (cm)
Observed		35.13	29.57	19.34	4.40
FD Model		36.18	32.12	20.37	5.60
% error		2.99%	8.64%	5.34%	27.33%

average percent error	8.04%
average absolute percent error	8.04%

For definition of column headings see Figure 5-12.

conditions lay in the zone between the impermeable upstream face and the impermeable base of the dam.

It was found that that no severe discontinuities in piezometric head were introduced near the boundaries of the numerically modelled embankments. This is the case even though finite difference nodes associated with linear Darcy-type flow were used as an interface between the imposed boundary conditions and the internal nodes defined by equation [2-38]. The absence of discontinuities was probably due to the relatively large number of non-Darcy finite difference nodes (numbering about 2960), as compared to Darcy finite difference nodes (numbering about 160), and this ratio had a dominating effect on the piezometric head.

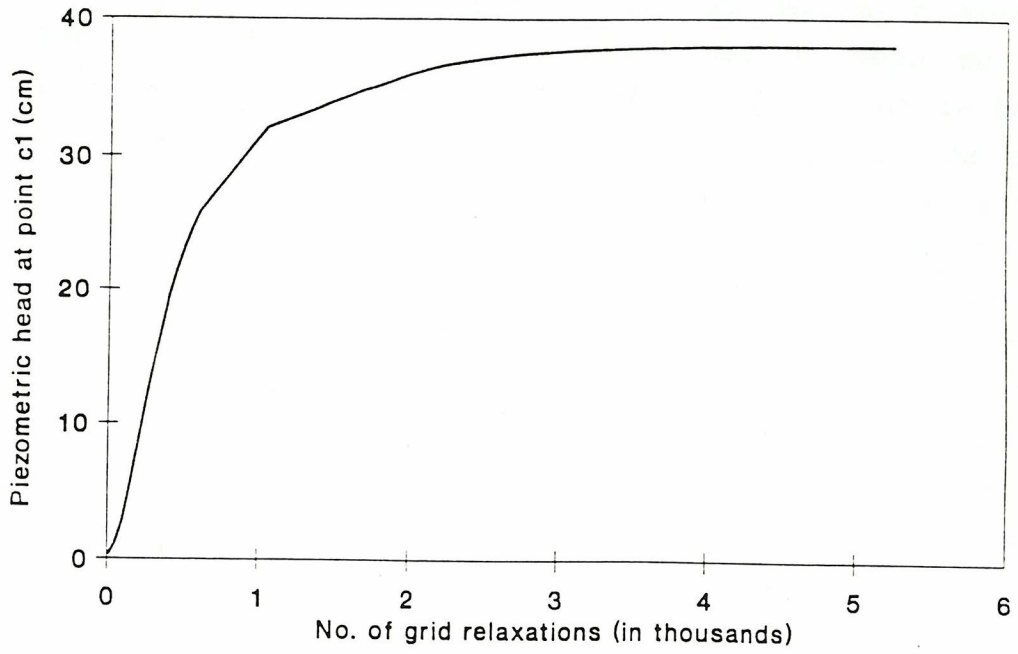
It was found that the maximum hydraulic gradient within the toe of the dam for test GF25 was 0.57, and was 0.56 for GF25. It would appear therefore that the presence of an impermeable facing does not seriously affect stability from the point of view of seepage forces. Pore pressure simulations under boundary conditions similar to GF25 for model test GF29 yielded a maximum hydraulic gradient of 0.8, again near the toe of the dam.

Figure 5-14(a) shows how the convergence of a cell within the body of the dam used in GF25 (denoted as "c1" in Figure 5-12(a)) proceeded as the number of iterations increased. A comparison of the characteristics of the convergence for the two tests are given in Table 5-6. Clearly, the numerical modelling of GF26 had poorer convergence characteristics than that of GF25. This was due to the presence of the upstream impermeable facing.

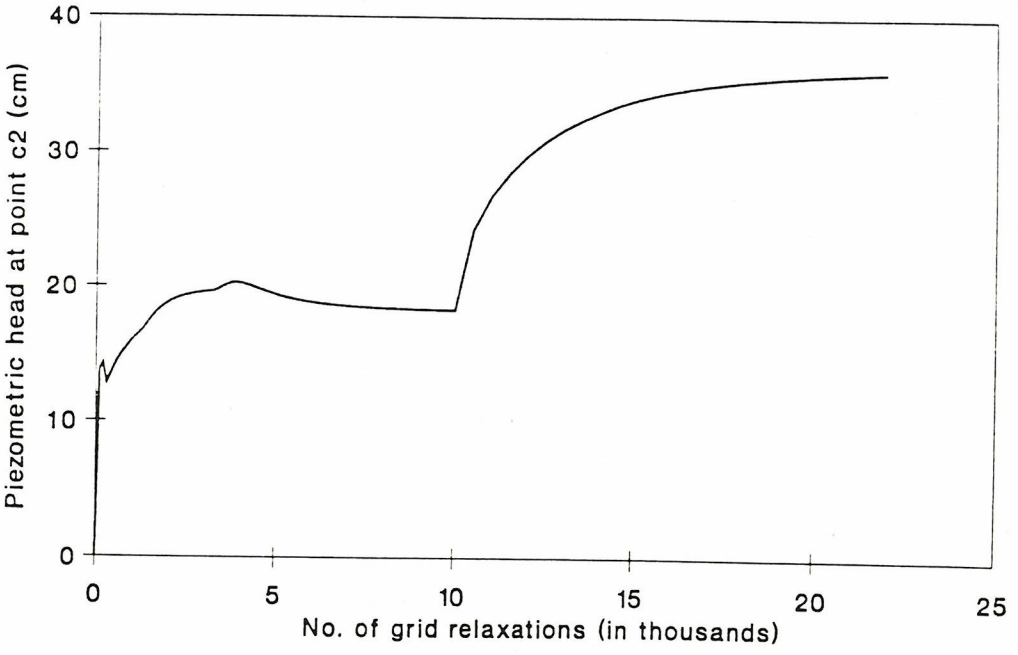
Table 5-6

Comparison of Convergence Characteristics

	Total Number of Relaxations	Final Rate of Change of Head
Test GF25	5290	0.0001 cm per relaxation
Test GF26	22050	0.0049 cm per relaxation



a) test GF25, without upstream impermeable facing.



b) test GF26, with upstream impermeable facing.

Figure 5-14. Convergence characteristics of numerical simulation of piezometric heads for model tests GF25 and GF26.

Figure 5-14(b) shows how the convergence of a cell within the body of the dam used in test GF26 (denoted as "c2" in Figure 5-12b) proceeded as the number of iterations increased. The rapid rise in head was accomplished by sparsely "seeding" the grid with a fixed value of head at a number of internal locations. The distinct shift in the trend, which can be seen in Figure 5-14(b), occurred when these fixed values were removed and replaced with equation [2-38]. As more knowledge is gained regarding typical patterns of piezometric head within rockfill dams it will be possible to seed the associated finite difference grid with a pattern of heads which is closer to the final solution, which will make for more rapid convergence toward a given solution.

The following conclusions are made regarding the simulation of piezometric pressure heads in two model rockfill dams in which the steady-state discharge through the dams did not follow Darcy's law:

1. It was found that applying finite difference expressions associated with Darcy's law for edge nodes provided a workable model for piezometric pressure head even though flow through the embankment was non-linear. Mean absolute deviations from observed piezometric heads were less than 10 percent. About 3100 nodes were used for each model and this high density of nodes was considered to be important for the success of the model.

2. The introduction of an impermeable upstream face on the dam necessitated a greater number of relaxations of the finite difference grid. It was found to be computationally intensive to model the piezometric heads in the zone between the impermeable face and the base of the dam.

5.2.2 Analysis of Possible Rotational Failure

One of the most well-known and widely-applied methods for examining the possibility of massive rotational failure in a slope is known as Bishop's Simplified Method (described in Craig 1987). This method

has the following features:

i) It is a limit equilibrium method. At incipient failure the shear strength is fully mobilized all along the assumed failure surface, and the overall slope and each part of it are in static equilibrium. This implies that that no part of the slope fails before any other part; the slope fails as a unit (Nash 1987).

ii) It involves the calculation of the Factor of Safety (FOS). A computed FOS *greater* than unity means that *mobilized* shear *strength* is greater than the *applied* shear *stress*, and the slope is stable.

iii) It is based on a the Mohr-Coulomb model of soil behaviour.

iv) It represents an approximate method of solving a problem which is statically indeterminate. The best means of overcoming this statical indeterminacy has been the subject of a great deal of research (see for example the review by Nash 1987, pp.11-75). Under Bishop's Simplified Method it is assumed that the horizontal interslice forces have no vertical component. Since, in the derivation of Bishop's Simplified Method, forces are resolved vertically, it is then unnecessary to assume a spatial variation for the horizontal interslice forces. *Vertical* interslice forces, on the other hand, are assumed to cancel out for any given slice.

v) It requires the selection of a slip circle, about which failure is conceived to occur. The centre of this slip-circle is in a sense fictional, however, because this method is not a moment-based method (as is the older Fellenius Method). All material above the slip-circle is 'free' to rotate, as a unit, for any slip circle for which the FOS is less than unity. Figure 2-7(a) presents a number of possible slip circles suggested by Parkin (1971) for a rockfill embankment. Generally, it is necessary to assume a number of different slip circles before the computations show that one of these has the lowest value of any possible slip circle. The slip circle associated with the FOS equal to unity is often also of interest.

vi) The expression for the FOS depends on an assumed FOS. However, if the assumed FOS is set equal to the previously computed value of the FOS, the method converges rapidly in three of four iterations, for a given assumed slip circle.

Using Bishop's Simplified Method, the FOS can be computed, for a cohesionless material (such as rockfill), using the following expression:

$$FOS = \frac{\sum_{i=1}^{n} \frac{W_i - u_i b_i}{M}}{\sum_{i=1}^{n} W_i \sin\alpha_i} \qquad [5\text{-}24a]$$

$$M = \cos\alpha_i \left(1 + \frac{\tan\alpha_i \cdot \tan\phi}{FOS} \right) \qquad [5\text{-}24b]$$

where:
FOS = the factor of safety,
n = total number of slices, usually 5 to 10,
i = subscript denoting slice number,
W_i = saturated weight of slice i, per unit length of the dam,
α_i = angle (measured above the horizontal) at base of slice i,
b_i = width (measured horizontally) of slice i,
u_i = pore pressure at the centre of the base of slice i,
ϕ = internal angle of friction.

The numerator in [5-24] represents the mobilized shear strength. The denominator in represents the applied shear stress. The average pressure $\bar{u}$ is not identical to the the single value of pore pressure u_i taken at the centre of the base of slice i unless the pressure distribution at the base of the slice i is perfectly hydrostatic, but use of u_i is usually a sufficiently accurate approximation.

In this study, in addition to performing an analysis of the potential for slope failure by erosion, the possibility of rotational failure was examined. In these studies the effect of external restraint was considered. Table 5-7 presents a summary of the rotational failure analyses performed. (Figures 3-9 and 3-10 show the system used in the large flume). For both methods of deep-seated failure analyses (rotational and wedge), the angle of internal friction, ϕ, was set equal to 50° for the tests done in the large flume, and 44° for tests in the glass-walled flume and the fictitious prototype. These were chosen based on observations in the laboratory of the angle of repose of the crushed limestone used in the flume tests. Although the angle of internal friction of 50° used for the large flume tests is larger than commonly reported values, it may in fact have been somewhat larger. As was mentioned in the literature review on slope stability (see Table 2-4 in section 2.1.5), high normal stress generally results in a low apparent angle of internal friction, and this is particularly true of large particles. The value of 50° was selected as a compromise value; a somewhat higher value may in fact apply but would not yield results which would be very meaningful to the design engineer, since such high values of ϕ are rarely seen in practice.

Table 5-7

Comparison of Actual and Theoretical Moments

1 Test	2 "N" in $i = \alpha V^N$	3 Moment using Bishop's Method (N-m)	4 Applied Moment (N-m)	5 Ratio	6 Ratio
GF29d	1.88	796.9	118.7	6.7	4.2
GF31c	1.88	262.7	8.34	31.5	25.8
FF17d	2.00	2872.9	87.6	32.8	31.1
FF18a	1.00	2763.2	162.4	17.0	16.2
	1.88	3449.4	136.4	25.3	19.6
	2.00	3517.9	136.5	25.8	20.2
FF19b	1.00	1028.6	133.1	7.7	6.9
	1.88	1917.5	139.6	13.7	12.4
	2.00	1611.9	139.2	11.6	10.4

2 recall from section 2.1.1.1 and equation [2-3a] that larger N implies that the level of turbulence is higher.

3 for the appropriate flume width and FOS = 1.

4 computed as the *experimentally* measured force multiplied by the moment-arm arising from the slip circle center found using Bishop's Simplified Method.

5 (column 3)/(column 4).

6 [(Moment associated with Bishop's Method) divided by (Radius from Bishop's Method)] ÷ applied force. See Appendix 3-4 regarding the net effect of applied force.

Five model tests were considered in detail with respect to rotational failure, these were tests GF29d and GF31c in the small (glass-walled) flume, and tests FF17d, FF18a, and FF19b in the large flume. For each of these test cases the factor of safety for rotational failure analysis was computed using the pore pressures determined by the pore pressure modelling method described in section 4.3.2.1 (ie. the finite difference method for non-Darcy flow). The non-Darcy pore pressure finite difference equation (equation [2-38]) permitted the examination of the effect of varying the level of turbulence simply by changing the value of N, which is the exponent in the equation $i = a\ V^N$. Each finite difference representation of the pore pressure field of each dam required re-relaxing the finite difference grid for that value of the exponent N.

Pore pressures associated with different values on N were used in the rotational analysis because the determination of non-Darcy pore pressures is much more computationally intensive. It was therefore of interest to determine how these pore pressures altered the results of rotational failure analyses. If pore pressures found using non-Darcy rather than Darcy finite difference modelling made little difference to the apparent potential for rotational failure, it could be argued that it is not justified for the designer to expend the effort to determine the pore pressures using a complex non-Darcy model.

The computed externally-applied moments shown in column 3 of Table

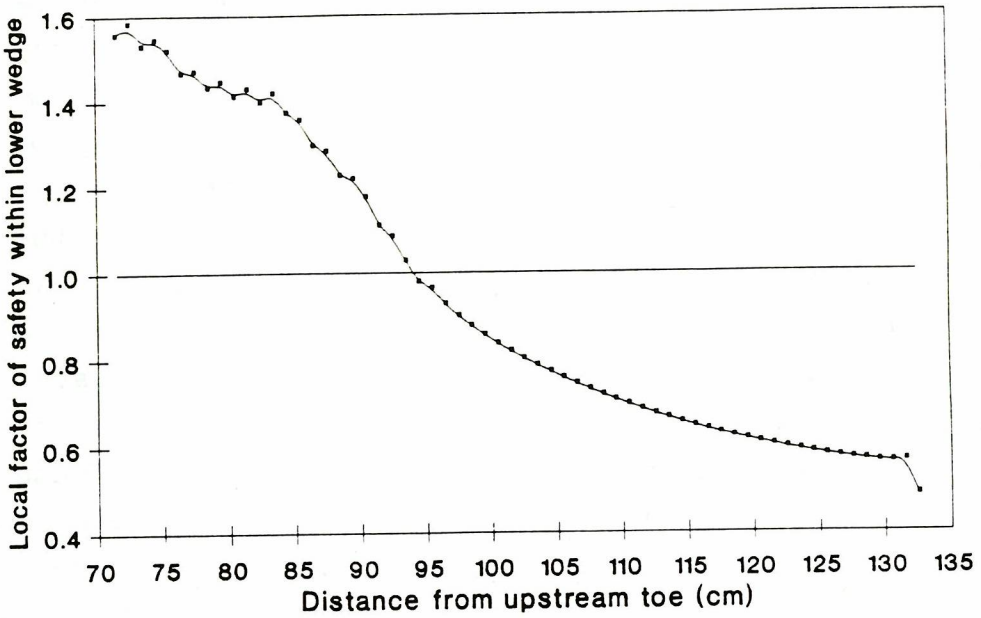
5-7 were the minimum moments which resulted in a factor of safety of unity. In each case the computed externally-applied moment was compared with actual physical measurements of the minimum moment required to prevent movement of the toe of the dam in the laboratory. This incipient failure condition, observed in the laboratory, implied that the factor of safety was also approximately unity for the stated applied moment. With regard to the results presented in Tables 5-7 it is noted that all models did indeed fail when no external restraint was introduced. However, it is difficult to state whether the *mode* of failure was due to a rotational slip. Such rotational slips were found to be difficult to observe for these model flowthrough rockfill structures because failure occurred quite suddenly. Qualitatively, however, it can be stated that the material in motion for failure of the model dams in the glass flume did not appear to be nearly as large in extent as that expected from a rotational failure analysis.

The theoretical slip surfaces for four model and one prototype embankment are shown in Figures 5-15(b) through 5-19(b). The approximate zone of application of the externally-applied restraint used in the laboratory cases is also shown. In connection with the results given in Table 5-7, it can be stated that:

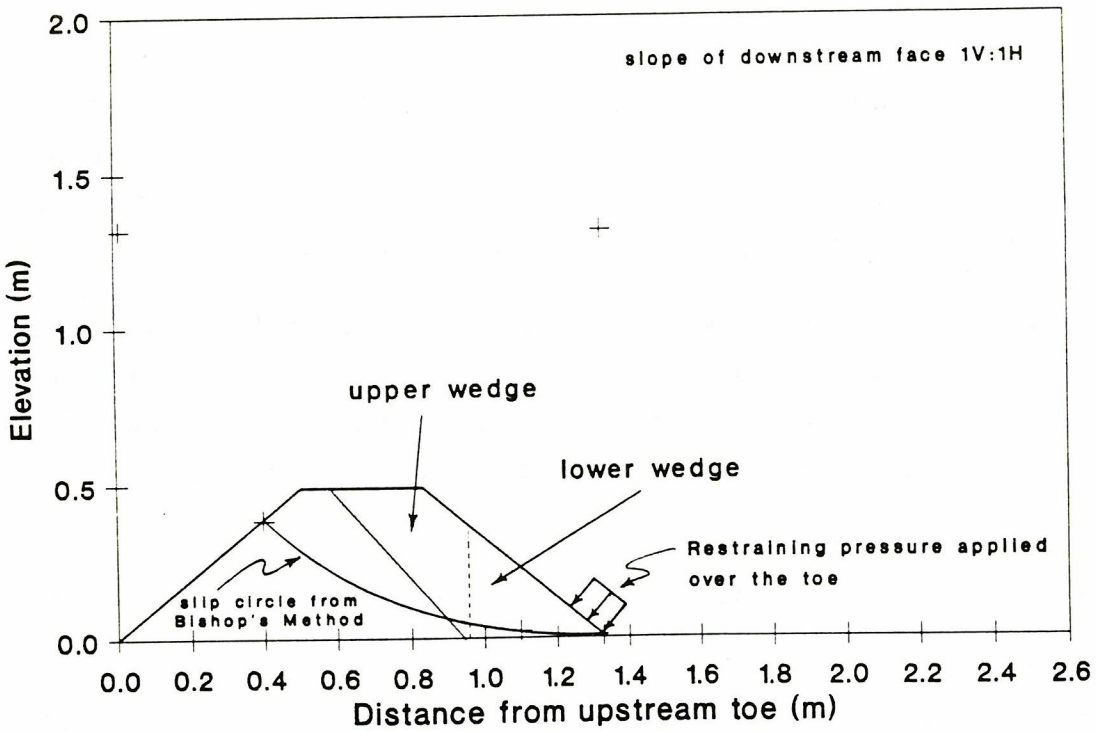
1. In each case failure was predicted using rotational failure analysis (Bishop's Simplified Method of Slices). This concurs with laboratory observations that the downstream slopes of these models were not stable under the hydraulic conditions in effect.

2. Use of pore pressures found from non-Darcy pore pressure modelling ($N > 1$) did not significantly change the factor of safety from the value obtained using $N = 1$ (Darcy flow).

3. The moment estimated from rotational failure analyses (Bishop's Method) was found to be conservative. The required moment predicted as being necessary to prevent rotational failure was 4 to 31 times larger than the observed moment when the appropriate non-Darcy pore pressures were used in the analysis.

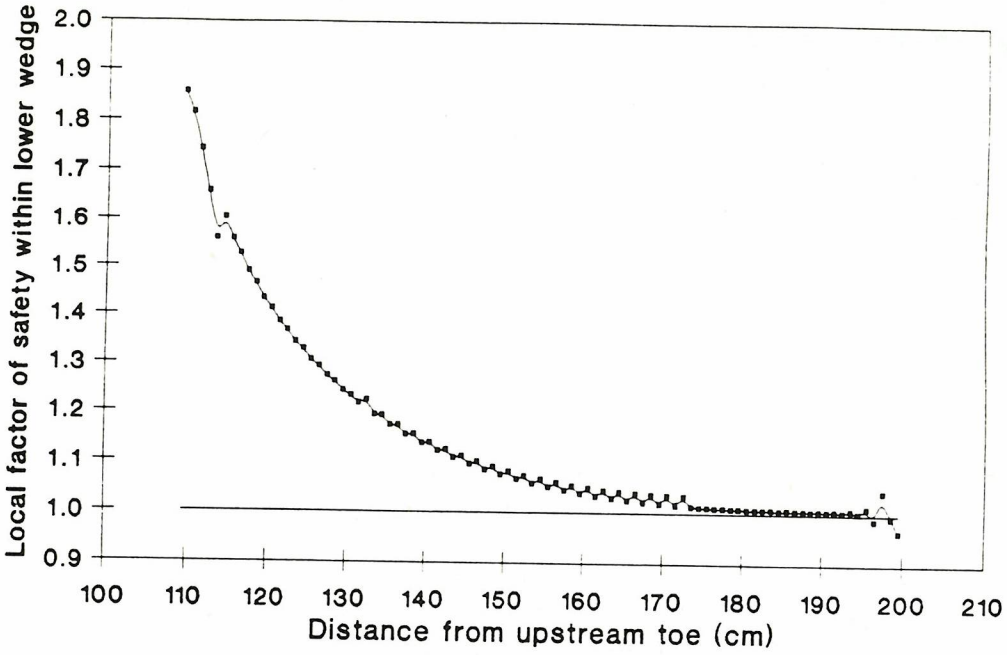


a) local FOS for lower wedge, in wedge method.

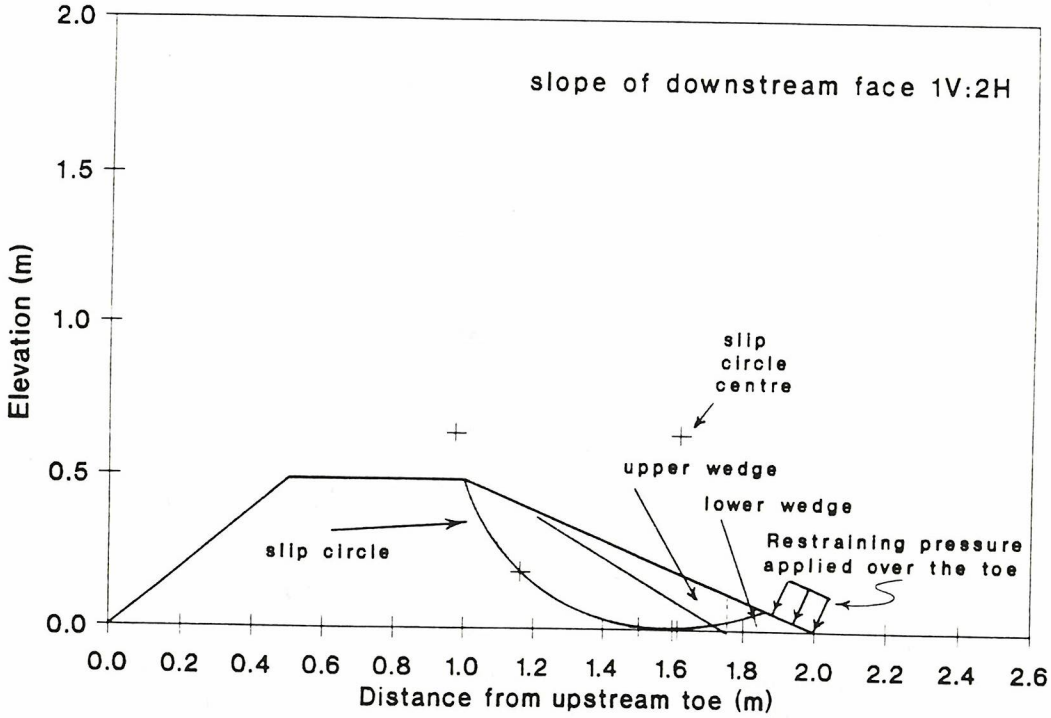


b) rotational and wedge failure surfaces.

Figure 5-15. Slope stability for test GF29d.

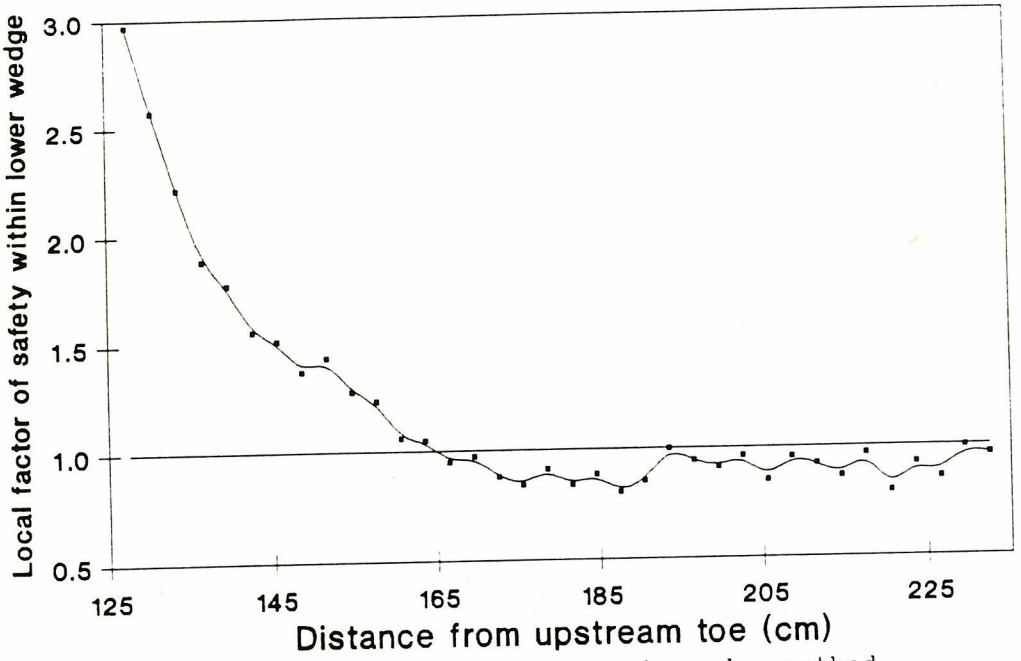


a) local FOS for lower wedge, in wedge method.

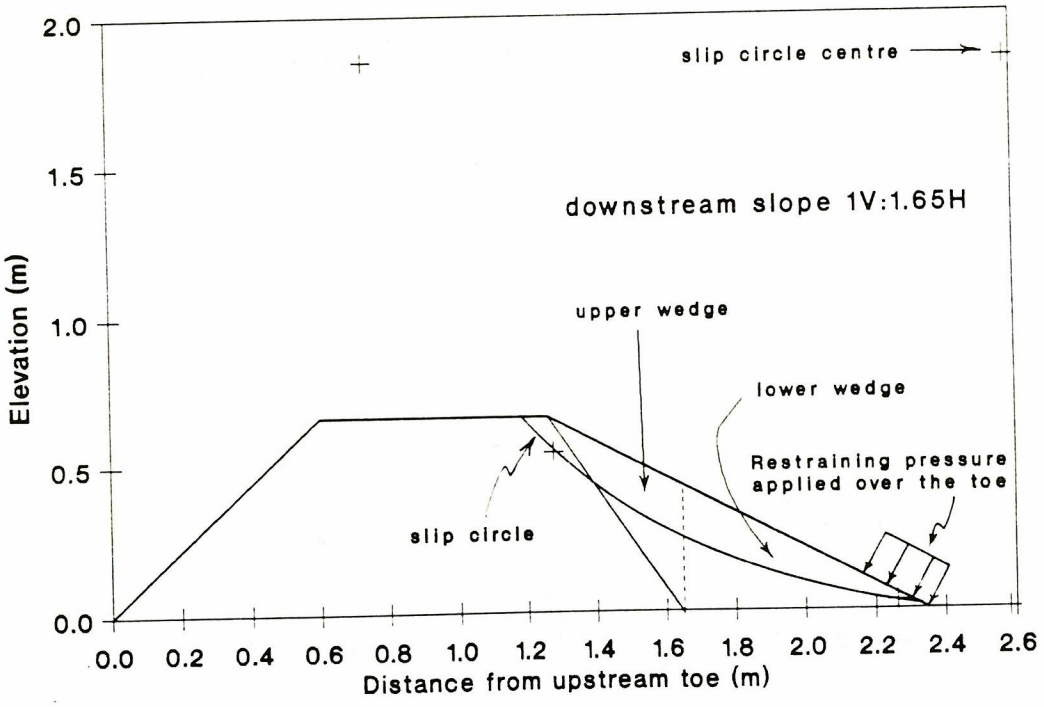


b) rotational and wedge failure surfaces.

Figure 5-16. Slope stability for test GF31c.

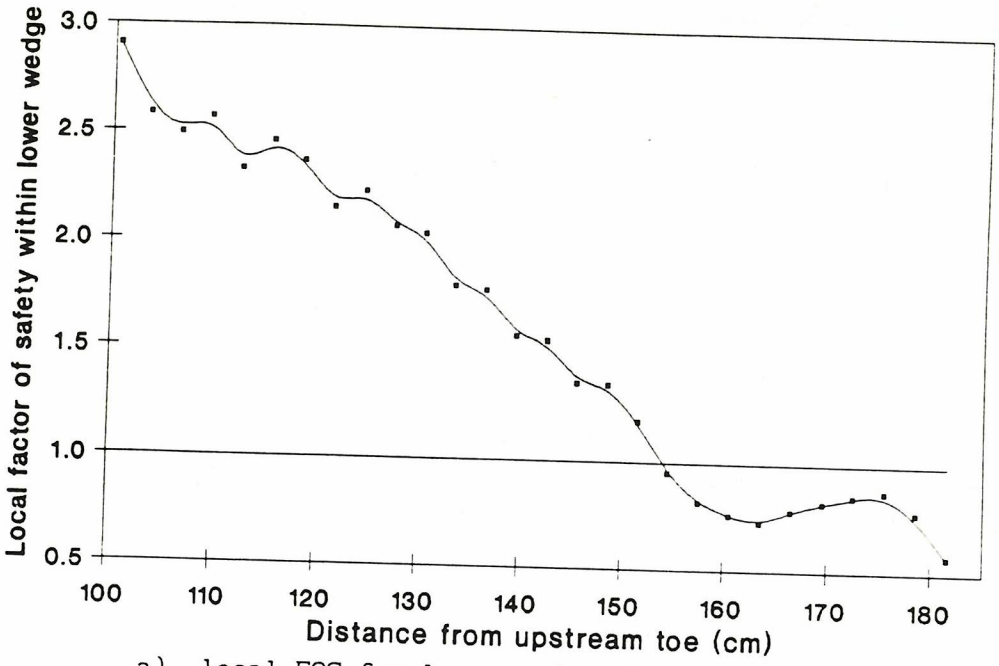


a) local FOS for lower wedge, in wedge method.

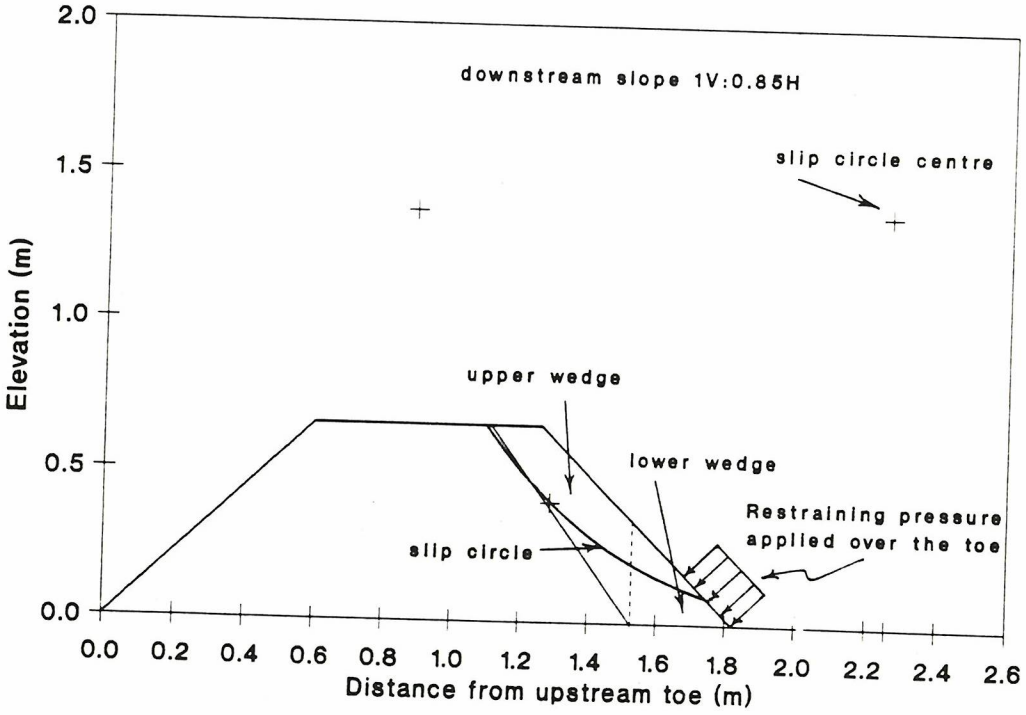


b) rotational and wedge failure surfaces.

Figure 5-17. Slope stability for test FF18a.

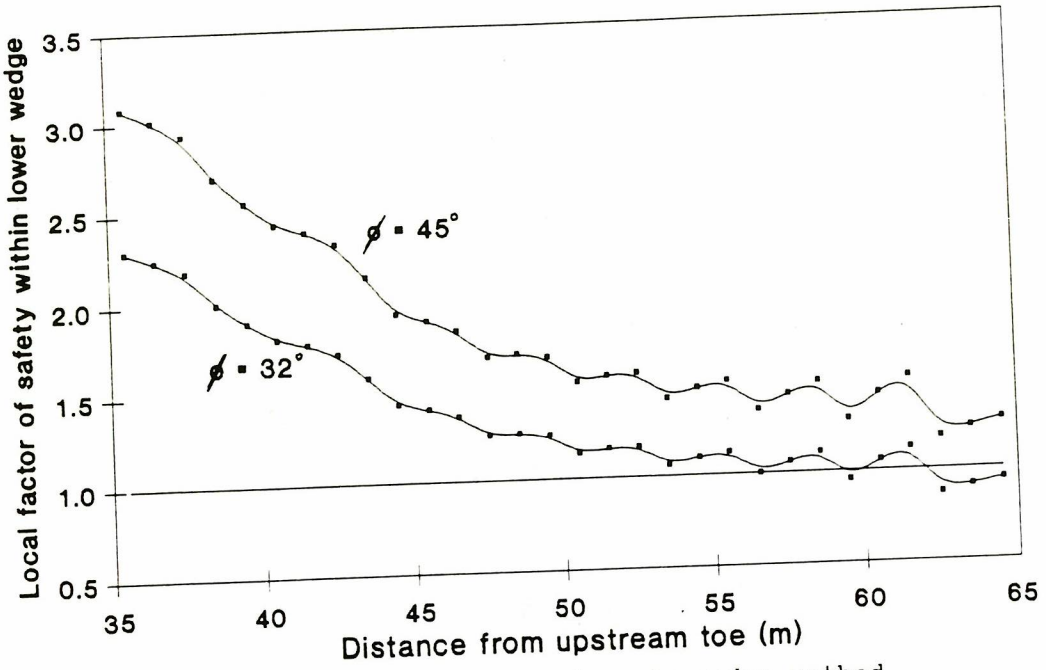


a) local FOS for lower wedge, in wedge method.

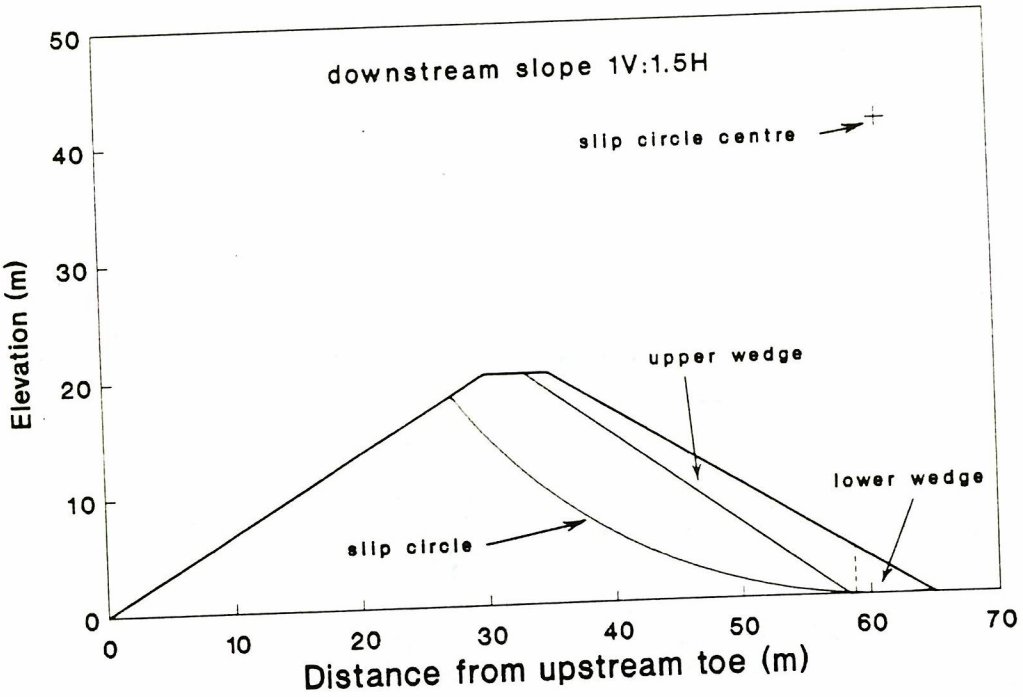


b) rotational and wedge failure surfaces.

Figure 5-18. Slope stability for test FF19b.



a) local FOS for lower wedge, in wedge method.



b) rotational and wedge failure surfaces.

Figure 5-19. Slope stability for prototype with N = 2.

It is noted that the position of the "FOS = 1" slip circle with no buttress at the toe of the dam will not be exactly the same as the position of the "FOS = 1" slip circle with the minimum amount of buttress (toe fill) applied over the toe, needed to prevent failure. The "no-toe-fill, FOS=1 slip circles" were used to estimate moments, however, because the computer program employed in the rotational failure analysis did not have a toe-fill option. Other programs having such an option did not have the ability to accept a specified (non-Darcy) pore pressure mesh, which was considered to be an important feature. It is assumed that the computed moment, associated with the FOS=1 slip circle with no toe-fill, is still *of interest* with respect to *minimum* restraint requirements. It may also be noted, for the purposes of the comparisons made,that the actual applied restraint was often of the order of 25 times less than that found from classical rotational failure analysis. It is therefore felt that the approximation described above would not have greatly altered this somewhat surprising finding.

It is surmised that part of the reason the predicted minimum restraint was so large (using Bishop's Method) is that, once the factor of safety becomes less than unity, the entire mass above the slip circle is considered to be free to rotate. As seen in Figures 5-15(b) to 5-19(b) this usually represented a significant fraction of the total embankment.

It is noted that test GF31c had the smallest computed moment using Bishop's Method. It also had the smallest experimentally applied force of any experiment. Yet, it can be seen from an examination of Figures 5-15(b) to 5-19(b) that the amount of material above the slip circle, as a fraction of all the material in the dam, is quite substantial. Using simplistic first approximations about the mobilized side-wall frictional resistance (computed using $K_o \gamma' h$ over the mobilized side-wall area), it was found that the moment associated with side-wall friction was about 8% of the moment appearing in column 3 of Table 5-7 for test GF31c. Even if this were tripled it would not explain the large discrepancy between the

minimum applied moment and the moment predicted using Bishop's method. For the other tests in Table 5-7 the theoretical moments were much larger than for GF31c. This would indicate that side-wall friction probably played too minor a role in this series of experiments, to explain overestimations of 6.7 to 32.8 times the observed moments. The predicted amount of material mobilized using Bishop's Method was larger than the observed amount of mobilized material, reducing the significance of such estimates of side-wall friction.

Due to the large restraint requirements found using Bishop's Method, an alternate method was considered. This wedge method will be described in the next section.

5.2.3 Description of Wedge Method and Comparison of Results

The wedge method developed in this study makes use of one the legitimate combinations described by Cedergren (1977, p.120) for determining the net pressure on a given plane in a porous media, with seepage in a given arbitrary direction. The combination used here considered the buoyant weight, γ', of the media, and the seepage force per unit volume acting on that media, $F/V = \gamma_w i$ (eqn [2-47]). In general, if these seepage forces are computed using the appropriate boundary conditions of piezometric head (by finite differences for example), there is no need to separately consider the external force due to "hydrostatic" pressure. The so-called resultant boundary neutral force (Cedergren 1977) (the sum of all external hydrostatic pressures) can be combined with the saturated weight of the soil, γ_{sat}, as another valid combination to determine the effective stress.

Under the influence of a hydraulic gradient this effective stress may actually be more or less than the effective stress computed simply as the depth of the saturated media multiplied by the buoyant unit weight of that media. It will be greater than this nominal value if

the seepage is downward (Yan and Byrne 1990), and less if the seepage is upward. If the seepage is sidelong but with a downward component (as it is in embankments), there will be two vectors affecting the "no-flow" effective stress ($\gamma'h$), the downward component increasing it, and the purely horizontal component. The downward component of seepage increases the effective stress at the base of a given slice, and this causes an increase in the mobilized friction at the base of the slice. This friction acts along the assumed slip surface and in a direction opposite to the horizontal seepage force.

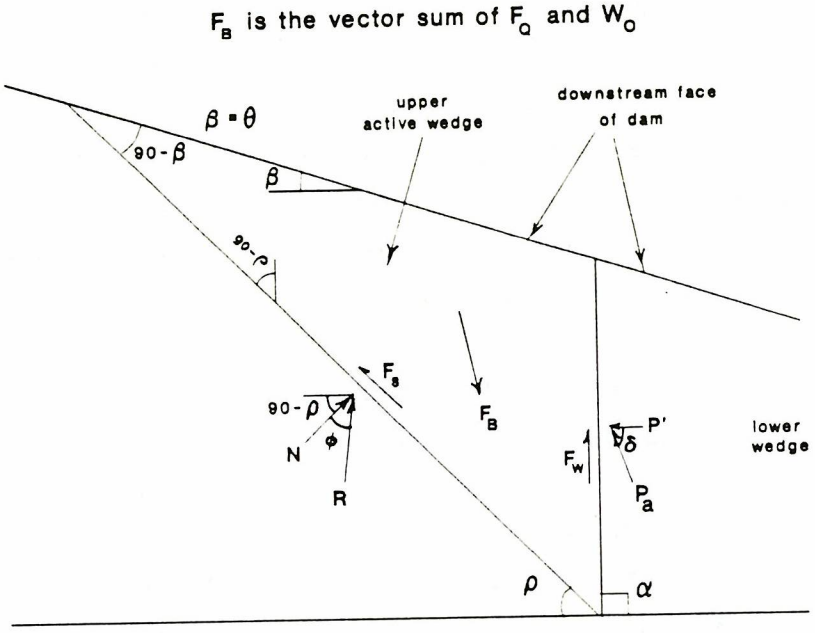
Bishop's Method and most other methods of slope stability analysis do not explicitly consider the horizontal component of seepage. At the toe of a flowthrough rockfill dam it was found that the horizontal component of the hydraulic gradient can be close to unity. This represents a localized destabilizing force on the toe not considered separately by Bishop's Method, or by other commonly used methods of slices. The description of the wedge method will be considered in three steps, each moving successively more upstream: the horizontal seepage force within the lower wedge, the selection of the boundary between the upper and lower wedges, and the active pressure exerted by the upper wedge. Figure 5-20 illustrates the upper and lower wedges of this method schematically.

1. *The horizontal seepage force within the lower wedge.*
This was the simplest step in the method, once the position of the fictitious wall had been decided upon. The finite difference pore pressure modelling provided a value of the piezometric head (also known as the total head) for any nodal point within the dam. The hydraulic gradient vector could therefore readily be computed at any FD node of interest. At a given node the horizontal component of this vector is:

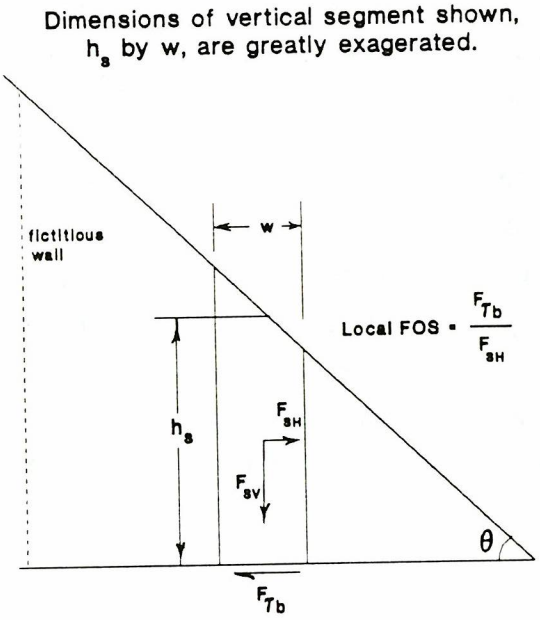
$$i_h = (h_5 - h_1)/2\Delta x, \qquad [5\text{-}16]$$

Since, in general, $F/V = \gamma_w i$, it is also true that:

$$F_{SHN} = \gamma_w \cdot (i_h) \cdot V \qquad [5\text{-}25a]$$



a) forces in the upper wedge.



b) determination of local FOS for a single vertical segment within the lower wedge.

Figure 5-20. Schematic diagrams pertaining to the wedge method.

For a unit L and a nodal area $\Delta x \cdot \Delta y$, [5-25a] may be then written:

$$F_{SHN} = \gamma_w \cdot (i_h) \cdot A_{node} \qquad [5\text{-}25b]$$

where:

F_{SHN}= horizontal seepage force for a given FD node,
i_h = horizontal component of the hydraulic gradient at that node,
A_{node}= area of the node, = $\Delta x \cdot \Delta y$, = Δx^2 (since $\Delta x \cdot \Delta y$).

The total horizontal seepage force within the lower wedge could the be computed as the sum of the all nodal horizontal seepage forces, using only those nodes in the lower wedge:

$$\text{Horizontal seepage force for lower wedge} = \sum_{\substack{all \\ nodes}} F_{SHN} \qquad [5\text{-}26]$$

2. *A rationale for selecting the vertical boundary between the upper and lower wedges.*

It should be emphasized that the following discussion is indeed the presentation of a *rationale* for selecting the location of said boundary. If the wedge method were to be formally coded in a given computer language, such coding should permit the user to *arbitrarily* select a range of locations for this vertical division. A computer search would then indicate the location of this vertical boundary which gives the highest total bursting pressure (upper and lower wedges combined).

However, in the absence of such a computer program, the position of the vertical (or fictitious wall) which divided the upper and lower wedges was selected such that following two opposing tendencies were balanced. The first tendency was to locate the dividing vertical at a more *downstream* position. By moving the dividing vertical *downstream*, a greater portion of material is included which has higher horizontal gradients. The inclusion of higher gradients in

the upper wedge will tend to increase the seepage force acting on the material in the upper wedge. The second tendency was to locate the dividing vertical at a more *upstream* location. The lower wedge included the most material (ie. that part of the toe of the dam) which had no ability to resist (along its base) the pressure exerted by the upper wedge.

Figure 5-20(b) and Appendix 3-1 show the lower wedge for the wedge method developed in this study. The upstream limit of the lower wedge was determined in each case by performing a force balance on successive vertical segments within the toe of the dam (that is, the lower wedge). Within each vertical segment, three forces were quantified (See also Appendix 3-2):

i) The horizontal seepage force for the segment, computed as the sum of the seepage forces acting on all the finite difference nodes within the vertical segment. These were calculated using equation [5-16] to find the horizontal gradient i_h at each finite difference node. The total horizontal seepage force for each vertical segment was then found as:

$$F_{SH} = \gamma_w h_s \cdot w \cdot \sum_{h=1}^{h_s} i_{h_h} \qquad [5\text{-}27]$$

where:

F_{SH} = total horizontal seepage force for the vertical segment of dimensions $w \cdot h_s \cdot$ unit L,

h_s = height of vertical segment,

w = width of vertical segment,

i_{h_h} = horizontal hydraulic gradient for node at height h within h_s.

ii) The vertical seepage force, similarly calculated as the sum of the seepage forces acting on all the individual finite difference nodes in the vertical segment. The vertical hydraulic gradient at each node was calculated using the equation:

$$i_v = (h_3 - h_7)/2\Delta y, \qquad [5\text{-}28]$$

(see Figure 2-4 for meaning of subscripts). In a manner analogous to equation 5-27 above, the total vertical seepage force within a given vertical was then found as:

$$F_{SV} = \gamma_w h_s \cdot w \cdot \sum_{h=1}^{s} i_{v_h} \qquad [5\text{-}29]$$

iii) The mobilized frictional resistance (as a shear) at the base of each vertical segment. This was calculated (per unit length of dam) as:

$$F_{\tau b} = [(\gamma_{sat} - \gamma_w) h_s \; w + F_{sv}] \tan\phi_b \qquad [5\text{-}30]$$

where:

$F_{\tau b}$ = mobilized shear at the base of a given vertical segment,

γ_{sat} = saturated unit weight of porous media,

γ_w = unit weight of water,

h_s = height of a given vertical segment,

w = width of vertical segment at its base,

F_{sv} = net vertical seepage force for the vertical segment, which is a summation of the seepage forces for all nodes in the segment.

ϕ_b = angle of friction between the rockfill and the foundation (the floor of the flume for the model dam cases).

A local FOS could then be defined along the base of the toe of the dam. This was:

$$FOS = \frac{F_{\tau b}}{F_{SH}} \qquad [5\text{-}31]$$

The upstream limit of the lower wedge was defined as the location where the horizontal seepage forces just equaled the mobilized shear. Downstream of this limit, the horizontal seepage forces exceeded the mobilized shear and the local factor of safety at the base of each vertical segment was less than unity. The lower wedge therefore represented the maximum zone which did not resist, via friction

mobilized at the base, the effect of the bursting-out force of the horizontal seepage in this wedge.

Figures 5-15(a) through 5-19(a) show how the local factor of safety at the base of each segment with in the lower wedge varied with the distance upstream of the toe. In most cases the vertical division between the upper and lower wedges was easily determined. However, for GF31c the local FOS was close to unity over much of the toe. A somewhat arbitrary location was therefore selected for the location of the dividing vertical (at 175 cm from the upstream toe). The position of the dividing vertical is shown as a vertical dashed line in Figures 5-15(b) through 5-19(b), respectively.

3. *Computing the active pressure exerted by the upper wedge.* Within the upper wedge the approach taken was to consider the unit as a whole, with the important unknown being the critical rupture plane angle, commonly denoted ρ (Bowles 1968). The method of analyzing the upper wedge was a modified version of Coulomb's formula for the active pressure of a fill against a retaining wall. The modification needed was the inclusion of the seepage force acting within the upper wedge. In the development of Coulomb's expression for the active earth pressure the fact that the seepage force may have some horizontal component is not considered. The only non-frictional force considered in the vector analysis is the buoyant weight plus the weight of the unsaturated portion, if any. Huntington (1957) has shown that the true angle of the rupture plane (under Coulomb's analysis) may be determined by successive trials, and that the answer is generally quite close to the standard Coulomb formula for the active pressure against a retaining wall. In this study, using successive trials to determine ρ was even more essential, since each angle of the rupture plane implied a different seepage vector acting on different upper wedge. Appendix 3-1 describes the development of the following formula in detail:

$$P_a = \frac{\sin(\rho - \phi + \xi)}{\sin(180 - \alpha - \rho + \phi + \delta)} F_B \qquad [5\text{-}32]$$

where:

P_a = force against the fictitious wall, acting at angle δ below the horizontal,

ρ = angle of the rupture plane, see Figures A-3(i) and (ii),

ξ = angle of the net force F_B, measured above the vertical,

ϕ = angle of internal friction of the media,

δ = angle of friction for the interaction between the media and the fictitious wall,

α = angle of the wall above the horizontal,

F_B = the force per unit length of dam acting on the material between the rupture plane and the wall; this is a vector combination of the buoyant weight and the seepage force (see Figure 5-20a and Appendix 3-1).

P_a is commonly referred to as the active earth pressure. However, the present conceptual framework includes consideration of the horizontal component of seepage, a factor not normally included. It is worth noting that in the absence of a seepage force, F_B is equal to the buoyant weight W_o, and ξ is therefore zero. Equation [5-32] then becomes the following standard expression for determining the active pressure against a retaining wall, stated by Bowles (1968) as:

$$P_a = \frac{\sin(\rho - \phi)}{\sin(180 - \alpha - \rho + \phi + \delta)} W_o \qquad [5\text{-}33]$$

Since for the present analysis α is always equal to 90° (the line separating the upper and lower wedges is always vertical) and δ always equals ϕ (the angle of friction between the media and the fictitious wall is in fact simply that of the media itself), equation [5-32] becomes:

$$P_a = \frac{\sin(\rho + \xi - \phi)}{\cos(2\phi - \rho)} F_B \qquad [5\text{-}34]$$

To summarize, the wedge method emphasizes seepage forces, which in the case of an embankment are primarily horizontal. The upstream extent of the *lower* wedge is found from the determination of the

point at which frictional shear resistance ceases to exist at the base of the dam. The upstream extent of the *upper* wedge, which thrusts against the lower wedge, is determined by successive trials to find the critical angle of the rupture plane ρ which causes P_a to be a maximum. At the critical ρ, the force against the fictitious wall is a maximum. The value of the critical angle ρ is affected by the angle of internal friction of the media and the 2-D configuration of the dam, as well as the pattern of pore pressures within the upper wedge. For any given ρ the spatial variation of the pore pressure pattern within the upper wedge implies a certain overall seepage force within this wedge, and the variation of this overall seepage force with ρ cannot be described in simple analytical terms. In general it will depend on the configuration (2-D shape) of the dam, the location of the phreatic line, and the magnitude and proximity of all the boundary conditions. Appendix 3-3 provides a series of equations to make computation of the area within the upper wedge more convenient.

The wedge method is different from classical rotational failure analyses, such as Bishop's Simplified Method, in the following manner. Classical slope stability methods indicate failure or non-failure, as determined by a computed factor of safety. Theoretically, if the FOS is greater than unity the slope requires no restraint to prevent movement. For any value of the FOS less than unity all the material above the assumed slip circle is considered unstable and will rotate in the absence of restraint. In contrast to this the wedge method, for a given angle ρ, provides a bursting pressure associated with the active pressure of the upper wedge against the lower wedge. The critical angle ρ of interest is that angle which gives the largest active pressure of the upper wedge. Figure 5-21 shows how this pressure P' varied with ρ for the four models examined using the wedge method. It is not surprising that very small values of ρ imply no active pressure at all.

The wedge method was tested by examining the *measured* minimum forces to prevent failure in four model dam tests conducted in this study.

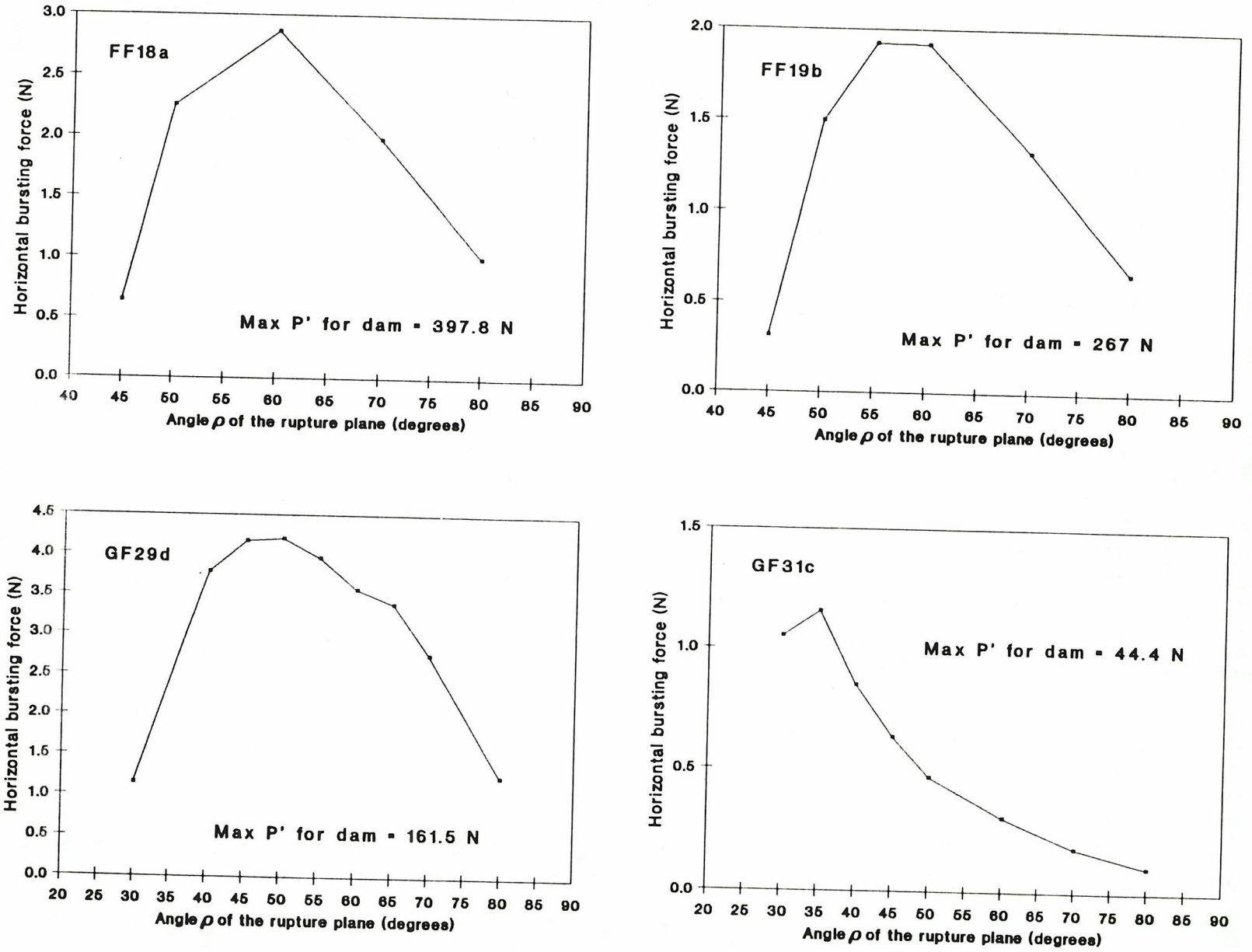


Figure 5-21. Variation in horizontal bursting force per unit L for four model tests.

Table 5-8 shows a comparison of the computed and measured forces.

Table 5-8

Comparison of Observed and Computed Bursting Forces at Incipient Failure

[1] Test	[2] Average External Normal Force(N)	[3] Net Effect of Applied External Force (N)	[4] Computed Force P′ (N)	[5] P′ plus Lower Wedge Seepage Force (N)	[6] Ratio
GF29d	133.1	144.4	161.5	326.6	2.26
GF31c	15.0	15.8	44.4	71.6	4.52
FF18a	89.2	94.1	397.8	632.3	6.72
FF19b	83.9	112.4	267.0	349.0	3.10

2. The applied force; based on at least 2 experimental repetitions.
3. These are larger than values in col.2 because of the additional frictional resistance induced (at the base of the flume) by the vertical component of the externally applied normal force. See Appendix 3-4 for details.
4. By wedge method. N = 1.88 for glass flume, 2.00 for large flume. See also Figure 5-21. $P' = P_a \cos\phi$, P_a from [5-32].
5. Lower wedge seepage force from equations [5-25] and [5-26].
6. Column 5 ÷ column 3.

The imposed external force contributed to stability in two ways. Firstly, the external force was applied (over a limited area over the toe) in a direction normal to the downstream face of each model dam. The *horizontal* component of this normal force directly opposed the force $P_a \cos\delta$, denoted as P′. Secondly, the *vertical* component increased the mobilized shear resistance at the base of the toe of the dam. (In the experimental context this 'base' is the interface between the model dam and the floor of the flume.) In addition, some friction was mobilized at the side-walls of the flume. The sum of these three effects acted against P′, as described in Appendix 3-4. Figures 5-15(b) to 5-19(b) show the wedge failure zones, as compared to the rotational failure zones. It is noted that in most cases the

rotational zone is much larger than the wedge failure zone.

A comparison of the results in Tables 5-7 and 5-8 shows that, on a case-by-case basis, the wedge method made predictions closer to the observed restraint requirements than did Bishop's Simplified Method of Slices (1956). It is postulated that for flowthrough rockfill structures, the horizontal thrust from seepage forces are mainly responsible for failure. Further, the failure surface does not appear to be represented by a circular arc. A circular failure arc is tangent to the floor of the flume (which is clearly immovable) at a single point whereas the wedge method can allow for sliding of part of the toe of the dam along this fixed plane. It is also noted that the force computed using the wedge method is still larger than the measured force. This is attributed to the following factors:

1) errors in force measurement relating to the calibration of the piston system. The minimum force needed to prevent failure was however repeatable to about ± 20%.

2) the rupture plane may not be a flat plane, as assumed here. There may be a number of compound failure planes, planes difficult to observe experimentally and difficult to handle computationally, under the proposed method.

3) errors in the specification of the angle of internal friction for the two materials used (2.5 cm rock for GF29 and GF31, and 13 cm rock for FF18 and FF19).

4) difficulties in assigning an exact value for the seepage force associated with each assumed value of the angle ρ. (The approximate method used to obtain the magnitude and direction of the hydraulic gradient for each assumed ρ is described in the context of the worked example given in Appendix 6. This difficulty could be overcome by formally coding a computer program to determine the seepage force at any ρ, and thereby also find the critical ρ.)

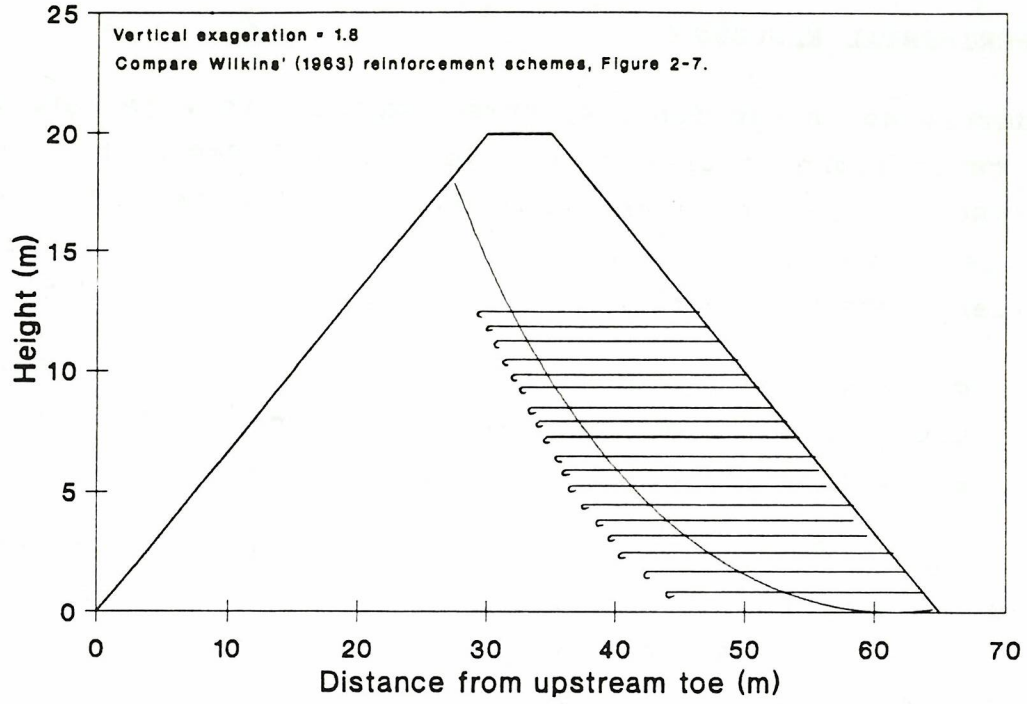
5) errors in the angle of friction between the base of the flume and

the rock, as determined from a relatively crude experiment in which a known mass was dragged along the surface of the flume in an open-ended container.

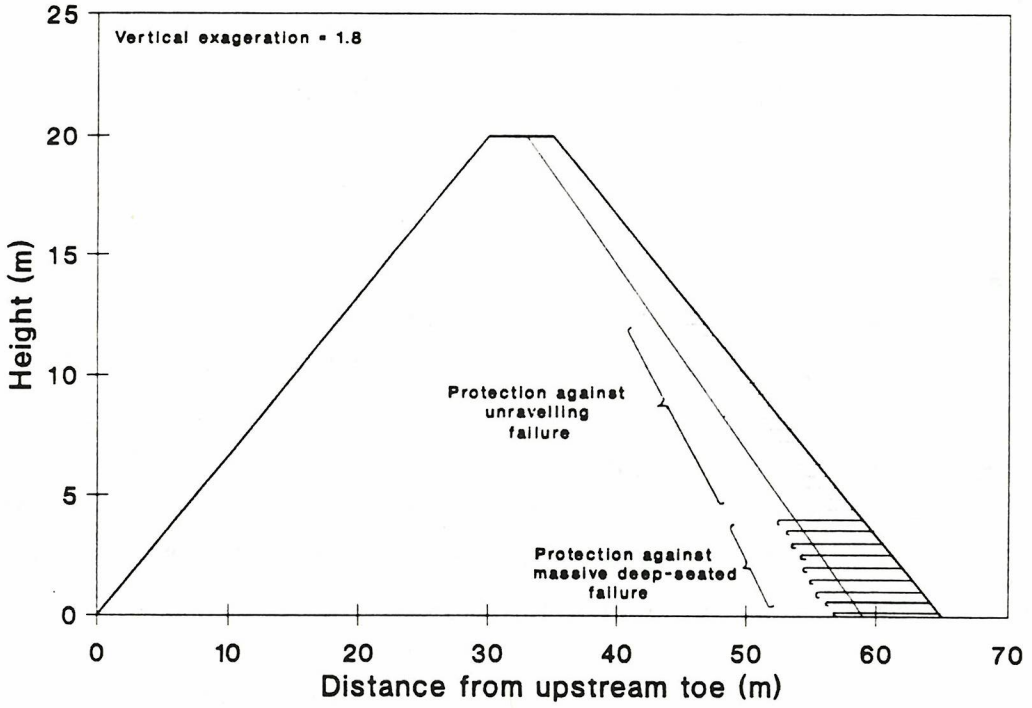
6) errors in determination of the porosity of the model dams.

7) omission of the fact that the upper wedge adds a downward shearing thrust at the fictitious wall interface between the upper and lower wedges. This vertical shearing thrust, $P_a \sin\delta$ ($= P_a \sin\phi$), would change the location of the fictitious wall, and represents an additional stabilizing factor, theoretically. The effect of $P_a \sin\delta$ omitted because of the additional level of computational difficulty it would introduce if included, and because it was thought that at the moment of failure when the material is in a state of incipient collapse, this contribution to stability would be small, especially at the toe. It will be conservative to omit the effect of $P_a \sin\delta$ on increased friction at the base of the lower wedge. This effect could also be handled more easily with formal coding of the wedge method.

Figure 5-22 shows the reinforcement implied by the two different methods considered, as applied to a fictitious prototype. The calculations for these two reinforcement schemes are given in the worked example in Appendix 6. For the determination of the diameter and spacing of the rebar in the worked example, it was assumed that: (i) the outer mesh transmits the bursting forces occurring between rebar anchors to these anchors perfectly; the mesh does not fail and the bursting forces on the mesh are transfered to the rebar such that the anchors bear the load, and (ii) the rebar fails in tension, not in pull-out. These were necessary assumptions since pull-out resistance and the interaction between the rockfill, the mesh and the rebar was beyond the scope of this study. It is evident from Figure 5-22 that rotational failure implies more reinforcement than does wedge failure. Experimental results indicate that the wedge method is more appropriate for reinforcement design than Bishop's Simplified Method. However, failure may well *be* rotational in nature if the dam is located on a weak foundation. The wedge method described herein does not consider the consequences of a weak underlying foundation.



a) from rotational failure analysis.



b) from wedge failure analysis.

Figure 5-22. Reinforcement schemes implied by rotational and wedge failure analyses.

6.0 BEHAVIOUR IN SUBZERO TEMPERATURES

6.1 EXPERIMENTAL RESULTS

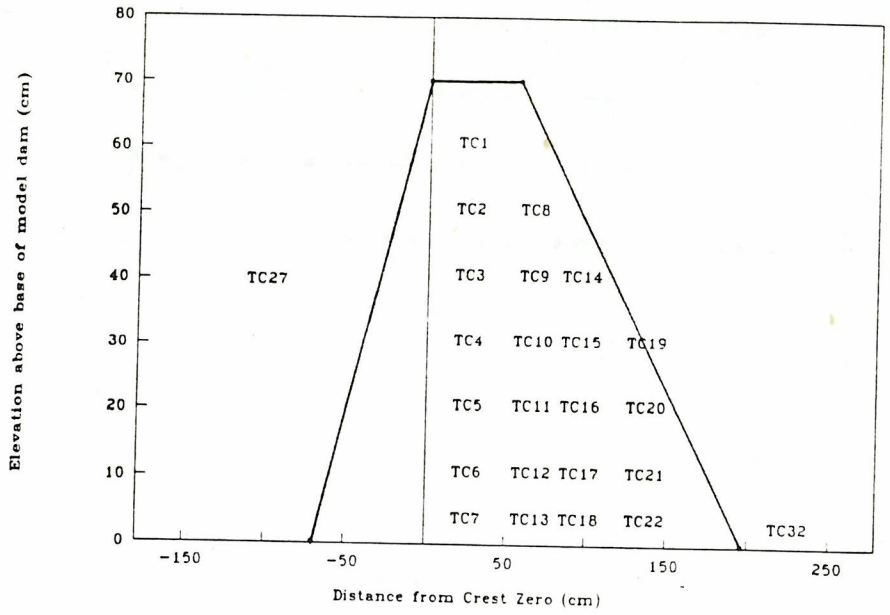
As was described in section 3.4, three experiments were performed in the low temperature laboratory of the National Research Council of Canada (NRCC). Each of these experiments lasted two to three days and was performed at an average room temperature of about -13°C. These experiments were performed under the following conditions:

Test 1: maximum flow (about 69 L/s) with no impermeable facing,
Test 2: same maximum flow, but with an impermeable facing,
Test 3: a low flow (about 20 L/s) with an impermeable facing.

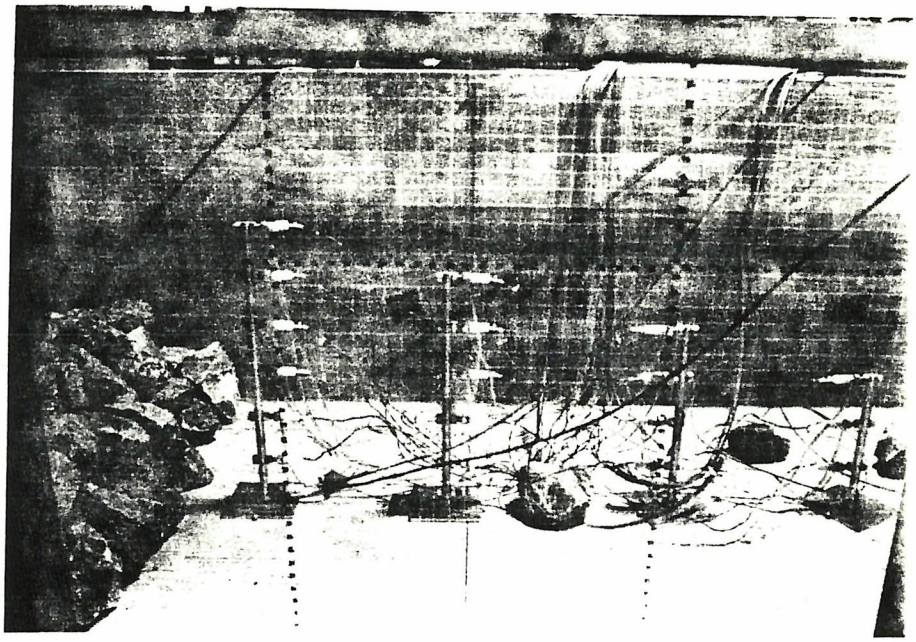
Figure 6-1(a) shows the two-dimensional configuration of the dam, which was the same for all three tests, and also shows the locations of the 32 thermocouples (denoted TC) within the dam. The flume was 1.2 m wide, 4.9 m long, and was insulated on the sides and bottom except where the viewing window was installed. The model dam was constructed of 130 mm rock at a porosity of approximately 41%. Figure 6-1(b) shows the piezometer and thermocouple arrays before these were covered with rock. The fluid in the piezometer lines was 50% water and 50% ethylene glycol.

Test 1.

Figure 6-2(a) shows the variation in temperature for selected thermocouples for Test 1. It is evident that although there was a short period of below zero temperatures near the end of the test, this was not sustained and ice therefore did not block the voids within the embankment. Figure 6-2(b) shows the variation in ambient temperature during the test as monitored by a hand held thermometer and by a thermocouple located on the viewing window at the side of the flume. The regular in room temperature was due to the cycling of the refrigeration compressors. This test lasted 2.04 days at an average temperature of -12.9 °C. Ice only formed at the free surface of the dam, and this had no significant effect on piezometric pressures within the model dam. Figure 6-4(a) shows the ice at the phreatic surface after 48 hours of testing.

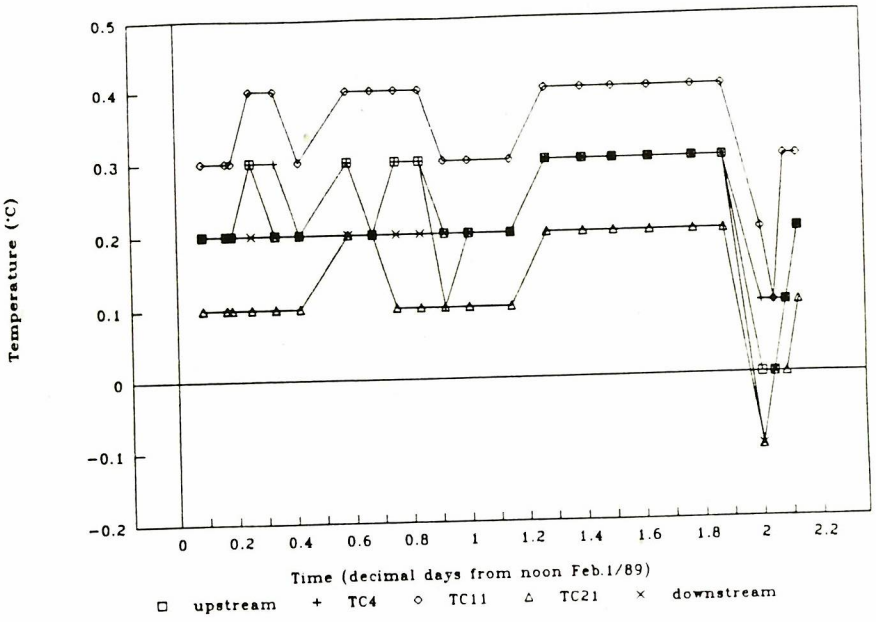


a) two-dimensional configuration of model dam, showing thermocouple locations.

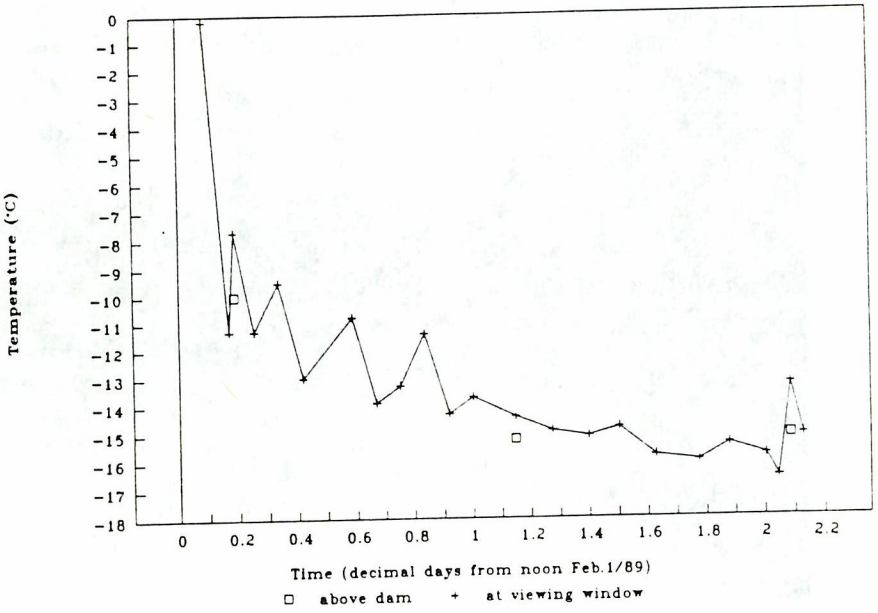


b) side view of flume showing thermocouples and piezotaps before coverage by 130 mm rock.

Figure 6-1. Temperature and piezometric data collection arrangements for model dam in the low temperature laboratory of the NRCC.



a) temperature variations for selected thermocouples.



b) ambient air temperatures.

Figure 6-2. Observed temperatures in and above model dam for Test 1 in low temperature laboratory.

Test 2.

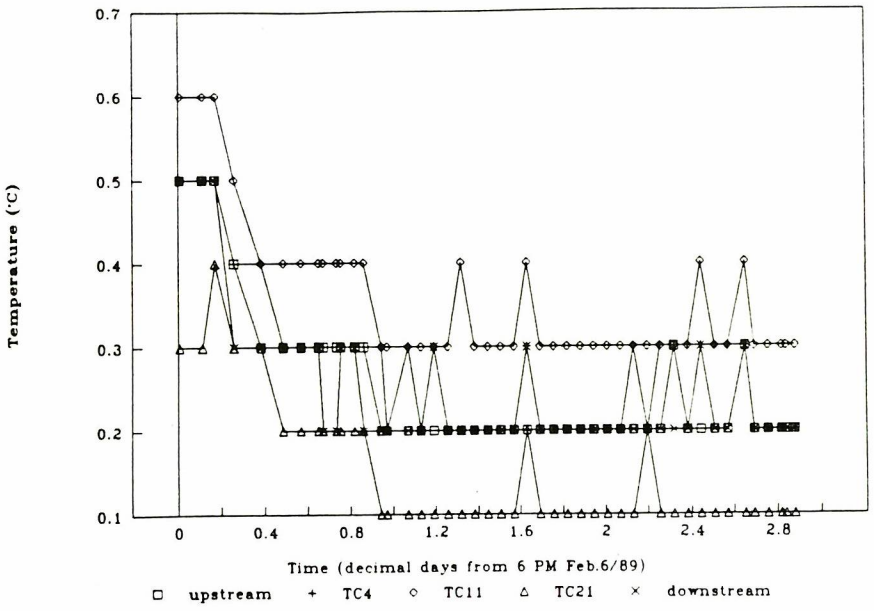
Figure 6-3(a) shows the variation in temperature for selected thermocouples for Test 2. In this test temperatures below zero did not occur within the dam. Figure 6-3(b) shows the variation in ambient temperature during the test as monitored by a hand-held thermometer and by the thermocouple located on the viewing window at the side of the flume. This test lasted 2.88 days at an average temperature of -11.0 °C. Ice only formed at the free surface of the dam, but again, this had no apparent effect on internal piezometric pressures. Figure 6-4(b) shows the ice which partially covered the seepage surface after about 22 hours of run time.

Test 3.

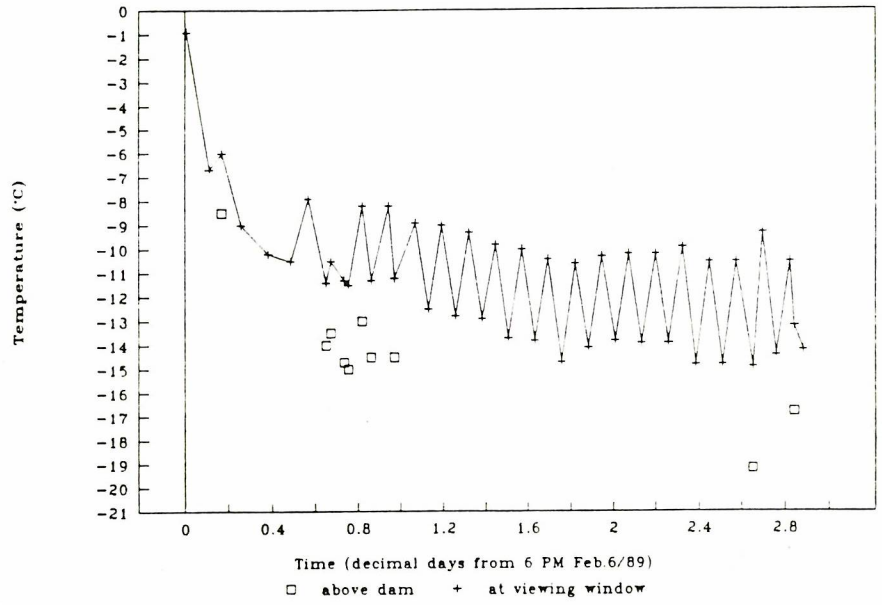
This test lasted 3.46 days at an average temperature of -14.3 °C. Figure 6-5(a) shows that ice formed within the voids in one zone of the dam for this test. Toward the end of the test thermocouple #2 remained below zero, an observation that is corroborated by the appearance of an ice lens in the free-fall zone just downstream of the UIF. As seen in Figure 6-5(b), other (representative) thermocouples did not maintain a subzero temperature. This ice formation, however, apparently had little effect on internal piezometric pressures. The ice lens probably formed due to mixing of the cold air within the free-fall zone just downstream of the impermeable upstream facing, and is marked with a circle in Figure 6-6(a). Figure 6-6(b) gives an overhead view of this test after 65 hours of run time.

6.2 ESTIMATING ICE GROWTH AT THE PHREATIC SURFACE

It is suggested that due to the viscous dissipation of hydraulic energy and to the fact that water temperature in the small upstream reservoir was slightly above zero, temperatures within the dam generally stayed above zero. The ice which formed at the phreatic surface also partially formed over the seepage surface, but this caused little or no change in the piezometric pressures or in the extent of the seepage surface. Figure 6-4(b) shows the seepage surface almost completely frozen over with the flow continuing to emerge at the toe. The mechanism for the formation of ice in a

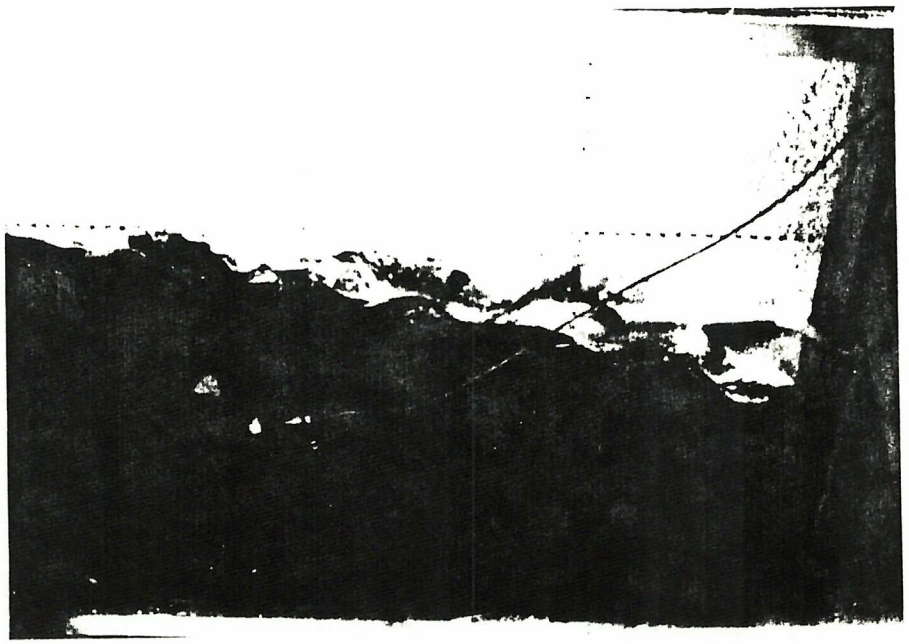


a) temperature variations for selected thermocouples.



b) ambient air temperatures.

Figure 6-3. Observed temperatures in and above model dam for Test 2 in low temperature laboratory.

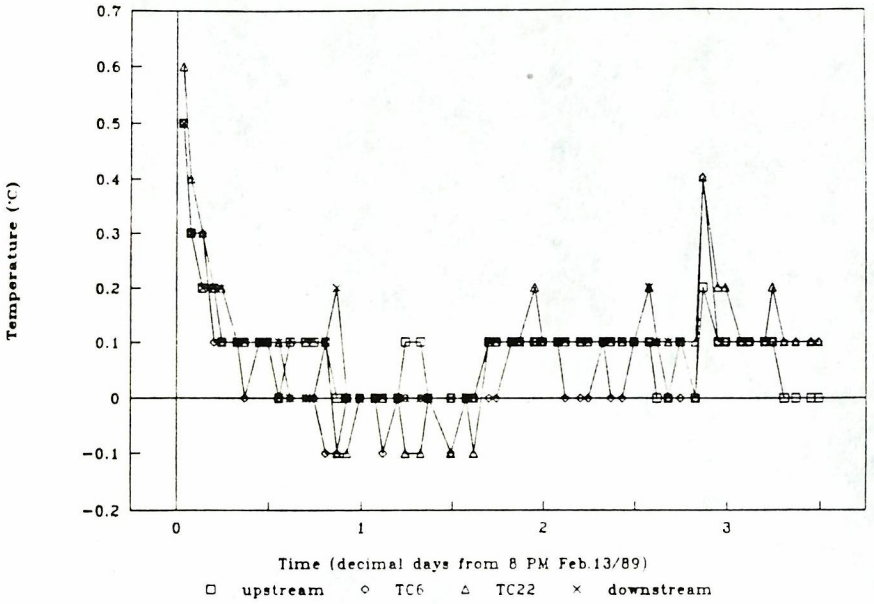


a) ice at phreatic surface after 48 hours, Test 1.

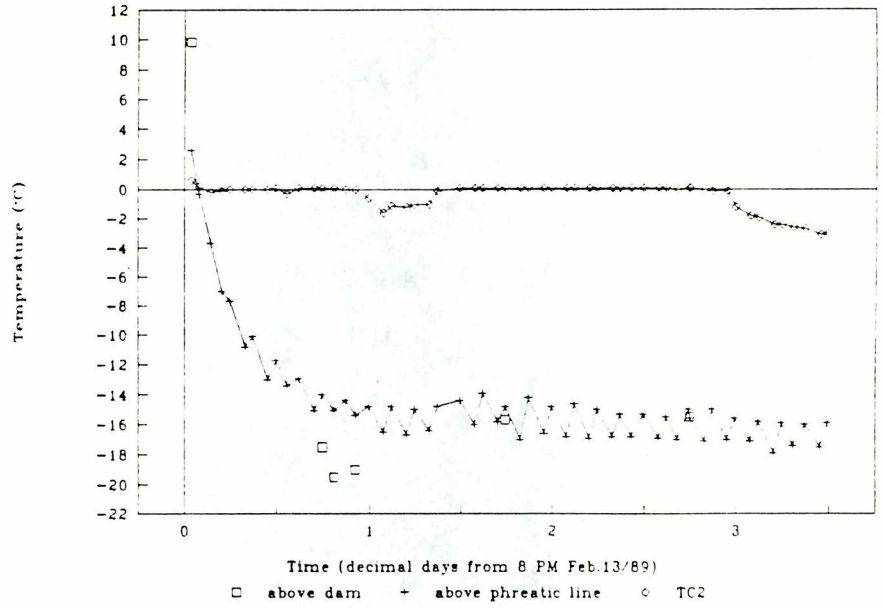


b) ice covering most of seepage surface after 22 hours, Test 2.

Figure 6-4. Ice growth for Tests 1 and 2 in low temperature laboratory.

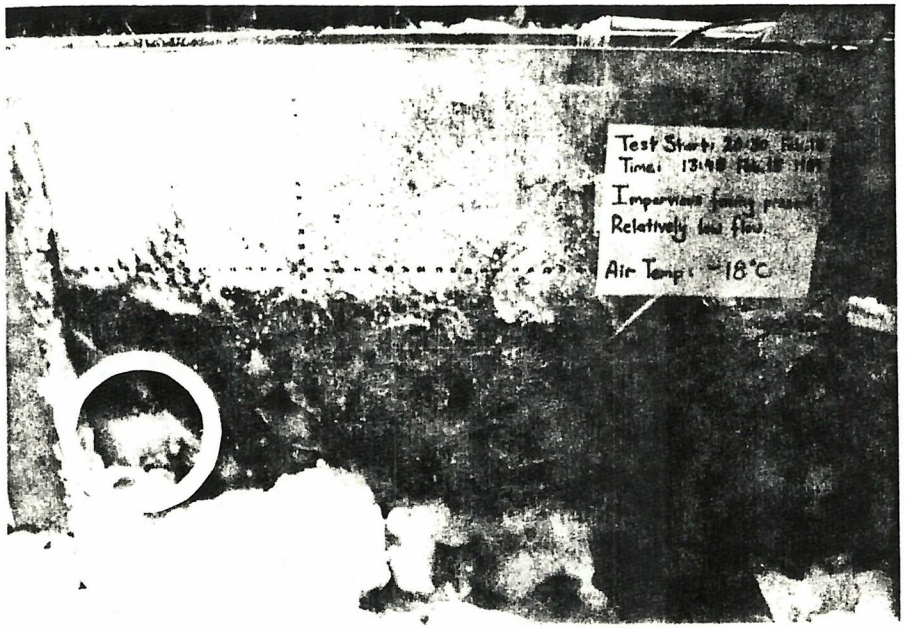


a) temperature variations for selected thermocouples.

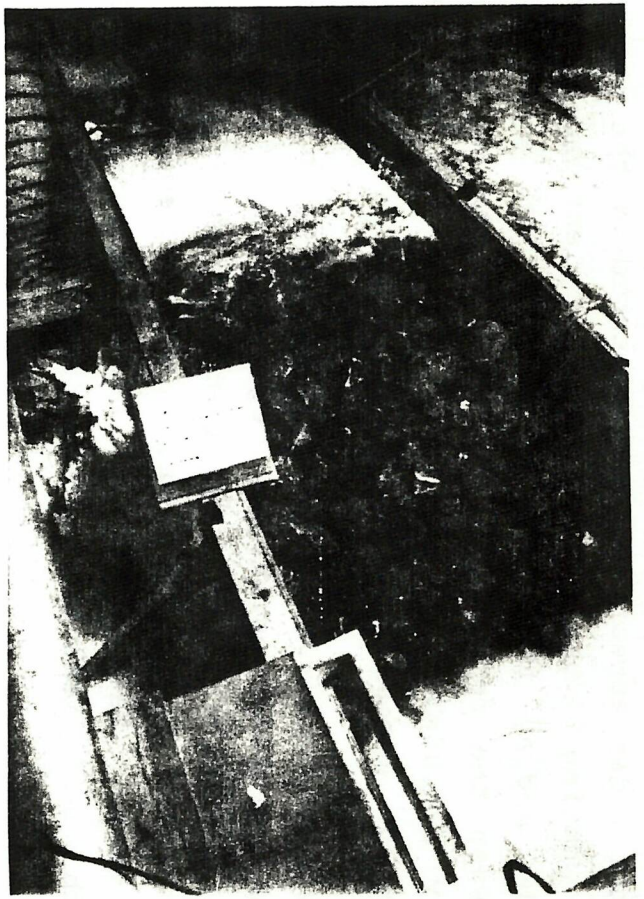


b) ambient air temperatures.

Figure 6-5. Observed temperatures in and above model dam for Test 3 in low temperature laboratory.



a) ice at phreatic surface and in freefall zone just downstream of impermeable facing (circled); elapsed time 41 hours.



b) top view of dam after 65 hours.

Figure 6-6. Ice growth for Test 3 in low temperature laboratory.

flowthrough rockfill dam appears to be influenced by the phenomenon of intermittent wetting. Due to the semi-turbulent nature of the flow through the media, the phreatic surface has a noticeable fluctuation between the rock spaces. It was observed that these spaces gradually occluded as ice slowly accumulated on the ice already formed on the exposed rock surfaces.

In each experiment approximately 20 mm of ice formed at the phreatic surface. More detailed estimates regarding the average ice thickness at the phreatic surface for each test were not obtained because the thickness of the ice was highly irregular and very difficult to estimate. Based on the following equation an estimate of the ice growth coefficient can be made (Zarling 1978):

$$I_T = \vartheta \sqrt{\Psi} \qquad [2\text{-}50a]$$

where:

$$\Psi = \sum_{i=1}^{n} (0 - T_{air}) \qquad [2\text{-}50b]$$

and where:

I_T = ice thickness (mm),

ϑ = an empirical coefficient dependent on degree of exposure, weather conditions, and flow velocity,

Ψ = a freezing index (Celcius degree-days),

n = number of days,

T_{air}: ambient air temperature.

The following table shows that by setting ϑ = 3.5, reasonable estimates of the observed ice thicknesses were obtained:

Table 6-1

Ice Growth for Low Temperature Flume Tests

Test	Average Duration (days)	Temperature (Celcius)	Thickness of Ice (mm) Predicted (ϑ = 3.5)	Observed
1	2.04	-12.9	18.0	~20
2	2.88	-11.0	19.7	~20
3	3.46	-14.3	24.6	~20

According to Prowse (unpublished), an ϑ of 7 implies a "sheltered small river with rapid flow", and this description would appear to approximate conditions for flow through the model rockfill dams in the low temperature laboratory. However, a value of $\vartheta = 3.5$ is quite low since ϑ typically falls in the range of 7 to 34, with 34 being a theoretical maximum. It is noted that the coefficient ϑ determined in this study includes the effect of intermittent wetting in the void spaces at or near the phreatic surface. The relatively low value of ϑ may be due to the addition of heat (beneath the ice forming at the phreatic surface) by viscous dissipation of hydraulic energy. It is expected that this phenomenon will in general inhibit ice growth.

6.3 HEAT EXCHANGE WITH THE ENVIRONMENT

The following text provides a detailed discussion of the various heat exchange processes which occur between a free water surface and the environment. As was noted in section 2.1.6, the following factors are the most important governing the net heat exchange between a water surface and the environment (Tsang 1982):

1. Shortwave insolation, a heat gain,
2. Net long wave radiation,
3. Convective heat loss,
4. Evaporative heat loss,
5. Snowfall, a heat loss.

These five mechanisms will be referred to as heat fluxes 1 through 5 in the following discussion. Heat flux 3 is usually the most important. It was considered that it would be valuable to be able to estimate, for a given flowthrough rockfill prototype dam, whether the net heat loss to the environment is greater than the heat added due to the viscous dissipation of hydraulic energy. It should be kept in mind that although the amount of heat added by viscous dissipation is small, the travel time for an elementary volume of fluid moving through a rockfill dam is also quite short. This means that the opportunity for heat loss to the environment is minimal. An interactive BASIC computer program "Q-BUDGET" was therefore

developed, based on the monograph of Tsang (1982), which computes the net heat flux to (or from) the environment. The program coding is listed in Appendix 7, together with example input and output screens. The main unit of heat flux in Q-BUDGET is the Langley per hour, which is 1 calorie per cm^2 per hour.

With regard to heat flux 1, the shortwave insolation (a heat gain) is computed in Q-BUDGET as the average result of the following two equations:

Tsang (1982): $$q_1 = q_{1C}(1-\Phi)(0.35 + 0.061(10-C)) \quad [6-1]$$

Devik (1931): $$q_1 = q_{1C}(1-\Phi)(1 - 0.09\ C) \quad [6-2]$$

where:
q_1 = shortwave insolation in Langleys/hr,
q_{1C} = shortwave insolation under clear sky conditions,
C = cloud cover index, 0 for clear sky, 10 for overcast,
Φ = albedo of water surface, equal to between 0.08 and 0.10.

In Ottawa, for example, 9.2 Langleys per hour is the average clear sky insolation (q_{1C}) on January 15 in Ottawa. Values of clear sky insolation for different locals and for different months can be found in the insolation maps cited in Gray (1970). The default value in the program is 9.2 Langleys per hour.

Heat flux 2 is the *net* longwave radiation input from the environment. The longwave heat *input*, q_{2a}, depends on whether or not there is cloud cover. For clear sky conditions this heat input is:

$$q_{2a} = (0.68 + 0.036\ e_a)\ \sigma\ (T_{AIR})^4 \quad [6-3]$$

where T_{AIR} is in $^{\circ}K$.

Under cloudy conditions the longwave input is:

$$q_{2a} = (a + b\ e_a)\ \sigma\ (T_{AIR})^4 \quad [6-4]$$

where:

$a = 0.740 + 0.025\ C\ e^{-0.000192H}$

$b = 0.0049 - 0.00054\ C\ e^{-0.000197H}$

H = elevation of cloud cover above 500 m,

T_{AIR} = temperature of the air in degrees °K,

σ = Stefan-Boltzmann constant = $4.879 \cdot 10^{-9}$ cal/(cm^2 hr °K^4),

e_a = vapour pressure of the air.

In order to compute q_{2a} the vapour pressure of the air, e_a is needed. This is found from the saturation vapour pressure, e_s, and the relative humidity, f (Linsley *et al* 1982):

$$e_s = 33.8639 \left[(0.00738\ T_{AIR} + 0.8072)^8 - 0.000019|1.8T_{AIR} + 48| + 0.001316 \right] \quad [6\text{-}5]$$

The vapour pressure of the air is then:

$$e_a = e_s\ f/100 \quad [6\text{-}6]$$

where:

e_a = vapour pressure of the air (millibars),

e_s = saturation vapour pressure,

f = relative humidity,

T_{AIR} = temperature of the air in degrees Celcius.

In the same way that the atmosphere contributes longwave radiation, the body of water under consideration also loses heat via the same process. The longwave heat *output* is:

$$q_{2W} = \varepsilon\ \sigma\ (T_W)^4 \quad [6\text{-}7]$$

ε = emissivity of the water surface (set at 0.97),

T_W = temperature of water surface in degrees K, assumed equal to 273 K (0°C).

Therefore, the net longwave radiation is:

$$q_2 = q_{2W} - q_{2a} \quad [6\text{-}8]$$

where q_{2a} is computed from equation [6-3] or equation [6-4], depending on whether or not there is cloud cover.

Heat flux 3, convective heat loss, is computed using the average result obtained from the following two equations:

Tsang (1982) $$q_3 = (0.080 + 0.186\ v_{a2})(T_W - T_{AIR}) \qquad [6\text{-}9]$$

Rimsha-Donchenko (1957)

$$q_3 = \left[(0.333 + 0.0146(T_W - T_{AIR})) + 0.1625 v_{a2}\right](T_W - T_{AIR}) \qquad [6\text{-}10]$$

where:

T_W = temperature of water (assumed to be 0°C for the purpose of estimating q_3),

v_{a2} = wind velocity at 2 m height.

Average results from equation 94 and equation 95 are suggested since it was found that the above two equations can give quite different results. By using Q-BUDGET to compute convective heat loss the conservative assumption is made that a solid ice cover has not yet formed at the phreatic surface. If such a cover has already formed, convective losses would be greatly reduced. This is because heat in the water would have to be conducted through the cover before being convected away.

The evaporative heat loss is computed using the average of the following two equations:

Tsang (1982) $$q_4 = (0.131 + 0.306\ V_{a2})(e_s - e_a) \qquad [6\text{-}11]$$

Rimsha-Donchenko (1957)

$$q_4 = \left[0.520 + 0.02275(T_W - T_{AIR}) + 0.253\ V_{a2}\right](e_s - e_a) \qquad [6\text{-}12]$$

The heat loss due to snowfall is computed using:

$$q_5 = p_S\left[(H_L + c_S(T_W - T_S)\right] \qquad [6\text{-}13]$$

where:

p_S = rate of snowfall per unit area, g/(cm^{2}hr),

($p_S = \rho_{SNOW} \cdot$ (depth rate of snowfall)),

ρ_{SNOW} = 0.1 g/cm^3 (typically),

c_s = specific heat of snow, 0.5 cal/(g °C),

H_L = latent heat of fusion of ice, 79.7 cal/g,

T_S = temperature of the snow, assumed equal to the air temperature.

It is noted that in Q-BUDGET no consideration is given to the effect of the rocks at the surface of the structure. These will absorb shortwave radiation and emit longwave radiation at different rates than a water surface. These differences will in turn be affected by the convective effects of the water, as it flows past these rocks just below and at the phreatic surface. Other factors, such as the compass orientation of the downstream face of the dam (which will affect the efficiency of insolation) and possible shading of the dam (quite possible for small rivers), are also not considered. This program has been developed as a tool to give indication of the overall heat budget for a flowthrough rockfill structure. Prototype cases in which heat loss appears to be greater than heat gain based on the methods described in this section should be examined in greater detail.

Using the above equations it is possible to obtain an overall heat transfer coefficient for the structure. This heat transfer coefficient C_o is defined using Newtons' law of cooling as:

$$Q_* = C_o(T_W - T_{AIR}) \qquad [6\text{-}14]$$

Q_* = heat flux, in units such as Watts/m^2 or Langleys per hour,

(1 Langley per hour = 11.63 Watts/m^2),

C_o = heat transfer coefficient, in units such as Watts/(m^{2}C°).

For the specified air temperature and under the assumption that T_W is 0 °C, Q-BUDGET computes C_o and provides this as part of the output. According to Prowse (unpublished), values of C_o typically vary between 25 and 50 W/(m^{2}C°) for rivers in Canada, with the latter associated with "extremely cold windy conditions".

It is of interest to consider for a typical prototype whether or not the heat lost from the water passing through a flowthrough rockfill dam is greater than the heat gained by viscous dissipation. The heat gained by viscous dissipation of hydraulic energy is:

$$q_v = 2.342\ Q\ \Delta h \qquad [2\text{-}49]$$

where:

q_v = heat added due to viscous dissipation (kcal/sec),

2.342 = 1000/427, a constant to convert work (kgf-m) to heat (kcal),

Q = discharge (m^3/s),

Δh = drop in elevation, m (in this context, from upstream pool elevation to downstream pool level).

The worked example in part 8 of Appendix 6 shows that, for a typical prototype 20 m high, ratio of heat added by viscous dissipation to heat lost to the environment is about 10.7. A heat transfer coefficient C_o of 60 $W/(m^2\text{-}C^\circ)$ was used for this calculation, which is a very severe and therefore conservative value. However, using Q-BUDGET the actual C_o could be determined for the specific weather conditions for the case of interest.

It therefore appears that the heat gained will in general be greater than the heat lost, even for very extreme conditions. It must be emphasized however that the value of the ratio of 10.7 is only valid for the physical and hydraulic characteristics of the prototype structure described in Appendix 6. A similar calculation could be generated for any prototype dimensions of interest and for other hydraulic parameters. Longer travel times and smaller vertical drops alter the ratio in favour of greater heat loss to the environment. Nonetheless it would appear that the heat gained will usually be greater than the heat lost for prototype flowthrough rockfill dams. The procedure for computing the ratio of heat lost to heat gained is described as follows:

1. Determine the net time-rate of heat flux Q_* (usually a heat loss to the environment) either by using Q-BUDGET or by assuming a value for C_o for a known temperature difference. Equation [6-14] is used if the latter approach is taken. Typical units of Q_* are Langleys/hour or $Watts/meter^2$.

2. Determine the area A through which heat is lost from the dam. This is the length L multiplied by the distance travelled for an elementary volume of water.

3. Convert Q_* to a quantity of heat using:

$$\text{Heat out} = Q_* \cdot A \cdot t \qquad [6\text{-}15]$$

4. Compute the rate of heat added by viscous dissipation from equation [2-49]. The result is typically in units of kcal/sec.

5. Compute heat added per unit volume of water:

$$\text{Heat added per unit volume} = \frac{q_v}{Q} = \frac{(\text{kcal/sec})}{(\text{m}^3/\text{sec})} = \text{kcal/m}^3$$

6. Compute volume of flow as area A multiplied by average depth.

7. Heat added by viscous dissipation is the result of step 5 multiplied by the result of step 6.

8. The ratio of the result of step 3 to the result step 7 then indicates whether or not heat is being added more rapidly than it is being removed.

6.4 CONCLUDING REMARKS

It is concluded that the formation of frazil is unlikely in a flowthrough rockfill dam. Heat added by viscous dissipation will normally be greater than heat lost to the environment. This does not preclude, however, the formation of ice at the phreatic surface. Once this cover has formed heat loss will be reduced, and the formation of ice in the voids made even more unlikely. This process of reduction of heat loss due to the formation of a sheet-ice cover is also known to occur in rivers.

For the experiments performed in this study it was found that a relatively low ice growth coefficient ($\vartheta = 3.5$) characterized the formation of ice at the phreatic surface quite well. The only case

of ice formation occurring inside the voids of the dam was observed at low flow conditions when an upstream impermeable facing was present. For this case an ice lens developed in the free-fall zone, near the base of Parkin's (1963a) "Zone 3" (see Figure 2-2), but this apparently had little effect on piezometric pressures.

7.0 DESIGN GUIDELINES

Based on the foregoing analyses, the following design guidelines can be stated:

1. A variety of equations are available to compute the velocity of (non-Darcy) flow in a porous media as a function of hydraulic gradient. Wilkins' (1956) equation tends to give velocities at the low end of the range, especially for smaller particle sizes. Martins' (1990) equation tends to give velocities at the upper end of the range. If the hydraulic mean radius is required it can be evaluated using equation [4-7]:

$$m = \frac{e\ d}{6\ r_E} \qquad [4\text{-}7]$$

It was found that for crushed limestone $r_E \cong 1.6$. If the available rockfill is more angular than the material used in this study (see Figure 3-3), a higher value of r_E can be used. An upper limit for the average value of r_E for crushed rock is expected to be approximately 2. The lower limit on r_E is 1, the value associated with spheres.

Use of higher values of r_E results in smaller computed values of m and a smaller capacity to handle flow at a given hydraulic gradient. Graded materials can be expected to have lower values of m due to the reduction in the void ratio in equation [4-7]. Equation [4-7] should not be used with plate-like rocks such as shale, in which a significant amount of surface area is lost to interparticle contact.

2. Wilkins' equation can be used to estimate the parameter *a* in a non-Darcy flow equation of the form of equation [2-3a]:

$$i = a\ V_v^N \qquad [2\text{-}3a]$$

This was confirmed through agreement with the results of column tests. Other equations such as the Ergun and the McCorquodale

equations have the advantage that the work at any level of turbulence. However, these equations have the disadavantage that the result in the form $i = st + tV^2$ must be converted to the form of [2-3a] before being useful for the type of finite difference numerical pore pressure model described in this report.

The following form of non-Darcy flow equation:

$$V_v = K\sqrt{gedi} \qquad [2\text{-}11]$$

is convenient to use and applies to fully-developed turbulence. The value of K for crushed rock is about 0.75.

3. The stage-discharge curve of a flowthough rockfill structure for the case of no impermeable facing and for h < H can be estimated using equation [4-12]:

$$Q = \left(a' i^{N'}\right) h L \qquad [4\text{-}12]$$

where a' is defined by [2-3c] and the effective i for the structure as a whole is computed from equation [4-11]. The rating curve so obtained can be used as a guide for estimating the rating curve when an imposed tailwater level is present.

4. When an upstream impermeable facing is present, the stage-discharge curve is difficult to compute directly but the rating can be expected to be fairly linear up to $h_c < (H - h_F)$. However, once the flow enters the crest of the dam at a distance of approximately one third of the way along the crest, the upstream impermeable facing ceases to affect the upstream water level or the phreatic surface. At this stage the phreatic surface is a straight line. An alternative method of obtaining a rating curve when an impermeable facing is present is to use the exit height h_e as opposed to h_c, to be described under #5 below.

5. For h_e less than approximately 0.5 H the exit height on the downstream face can rapidly estimated using equations [4-16] and [2-26]:

$$\frac{\theta_{ff}}{\theta} = 1.41 \frac{h_e}{H} + 0.17 \qquad [4\text{-}16]$$

$$h_e = \frac{q}{n} \left[\frac{a}{\tan \theta} \right]^{(1/N)} \qquad [2\text{-}27]$$

where *a* is defined by equation [2-3a]. The computed exit height can be used as the starting point for computation of the location of the phreatic surface. It can also be used to generate a partial rating curve using equation [2-27]. It is expected, however, that the constant 1.41 may decrease and the constant 0.17 may increase somewhat for dams with larger ratio of H/d than could be tested in this study. In the absence of data on the performance of a prototype with large H/d, the constants in equation [4-16] are suggested.

6. Gradually varied flow theory (GVFT) was found to accurately describe the position of the phreatic surface. For rectangular channels with fully-developed turbulence within the porous media, the modified Stephenson equation was found to give results:

$$\frac{3}{K^2 ed} x = \left(\frac{h}{h_e} \right)^3 - 3 \ln \left(\frac{h}{h_e} \right) - 1 \qquad [4\text{-}21]$$

For h_e/H greater than about 0.5, GVFT should not be used to compute the location of the phreatic surface. At $h_e/H \cong 0.6$, a straight line between h_e and the upstream limit of the crest is a good approximation of the path of the phreatic surface. For prismatic non-rectangular channels the direct step method may be employed, together with a non-Darcy flow equation for computing the friction slope. For non-prismatic channels the standard step method may be used, again with a non-Darcy flow equation of the user's choice, for computing the friction slope. Equation [2-11] is convenient choice

due to its similarity to the Chezy equation. Care must be taken to compute the velocity head with V_v rather than simply the bulk velocity V.

7. Unravelling failure of the downstream face is a progressive phenomenon which begins at relatively low flows. The extent of mesh protection needed for the case of maximum flowthrough (at h = H) depends mainly on the steepness of the downstream face and the particle size. No single equation to compute the minimum height can be presented. However, a detailed procedure has been presented, and an example of the applcation of the procedure is given in Appendix 6 for a prototype 20 m high made of up 30 cm rocks, and with a downstream slope of 1V:1.5H. It is estimated that for this particular dam a minimum of 75% of the wetted downstream face would require protection against unravelling.

8. Pore pressure modelling using the finite difference scheme of Curtis and Lawson (1967) showed that the hydraulic gradient near the toe of steep (1V:1H) flowthrough structures varied from approximately 0.5 for downstream slopes of 1V:2H to nearly unity for downstream slopes of 1V:1H. However, the determination of pore pressures must be approached on an individual basis, for the given configuration of dam and boundary conditions.

9. For rotational failure analyses it makes little difference whether or not pore pressures are determined from non-Darcy or Darcy pore pressure modelling. The minimum restraint against rotational failure was found to be significantly higher than the minimum observed restraint for a series of model tests.

10. An alternate method for performing calculations related to massive deep-seated failure has been presented. This is based on a wedge-type analysis and gave predicted minimum restraint requirements much closer to what was measured in the laboratory. An example of the restraint requirements arising from the wedge method has been presented. This method assumes a very firm foundation beneath the dam, and emphasises the role of seepage forces to determine the

rupture plane which gives the maximum bursting pressure. The expression for the bursting pressure is:

$$P_a = \frac{\sin(\rho + \xi - \phi)}{\cos(2\phi - \rho)} F_B \qquad [5\text{-}29]$$

where F_B is the vector sum of the seepage force and the buoyant weight for the material above the assumed rupture plane, where this plane is at an angle ρ above the horizontal.

11. The formation of frazil is unlikely in a flowthrough rockfill dam. Heat added by viscous dissipation is usually much greater than heat lost to the environment. Ice formation inside the voids of the dam was observed at low flow conditions when an upstream impermeable facing was present. For this case an ice lens developed in the free-fall zone, but this had little effect on piezometric pressures. This does not preclude the formation of ice at the phreatic surface. It was found that a relatively low ice growth coefficient ($\vartheta = 3.5$) characterized the formation of ice at the phreatic surface.

8.0 SUMMARY AND CONCLUSIONS

1. A variety of equations are available for describing non-Darcy flow through porous media. It is important to note that Wilkins' equation is a single regime equation, whereas the Ergun and McCorquodale equations adjust their parameters to allow for the relative effects of factors such as fluid viscosity. The parameters of hydraulic mean radius and porosity are important physical parameters of the media in equations of this type. The particle size d can be simply related to the hydraulic mean radius if the non-Darcy flow equation being used (such as Martins equation) uses d rather than m. For crushed rock the range of variability in the predictive nature of non-Darcy flow equations is approximately 20% for a given size, roughess, and shape of rock material.

2. In this study an experimental program was successfully carried out in five areas:

i) particle characterization,
ii) packed column tests,
iii) parametric study in glass-walled flume,
iv) additional measurements using large rock in floor flume,
v) experiments in the NRCC low temperature laboratory.

Data from these areas of study was used to check the validity of various non-Darcy flow equations to develop and/or refine numerical techniques for describing the hydraulic behaviour of flowthrough rockfill dams. Innovative experiments on restraint requirements with respect to slope stability, and on hydraulic behaviour in low temperatures, yielded new information not found in the literature.

3. Successful flowthrough rockfill dams and spillways of the past have, in general, been designed such that a reinforcing mesh, tied back into the body of the dam, has covered the downstream face. A number of such structures are still functioning. With regard to the hydraulic capacity of coarse rockfill, it is of interest to note that velocities of about 0.2 m/s have been observed for flowthrough rockfill drains in British Columbia. However, the gradient of such drains is typically much smaller than that envisaged for flowthrough

rockfill dams.

4. A method of determining the surface area of crushed rock was developed, and a useful parameter associated with surface area efficiency was described. For non-platy rocks the surface area efficiency ratio, r_E, was found to be useful in calculating the hydraulic mean radius.

5. In seeking an appropriate non-Darcy flow equation, five equations from the literature were quantitatively considered. The results from the Wilkins and Ergun equations for nearly fully-developed turbulence were found to give low yet comparable values for the parameters governing the flow. The equations of Martins and McCorquodale gave relatively high comparable results. Application of the simpler Wilkins' equation to laboratory cases demonstrated its usefulness for non-Darcy flow through rockfill for the case of nearly fully-developed turbulence. It was found that, for example, Wilkins' equation gave reasonable estimates of the empirical parameters determined independently from packed column tests in this study. This was also seen as a confirmation of the method used to experimentally estimate the hydraulic mean radius.

6. A new equation was developed which provides a stage-discharge curve for a flowthrough rockfill dam with no upstream impermeable facing. This equation was found to perform well when applied to a model dam of larger rock and different dimensions from the model tests from which the equation was derived. The aspect ratio and the effective width of the dam were found to be important parameters in characterizing the structure hydraulically.

7. At relatively high upstream water levels, for which the point of entry of the flow is approximately one third of the way along the crest, an upstream impermeable facing has little or no effect on the upstream water level or the position of the phreatic surface. The rating curve for the case of an upstream facing being present was difficult to determine for the general case. Parkin's assumption of $i = 0.82$ was found to describe the rating curve poorly. For this case it is suggested that a rating curve be developed based on the exit height on the downstream face of the dam.

8. A new method for computing the exit height h_e was developed. This was found to more accurately describe the h_e versus discharge curve than Parkin's equation, in which it is assumed that $i = \tan \theta$ is valid for all levels of discharge.

9. A tailwater level of 25% of the height of the model dams tested was found to alter the rating curve only when $h < 0.6\ H$.

10. Application of Stephenson's analytic equation for the phreatic line was found to give accurate estimation of the location of the phreatic surface for $h_e < H$. When $h_e > 0.6\ H$ a straight line between h_e and the upstream limit of the crest was found to approximate of the position of the phreatic surface reasonably well. This equation can also be used to estimate the exit height on the downstream face as long as the *intersection* of the projected curve with the downstream face of the dam is used, rather than the critical depth as defined for a porous media.

11. Unravelling failure was observed to begin at very low flows. Seeking to identifying the threshold discharge of the structure as a whole, using the classical inititiation of motion approach, was not considered meaningful. A framework for the analysis of unravelling failure on a case-by-case basis has been presented.

12. The results of rotational failure analysis were not significantly altered if Darcy pore pressures were used instead of non-Darcy pore pressures. However, the associated minimum restraint requirement appears to be very large from any rotational failure analysis.

13. A wedge method proposed herein for deep-seated failure analysis gave a more reasonable yet still conservative indication of the minimum amount of restraint needed to prevent massive failure.

14. The finite difference method proposed by Curtis and Lawson (1967) was successfully employed to compute non-Darcy pore pressures. Scale defects regarding the modelling of observed pore pressures were thought to be relatively unimportant because:

(i) pore Reynolds numbers were > 400.

(ii) use of N = 1.88 in the mathematical model gave reasonable results, and this value implied an adequate level of turbulence.

The presence of an upstream impermeable facing was found to make pore pressure modelling more computationally intensive, but still possible, with average errors less than about 10%.

15. It was found that such finite difference modelling could be efficiently carried out using an electronic spreadsheet. This computational tool made for the convenient computation of the magnitude and direction of the hydraulic gradients and of the associated seepage forces. The internal hydraulic gradients near the toe of a flowthrough rockfill dam was found to approach unity for steep (1V:1H) slopes.

16. The formation of frazil within the voids of a flowthrough rockfill dam is very unlikely due to the phenomenon of the viscous dissipation of hydraulic energy. A computer program for estimating the overall heat transfer coefficient of the phreatic and seepage surfaces under given ambient conditions was developed and is included in Appendix 7. Ice growth at the free surface of flowthrough rockfill dams appears to be slower than for other natural bodies of water, with ϑ = 3.5 based on the experiments performed in this study. Ice may form in the voids of the free-fall zone (Parkin's Zone 3, Figure 2-2) but it is doubtful that this affects the hydraulic behaviour of the structure significantly.

9.0 REFERENCES

Ahmed N and Sunada D.K., 1969. Nonlinear flow in porous media. ASCE Journal of the Hydraulics Division, vol.95, HY6, Nov., p.1847-1857.

Airapetyan R.A., 1968. Modern rockfill dams. Israel Program for Scientific Translations, Jerusalem 1970.

Alger G.R. and Simons D.B., 1968. Fall velocity of irregular shaped particles. ASCE Journal of the Hydraulics Division, vol.94, HY3, May, p.721-737.

Allen D.N. de G., 1954. Relaxation methods. McGraw-Hill, NY.

Arbhabhirama A. and Dinoy A.A., 1973. Friction factor and Reynolds number in porous media flow. ASCE Journal of the Hydraulics Division, vol.99, HY6, June, p.901-911.

Barr D.W. and Rosene R.W., 1958. Loose-rock spillway for low head dam. ASCE Civil Engineering Magazine, April, p.50-51.

Basak P., 1976. Steady non-Darcian seepage through embankments. Journal of the Irrigation and Drainage Division, vol.102, IR4, Dec., p. 435-443.

Basak P., 1977. Non-Darcy flow and its implications to seepage problems. Journal of the Irrigation and Drainage Division, vol.103, IR4, Dec., p. 459-473.

Beard D.C. and Weyl P.K., 1973. The influence of texture on porosity and permeability of unconsolidated sand. Amer. Assoc. Petrol. Geol. Bull., p. 349-369.

Berubé Y., Gilbert R., Frenette M., LaRochelle P., and Pantu I., 1972. Mine waste containment and water quality in a northern environment. Department of Indian and Northern Affairs, ALUR 71-72-31. 184 pp.

Bessy G.E. and Soul D.C., 1954. The application of methods of particle size and surface area measurements to whiting. British Journal of Applied Physics, supplement #3, Conference on Physics of Particle Sizing, University of Nottingham, Apr.6-9, Session H, Paper H1, The Institute of Physics, London, p.S181-S189.

Bishop A.W., 1956. The use of the slip circle in the stability analysis of earth slopes. Geotechnique, vol.5, no.1, p.7-17.

Bowles J.E., 1968. Foundation analysis and design. McGraw-Hill, New York, 750 pp.

Bray D.I. and Davar K.S., 1987. Resistance to flow in gravel-bed rivers. Can.J.Civ.Eng.,14(1):77-86.

Bray D.I., 1987. Hydraulics of open channels - CE5701 course notes. University of New Brunswick, 378 pp.

Brownell L.E. and Katz D.L., 1947. Flow of fluids through porous media. AICE Chemical Engineering Progress, vol.43, Oct., p.537-548.

Brownell L.E., Dombrowski H.S., and Dickey C.A., 1950. Pressure drop through porous media. AICE Chemical Engineering Progress, vol.46, Aug., p. 415-422.

Campbell D.B., 1989. Some observations relative to the performance of flow-through rock drains. 13th Annual BC Mine Reclamation Symposium, June 7-9, p.119-128.

Casagrande L., 1932. Näherungsmethoden zur Bestimmung von Art und Menge der Sickerung durche geschüttete Dämme. Thesis, Technische Hochschule, Vienna. Translated by the US Army Corps of Engineers, Waterways Experimental Station, Vicksburg, Miss.

Cedergren H.R., 1977. Seepage drainage and flow nets. Wiley, NY, 534 pp.

Chow V.T., 1959. Open-channel hydraulics. McGraw-Hill, NY, 680 pp.

Cohen de Lara G., 1956. Etude d'infiltration dans les barrages en enrochements. Application au cas des batardeaux de coupure . Fourth Hydraulic Conference of the Hydrotechnical Society of France, Paris. Question IV, no.7, p.365-380.

Craig R.F., 1987. Soil mechanics, 4th edition. Van-Nostrand Reinhold UK, Berkshire, 410 pp.

Crawford C.W. and Plumb O.A., 1986. The influence of surface roughness on resistance to flow through packed beds. ASME Journal of Fluids Engineering, vol.108, Sept., p.343-347.

Curtis R.P. and Lawson J.D., 1967. Flow over and through rockfill banks. ASCE Journal of the Hydraulics Division, Sept., vol. 93, HY5, p. 1-21.

Curtis R.P. and Lawson J.D., 1969. Closure to "Flow over and through rockfill banks.", ASCE Journal of the Hydraulics Division, vol.95, HY1, Jan., p.452-453.

Davey G.I., 1960. Rockfill dams at Mary Kathleen and Mt. Isa. Journal of the Institution of Civil Engineers (Australia), Dec., p.291-302.

de Prony, Baron G.C.F.M.R., 1804. Recherches physico-mathématiques sur la théorie du mouvement des eaux courantes. Paris. (see Rouse and Ince, 1957).

Devik O., 1931. Thermische und dynamische Bedingungen der Eisbildung im Wasserlauffen. Geofys. Publ.IX, 1.

Dinoy A.A., 1971. Friction factor and Reynolds number relationship in flow through porous media. M.Eng. thesis, Asian Institute of Technology, Bangkok, Thailand.

Dudgeon C.R., 1964. Flow of water through coarse granular materials. M.Eng. thesis, University of New South Wales, Manly Vale, Australia.

Dudgeon C.R., 1966. Wall effects in permeameters. ASCE Journal of the Hydraulics Division, vol.93, HY5, Sept., p.137-148.

Dullien F.A.L., 1979. Porous media transport and pore structure. Academic Press, NY.

Duncan J.M. and Wong K.S., 1985. STABR: A computer program for slope stability analysis with circular slip surfaces - Microcomputer version. Dept of Civil Engineering, 104 Patton Hall, Virginia Polytechnic Institute and State University, Blacksburg, VA, 24061.

Ergun S., 1952. Fluid flow through packed columns. Chemical Engineering Progress, vol.48 no.2, p.89.

Escande L., 1953. Experiments concerning the infiltration of water through a rock mass. Proc. Minnesota International Hydraulics Convention, Sept.1-4, Minneapolis, p.547-553.

Farhoudi J. and Smith K.V.H., 1982. Time scale for scour downstream of hydraulic jump. ASCE Journal of the Hydraulics Division, vol.108, HY10, Oct., p.1147-1162.

Fand R.M. and Thinakaran R., 1990. The influence of the wall on flow through pipes packed with spheres. ASME Journal of Fluids Engineering, vol.112, March, p.84-88.

Fitzpatrick M.D., Cole B.A., Kinstler F.L., and Knoop B.P., 1985. Design of concrete-faced rockfill dams. ASCE Convention on Concrete-Faced Rockfill Dams - Design, Construction and Performance, Edited by J.B. Cooke and J.L. Sherard, Detroit Michigan, p.410-434.

Findikakis A.N. and Tu S-W, 1985. Flood routing through rock dumps in natural channels. ASCE Conference on Hydraulics and Hydrology in the Small Computer Age, Lake Buena Vista, Florida, Aug.12-17, p.1213-1218.

Forcheimer P., 1901. Wasserbewegung durch boden, Zeit. Ver. Deutsch. Ing., 45.

Franzini J.B., 1956. Permeameter wall effect. Transactions American Geophysical Union, vol.37, no.6, Dec., p.735-737.

Freeze R.A. and Cherry J.A., 1979. Groundwater. Prentice-Hall, Englewood Cliffs, NJ.

Garga V.K., Smith H.R., and Scharer J., 1983. Abandonment of acid-generating mine tailings. VII Pan-American Conference on Soil Mechanics and Foundation Engineering, Vancouver, BC, vol.2, p.613-626.

Gerodetti M., 1981. Model studies of an overtopped rockfill dam. Water Power and Dam Construction, Sept., p.25-31.

Giles R.V., 1977. Fluid mechanics and hydraulics, SI edition. McGraw-Hill, NY, 275 pp.

Gorchakov M.P., 1953. The design of a spillway dam of rockfill construction. Hydrotechnical Construction, no.4, USSR.

Gordon J.L. and Noel R.C.R., 1986. The economic limits of small and low-head hydro. Water Power and Dam Construction, April, p. 23-26.

Goulter I.C., 1986. Course Notes for "Fundamentals of River Engineering", University of Manitoba, Winnipeg, 114 pp.

Gray D.M., ed, 1970. Handbook on the principles of hydrology. Water Information Center, Huntington, N.Y.

Guidici S., 1967. Discussion of "Rockfill structures subject to water flow", ASCE Journal of the Soil Mechanics and Foundations Division, SM5, Sept. p.329-336.

Guskov G.D., and Pravdivets Y.P., 1987. Model of stability of revetments on earth spillway slopes. Hydrotechnical Construction, vol.20, no.7, Jan., p.405-411.

Harr M.E., 1962. Groundwater and seepage. McGraw-Hill, NY, 315 pp.

Hartung F., and Scheuerlein H., 1970. Design of overflow rockfill dams. Proceedings of Tenth International Congress on Large Dams, Montreal, Quebec, June 1-5, vol. 1, p.587-595.

HEC - Hydrologic Engineering Centre, undated, Davis, CA, 95616-4687.

Hedlin C.P. and Collins S.H., 1961. A method of measuring the surface area of granular material. Canadian Journal of Chemical Engineering, Feb., p.49-51.

Henderson F.M., 1966. Open channel flow. MacMillan, NY, 522 pp.

Holtz R.D. and Kovacs W.D., 1982. An introduction to geotechnical engineering. Prentice-Hall, Englewood Cliffs, NJ, 733 pp.

Huntington W.C., 1957. Earth pressure and retaining walls. J.Wiley and Sons, New York, 534 pp.

Hydro-Electric Commission, Tasmania, 1969. Failure of Cethana Dam, flood breach of a partly completed rockfill dam. Australian National Committee of the International Commission on Large Dams Bulletin, no.28, Hobart Tasmania, p.23-36.

Jaeger C. 1956. Engineering fluid mechanics. Blackie and Son Ltd., London, 529 p.

Jain S., Holly F.M., Lee T., 1988. Head loss through porous dikes. Canadian Journal of Civil Engineering, Oct., vol.15, p.766-775.

Johnson H.A., 1971. Flow through rockfill dam. Journal of Soil Mechanics & Foundations Div., vol.97, SM2, Feb., p.329-340.

Kells J.A., 1991. Spatially varied flow over rockfill embankments. 10th Annual CSCE Conference, Vancouver, May 29-31, p.155-165.

King H.W. and Brater E.F. 1963. Handbook of hydraulics. 5th Edition, McGraw-Hill, NY.

Kirkham C.E., 1967. Turbulent flow in porous media. Report DR11, University of Melbourne, Dept of Civl Engineering, Feb., 146 pp.

Kirkham C.E., 1968. Discussion of "Flow over and through rockfill banks.", ASCE Journal of the Hydraulics Division, vol.94, HY2, March, p.606-607.

Kleiner D.E., 1985. Engineering with spreadsheets. ASCE Civil Engineering Magazine, October, p.55-57.

Kluber and Breth, 1971. Discussion of "Flow through rockfill dam" SM11, Nov. 71, p.1609-1612.

Krumbein W.C. and Pettijohn F.J., 1938. Manual of sedimentary petrography. D. Appleton-Century and Co., NY, NY.

Lambe T.W. and Whitman R.V., 1979. Soil mechanics - SI version. J.Wiley and Sons, NY, 553 pp.

Lane D., Berdusco R., and Jones R., 1986. Five years experience with the Swift Creek rock drain at Fording Coal Limited. Proceedings of the International Symposium on Flowthrough Rock Drains, Cranbrook, British Columbia, September 8-11, p.7-11.

LCPC - Laboratoire Centrale Ponts et Chausées, 1984. Notice d'utilization pour PETAL (slope stability program), Marseilles, Sept., 60 pp.

Leps T.M. 1973. Flow through rockfill, in "Embankment-Dam Engineering", R.C. Hirschfeld, Ed., John Wiley and Sons, p.87-107.

Linsley R.K., Kohler M.A., and Paulhus J.L.H., 1982. Hydrology for engineers. McGraw-Hill, N.Y., 508 pp.

Linford A., and Saunders D.H., 1967. A hydraulic investigation of through and overflow rockfill dams. British Hydromechanics Research Association RR888, March, 17 pp.

MacIntosh K.J., 1985. Ice interaction with rubble mound breakwater. M.Eng. thesis, Carleton University, Faculty of Engineering, September.

Marachi N.D., Chan C.K., Seed H.B., and Duncan J.M., 1969. Strength and deformation characteristics of rockfill materials. Report TE-69-5 for the State of California Department of Water Resources. University of California, Berkeley, Sept.

Martins R., 1990. Turbulent seepage flow through rockfill structures. Water Power and Dam Construction, March, p.41-45.

McCorquodale J.A., 1970. Finite element analysis of non-Darcy flow in porous media. PhD thesis, University of Windsor, Windsor, Ontario.

McCorquodale J.A., Hannoura A.A., and Nasser M.S., 1978. Hydraulic conductivity of rockfill. Journal of Hydraulic Research, vol.16 no. 2, p.123-137.

Mustafa S., and Rafindadi N.A., 1989. Nonlinear steady state seepage into drains. ASCE Journal of Irrigation and Drainage Engineering, vol.115, no.3, June, p.358-376.

Nash D. 1987. A comparative review of limit equilibrium methods of stability analysis. Chapter 2 in "Slope Stability", edited by M.G. Anderson and K.S. Richards, J.Wiley & Sons, NY, p.11-75.

National Water Research Institute, J.S. Ford, Ed., 1982. Prototype designs for surveys and measurement in an aquatic environment. NWRI Contribution 84-25 ES550, National Water Research Institute, Burlington, Ont., 41 pp.

Neill C.R. and Yalin M.S., 1969. Quantitative definition of beginning of bed movement. ASCE Journal of the Hydraulics Division, vol.95, HY1, Jan., p.585-588.

Nirandra H.S., 1973. Non-Darcy flow through porous media. M.Tech. thesis, Dept of Civil Engineering, I.I.T. Kanpur, India, July.

Olivier H., 1967. Through and overflow rockfill dams - new design techniques. Proceedings of the Institute of Civil Engineers, paper no.7012, vol.36, p.433-471.

Olsthoorn T.N., 1985. Computer notes - the power of the electronic worksheet: modeling without special programs. Groundwater, May-June, p. 381-390.

Osterkamp T.E., 1978. Frazil formation: a review. ASCE Journal of the Hydraulics Division, vol.104, HY9, Sept., p. 1239-1255.

Parkin A.K., 1963a. Rockfill dams with inbuilt spillways. Part I, hydraulic characteristics. Bull. 6, University of Melbourne and Water Res. Found. of Australia, March, 88 pp.

Parkin A.K., 1963b. Rockfill dams with inbuilt spillways, stability characteristics. Bull. 7, University of Melbourne, publ. by Water Res. Found. of Australia. December.

Parkin A.K., Trollope D.H., and Lawson J.D., 1966. Rockfill structures subject to water flow. Journal of the Soil Mechanics & Foundations Division, vol. 92, SM6, Nov., p. 135-151.

Parkin A.K., 1971. Field solutions for turbulent seepage flow. ASCE Journal of Soil Mechanics and Foundations, vol.97 SM1, Jan., p.209-218.

Prowse T.D., unpublished. River ice processes. Chapter II in "Primer on Hydraulics of Ice-covered Rivers", K.S. Davar editor. National Hydrology Research Institute, Saskatoon, Sask.

Reese A., 1984. Riprap sizing - four methods. Proceedings of the ASCE Specialty Conference on Water Resources for Development, Coeur d'Alene, Idaho, p.397-401.

Rimsha V.A. and Donchenko R.V., 1957. The investigation of heat loss from free water surfaces in winter time. (In Russian), Truddy Leningrad, Gosud. Gidrol. Inst. 65, p.54-83.

Rose H.E., 1945a. An investigation into the laws of flow of fluids through beds of granular materials. Proceedings of the Institute of Mechanical Engineers, War Emergency Issues 1-12, p.141-147.

Rose H.E., 1945b. The isothermal flow of gases through beds of granular materials. Proceedings of the Institute of Mechanical Engineers, War Emergency Issues 1-12, p.148-153.

Rose H.E., 1945c. On the resistance coefficient-Reynolds number relationship for fluid flow through a bed of granular material. Proceedings of the Institute of Mechanical Engineers, War Emergency Issues 1-12, p.154-168.

Rose H.E., 1948. Further researches in fluid flow through beds of granular materials. Proceedings of the Institute of Mechanical Engineers, p.493-511.

Rouse H. and Ince S., 1957. History of hydraulics. Dover Books, NY, 269 pp.

Sabin G. 1991. Personal communication, Memorial University of Nfld.

Sandie R.B., 1962. A laboratory investigation of self spillway rockfill dams. Thesis, M.E.Sc., Univ. of Melbourne.

Sarkaria G.S. and Dworsky B.H., 1968. Model studies of an armoured rockfill overflow dam. Water Power, Nov., p.455-462.

Scheidegger A.E., 1974. The physics of flow through porous media. MacMillan, New York.

Schlichting H., 1955. Boundary layer theory. McGraw-Hill, NY.

Sên Z., 1989. Nonlinear flow toward wells. ASCE Journal of Hydraulic Engineering, Division, vol.115, no.2, Feb.., p.193-209.

Shand N. and Pells P.J.N., 1970. Experience in the design and construction of reinforced rockfill dams. Tenth International Congress on Large Dams, Montreal, Quebec, June 1-5, p.291-319.

Sharp B.B. and James J.P., 1963. Spatially varied flow at the toe of a rock-fill slope. Proceedings of the First Australasian Conference on Hydraulics and Fluid Mechanics, Perth, Australia.

Sherard J.L., 1959. A steel-faced rockfill dam. ASCE Civil Engineering Magazine, October, p.42-45.

Shields A., 1936. Anwendung der aehnlichkeitsmechanik und der turbulenzforschung auf die geschiebebewegung. (Application of similarity principles and turbulence research to bed load movement), Mitteilungen der Preuss Versuchsanst fur Wasserbau und Schiffbau, Berlin, no.26.

Shulits S., 1935. The Schoklitsch bed-load formula. *Engineering*, London, England, June 21, p.644-646; see also June 28, p.687.

Sissom L.E. and Pitts D.R., 1972. Elements of transport phenomena. McGraw-Hill, NY, 814 pp.

Smith K.V.H., 1986. Probabilistic approach to the stability analsis of rock protection for earth weirs. Proc. Inst. of Civil Engineers, June, p.243-253.

Solvik O., 1966. Two-dimensional turbulent flow through an isotropic rockfill. Technical University of Norway River, Harbour Research Laboratory, Bulletin 8E, p.35-49.

Somerton C.W. and Wood P., 1988. Effect of walls in modelling flow through porous media. ASCE Journal of the Hydraulics Division, vol.114, no.12, Dec., p.1431-1447.

Sparks A.D., 1967. The sloughing, overtopping, and reinforcement of rockfill and earth dams. 9th International Congress on Large Dams, Istanbul, Turkey, Sept.4-8, vol.4, pp.327-349.

Stephenson D., 1978. Hydraulics of gabions and rockfill. XVI Convegno di Idraulica e Costruzioni Idrauliche, Torino, Italy, Sept., B-31-1 to B-31-11.

Stephenson D., 1979. Rockfill in hydraulic engineering. Elsevier Scientific, Amsterdam, 215 pp.

Stevens M.A. and Simons D.B., 1971. Stability analysis for coarse granular material on slopes. Chapter 17 in "River Mechanics" vol.I, ed. and publ. by H.W. Shen, Fort Collins, Colorado.

Sunada D.K., 1964. Laminar and turbulent flow through porous media. PhD thesis, University of California at Berkeley, 74 pp.

Taylor D.M., 1948. Fundamentals of soil mechanics. John Wiley & Sons, New York.

Tsang G., 1982. Frazil and anchor ice, a monograph. Canada Centre for Inland Waters, NRC Assoc. Comm. on Hydrology, Ottawa, Ont., 89 pp.

Ulrich T., 1987. Stability of rock protection on slopes. ASCE Journal of Hydraulics, vol.113, no.7, July, p.879-891.

United States Army Corps of Engineers Hydraulic Engineering Centre, 1982. Ice engineering, an engineering manual. Publ. EM 110-2-1612.

Uzuner M.S., 1975. The composite roughness of ice covered streams. Journal of Hydraulic Research, vol.13, p.79.

Varty A., Boyle R.J., Pritchard E.D., and Gill R.E., 1985. Construction of concrete-faced rockfill dams. ASCE Convention on Concrete-Faced Rockfill Dams - Design, Construction and Performance, Edited by J.B. Cooke and J.L. Sherard, Detroit Michigan, p.435-458.

Volker R.E., 1969. Nonlinear flow in porous media by finite elements. ASCE Journal of the Hydraulics Division, vol.95, HY6, Nov., p.2093-2114.

Volker R.E., 1975. Solutions for unconfined non-Darcy seepage. ASCE Journal of the Irrigation and Drainage Division, vol.101, IR4, March, p.53-65.

Ward J.C., 1964. Turbulent flow in porous media. Journal of the Hydraulics Division, ASCE, vol.92, HY4, Sept., p.1-12.

Watters F.H. and Rao M.V.P., 1967. Stabilization of channels with gravel. M.S. thesis, Colorado State University, Fort Collins, Colorado.

Weiss A., 1951. Construction technique of passing floods over earth dams. Transactions of the ASCE, vol.116, paper 2461, p.1158-1178.

Wilkins J.K., 1956. The flow of water through rockfill and its application to the design of dams. Proc. 2nd Australia-New Zealand Conference on Soil Mechanics and Foundation Engineering.

Wilkins J.K., 1963. The stability of overtopped rockfill dams. Proc. of 4nd Australia-New Zealand Conference on Soil Mechanics and Foundation Engineering, Aug. 19-23, p.1-7.

Wright D.E., 1968. Non-linear flow through granular materials. Journal of the Hydraulics Division, vol.94, HY4, paper 6018, July, p.851-872.

Yan L. and Byrne P.M., 1990. Simulation of downhole and crosshole seismic tests on sand using the hydraulic gradient similitude method. Canadian Geotechnical Journal, vol.27, no.4, August, p.441-460.

Youngs E.G., 1990. An examination of computed steady-state water-table heights in unconfined aquifers: Dupuit-Forchiemer estimates and exact analytical results. Journal of Hydrology, vol.119, p.201-214.

Zarling J.P., 1978. Growth rates of ice. ASCE Conference on Applied Techniques for Cold Environments, Anchorage Alaska, May 17-19, p.100-111.

Appendices

Appendix No.	Contents	Page
1	**Selected Data and Test Results.**	243
2	**Derivations Pertaining to Pore Pressure Determination.**	252
	2-1 Deriving a Partial Differential Equation for non-Darcy Flow through Porous Media.	252
	2-2 Deriving a Finite Difference Equation for Pore Pressure Determination for non-Darcy Flow through Porous Media.	257
3	**Appendices Pertaining to the Wedge Method.**	260
	3-1 Development of Expression for Active Pressure Exerted by Upper Wedge.	260
	3-2 Analysis of the Factor of Safety of a Vertical Segment within the Lower Wedge.	265
	3-3 Formulae for Upper Wedge Area as a Function of the Angle ρ.	266
	3-4 How the Experimentally Applied Force Resisted the Bursting Force.	267
4	**Appendices Pertaining to the Phreatic Surface.**	269
	4-1 Derivation of the Expressions for the Modified Stephenson, Dimensional Basak, and Basak with KE Methods.	269
	4-2 Phreatic Surfaces for GF34.	278
5	**Appendices Pertaining to Unravelling Theory.**	280
	5-1 Derivation of Differential Equation for Spatially Varied Flow over a Steep Slope.	280
	5-2 Estimating Shear Stress under Spatially Varied Flow.	283
	5-3 Equations for Forces in Simplified Erosion Analysison a Particle Basis.	285
	5-4 Summary of Moments acting on a Semi-exposed Particle residing on the Downstream Face of a Flowthrough Rockfill Dam.	286
6	**Worked Example:** Analysis and Design of a Hypothetical Prototype.	288
7	**Q-Budget Heat Flux Computer Program.**	313
	7-1 Example input and output screens for program Q-Budget.	313
	7-2 Program Q-Budget for Estimating Heat Flux from a Body of Water.	314
8	**On Using a Spreadsheet for non-Darcy Pore Pressure Computations.**	316

Appendix 1
Selected Data and Test Results

Table A-1 (i)

Column Tests 1 to 21, Part I.
Summary of Physical Characteristics of Porous Media

Column Test	Number of Particles Analyzed	Nominal Sieve Size (in)	Mean b axis (mm)	Std Dev b axis (mm)	Coefficient of Variation (percent)	Mean a axis (mm)
1	200	1" clear	25.2	4.7	18.7	39.0
2	200	1" clear	25.2	4.7	18.7	39.0
3	200	1" clear	25.2	4.7	18.7	39.0
4	200	1" clear	25.2	4.7	18.7	39.0
4 B	200	1" clear	25.2	4.7	18.7	39.0
5	100	3/4" minus	16.1	4.5	28.0	22.6
6	25	1/2" sieved	19.4	3.2	16.5	33.5
7	100	3/4" sieved	24.6	3.3	13.4	36.7
8	25	1" sieved	35.9	4.6	12.8	54.3
9	* NA	mixture	26.6	3.7	13.9	41.5
10	20	0.61"	15.6	0.3	2.0	15.6
11	25	1/2" sieved	19.4	3.2	16.5	33.5
12	25	1/2" sieved	19.4	3.2	16.5	33.5
13	100	3/4" sieved	24.6	3.3	13.4	36.7
14	50	1/2" sieved	19.0	3.2	16.8	25.9
15	15	NA **	21.2	0.5	2.3	21.2
16	20	NA ***	15.7	0.03	0.2	15.7
17	200 #	1" clear	25.2	4.7	18.7	39.0
18	200 #	1" clear	25.2	4.7	18.7	39.0
19	50	1 1/2"	40.5	5.2	12.8	49.5
20	50	1 1/2"	40.5	5.2	12.8	49.5
21	200	1" clear	25.2	4.7	18.7	39.0

* some parameters inferred from material used for tests 6, 7, and 8.
** small marbles, diameter 15.7 mm
*** large marbles, diameter 21.2 mm

Table A-1 (ii)

Column Tests 1 to 21, Part II.
Summary of Physical Characteristics of Porous Media, continued

Column Test	Mean c axis (mm)	Porosity (percent)	Coeff. of Uniformity D_{60}/D_{10}	Percent of Most Common Particle Shape	Most Common Particle Shape	Density of Material (g/cm3)
1	15.0	NA	1.30	34	Disk	2.695
2	15.0	NA	1.30	34	Disk	2.695
3	15.0	46.7	1.30	34	Disk	2.695
4	15.0	47.0	1.30	34	Disk	2.695
4 B	15.0	46.6	1.30	34	Disk	2.695
5	10.9	40.1	1.60	34	Spheroid	2.653
6	11.6	48.1	1.50	32	Disk	2.695
7	15.7	47.4	1.24	39	Disk	2.695
8	23.1	46.9	1.28	36	Disk	2.695
9	16.8	45.7	1.62	36	Disk	2.695
10	15.6	40.0	*1.00	100	Sphere	2.460
11	11.6	45.1	1.50	32	Disk	2.695
12	11.6	40.0	1.50	32	Disk	2.695
13	15.7	47.2	1.24	39	Disk	2.695
14	10.3	41.8	1.34	46	Spheroid	2.653
15	21.2	41.6	1.00	100	Sphere	2.460
16	15.7	40.9	1.00	100	Sphere	2.460
17	15.0	47.9	1.30	34	Disk	2.695
18	15.0	44.5	1.30	34	Disk	2.695
19	31.0	43.5	1.29	82	Spheroid	2.734
20	31.0	38.9	1.29	82	Spheroid	2.734
21	15.0	41.6	1.30	34	Disk	2.695

* top layer of marbles slightly smaller (11% of total).

Table A-1 (iii)

Column Tests 1 to 21, Part III.
Summary of Characteristics of Porous Media, continued

Column Test	Mean Particle Shape Factor	Mean Particle Spher-icity	Surface Area per unit Rock Mass (cm^2/g)	Mass of Material (kg)	Hydraulic Mean Radius (cm)	Approxi-mate Krumbein Round-ness
1	0.49	0.64	1.151	NA	NA	0.2
2	0.49	0.64	1.151	NA	NA	0.2
3	0.49	0.64	1.151	96.21	0.283	0.2
4	0.49	0.64	1.151	95.74	0.286	0.2
4 B	0.49	0.64	1.151	96.44	0.281	0.2
5	0.57	0.70	1.843	106.57	0.137	0.8
6	0.45	0.59	1.831	93.80	0.188	0.2
7	0.52	0.66	1.424	94.92	0.235	0.2
8	0.52	0.65	1.135	95.98	0.288	0.2
9	0.50	0.63	1.463	98.08	0.213	0.2
10	1.00	1.00	1.564	98.99	0.173	1.0
11	0.45	0.59	1.831	99.14	0.167	0.2
12	0.45	0.59	1.831	108.36	0.135	0.2
13	0.52	0.66	1.424	94.27	0.236	0.2
14	0.56	0.71	1.742	103.44	0.155	0.8
15	1.00	1.00	1.077	40.46	0.252	1.0
16	1.00	1.00	1.500	39.71	0.181	1.0
17	0.49	0.64	1.317	94.07	0.259	0.2
18	0.49	0.64	1.317	100.30	0.226	0.2
19	0.69	0.80	0.752	103.46	0.374	0.9
20	0.69	0.80	0.752	111.93	0.310	0.9
21	0.49	0.64	1.317	103.45	0.205	0.2

Table A-1 (iv)

Coverage Rates C_o Determined for Calibration of Nickel Coating Technique to Determine Surface Area

Calibration Technique #1

Saw-cut limestone cubes:

number coated	20
mean rate of coverage	11.292 cm^2/g
sample standard deviation	0.878 cm^2/g
coefficient of variation	7.8 %
maximum rate of coverage	12.408 cm^2/g
minimum rate of coverage	9.104 cm^2/g

Calibration Technique #2

Aluminium shapes (four blocks and a cylinder):

number coated	5
mean rate of coverage	11.192 cm^2/g
sample standard deviation	0.549 cm^2/g
coefficient of variation	4.9 %
maximum rate of coverage	12.011 cm^2/g
minimum rate of coverage	10.502 cm^2/g

Calibration Technique #3

Specially-cut rock pieces, each having one flat surface with natural roughness:

number coated	11
mean rate of coverage	9.773 cm^2/g
sample standard deviation	0.690 cm^2/g
coefficient of variation	7.1 %
maximum rate of coverage	11.077 cm^2/g
minimum rate of coverage	8.853 cm^2/g

Table A-1 (v)

Model Dam Tests carried out in Glass-walled Flume

Width = 38.5 cm

All tests used 25 mm (3/4") sieved crushed limestone (as was used for CT7) except GF1 and GF2 in which '1" clear' was used.

Test	Date Performed	Main Purpose
GF1	June 23-24/87	Comparison of rating curve with GF2.
GF2	June 29-July 3/87	Comparison of rating curve with GF2, tailwater effects on rating curve.
GF3	August 21/87	Rating curve for full height impervious element.
GF4	August 22/87	Rating curve for half-height upstream impermeable facing.
GF5	November 20/87 December 22/87	Internal pore pressure measurements. Stage-discharge curve.
GF6	January 5/88	Videotaping of failure.
GF7	January 6/88	Effect of a shorter crest.
GF8	January 7/88	Effect of a no crest.
GF9	February 5/88	Qt versus θ, 5 free surfaces recorded.
GF10	February 11/88	Qt versus θ.
GF11	February 17/88	Qt versus θ, 3 free surfaces recorded.
GF12	February 17/88	Qt versus θ.
GF13	February 17/88	Videotape and slides. Failure too rapid.
GF14	February 23/88	Qt versus θ.
GF15	February 24/88	Qt versus θ.
GF16	March 3/88	For sizing of pump for NRC ice work.
GF17	March 10/88	Slides for NRC presentation.
GF18	July 8/88	Scale model of FF4, FF13, FF14.

Table A-1 (v) continued.

Model Dam Tests carried out in Glass-walled Flume

Width = 38.5 cm

Test	Date Performed	Main Purpose
GF19	July 11/88	Compare free surfaces with FF15.
GF20	July 20/88	Compare free surfaces with FF15.
GF21	August 5/88	1st reinforcing mesh test. Hydraulics.
GF22	August 11/88	Model of future FF tests with mesh = 90cm
GF23	August 16/88	Test of F1 measurement.
GF24	August 16-23/88	Six force measurements of F1 and F2.
GF25	August 23/88	Hydraulics plus force measurements.
GF26	August 25/88	Hydraulics to complement GF24.

Beginning of Systematic Parametric Study
(see Figure 1-1 for definitions)
Upstream face at 1V:1H for this series.
Height of all dams ≅ 49 cm
Dimensions in centimeters

GF27	August 1/89	B_d= 50, B_W=100, B_C= 0 a: no UIF, b: with UIF
GF28	Sept.12/89	B_d= 100, B_W=150, B_C= 0 a: no UIF, b: with UIF
GF29	Sept.20/89	B_d= 50, B_W=133.3, B_C= 33.3 a: with UIF, no TW; b: with UIF, with TW c: no UIF, with TW; d: no UIF, no TW
GF30	Sept.27/89	B_d= 150, B_W=200, B_C= 0 a: no UIF, b: with UIF
GF31	Oct.2/89	B_d= 100, B_W=200, B_C= 50 a: with UIF, no TW; b: with UIF, with TW c: no UIF, no TW; d: no UIF, with TW
GF32	Oct.29/89	B_d= 50, B_W=150, B_C= 50 a: no UIF, b: with UIF

Table A-1 (v) continued.

Model Dam Tests carried out in Glass-walled Flume

(Parametric Study, continued)

GF33	Oct.30/89	B_d= 100, B_w=225, B_c= 75 a: with UIF, b: no UIF
GF34	Nov.2/89	B_d= 150, B_w=266.7, B_c= 66.7 a: no UIF, no TW; b: no UIF, with TW c: with UIF, no TW; d: with UIF, with TW
GF35	Nov.6/89	B_d= 150, B_w= 300, B_c= 100 a: with UIF, b: no UIF

Table A-1 (vi)

Tests carried out in Floor Flume

Width of Channel = 138 cm.

Tests 1 to 16 used "2 inch clear" (~35 mm) crushed limestone.
Tests series 17 used 130 mm crushed limestone.

Test	Date Performed	Main Purpose
FF1	May 19/88	Test of viewing box and floor taps.
FF2	May 24-27/88	Qt versus θ.
FF3	May 31-June 3/88	Qt versus θ.
FF4	June 3-6/88	Qt versus θ.
FF5	June 8-9/88	Qt versus θ.
FF6	June 9-10/88	Qt versus θ, 1/2 height impervious element.
FF7	June 13/88	Qt versus θ, no impervious element.
FF8	June 15/88	Layer of large rock. Pump sizing for NRC.
FF9	June 27/88	Qt versus θ, compaction applied.
FF10	June 29-30/88	Qt versus θ, compaction applied
FF11	July 4/88	Qt versus θ.
FF12	July 5/88	Qt versus θ.
FF13	July 6/88	Check on FF4, Qt versus θ.
FF14	July 7/88	Qt versus θ; videotaping.
FF15	July 11-12/88	Free surface comparison with GF19, GF20.
FF16	July 28/88	Trial with strain gauges.
FF17	NA: series	Tests on 130 mm rock with pneumatic system to measure bursting forces.
FF18 & 19	series	measure bursting forces.

Table A-1 (vii)

Summary of Empirical Parameters from Column Tests

	Mean "α" for piezotaps h6-h3 & h7-h2	Mean "N" for piezotaps h6-h3 & h7-h2	
CT1	0.0085	1.89	'1" clear' uncompacted
CT2	0.0100	1.80	'1" clear' uncompacted
CT3	0.0248	1.83	'1" clear' compacted
CT4	0.0094	1.84	'1" clear' uncompacted
CT4B	0.0107	1.87	'1" clear' uncompacted
CT5	0.0314	1.79	subrounded and graded
CT6	0.0133	1.91	1/2" sieved crushed limestone
CT7	0.0088	1.88	3/4" sieved crushed limestone
CT8	0.0053	1.94	1" sieved crushed limestone
CT9	0.0117	1.87	mix of above three
CT10	0.0140	1.82	15.7 mm marbles.
CT11	0.0190	1.84	1/2" sieved crushed limestone
CT12	0.0225	1.84	1/2" sieved crushed limestone
CT13	NA	NA	3/4" sieved crushed limestone
CT14	0.0194	1.84	1/2" sieved glacial gravel
CT15	0.0100	1.81	1/3 full of 21.2 mm marbles
CT16	0.0160	1.78	1/3 full of 15.7 mm marbles
CT17a	0.0107	1.87	'1" clear', wall effect test
CT18	0.0157	1.81	'1" clear' compacted
CT19	0.0038	1.79	1 1/2" round gravel, handpicked
CT20	0.0058	1.76	1 1/2" compacted round gravel
CT21	0.0183	1.81	'1" clear' heavily compacted
mean	0.0138	1.8376	
sam.std.	0.0071	0.0479	
Co.Var.	51.5%	2.6%	

NA: unsuccessful attempt at directly measuring wall velocity.

The above experimentally determined values for α and N are associated with the following form of non-Darcy flow equation:

$$i = \alpha \cdot V^N \qquad [2\text{-}3c]$$

where:
i = hydraulic gradient (dimensionless)
V = bulk velocity (Q/A) in cm/sec.

Appendix 2.1

Deriving a Partial Differential Equation (PDE) for non-Darcy Flow through Porous Media

An abbreviated form of this derivation appears in Parkin (1963a). It is being re-presented for the following reasons:

1) It is supporting material for the method used to compute pore pressures. This derivation will use a notation which is consistent with notation found elsewhere in this document, and not solely that of Parkin (1963a).

2) It is somewhat controversial. Sharp and James (1963) commented that a Laplacian analogy should not be used to model non-Darcy flow, but did not offer a detailed explanation as to why such an analogy is deemed inappropriate. Kirkham (1968) (a doctoral student of Sharp) criticized the PDE of Curtis and Lawson (1967) as theoretically imperfect. The reply of Curtis and Lawson (1969) to the discussion of Kirkham (1968) indicated that use of average values of a and N may have the effect of causing some *under*estimation of the "true" non-Darcy pore pressures. However, since the ratio of non-Darcy to Darcy pore pressures does not usually exceed about 1.1 in a given embankment, Kirkham's *refinement* probably represents a few percent difference. This error is considerably less than the uncertainty in the non-Darcy flow parameters a and N which would be encountered in a design problem. Moreover, results from this study showed that whether non-Darcy or Darcy pore pressures are used seems to have little effect on the results of classical slope stability analyses.

3) In order to apply the resulting PDE a numerical method is needed. A finite difference form was suggested by Curtis and Lawson (1967). The published FD equation has a slight error in it. It is well to confirm that this is indeed an error, and that the error is not related to the PDE, from which the FD equation arises.

For flows which *obey* Darcy's Law, the usual procedure for developing the PDE to describe seepage is essentially to substitute Darcy's Law into the continuity equation, [A2-1a] below. For the case of a homogeneous isotropic porous medium, the resulting PDE is known as the Laplacian. The following procedure seeks to handle the case of seepage which *does not* obey Darcy's Law. The 2-D continuity equation for the case of time-invariant flow with constant fluid density can be expressed as:

$$\nabla \cdot \tilde{V} = 0$$

where the operator $\nabla = \hat{i}\,\frac{\partial}{\partial x} + \hat{j}\,\frac{\partial}{\partial y}$ and where $\hat{i}$ and $\hat{j}$ are unit vectors.

The equation $\nabla \cdot \tilde{V} = 0$ can be rewritten in cartesian form as:

$$\frac{\partial u}{\partial x} + \frac{\partial v}{\partial y} = 0 \qquad [A2\text{-}1a]$$

for

$$\tilde{V} = \hat{i}\,u + \hat{j}\,v \qquad [A2\text{-}1b]$$

In general, the speed of the flow is the magnitude of the velocity vector. Making use of a power-function form for a non-Darcy flow expression, this speed can be expressed as:

$$|\tilde{V}| = a' i^{N'} \qquad [A2\text{-}2]$$

where:
$\tilde{V}$ = *bulk* velocity vector (see Verruijt 1970),
a' = empirical coefficient in [2-3d],
N' = 1/N, an empirical exponent such that $0.5 \leq N' \leq 1$,
i = hydraulic gradient.

Here, a' and N' are constants for a given porous medium. The rate of degradation of piezometric head, "i", can be expressed as:

$$i = |\nabla \phi| = \left| \hat{i} \frac{\partial \phi}{\partial x} + \hat{j} \frac{\partial \phi}{\partial y} \right| \qquad [A2\text{-}3]$$

where ϕ is equal to the piezometric head for the case of a homogeneous isotropic porous media. For given boundary conditions, the function $\phi(x,y)$ represents the solution to a given problem and describes the potentiometric field through which flow takes place. A vector expression for $\tilde{V}$ is needed, where $\tilde{V}$ has magnitude:

$$|\tilde{V}| = a' \left| \hat{i} \frac{\partial \phi}{\partial x} + \hat{j} \frac{\partial \phi}{\partial y} \right|^{N'} \qquad [A2\text{-}4]$$

If it is assumed that the flow occurs in the direction of the greatest rate of change in ϕ (a logical and intuitive assumption), then:

$$\hat{V} = \frac{\nabla \phi}{|\nabla \phi|} \qquad [A2\text{-}5]$$

Equation [A2-5] is the vector $\tilde{V}$ divided by its magnitude. The symbol ^ denotes unit vector. The flow equation may then be written, by combining [A2-2], [A2-3], [A2-4], and [A2-5] as:

$$\tilde{V} = a' \left| \hat{i} \frac{\partial \phi}{\partial x} + \hat{j} \frac{\partial \phi}{\partial y} \right|^{N'} \hat{V} \qquad [A2\text{-}6a]$$

or:

$$\tilde{V} = a' |\nabla \phi|^{N'} \hat{V} \qquad [A2\text{-}6b]$$

Combining [A2-5] and [A2-6b] gives:

$$\tilde{V} = a' |\nabla \phi|^{N'-1} (\nabla \phi) \qquad [A2\text{-}7a]$$

The following notation applies:

$$\frac{\partial \phi}{\partial x} = \phi_x \; ; \qquad \frac{\partial \phi}{\partial y} = \phi_y \; ; \qquad \frac{\partial^2 \phi}{\partial x^2} = \phi_{xx} \; ; \qquad \frac{\partial^2 \phi}{\partial y^2} = \phi_{yy} \; ;$$

$$\left(\frac{\partial \phi}{\partial x}\right)^2 = \phi_x^2 \; ; \qquad \left(\frac{\partial \phi}{\partial y}\right)^2 = \phi_y^2 \; ; \qquad \frac{\partial^2 \phi}{\partial x \partial y} = \phi_{xy}$$

Rewriting equation [A2-7a]:

$$\tilde{V} = a' |\hat{i}\,\phi_x + \hat{j}\,\phi_y|^{N'-1}(\hat{i}\,\phi_x + \hat{j}\,\phi_y) \qquad [A2\text{-}7b]$$

Using Pythagoras' Theorem to evaluate $|\hat{i}\,\phi_x + \hat{j}\,\phi_y|$:

$$|\hat{i}\,\phi_x + \hat{j}\,\phi_y| = \sqrt{(\hat{i}\,\phi_x + \hat{j}\,\phi_y)^2} = (\phi_x^2 + \phi_y^2)^{1/2}$$

since $\hat{i}\cdot\hat{i} = 1$, $\hat{j}\cdot\hat{j} = 1$, and $\hat{i}\cdot\hat{j} = 0$.

Then:

$$\tilde{V} = a'(\phi_x^2 + \phi_y^2)^{(N'-1)/2}(\hat{i}\,\phi_x + \hat{j}\,\phi_y) \qquad [A2\text{-}8]$$

It is now possible to obtain expressions for the velocity components u and v by equating the coefficients of $\hat{i}$ and $\hat{j}$ in equation [A2-8] to the coefficients on $\hat{i}$ and $\hat{j}$ in equation [A2-1b]:

$$u = \phi_x(\phi_x^2 + \phi_y^2)^{(N'-1)/2} \qquad [A2\text{-}10a]$$

$$v = \phi_y(\phi_x^2 + \phi_y^2)^{(N'-1)/2} \qquad [A2\text{-}10b]$$

In [A2-1] we need expressions for $\frac{\partial u}{\partial x}$ (now denoted u_x) and for $\frac{\partial v}{\partial y}$ (now denoted v_y). Applying the chain rule for differentiation to [A2-10a] and [A2-10b]:

$$u_x = \phi_x\left\{\frac{N'-1}{2}\left[\phi_x^2 + \phi_y^2\right]^{\frac{(N'-3)}{2}}\frac{\partial}{\partial x}\left[\phi_x^2 + \phi_y^2\right]\right\} + \left[\phi_x^2 + \phi_y^2\right]^{\frac{(N'-1)}{2}}\phi_{xx}$$

or

$$u_x = \phi_x\left\{\frac{N'-1}{2}\left[\phi_x^2 + \phi_y^2\right]^{\frac{(N'-3)}{2}}\left[2\phi_x\phi_{xx} + 2\phi_y\phi_{yx}\right]\right\} + \phi_{xx}\left[\phi_x^2 + \phi_y^2\right]^{\frac{(N'-1)}{2}}$$

or

$$u_x = (N'-1)\left\{\left[\phi_x^2 + \phi_y^2\right]^{\frac{(N'-3)}{2}}\left[\phi_x^2\phi_{xx} + \phi_x\phi_y\phi_{yx}\right]\right\} + \phi_{xx}\left[\phi_x^2 + \phi_y^2\right]^{\frac{(N'-1)}{2}} \quad [A2\text{-}11]$$

by similar reasoning:

$$v_y = (N'-1)\left\{\left[\phi_x^2 + \phi_y^2\right]^{\frac{(N'-3)}{2}}\left[\phi_y^2\phi_{yy} + \phi_y\phi_x\phi_{xy}\right]\right\} + \phi_{yy}\left[\phi_x^2 + \phi_y^2\right]^{\frac{(N'-1)}{2}} \quad [A2\text{-}12]$$

Adding [A2-11] and [A2-12] according to [A2-1]:

$$\left[\phi_x^2 + \phi_y^2\right]^{\frac{(N'-1)}{2}}(\phi_{xx} + \phi_{yy}) +$$

$$(N'-1)\left[\phi_x^2 + \phi_y^2\right]^{\frac{(N'-3)}{2}} \cdot \left\{\phi_x^2\phi_{xx} + \phi_x\phi_y\phi_{yx} + \phi_y^2\phi_{yy} + \phi_y\phi_x\phi_{xy}\right\} = 0$$

Assuming that $\phi_x\phi_y\phi_{yx} = \phi_y\phi_x\phi_{xy}$ permits collection of two terms:

$$\left[\phi_x^2+\phi_y^2\right]^{\frac{(N'-1)}{2}}(\phi_{xx}+\phi_{yy})+(N'-1)\left[\phi_x^2+\phi_y^2\right]^{\frac{(N'-3)}{2}}\left\{\phi_x^2\phi_{xx}+2\phi_x\phi_y\phi_{xy}+\phi_y^2\phi_{yy}\right\} = 0$$

Since:

$$\left[\phi_x^2+\phi_y^2\right]^{\frac{(N'-3)}{2}}\left[\phi_x^2+\phi_y^2\right]^{2/2}(\phi_{xx}+\phi_{yy}) = \left[\phi_x^2+\phi_y^2\right]^{\frac{(N'-1)}{2}}(\phi_{xx}+\phi_{yy})$$

a common factor can be removed, and the expression becomes:

$$\left[\phi_x^2 + \phi_y^2\right]^{\frac{(N'-3)}{2}}\left[\left(\phi_x^2 + \phi_y^2\right)(\phi_{xx}+\phi_{yy}) + (N'-1)\left[\phi_x^2\phi_{xx}+2\phi_x\phi_y\phi_{xy}+\phi_y^2\phi_{yy}\right]\right] = 0$$

Clearly, either the term $\left[\phi_x^2 + \phi_y^2\right]^{\frac{(N'-3)}{2}}$ is equal to zero, or the expression following it (of which it is a coefficient), is equal to zero. The term $\left[\phi_x^2 + \phi_y^2\right]^{\frac{(N'-3)}{2}}$ can only be zero if *both* ϕ_x and ϕ_y are zero. Such a condition can only occur if no gradients exist within the potentiometric field. This case, with no flow, is not of interest.

Therefore, the final expression is:

$$\left(\phi_x^2 + \phi_y^2\right)(\phi_{xx} + \phi_{yy}) + (N'-1)\left[\phi_x^2\phi_{xx} + 2\phi_x\phi_y\phi_{xy} + \phi_y^2\phi_{yy}\right] = 0 \qquad [A2\text{-}13]$$

It can be readily seen that if N' = 1 (corresponding to flow which *follows* Darcy's Law) then:

either: $\phi_{xx} + \phi_{yy} = 0$ (ie. no flow, which is not of interest),

or:
$$\frac{\partial^2\phi}{\partial x^2} + \frac{\partial^2\phi}{\partial y^2} = 0 \qquad [A2\text{-}14]$$

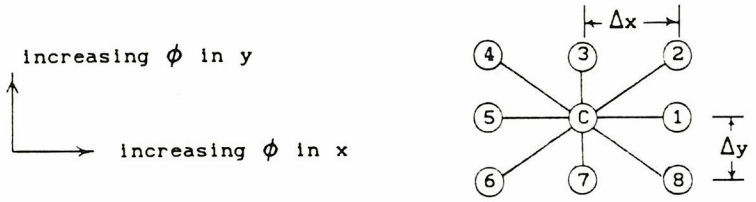
Equation [A2-14] is the familiar expression (the Laplacian) governing *laminar* flow through a porous media.

Appendix 2.2

Deriving a Finite Difference Equation for Pore Pressure Determination for non-Darcy Flow through Porous Media

The term "pore pressure" in the context of flow through porous media is often loosely applied. Strictly speaking, a given solution of the Laplace's equation (as applied to flow in porous media) under a given set of boundary conditions, provides a field of values of piezometric head, where piezometric head (sometimes called total head) is defined as the sum of elevation head and the pressure head (Holtz and Kovacs 1981, p.228). The pore *pressure*, having units of pressure, can readily be determined at any point within such a field by subtracting the elevation at any such point from the piezometric head, and converting the result to units of pressure using γ_{water}.

Only the initial set of equations and the final answer for this derivation are presented in Curtis and Lawson (1967). The 9-point finite difference star previously given in Figure 2-4 is re-presented here for ease of reference:



Denote Δx (= Δy) as S.

From inspection of equation [A2-13], it is evident that FD forms of various gradients are required. These are defined as follows:

$$\phi_x = \frac{\phi_1 - \phi_5}{2S} \qquad [A2\text{-}15a] \qquad ; \qquad \phi_y = \frac{\phi_3 - \phi_7}{2S} \qquad [A2\text{-}15b]$$

$$\phi_{xx} = \frac{\left(\frac{\phi_1 - \phi_C}{S}\right) - \left(\frac{\phi_C - \phi_5}{S}\right)}{S} = \frac{\phi_1 - 2\phi_C + \phi_5}{S^2} \qquad [A2\text{-}15c]$$

similarly:

$$\phi_{yy} = \frac{\phi_3 - 2\phi_C + \phi_7}{S^2} \qquad [A2\text{-}15d]$$

ϕ_{xy} is also required. One FD form of ϕ_{xy} is:

$$\phi_{xy} = \frac{1}{2S} \cdot \left(\frac{\phi_{y@1}}{2S} - \frac{\phi_{y@5}}{2S} \right)$$

where $\phi_{y@1}$ denotes ϕ_y at position 1, and $\phi_{y@5}$ denotes ϕ_y at position 5.

Substituting $\phi_{y@1} = \frac{\phi_2 - \phi_8}{2S}$ and $\phi_{y@5} = \frac{\phi_4 - \phi_6}{2S}$ into the previous equation:

$$\phi_{xy} = \frac{\left(\frac{\phi_2 - \phi_8}{2S}\right) - \left(\frac{\phi_4 - \phi_6}{2S}\right)}{2S} = \frac{\phi_2 - \phi_8 - \phi_4 + \phi_6}{4S^2} \qquad [A2\text{-}15e]$$

Substituting equations [A2-15a] through [A2-15e] into equation [A2-13]:

$$\left[\frac{\phi_1 - 2\phi_C + \phi_5}{S^2} + \frac{\phi_3 - 2\phi_C + \phi_7}{S^2}\right]\left[\frac{(\phi_1 - \phi_5)^2}{4S^2} + \frac{(\phi_3 - \phi_7)^2}{4S^2}\right] + \ldots$$

$$(N'-1)\left[\frac{(\phi_1 - \phi_5)^2}{4S^2} \cdot \frac{(\phi_1 - 2\phi_C + \phi_5)}{S^2} + \frac{2(\phi_1 - \phi_5)}{2S} \cdot \frac{(\phi_3 - \phi_7)}{2S} \cdot \frac{(\phi_2 - \phi_8 - \phi_4 + \phi_6)}{4S^2} + \ldots\right.$$

$$\left.\frac{(\phi_3 - \phi_7)^2}{4S^2} \cdot \frac{(\phi_3 - 2\phi_C + \phi_7)}{S^2}\right] = 0$$

Multiplying both sides by $4S^4$ and collecting some ϕ_C terms:

$$(\phi_1 + \phi_5 + \phi_3 + \phi_7 - 4\phi_C)\left[(\phi_1 - \phi_5)^2 + (\phi_3 - \phi_7)^2\right] + \ldots$$

$$(N'-1)\left[(\phi_1 - \phi_5)^2(\phi_1 + \phi_5 - 2\phi_C) + 2(\phi_1 - \phi_5)(\phi_3 - \phi_7)(\phi_2 - \phi_8 - \phi_4 + \phi_6) + \ldots\right.$$

$$\left.(\phi_3 - \phi_7)^2(\phi_3 + \phi_7 - 2\phi_C)\right] = 0$$

Denoting the term $\left[(\phi_1 - \phi_5)^2 + (\phi_3 - \phi_7)^2\right]$ as Ω, and rearranging:

$$(\phi_1 + \phi_5 + \phi_3 + \phi_7)\Omega + \ldots$$

$$(N'-1)\cdot\left[(\phi_1 - \phi_5)^2(\phi_1 + \phi_5 - 2\phi_C) + 2(\phi_1 - \phi_5)(\phi_3 - \phi_7)(\phi_2 - \phi_8 - \phi_4 + \phi_6) + \ldots\right.$$

$$\left.(\phi_3 - \phi_7)^2(\phi_3 + \phi_7 - 2\phi_C)\right] = 4\phi_C\Omega$$

OR:

$$(\phi_1 + \phi_5 + \phi_3 + \phi_7)\Omega + (N'-1)\cdot\left[(\phi_1 - \phi_5)^2(\phi_1 + \phi_5) - 2\phi_C(\phi_1 - \phi_5)^2\right.$$

$$\left. + 2(\phi_1 - \phi_5)(\phi_3 - \phi_7)(\phi_2 - \phi_8 - \phi_4 + \phi_6) + (\phi_3 - \phi_7)^2(\phi_3 + \phi_7) - 2\phi_C(\phi_3 - \phi_7)^2\right] = 4\phi_C\Omega$$

using the definition of Ω:

$$(\phi_1 + \phi_5 + \phi_3 + \phi_7)\Omega + (N'-1)\cdot\Big[(\phi_1 - \phi_5)^2(\phi_1 + \phi_5)$$

$$+ 2(\phi_1-\phi_5)(\phi_3-\phi_7)(\phi_2-\phi_8-\phi_4+\phi_6)+(\phi_3-\phi_7)^2(\phi_3+\phi_7) - 2\phi_C\Omega\Big] = 4\phi_C\Omega$$

OR:

$$(\phi_1 + \phi_5 + \phi_3 + \phi_7)\Omega + (N'-1)\cdot\Big[(\phi_1 - \phi_5)^2 (\phi_1 + \phi_5)$$

$$+ 2(\phi_1-\phi_5)(\phi_3-\phi_7)(\phi_2-\phi_8-\phi_4+\phi_6)+(\phi_3-\phi_7)^2(\phi_3+ \phi_7)\Big] = 4\phi_C\Omega+ 2\phi_C\Omega(N'-1)$$

The RHS is: $= \phi_C 2\Omega(N'+1)$

Thus, the final result is:

$$\frac{1}{2(N'+1)}(\phi_1 + \phi_3 + \phi_5 + \phi_7) + \frac{(N'-1)}{2(N'+1)\Omega}\cdot\Big[(\phi_1 - \phi_5)^2 (\phi_1 + \phi_5)$$

$$+ 2(\phi_1-\phi_5)(\phi_3-\phi_7)(\phi_2+\phi_6-\phi_4-\phi_8)+(\phi_3-\phi_7)^{2\,*}(\phi_3+ \phi_7)\Big] = \phi_C \qquad [A2\text{-}16]$$

(* correct; * published)

where: $\Omega = \Big[(\phi_1-\phi_5)^2 + (\phi_3-\phi_7)^2\Big]$

As required, if N'=1 (flow according to Darcy's Law) equation [A2-16] reduces to the standard FD expression for laminar flow through a homogeneous isotropic porous media:

$$\phi_C = \frac{1}{4}(\phi_1 + \phi_3 + \phi_5 + \phi_7) \qquad [A2\text{-}17]$$

* Equation [A2-16] is presented as equation "17h" in Curtis and Lawson (1967, pg.13), except that an exponent has been misplaced in Curtis and Lawson. The arrows indicate the correct and published locations of the exponent 2.

Appendix 3-1

Development of Expression for Active Pressure Exerted by Upper Wedge

This derivation is adapted from the development of Coulomb's expression for the active earth pressure against a retaining wall. As much as possible the notation follows that of Bowles (1968):

Nomenclature for Figures A-3 (i) through (iii):

W_o = buoyant weight of upper wedge,

F_Q = seepage force on upper wedge,

P_a, P': active pressure resultant on fictitious wall, and the component of P_a normal to the wall, respectively,

N, R: normal and resultant forces acting on the rupture plane,

F_S, F_W: frictional forces along the two boundaries of the upper (active) wedge,

ρ = angle of rupture plane (most important unknown angle),

ϕ = angle of internal friction of the rockfill.

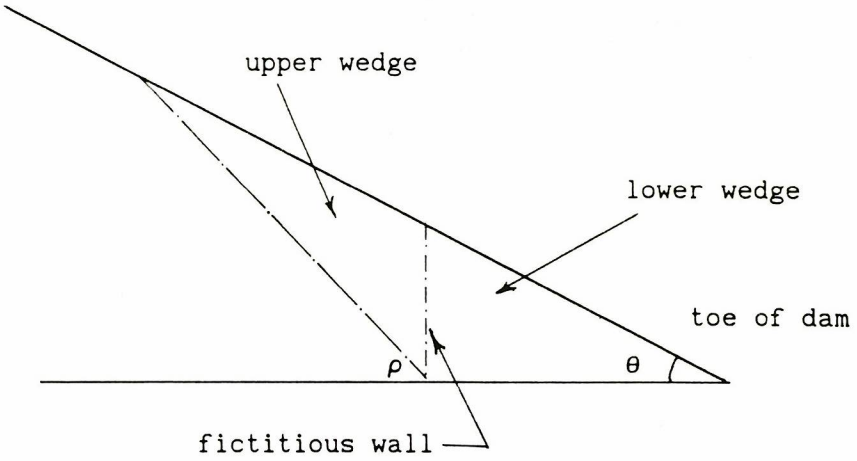


Figure A-3 (i) Basic definitions for wedge method.

F_B is the vector sum of F_Q and W_o.

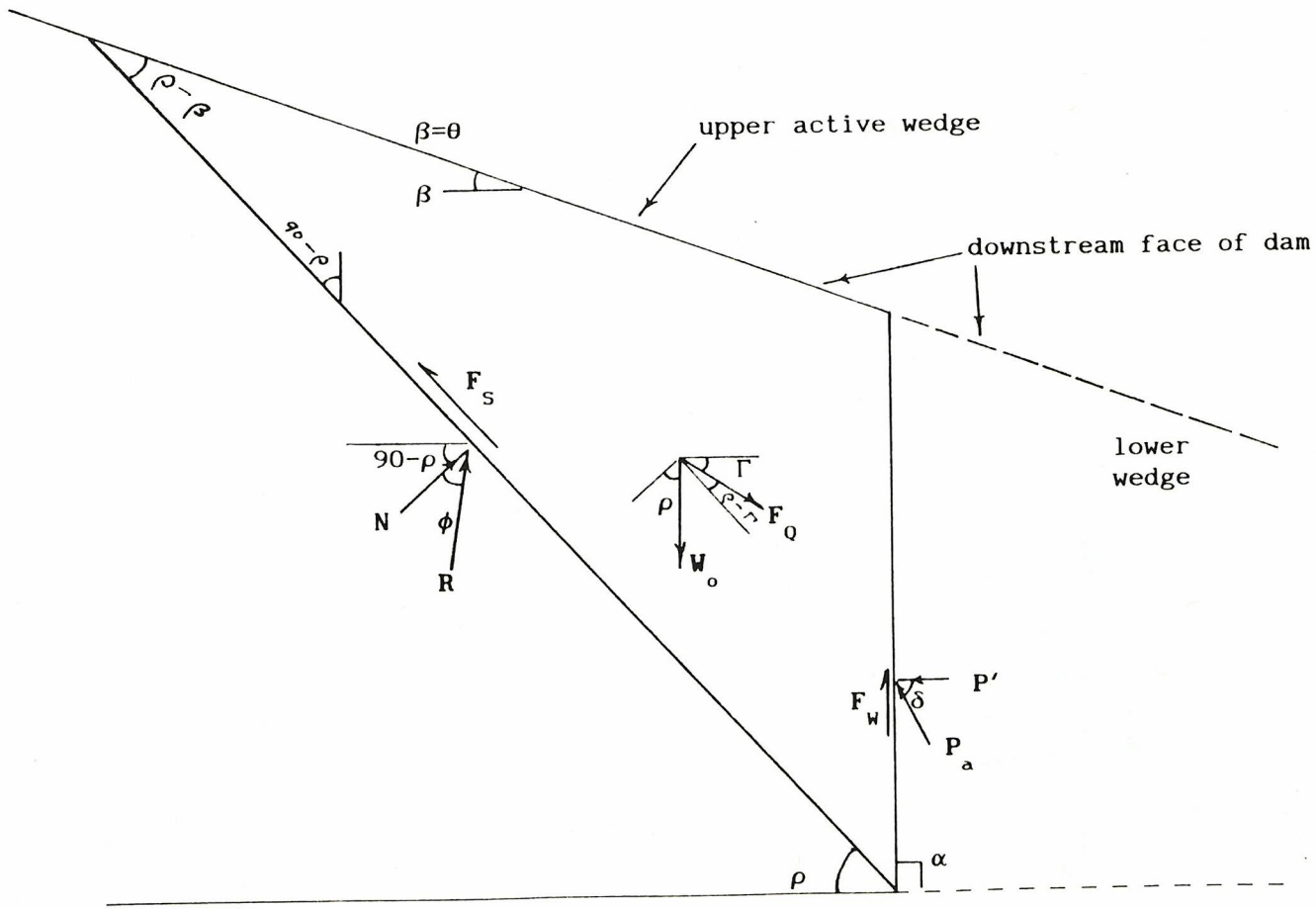


Figure A-3(ii). Defining diagram for wedge method of slope stability analysis.

Lengths of vectors not to scale.

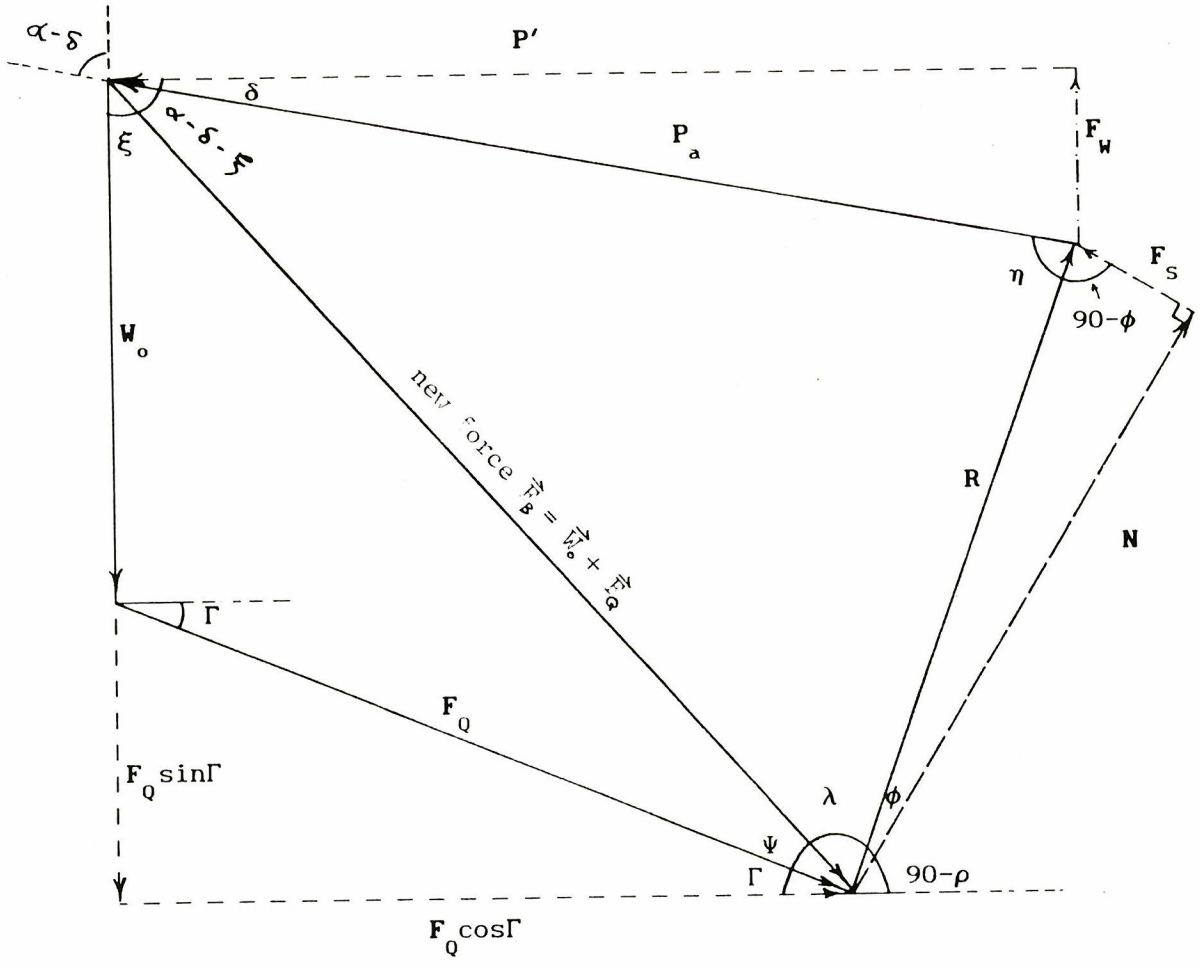


Figure A-3(iii). Vector diagram for upper active wedge.

Consider a triangle of forces made up of W_o, F_Q, and F_B, as shown in Figure A-3(ii). F_B is the vector sum of F_Q and W_o. The angle ξ is:

$$\xi = \arctan\left[\frac{F_Q \cos\Gamma}{W_o + F_Q\cos\Gamma}\right]$$

Γ is determined from seepage force analysis, which is made possible by pore pressure modelling and subsequent study of the gradient causing F_Q for a given assumed angle ρ.

Ψ is required:

$$\xi + 90 + \Gamma + \Psi = 180$$

$$\xi + \Gamma + \Psi = 90$$

$$\Psi = 90 - \xi - \Gamma$$

λ is also required:

$$\Gamma + \Psi + \lambda + \phi + 90 - \rho = 180$$

$$\Gamma + \Psi + \lambda + \phi - \rho = 90$$

$$\lambda = 90 + \rho - \Gamma - \Psi - \phi$$

but

$$\Psi = 90 - \xi - \Gamma$$

so

$$\lambda = 90 + \rho - \Gamma - (90 - \xi - \Gamma) - \phi$$

$$\lambda = \rho - \Gamma + \xi + \Gamma - \phi$$

$$\lambda = \rho + \xi - \phi$$

η is required:

$$\alpha - \delta - \xi + \lambda + \eta = 180$$

$$\alpha - \delta + \rho - \phi + \eta = 180$$

$$\eta = 180 + \delta + \phi - \rho - \alpha$$

Now the expression for P_a can be found by applying the Law of Sines:

$$\frac{P_a}{\sin\lambda} = \frac{F_B}{\sin\eta}$$

$$P_a = \frac{\sin(\rho + \xi - \phi)}{\sin(180 + \delta + \phi - \rho - \alpha)} F_B$$

where:

$$|F_B| = \left[(W_o + F_Q\sin\Gamma)^2 + (F_Q\cos\Gamma)^2\right]$$

$|F_B|$ is the magnitude of the vector sum of F_Q and W_o

Note that when $F_Q = 0$, $\xi = 0$, and $F_B = W_o$, the expression for P_a becomes identical with that given by Bowles (1968, p.325).

Also note that for $\alpha = 90^\circ$ and $\delta = \phi$, as will always be the case herein, P_a reduces to:

$$P_a = \frac{\sin(\rho + \xi - \phi)}{\sin(2\phi - \rho)} F_B$$

The basis for determining the position of the vertical fictitious retaining wall which separates the upper and lower wedges is given in Appendix 3-2. Formulae to assist in the determination of W_o are given in Appendix 3-3.

Appendix 3-2

Analysis of the Factor of Safety of a Vertical Segment within the Lower Wedge, for the Wedge Method

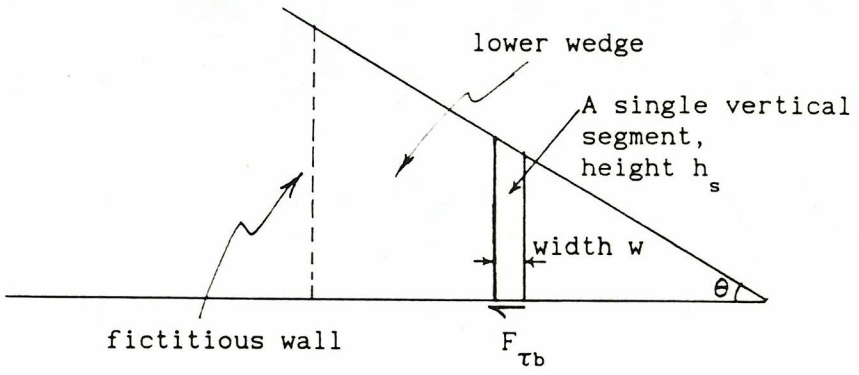


Figure A-3(iv)

A. Mobilized horizontal shear force $F_{\tau b}$ at the base of a vertical segment of width w (per unit length L of dam).

$$F_{\tau b} = (\gamma' \; h_s \; w + F_{sv}) \cdot \tan\phi'_b$$

h_s: local height of this segment (completely saturated in this case).

w: width of segment.

F_{sv}: vertical component of the seepage force within the segment.

γ': buoyant unit weight of saturated media.

$\tan\phi'_b$: angle of friction at the *interface* of rock and floor of flume.

B. Seepage forces. Note that $V = w \cdot L \cdot h_s$

using $(F/V) = \gamma_w i$, or $\quad \frac{F}{L} = \gamma_w i \; h_s w$

• vertical seepage force for w = 1 (total for the vertical segment):

$$\frac{F}{L} = F_{sv} = \gamma_w h_s \cdot \sum_{h=1}^{h_s} iv_h \qquad \text{where:} \quad iv_h = \frac{(h_3 - h_7)}{2\Delta y} \quad \text{(see Figure 2-4)}$$

where: F_{sv} = total vertical seepage force for the vertical segment.

iv_h = vertical component of the hydraulic gradient at height h.

For example, iv_6 in the following diagram ($h_s = 8 \cdot \Delta y$) is equal to 0.25:

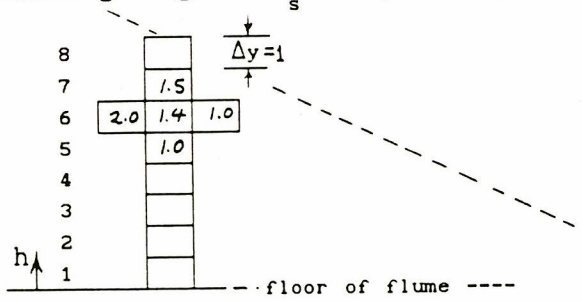


Figure A-3(v)

- similarly, the horizontal seepage force for w = 1 (total for the vertical segment) is:

$$\frac{F}{L} = F_{SH} = \gamma_w h_s \cdot \sum_{h=1}^{h_s} ih_h \qquad \text{where:} \quad ih_h = \frac{(h_5 - h_1)}{2\Delta x} \quad \text{(see Figure 2-4)}$$

where: F_{SH} = total horizontal seepage force for the vertical segment.

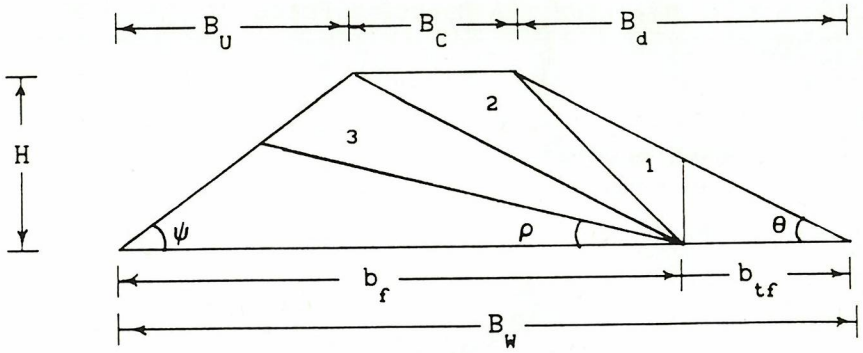
ih_h = horizontal component of the hydraulic gradient at height h.
For $\Delta x = 1$, $ih_6 = 0.5$ in previous example.

Therefore, the local factor of safety at the base of the vertical segment is:

$$FOS = \frac{F_{\tau b}}{F_{SH}} \qquad \text{see Figure 5-20(b)}$$

The foregoing has assumed that the entire vertical segment is saturated and that flow is moving through it.

Formulae for Upper Wedge Area as a Function of the Angle ρ



An area subtended by ρ within zone n is denoted A_n

Zone 1 $A_1 = \frac{L}{2} b_{tf} \cdot \tan\theta \cdot \cos\rho$ $\qquad A_{1MAX} = \frac{1}{2} b_{tf} \tan\theta \cdot (B_d - b_{tf})$

where $L = b_{tf} \cdot \frac{\sin\theta}{\sin(\rho-\theta)}$

A_1 valid for: $\arctan\left[\frac{H}{b_f - B_u - B_c}\right] \le \rho \le 90^\circ$

Zone 2 (formula below include contribution from zone 1)

$$A_{2+1} = A_1 - \frac{(L\sin\rho - H)^2}{2} \cdot \left[\frac{1}{\tan\theta} - \frac{1}{\tan\rho}\right]$$ L as before

OR $$A_{2+1} = A_{1MAX} + \frac{H}{2}\left[B_u + B_c - b_f + \frac{H}{\tan\theta}\right]$$

A_{2+1} valid for: $\theta < \rho \le \arctan\left[\frac{H}{b_f - B_u - B_c}\right]$

NOTE: If $b_{tf} < B_c$, ρ plane intersects crest for $\rho < \theta$.

For this condition the bounds are: $\arctan\left[\frac{H}{b_f - B_u}\right] \le \rho \le \theta$

The area is then: $A_{2+1} = b_{tf}H + \frac{H}{2}\left[\frac{H}{\tan\rho} - B_d\right] - \frac{1}{2} b_{tf}^2 \tan\theta$

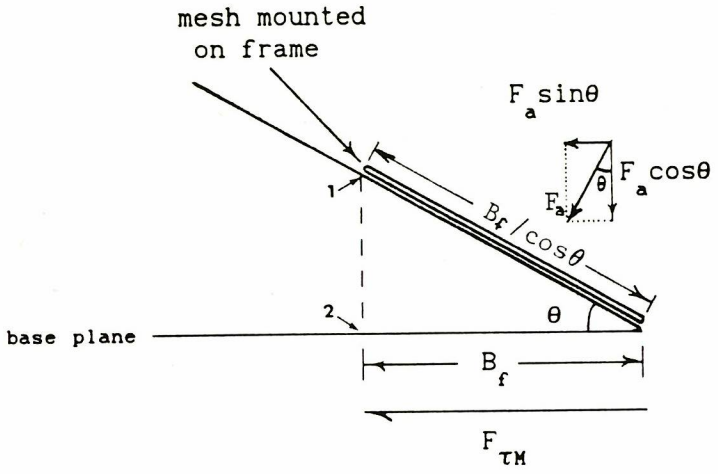
Zone 3 (formula below include contributions from zones 1 and 2)

$$A_{3+2+1} = A_{dam} - \frac{1}{2} b_f^2 \left[\frac{\tan\rho \sin\psi}{\cos\psi\tan\rho + \sin\psi}\right] - \frac{1}{2} b_{tf}^2 \cdot \tan\theta$$

where $A_{dam} = \frac{H}{2}\left[B_c + B_W\right]$

A_{3+2+1} valid for: $\rho \le \arctan\left[\frac{H}{b_f - B_u}\right]$

How the Experimentally Applied Force Resisted the Bursting Force



B_f = width of frame, as projected onto base of dam.

L_f = length of frame (along L), slightly less than width of flume.

F_a = externally applied force.

σ_{ab} = component of applied stress acting along $L_f B_f$:

$$\sigma_{ab} = \frac{F_a \cos\theta}{L_f B_f}$$

$F_{\tau M}$ = mobilized frictional shear acting on $L_f B_f$:

$$F_{\tau M} = \sigma_{ab} (L_f B_f) \tan\phi'_b$$

where $\tan\phi'_b$ is the angle of friction between the base plane material and the porous media.

Therefore: $$F_{\tau M} = F_a \cdot \cos\theta \cdot \tan\phi'_b$$

The total horizontal force resisting P′ is therefore:

$$F_{ah} = F_a \cdot \sin\theta + F_a \cdot \cos\theta \cdot \tan\phi'_b$$

where F_{ah} = total horizontal force due to F_a acting normal to a restraining frame of dimensions $L_f B_f/\cos\theta$ inclined at an angle θ.

Consideration of friction mobilized at the sides of the flume due to the application of F_a will include the following assumptions: (1) no lateral strain at the side of the flume, and (2) no strain in an upstream direction, since the self-weight of the model dams was more than 50 times the applied force. As an approximation, the coefficient of earth pressure at rest, K_o, was used in the estimation of side-wall pressures.

A right-angled force wedge can be constructed using the following known points (see figure on preceding page):

Point 1:	$K_o \sigma_v$
Point 2:	$K_o(\sigma_v + \gamma' B_f \tan\theta)$
Toe of the dam:	$K_o \sigma_v$

Overall average side-wall stress: $K_o B_f \tan\theta\gamma' + K_o \sigma_v$

Assume $K_o = (1 - \sin\phi)$

The total mobilized friction at the two side-walls (due to F_a) is:

$$F_{side} = (\tan\phi_{side}) \cdot 2 \cdot \text{Area} \cdot \left[K_o B_f \tan\theta\gamma' + K_o \sigma_v\right]$$

where each side area is $(0.5\ B_f)B_f \tan\theta$.

The final expression is therefore:

$$F_{side} = B_f^2 \cdot \tan\theta \cdot \tan\phi_{side} \left[K_o B_f \tan\theta\gamma' + K_o \sigma_v\right]$$

The following table shows the values used for key parameters:

Table A-3-2 (i)

Parameters used in side-wall friction calculations

	K_o	ϕ_{side}	ϕ_{base}
Floor flume	0.23	23.3°	23.3°
Glass flume	0.30	15.6°	23.3°

Derivation of the Expressions for the Modified Stephenson, Dimensional Basak, and Basak with KE Methods

A. *Modified Stephenson Equation (see Stephenson 1979).*

The following for will be used to describe non-Darcy flow:

$$V_v = K\sqrt{gedi} \qquad [A4\text{-}1]$$

V_v = void velocity (V/n),
K = empirical coefficient, about 0.75 for crushed rock,
g = gravity,
e = void ratio,
d = representative particle diameter,
i = hydraulic gradient.

The above equation can be re-expressed as:

$$i = \frac{V_v^2}{K^2 ged} \quad \text{OR} \quad i = \frac{V^2}{K^2 gedn^2} \qquad [A4\text{-}2]$$

V = q/y for a rectangular channel, so:

$$i = \frac{q^2}{K^2 gedn^2 y^2} \qquad [A4\text{-}3]$$

In general, the specific energy of an open channel flow is defined as:

$$E = y + \frac{V^2}{2g}$$

Since in the case of a porous media V_v is more representative of the velocity of the fluid itself, the specific energy for flow through a porous media is defined as:

$$E = y + \frac{V_v^2}{2g} \qquad [A4\text{-}4]$$

Since $V_v = V/n$ and $V = q/y$ for a rectangular channel, then

$$V_v = \frac{q^2}{n^2 y^2}$$

Then the specific energy can be written:

$$E = y + \frac{q^2}{2gn^2 y^2} \qquad [A4\text{-}5]$$

If the bed slope is zero or nearly zero it can also be stated that:

$$\frac{dE}{dx} = -i \qquad [A4\text{-}6]$$

[A4-6] is exactly true for one-dimensional flow. For two-dimensional flow it is an additional assumption analogous to the Dupuit assumption that dh/dx = i. It is of interest to note that for gradually-varied open channel flow in a prismatic channel, the governing equation is often written:

$$\frac{dE}{dx} = S_o - S_f$$

If S_o is zero (as is the usual assumption when computing the phreatic line in an embankment) then $dE/dx = -S_f$. Stephenson assumes that S_f is equal to the hydraulic gradient i. This is a further approximation away from the truth for two-dimensional flow in a porous media, since the velocity head term $V^2/2g$ will further steepen the computed slope (slightly) above the value of dh/dx (for a two-dimensional flow), where dh/dx is associated with the ordinary Dupuit assumption.

If the bed slope at the foundation of the embankment cannot be neglected, a numerical integration technique, such as the standard step or direct step method, may be invoked in order to compute the position of the phreatic line.

Differentiating equation [A4-5]:

$$\frac{dE}{dx} = \frac{dy}{dx} - \frac{q^2}{2gn^2y^3}.\frac{dy}{dx} \qquad [A4\text{-}7]$$

Substituting equations [A4-3] and [A4-6] into [A4-7] gives:

$$-\frac{q^2}{K^2gedn^2} \cdot \frac{1}{y^2} = \frac{dy}{dx} - \frac{q^2}{2gn^2y^3}.\frac{dy}{dx}$$

So:

$$\frac{q^2}{K^2gedn^2}.\frac{1}{y^2} = \left[\frac{q^2}{gn^2y^3} - 1\right].\frac{dy}{dx}$$

Then: $$1 = K^2ed\cdot\left[\frac{1}{y} - \frac{gn^2}{q^2}y^2\right]\cdot\frac{dy}{dx} \qquad [A4\text{-}8]$$

However, since in general $y_c^3 = \frac{q^2}{gn^2}$ for flow through a porous media in a rectangular cross-section:

$$1 = K^2ed\cdot\left[\frac{1}{y} - \frac{1}{y_c^3}y^2\right]\cdot\frac{dy}{dx}$$

Separating variables:

$$dx = K^2ed\cdot\left[\frac{1}{y} - \frac{1}{y_c^3}y^2\right]\cdot dy$$

Integrating:

$$x = K^2ed\cdot\int\left[\frac{1}{y} - \frac{1}{y_c^3}y^2\right]\cdot dy = K^2ed\cdot\left[\ln y - \frac{1}{3}\left(\frac{y}{y_c}\right)^3 + C\right] \qquad [A4\text{-}9]$$

Using the assumption that $y = y_c$ at $x = b_e$ (see Figure 1) to evaluate the constant of integration C:

$$b_e = K^2ed\cdot\left[\ln y - \frac{1}{3} + C\right] \quad \text{then} \quad C = \frac{b_e}{K^2ed} + \frac{1}{3} - \ln y_c \quad \text{substituting:}$$

$$x = K^2ed\cdot\left[\ln y - \frac{1}{3}\left(\frac{y}{y_c}\right)^3 + \frac{b_e}{K^2ed} + \frac{1}{3} - \ln y_c\right]$$

The final result is then:

$$\frac{3}{K^2ed}\cdot(b_e - x) = \left(\frac{y}{y_c}\right)^3 - 1 - 3\ln\left(\frac{y}{y_c}\right) \qquad [A4\text{-}10a]$$

The coefficient $\frac{3}{K^2ed}$ is different than Stephenson's because equation [A4-1] was the starting point, not Stephenson's suggested non-Darcy flow relationship. Also, the coefficient 3 on the term $\ln(y/y_c)$ in equation [A4-10] does not appear in Stephenson (1979), but is mathematically required. For these two reasons, equation [A4-10] is referred to as the Modified Stephenson equation for the phreatic line.

It will be more convenient to avoid use of b_e. It is unknown, but could be assumed. For an assumed b_e the calculations (which proceed in an upstream direction since the flow is subcritical) stop when the upstream

face of the dam is encountered. Alternatively, the use of b_e could be avoided entirely if the vertical where y_c occurs is used as the starting point of the calculations. The vertical at y_c was observed to be associated with a distance greater than b_e in general (as discussed in Section 4.2.2). Without b_e equation [A4-*10*] becomes:

$$-\frac{3}{K^2 ed}\cdot x = \left(\frac{y}{y_c}\right)^3 - 1 - 3\ln\left(\frac{y}{y_c}\right) \qquad \text{[A4-10b]}$$

The above formula yields increasingly negative values of x. This is because $\frac{dE}{dx}$ was made equal to negative i. The upcoming derivation of Basak's formula (1976) will not define i as negative. The formula arising from Stephenson's (1979) approach is therefore be stated as:

$$\frac{3}{K^2 ed}\cdot x = \left(\frac{y}{y_c}\right)^3 - 3\ln\left(\frac{y}{y_c}\right) - 1 \qquad \text{[4-21]}$$

in which case the resulting x is positive but indicates the distance *upstream* of the vertical through y_c.

2. *Dimensional Version of Basak's (1976) Equation for the Phreatic Line.*

The so-called Forcheimer form of the non-Darcy flow expression is:

$$i = \alpha V + tV^2$$

i = hydraulic gradient

α, t = empirical parameters

V = bulk velocity (Q/A)

Under the Dupuit assumption (described on pg.40 of Harr 1962), and for a rectangular channel, this can be restated as:

$$\frac{dh}{dx} = \alpha\left(\frac{q}{h}\right) + t\left(\frac{q}{h}\right)^2$$

or:

$$\frac{dh}{dx} = \frac{\alpha q h^2 + tqh}{h^3}$$

separating of variables for integration:

$$dx = \frac{h^3}{\Delta q h^2 + t q h} \cdot dh$$

$$x = \frac{1}{\Delta q} \int \left(\frac{h^3}{h^2 + \left(\frac{tq}{\Delta}\right) h} \right) dh$$

$$x = \frac{1}{\Delta q} \int \left(h - \frac{tq}{\Delta} + \frac{\left(\frac{tq}{\Delta}\right)^2}{h^2 + \left(\frac{tq}{\Delta}\right) h} \right) dh$$

Integrating:

$$x = \frac{1}{\Delta q} \left[\frac{h^2}{2} - \left(\frac{tq}{\Delta}\right) h + \left(\frac{tq}{\Delta}\right)^2 \ln\left(h + \frac{tq}{\Delta}\right) + C \right]$$

where C is the constant of integration. Assume that at $x = 0$, $h = h_e$.

Therefore:

$$0 = \frac{h_e^2}{2} - \left(\frac{tq}{\Delta}\right) h_e + \left(\frac{tq}{\Delta}\right)^2 \ln\left(h_e + \frac{tq}{\Delta}\right) + C$$

Substituting the resulting value of C into the previous result of integration gives:

$$x = \frac{1}{\Delta q} \left[\frac{h^2}{2} - \frac{h_e^2}{2} - \left(\frac{tq}{\Delta}\right) h + \left(\frac{tq}{\Delta}\right) h_e + \left(\frac{tq}{\Delta}\right)^2 \ln\left(h + \frac{tq}{\Delta}\right) - \left(\frac{tq}{\Delta}\right)^2 \ln\left(h_e + \frac{tq}{\Delta}\right) \right]$$

which can be readily simplified to:

$$x = \frac{t}{\Delta^2} \cdot (h_e - h) + \frac{1}{2q\Delta} \left(h^2 - h_e^2\right) + \frac{t^2 q}{\Delta^3} \ln\left(\frac{\Delta h + tq}{\Delta h_e + tq} \right) \qquad [4\text{-}23]$$

x = distance upstream of h_e (a positive number)

q = unit width discharge

h = local piezometric head (height of phreatic line)

h_e = exit height on downstream face of rectangular embankment.

See Basak (1976) for dimension*less* form of [4-23].

3. *Modification to Basak's (1976) Equation for the Phreatic Line so that Kinetic Energy is included.*

The specific energy of a flow through a porous media can be represented:

$$E = h + \frac{V_v^2}{2g}$$

Knowing that $V_v = q/(nh)$ and differentiating E with respect to x gives:

$$\frac{dE}{dx} = \frac{dh}{dx} - \frac{q^2}{2gn^2h^3}\cdot\frac{dh}{dx} \qquad [A4\text{-}12]$$

$$\text{Take} \quad \frac{dE}{dx} = i = \alpha V + tV^2 \qquad [A4\text{-}13]$$

[A4-13] is not strictly true because in it dE/dx should be equated to a non-Darcy flow law associated with *void* velocity not *bulk* velocity, as was done by Stephenson in the power-law case. The coefficients s and t in [2-4c], and not α and t in [2-4a], should be used. However, since a comparison of equations [2-4a] and [2-4c] yields the relationships $s = \alpha n$ and $t = tn^2$, it will be possible to adjust the upcoming final result accordingly, even if [A4-13] is used as stated above.
Equating [A4-12] and [A4-13] gives:

$$\alpha V + tV^2 = \frac{dh}{dx}\left[1 - \frac{q^2}{2gn^2h^3}\right]$$

and

$$\alpha\left(\frac{q}{h}\right) + t\left(\frac{q^2}{h^2}\right) = \frac{dh}{dx}\left[1 - \frac{q^2}{2gn^2h^3}\right]$$

so

$$\frac{dh}{dx} = \frac{\left(\alpha q\cdot\frac{1}{h} + tq^2\cdot\frac{1}{h^2}\right)}{\left(1 - \frac{q^2}{gn^2}\cdot\frac{1}{h^3}\right)}$$

Call $k_1 = \alpha q$, $k_2 = \beta q^2$, and $k_3 = \frac{\alpha^2}{gn^2}$, then:

so
$$\frac{dh}{dx} = \frac{\left(\frac{k_1}{h} + \frac{k_2}{h^2} \right)}{\left(1 - \frac{k_3}{h^3} \right)}$$

Separating variables to permit integration:

$$dx = \left(\frac{h^3 - k_3}{k_1 h^2 + k_2 h} \right) dh$$

$$x = \int \left(\frac{h^2}{h + (k_2/k_1)} \right) dh - \frac{k_3}{k_1} \cdot \int \left(\frac{1}{h^2 + (k_2/k_1)h} \right) dh$$

Integrating;

$$x = \frac{1}{k_1} \left[\frac{h^2}{2} - \frac{k_2}{k_1} + \frac{k_2^2}{k_1^2} \ln \left(h + \frac{k_2}{k_1} \right) \right] - \frac{k_3}{k_1} \cdot \left[\frac{k_1^2}{k_2^2} \cdot \ln \left(\frac{h}{h + (k_2/k_1)} \right) \right] + C$$

Evaluate C by assuming that at $x = 0$, $h = h_e$, therefore:

$$C = \frac{k_3}{k_2} \cdot \ln \left(\frac{h_e}{h_e + (k_2/k_1)} \right) - \frac{h_e^2}{2k_1} + \frac{k_2}{k_1^2} \cdot h_e - \frac{k_2^2}{k_1^3} \cdot \ln \left(h_e + \frac{k_2}{k_1} \right)$$

Combining the expression for C with the result of the integration gives:

$$x = \frac{k_2}{k_1^2} \cdot \left(h_e - h \right) + \frac{1}{2k_1} \cdot \left(h^2 - h_e^2 \right) + \cdots$$

$$+ \frac{k_2^2}{k_1^3} \cdot \ln \left(\frac{k_1 h + k_2}{k_1 h_e + k_2} \right) + \frac{k_3}{k_2} \cdot \ln \left(\frac{h_e}{h_e + (k_2/k_1)} \cdot \frac{h + (k_2/k_1)}{h} \right)$$

But $k_1 = \alpha q$, $k_2 = tq^2$, and $k_3 = \dfrac{q^2}{gn^2}$; making these substitutions:

$$x = \frac{t}{\alpha^2}\cdot\left(h_e - h\right) + \frac{1}{2\alpha q}\cdot\left(h^2 - h_e^2\right) + \frac{t^2 q}{\alpha^3}\ \ln\left(\frac{\alpha h + tq}{\alpha h_e + tq}\right) +$$

$$\frac{1}{gn^2 t}\cdot\ln\left[\left(\frac{h_e}{h}\right)\cdot\frac{\alpha h + tq}{\alpha h_e + tq}\right] \qquad \text{[A4-14]}$$

Making the final substitutions that $\alpha = s/n$ and $t = t/n^2$ gives:

$$x = \frac{t}{s^2}\cdot\left(h_e - h\right) + \frac{n}{2sq}\cdot\left(h^2 - h_e^2\right) + \frac{t^2 q}{s^3 n}\ \ln\left(\frac{snh + tq}{snh_e + tq}\right) +$$

$$\frac{1}{tg}\cdot\ln\left[\left(\frac{h_e}{h}\right)\cdot\frac{snh + tq}{snh_e + tq}\right] \qquad \text{[4-24]}$$

where n is porosity and s and t were previously defined in [2-4a]:

$$i = sV_v + tV_v^2 \qquad \text{[2-4a]}$$

It was observed that for embankments having a sloping downstream face, the phreatic line was accurately predicted (except at high discharge) if the starting point for the calculations was taken as the critical depth for a porous media (see Section 4.2.2), as suggested by Stephenson (1979). On this basis h_e may be replaced by y_c, where y_c for a porous media flow in a rectangular ssection is defined by:

$$y_c^3 = \frac{q^2}{gn^2}$$

It is further noted that:

1) [A4-15] includes the effect of the velocity head, and has one more term than [A4-11] (which was derived using $i = \alpha V + tV^2$) and in which the velocity head was not considered.

2) The computed value of x is the distance upstream of *theoretical* critical depth for a porous media, y_c. This was found to give better predictions than using the *observed* h_e. The reason for this was discussed in Section 4.2.2 (see also Youngs 1990, p.202). However, the point where y_c intersects the downstream face will generally not be part of the phreatic surface at all. The useful portion of the predicted phreatic surface begins where the computed surface intersects the downstream face. The location of this predicted h_e was found to be increasingly inaccurate as the upstream water level approached H.

3) As *s* becomes large compared to *t* this implies a lower level of turbulence. As *t* becomes large relative to *s*, this implies a higher level of turbulence in the voids. The method of Stephenson (1979), on the other hand, is only intended for cases of fully-developed turbulence.

Observed and Computed Phreatic Surfaces for Flume Test GF34a

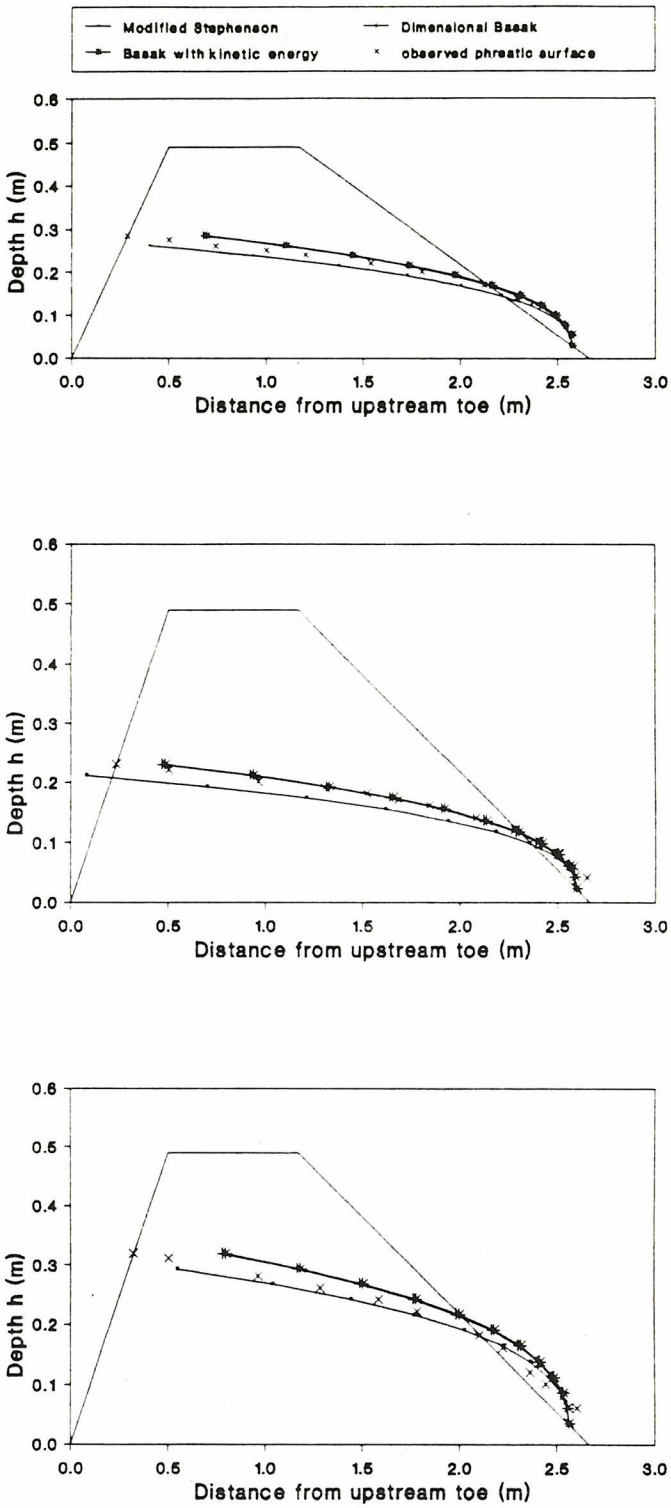


Figure A-4(i). Phreatic surfaces for flume test GF34a. 25 mm rock. Downstream slope 1V:3H.

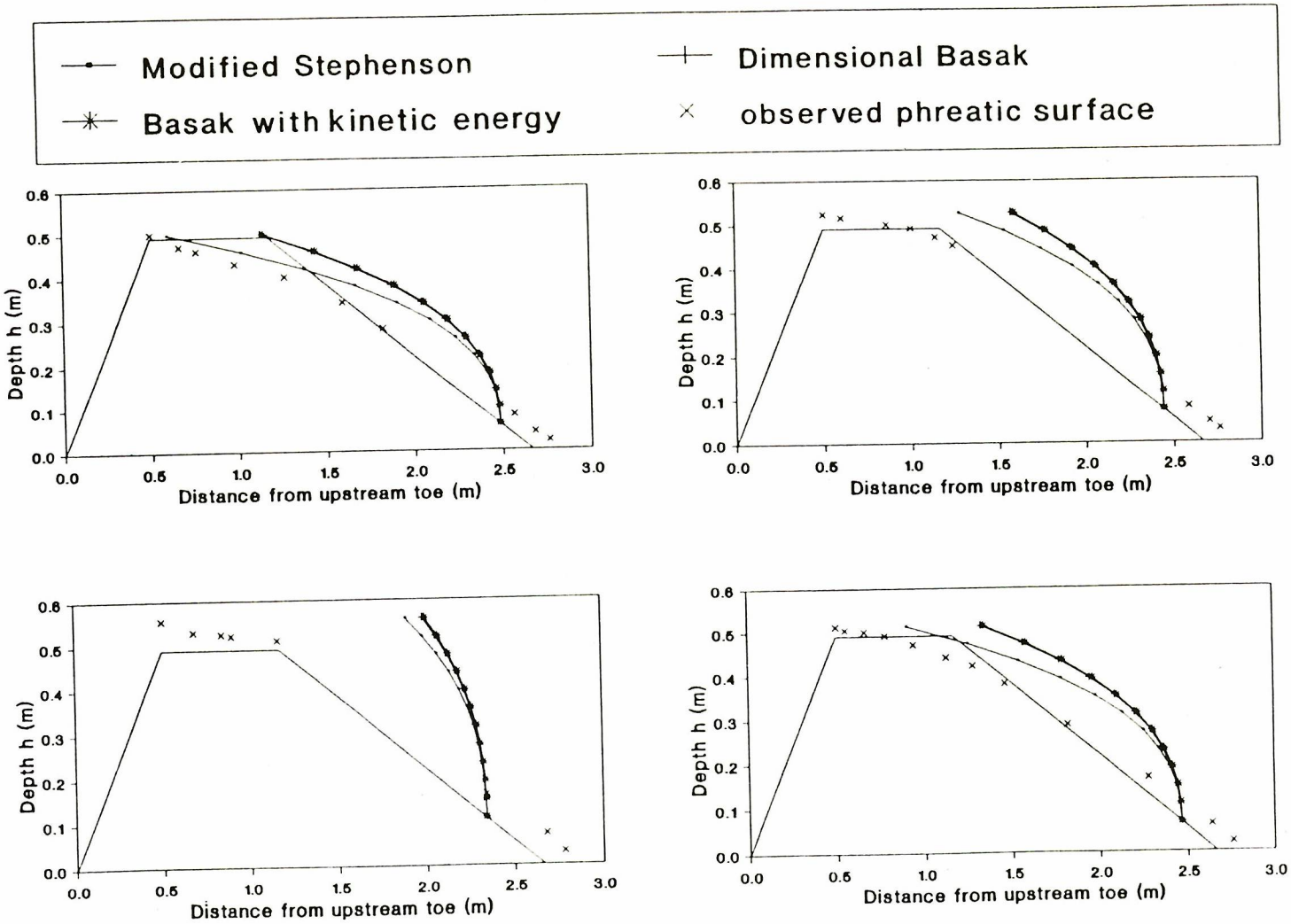
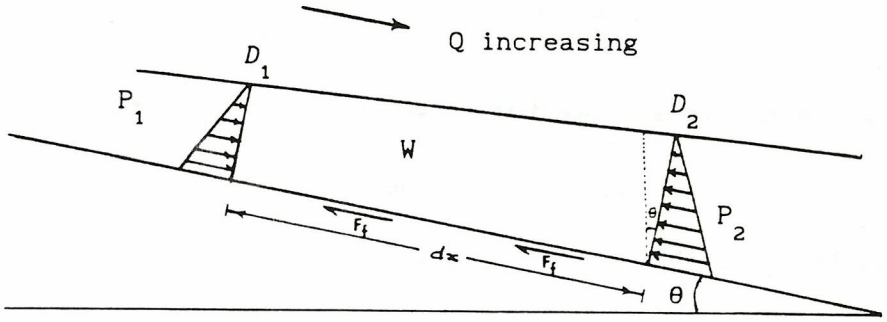


Figure A-4(ii). More phreatic surfaces for flume test GF34a. 25 mm rock. Downstream slope 1V:3H.

Derivation of Differential Equation for Spatially Varied Flow over a Steep Slope

"Spatially varied" means that the discharge is increasing with the distance x along the bed.



A channel is hydraulically "steep" if tanθ is significantly different than sinθ. "Steep" for $\theta > 4^{\circ}$ (Bray 1987). Note that Chow (1959, p.330) gives a very abbreviated derivation of the ordinary differential equation describing this class of flow, but only for the case of a gradual slope in which $\tan\theta \cong \sin\theta$. In the following development the sum of the forces acting on a control volume is equated to the change in momentum per unit time for this control volume:

$$\Delta\left[\frac{\text{Momentum}}{\text{unit time}}\right]_{\substack{\text{control}\\ \text{volume}}} = \sum \text{Forces}$$

Note that *d* refers to the depth measured perpendicular to the bed, so that d*d* is a differential depth measured at 90° to the bed. The cross-sectional area A for flow in a rectangular channel will therefore be the product of the channel width b and *d*.

A. Consider forces acting on control volume. Forces will be resolved in a direction *parallel to the bed* (unlike Chow's development in which they are resolved horizontally).

1. *Downslope component of weight:*

$$\text{Weight; } W = \gamma_w A\, dx$$

$$\text{In a downslope direction} = W \cdot \sin\theta = \gamma_w A\, dx \sin\theta = \gamma_w A\, S_o dx$$

2. *Boundary friction:*

$$F_f = -\gamma_w A\, S_f dx \quad \text{by similar argument to part A.1}$$

3. *Forces due to hydrostatic pressure:*

For small θ, $P_1 = \gamma_w \bar{z} A$, where $\bar{z} = y/2$, is a valid approximation.

However, in this case $P_1 = \frac{1}{2}\gamma_w d_1^2 \cos\theta \cdot A$

and $$P_2 = \gamma_w\left(\frac{1}{2}d_1^2\cos\theta + dd\cos\theta\right)A$$

So $$P_1 - P_2 = -\gamma_w A\cdot\cos\theta\, dd$$

B. Equating change in momentum to forces on control volume:

$$\rho\left[QdV + (V + dV)dQ\right] = -\gamma_w A\cdot\cos\theta\, dd + \gamma_w A S_o dx - \gamma_w A S_f dx$$

Dividing by γ_w and neglecting dVdQ gives:

$$-\frac{1}{g}(QdV + VdQ) = A\cos\theta\, dd + A(S_o - S_f)dx$$

Dividing by A gives:

$$-\frac{1}{g}\left[(Q/A)dV + (V/A)dQ\right] = \cos\theta\, dd + (S_o - S_f)dx$$

$$\cos\theta\, dd = -\frac{1}{g}\left[VdV + (V/A)dQ\right] + (S_o - S_f)dx$$

$$dd = -\frac{1}{g\cos\theta}\left[VdV + (V/A)dQ\right] + \frac{1}{\cos\theta}(S_o - S_f)dx$$

$$dd = -\frac{V}{g\cos\theta}\left[dV + \frac{1}{A}dQ\right] + \frac{1}{\cos\theta}(S_o - S_f)dx$$

Side development to obtain alternate expression for $dV + \frac{1}{A}dQ$

Since $Q = VA$, therefore $dQ = VdA + AdV + dVdA$

so $$dV(A+dA) = dQ - VdA$$

and $$dV = \frac{dQ - VdA}{A + dA}$$

Therefore $$dV + \frac{1}{A}dQ = \frac{dQ - VdA}{A + dA} + \frac{1}{A}dQ$$

$$= \frac{2AdQ - QdA + dAdQ}{A^2 + AdA}$$

But dAdQ is negligably small, and $AdA << A^2$, therefore:

$$dV + \frac{1}{A}dQ = \frac{2AdQ - QdA}{A^2}$$

Returning to the main development:

$$dd = -\frac{V}{g\cos\theta}\left[\frac{2AdQ - QdA}{A^2}\right] + \frac{1}{\cos\theta}(S_o - S_f)dx$$

Dividing by dx:

$$\frac{dd}{dx} = -\frac{V}{g\cos\theta}\left[\frac{2A\frac{dQ}{dx} - Q\frac{dA}{dx}}{A^2}\right] + \frac{1}{\cos\theta}(S_o - S_f)$$

Defining q_* as $\frac{dQ}{dx}$ and rearranging:

$$\frac{dd}{dx} = \frac{1}{\cos\theta}\cdot(S_o - S_f) - \frac{Q}{A^2 g\cos\theta}\left[2q_* + V\frac{dA}{dx}\right]$$

Since $V = \frac{q}{D}$ and $\frac{dA}{dx} = b\frac{dd}{dx}$, where b is the channel width

$$\frac{dd}{dx} = \frac{1}{\cos\theta}\cdot(S_o - S_f) - \frac{Q}{A^2 g\cos\theta}\left[2q_* + \frac{q}{D}b\frac{dd}{dx}\right]$$

The term $\frac{dd}{dx}$ is the rate of change of the depth (measured normal to the bed) at a specific location along x. At any given location x, let D denote the "hydraulic depth" (term used by to Chow 1959; D= A/T, where T is the top-width). Since in the context of flume studies $T = b = \frac{A}{D}$:

$$\frac{dd}{dx} = \frac{1}{\cos\theta}\cdot(S_o - S_f) - \frac{Q}{A^2 g\cos\theta}\left[2q_* + \frac{qA}{D^2}\frac{dd}{dx}\right]$$

$$\frac{dd}{dx} = \frac{1}{\cos\theta}\cdot(S_o - S_f) - \frac{2q^* Q}{gA^2\cos\theta} + \left[\frac{Q\,q\,A}{D^2A^2 g\cos\theta}\right]\frac{dd}{dx}$$

$$\frac{dd}{dx} = \frac{1}{\cos\theta}\cdot(S_o - S_f) - \frac{2q^* Q}{gA^2\cos\theta} + \left[\frac{q\,Q}{A\,D^2 g\cos\theta}\right]\frac{dd}{dx}$$

Since $q = VD$ then $\frac{qQ}{AD^2} = \frac{Q^2}{A^2 D}$

$$\frac{dd}{dx} = \frac{1}{\cos\theta}\cdot(S_o - S_f) - \frac{2q^* Q}{gA^2\cos\theta} + \left[\frac{Q^2}{A^2 D\, g\cos\theta}\right]\frac{dd}{dx}$$

Rearranging: $$\frac{dd}{dx}\left[1 - \frac{Q^2}{A^2 D\, g\cos\theta}\right] = \frac{1}{\cos\theta}\cdot(S_o - S_f) - \frac{2q^* Q}{gA^2\cos\theta}$$

Finally:

$$\frac{dd}{dx} = \frac{\frac{S_o - S_f}{\cos\theta} - \alpha\frac{2q^* Q}{gA^2\cos\theta}}{\left[1 - \alpha\frac{Q^2}{A^2 D\, g\cos\theta}\right]}$$

where α is introduced to allow for the nonuniform velocity distribution. Theoretically a momentum coefficient β should be used, but an energy coefficient α is used because the friction slope Sf is evaluated by a formula for energy loss. A, d, and D measured perpendicular to the bed.

Estimating Shear Stress under Spatially Varied Flow

A. **Simple method attempted.**
The following terms were defined:

$$\mathfrak{A} = \alpha \frac{2q^* Q}{gA^2 \cos\theta} \qquad \mathfrak{B} = \alpha \frac{Q^2}{gA^2 D \cos\theta}$$

Then $\frac{dd}{dx} = \frac{\frac{S_o - S_f}{\cos\theta} - \mathfrak{A}}{1 - \mathfrak{B}}$ and $S_o - S_f = \cos\theta\left[\mathfrak{A} + (1-\mathfrak{B})\frac{dd}{dx}\right]$

And $$S_f = S_o - \cos\theta\left[\mathfrak{A} + (1-\mathfrak{B})\frac{dd}{dx}\right]$$

An attempt was made to estimate the boundary shear stress using the following expression, with S_f defined above:

$$\tau = \gamma_w R S_f$$

However, it was found that no single value of $\frac{dd}{dx}$ gave meaningful results for shear stress; it was therefore necessary to numerically generate the entire flow profile using the method described in Chow (1959, p.545).

B. **Numerical generation of the flow profile.**
The following equation was used:

$$\Delta d' = \frac{1}{\cos\theta}\left[\frac{Q_1(V_1 + V_2)}{g(Q_1 + Q_2)}\left(\Delta V + \frac{V_2}{Q_1}\Delta Q\right) + S_f \Delta x\right]$$

Which is derived as follows (see also Chow 1959, p.341).
It was shown in Appendix 5-1 (beginning of Part B) that:

$$\rho\left[Q dV + (V + dV)dQ\right] = -\gamma_w A \cdot \cos\theta\, dd + \gamma_w A S_o dx - \gamma_w A S_f dx$$

This can be expressed in finite difference form as:

$$\rho\left[Q\Delta V + (V + \Delta V)\Delta Q\right] = -\gamma_w A \cdot \cos\theta\, \Delta d + \gamma_w A S_o \Delta x - \gamma_w A S_f \Delta x$$

The local average area of flow $\bar{A}$ can be expressed as:

$$\bar{A} = \frac{(Q_1 + Q_2)}{(V_1 + V_2)}$$

Let $Q = Q_1$, and $V + \Delta V = V_2$, then:

$$\cos\theta\, \Delta d = -\frac{Q_1}{g}\frac{(V_1 + V_2)}{(Q_1 + Q_2)}\left[\Delta V + \frac{V_2}{Q_1}\Delta Q\right] + S_o \Delta x - S_f \Delta x$$

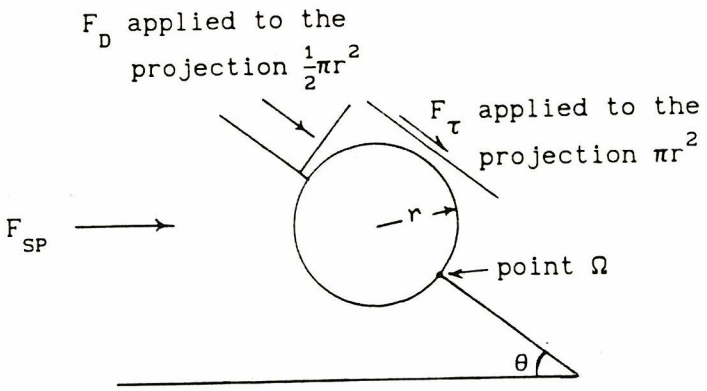
$$\Delta d' = -\frac{1}{\cos\theta}\left[\frac{Q_1}{g}\frac{(V_1 + V_2)}{(Q_1 + Q_2)}\left[\Delta V + \frac{V_2}{Q_1}\Delta Q\right] - S_f \Delta x\right]$$

where d' is the *local* drop in depth d relative to the bed.

By regenerating the flow profile according to the method described by Chow (1959) with the above modifications, the pure friction slope was evaluated at each position x along the bed. See Table A-6(i) for an example. The shear stress was then evaluated using:

$$\tau = \gamma_w R S_f$$

Equations for Forces in Simplified Erosion Analysis on a Particle Basis



Let r = representative particle radius.

1. $F_{DRAG} = F_D = C_D \rho_W A \frac{V^2}{2}$ so $F_D = C_D \pi r^2 \rho_W \frac{V^2}{4}$

It was assumed that the value of drag coefficient C_D for a coarse rock was the average of the C_D for a flat plate and the C_D for a sphere. C_D is dependent on the local Reynolds number, **Re**, as shown on the following page. Note that **Re** was both depth and velocity dependent. Local depth and the mean velocity vary with the distance x.

2. $F_{OVERFLOW} = F_\tau = \tau A = \tau \pi r^2$

where $\tau = \gamma_W R S_f$

where R = hydraulic radius measured perpendicularly to the bed.

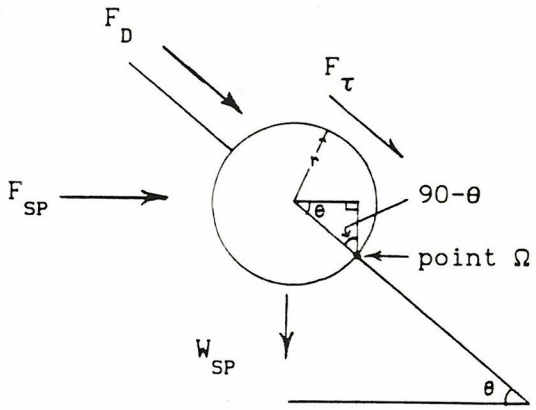
The friction slope S_f was determined using spatially varied flow considerations.

3. $F_{SEEP} = F_{SP} = (e\mathcal{V}_P + \mathcal{V}_P) \gamma_W i_H$

e = void ratio, $\mathcal{V}_P$ = representative particle volume.

The vertical component of F_{SP} was neglected. This was done because i_v was found to be both small and erratic in behaviour, as determined from finite difference pore pressure modelling.

Summary of Moments acting on a Semi-exposed Particle residing on the Downstream Face of a Flowthrough Rockfill Dam



F_D = drag force F_τ = shear force due to overflow

F_{SP} = seepage force W_{SP} = submerged weight of particle

r = representative radius of the particle

Ω = contact point with next most downstream particle

θ = angle of downstream toe of dam.

1. Moment about Ω for overflow shear force taken as $F_\tau \cdot r$.
2. Moment about Ω for drag force taken as $F_D \cdot (r/2)$.
3. Moment about Ω for horizontal seepage force is $F_{SP} \cdot r \cdot \cos(90-\theta)$, which is the same as $F_S \cdot r \cdot \sin\theta$.
4. Moment about Ω for submerged particle weight W_{SP} is: $W_{SP} \cdot r \cdot \sin(90-\theta) = W_{SP} \cdot r \cdot \cos\theta$.

Note that for a spherical particle:

$W_{SP} = (4/3)\pi r^3 g \cdot (\rho_{rock} - \rho_{water})$

(This can also be used if the *equivalent* spherical radius of the rock is known).

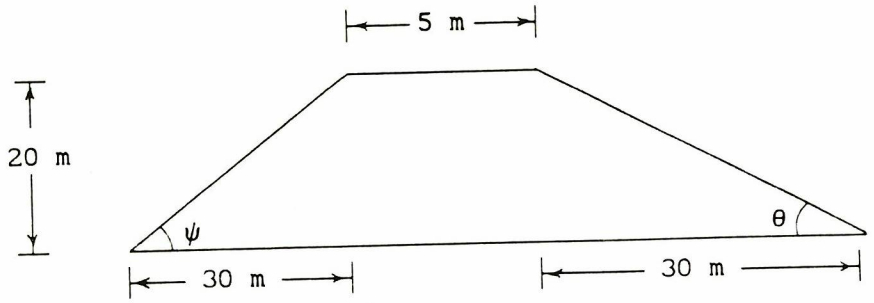
Summary of Moments

clockwise	counterclockwise
$F_\tau \cdot r$	$W_{SP} \cdot r \cdot \cos\theta$
$F_D \cdot (r/2)$	
$F_{SP} \cdot r \cdot \sin\theta$	

Appendix 6

Worked Example: Analysis and Design of a Hypothetical Prototype

Given:
- height of dam 20 m
- upstream slope = downstream slope = 1V:1.5H
- crest width = 5 m
- no imposed tailwater level and no upstream facing.



1. Particle/Porous-Media Characterization

It is recommended that a sample of 100 particles of the available crushed rock be characterized according to the Zingg diagram (see Figure 3-3). The following average values were assumed:

Mean b-axis: 0.30 m mean b/a: 2/3 mean c/b: 2/3

Therefore a = 0.45 m and c = 0.20 m. Assume that r_E = 1.6, n = 0.39, so e = 0.639. The assumption of r_E = 1.6 implies that the rock for the prototype has of the same degree of oblateness and rugosity as the crushed limestone used in this study.

The hydraulic mean radius is then:

$$m = \frac{e\ d}{6\ r_E} = 0.02 \text{ m}$$

The surface area of a perfect ellipsoid was estimated by (Sabin 1991):

$$SA = \pi(a_s b_s + b_s c_s) + 2\pi c_s \left[(a_s + b_s)/2\right]^{1/2} + 2\pi a_s \left[(b_s + c_s)/2\right]^{1/2}$$

where SA is surface area. Note that a_s = a/2, b_s = b/2, c_s = c/2.

The volume of an ellipsoid is:

$$\text{Volume} = \frac{4}{3}\pi\ a_s b_s c_s = \frac{1}{6}\pi\ a\ b\ c$$

Using the above formula, and by comparison with actual volumes and surface areas for the crushed limestone rock examined in this study, the following values were obtained:

$$\text{Surface area} = 0.446\ m^2, \quad \text{Volume} = 0.012\ m^3$$

2. Determination of Governing Non-Darcy Flow Equation

Four original equations and one suggested form will be considered. Note that $V_v = V/n$. All forms reduced to $V = a' i^{N'}$ [2-3d]:

Partially-developed turbulence: Wilkins; $V_v = 5.243 m^{1/2} i^{0.54}$
for this case $V = 0.29\ i^{0.54}$

Fully-developed turbulence: Stephenson; $V_v = \left[\frac{g\ d\ i}{4}\right]^{1/2}$
for this case $V = 0.33\ i^{1/2}$

Fully-developed turbulence: Martins; $V_v = 0.56\sqrt{2gde}\ i^{1/2}$
(Assuming uniform angular material.)
for this case $V = 0.42\ i^{1/2}$

Self-specified level of turbulence: McCorquodale for crushed rock;

$$i = \left(\frac{70\ \nu}{g\ n\ m^2}\right) V + \left(\frac{0.81}{g\ n^{1/2} m}\right) V^2$$

$i = 0.046\ V + 6.62\ V^2$
by regression $V = 0.40\ i^{0.53}$

Suggested form for fully-developed turbulence: $V_v = K\sqrt{gedi}$
based on Martins' data $K = 0.79$
based on Stephenson's data $K = 0.63$
Using an average K for this case yields: $V = 0.38\ i^{1/2}$

Based on the above, an average a' is selected, such that $V = 0.36\ i^{0.5}$

3. Obtain Rating Curve

a) Rapid Method.

Effective width: $B_{eff} = \left[B_u + B_c + 0.5\ B_d\right] = 30 + 5 + 15 = 50$ m

Aspect ratio: $A_R = B_{eff}/H = 50/20 = 2.5$

Effective hydraulic gradient formula:

$$i_{eff} = 0.8 \cdot A_R^{-3/2} \cdot (h/H)^{1.4} = 0.00305\ h^{1.4}$$

Then $\frac{Q}{L} = q = a'\ i_{eff}^{1/2}\ h$ (m^3/s) per m of dam

so $q = 0.40\ i_{eff}^{1/2}\ h$ (m^3/s) per m of dam, where $i_{eff} = 0.00305\ h^{1.4}$

b) Using Phreatic Surface Theory.

Let the upstream water level be equal to the height of the dam illustrative purposes. This depth is also of primary interest with regard to the associated seepage wedge generated on the downstream face. For h = 20 m, i_{eff} = 0.202 and q = 3.24 m^3/s per m. For reasons to be explained, this q was increased to 3.66 m^3/s.

The expression for the porous-media critical depth for a rectangular channel:

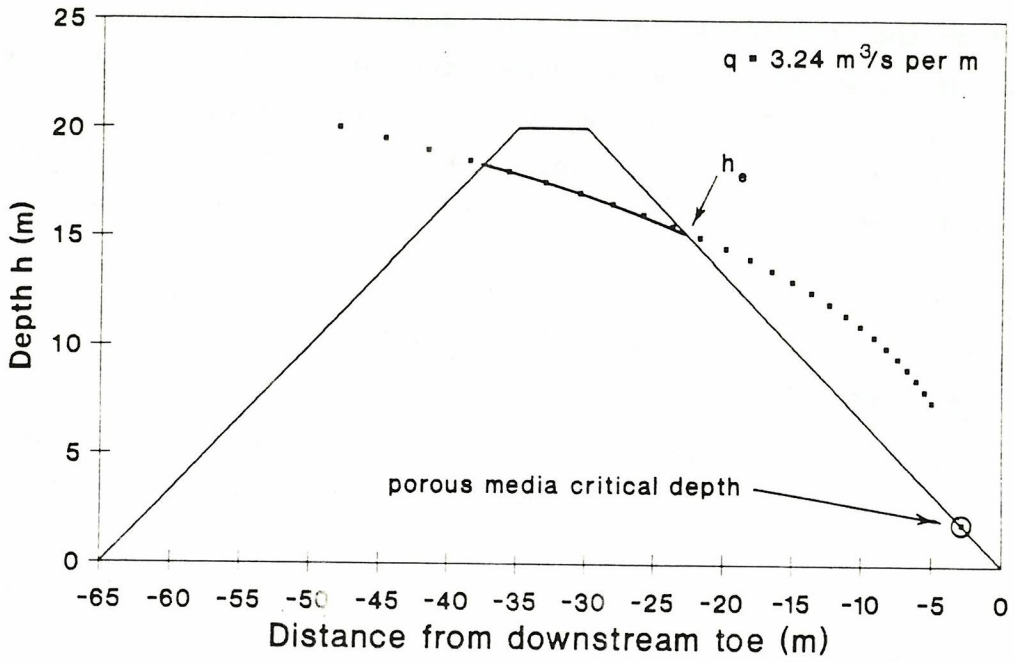
$$y_c = \left(\frac{q^2}{g\ n^2}\right) = 2.08 \text{ m}$$

Application of the modified Stephenson equation:

$$\frac{3}{K^2 ed}\ x = \left(\frac{h}{y_c}\right) - 3\ \ln\left(\frac{h}{y_c}\right) - 1$$

gives the phreatic line shown in Figure A-6(i) (using K = 0.79, and using y_c as the starting point of the calculations). Although the upstream water level does not quite match 20 m for the q estimated using i_{eff} for h = 20 m, a match can be obtained by either putting a 75% weighting on B_U in the equation for i_{eff} (since only 1V:1H were used to develop the expression for i_{eff}), or by setting the value of K to 0.76. This latter value of K implies a maximum unit-width flow of 3.66 m^3/s and a value for a' of 0.406. Considering the range of uncertainty regarding non-Darcy flow parameters for large rock material, this is not considered to be a serious anomaly within a design methodology.

A series of phreatic lines could be generated by assuming a range of q values from near zero to 3.66 m^3/s per m. As previously noted from the results of flume tests, phreatic line theory based on the Dupuit assumption, (which is inherent in the modified Stephenson equation)



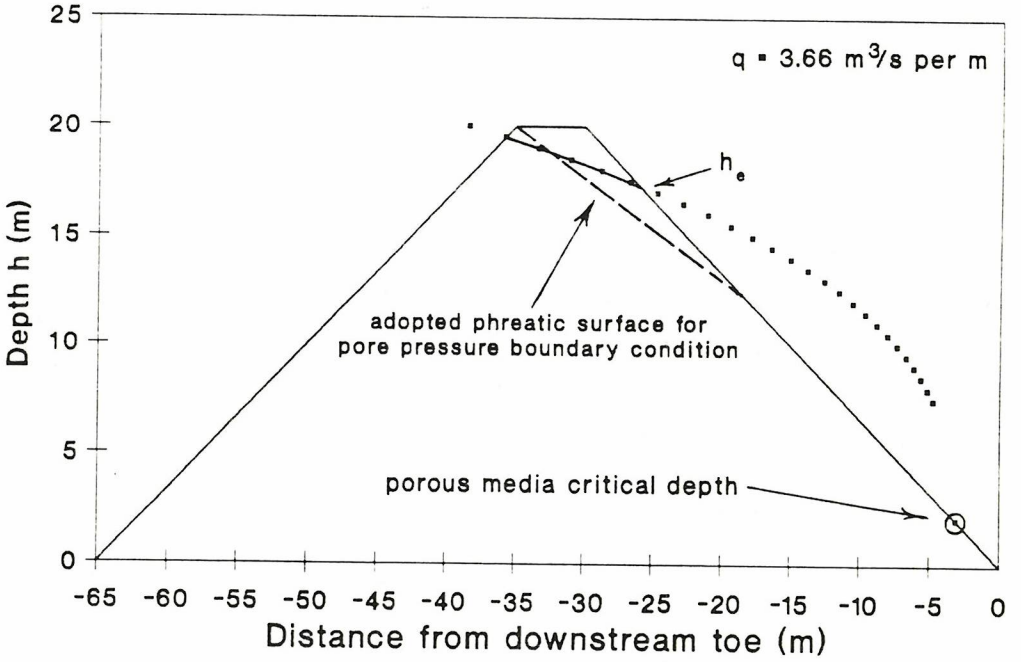


Figure A-6(i). Phreatic surfaces for prototype in worked example.

tends to give a computed phreatic lines which are increasingly too high as the upstream water level approaches the height of the dam. It was found that for the case of h = H, a better approximation for h_e was $h_e \cong 0.6$ H. The phreatic line joining h = H on the upstream side and $h_e = 0.6$ H on the downstream side is also shown in Figure A-6(i). The phreatic line also serves as the upper boundary condition for pore pressure modelling. It should be noted that an exaggeration in the vertical scale equal to 1.6 in Figure A-6(i) tends to exaggerate the difference between the theoretical and assumed phreatic surfaces.

4. Determination of the Variation in Depth with Distance for the Seepage Face.

This is needed for two purposes. The first is to provide the boundary conditions on the downstream face, which are needed for pore pressure modelling. The second is to permit estimation of the shear stresses contributing to unravelling failure. At the toe of the dam the following equation is used to obtain an estimate of the Froude number:

$$Fr_o = \frac{1}{4}\left(11 \log\left(h_e/H\right) + 12\right) \qquad \text{for } h_e/H = 12/20 = 0.6, \quad Fr_o = 2.39$$

This Froude number can be used with the following analytic equation for rectangular channels to find the corresponding depth:

$$\text{For } q = 3.66 \text{ m}^3/\text{s} \qquad y_o = \left(\frac{q^2}{Fr^2 g}\right) = 0.6205 \text{ m}$$

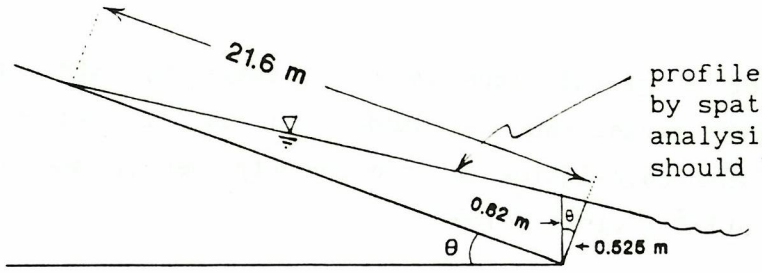
Strictly speaking, y_o (measured vertically from the bed) should be d_o (measured perpendicular to the bed). However, in collecting the experimental data to develop the expression for Fr_o, the vertical depth y_o, and not d_o, was measured. The depth d_o normal to the bed can be obtained from y_o using the following relation:

$$d = y\cos\theta\left(1 + \frac{dy}{dx}\sin\theta\right) \qquad \theta = 33.69^\circ$$

$$\Delta x = \left(h_e + (h_e/\tan\theta)^2\right)^{1/2} \qquad \Delta x = 21.63 \text{ m}$$

$$\text{estimated } \frac{dy}{dx} = \frac{0.6205}{21.63} = 0.029$$

$$\text{Estimated } d_o = 0.6205(\cos 33.7)(1+0.029\sin 33.7) = 0.525 \text{ m}$$



Assume a length of dam (L in Figure 1-1) equal to 30 m.
Then Q = 30(3.66) = 109.8 m^3/s

Estimate $q_* = dQ/dx$ as (109.8/21.63) = 5.08 m^3/s per m.

The starting x position for generation of the spatially varied flow profile occurs at **Fr** = 1 and is computed from:

$$x = \frac{8\cos\theta^2 q_*^2}{gL^2\sin^3\theta} = 0.095 \text{ m}$$

A variation in Manning's n must be assumed. Manning's n at the toe was found using Strickler's equation. d_{50} particle size = b = 0.30 m.

Strickler equation: $$n = 0.047 \cdot d_{50}^{1/6} = 0.038$$

It is known that friction has little effect near the point of emergence, a starting value of n=0.015, associated with a relatively smooth boundary, was therefore assumed. Table A-6(i) following shows how the variation in depth was computed. For ease of reference, the column numbers corresponding to those used in Chow (1959, p.535) are given. The depth at each x position was determined by successive trials until the assumed depth in column 4 matched the computed depth in column 17. It was found that the trial depth (column 4) had to be very close to the final correct depth in order for the computed depth (column 17) to begin to match the trial depth. This numerical instability has also been noted by Kells (1991). It is noted that the final computed depth at the toe (perpendicular to the bed) is in good agreement with that found from the equations for $\mathbf{Fr}_o$ and d_o. To obtain a perfect match would require reiteration of the entire supercritical flow profile until the final depth matched 0.525m. Given the approximate nature of the equation for $\mathbf{Fr}_o$, this is not justified.

5. Unravelling Failure

The purpose of this set of calculations is to estimate the minimum height over which mesh protection is needed so as to prevent unravelling failure. The calculation of the moments pertaining to particle stability are briefly given below.

a) Particle moment due to overflow shear. See Table A-6(i).

The shear stress was estimated from:

$$\tau = \gamma_w R S_f$$

where R = depth for a wide channel.

S_f = pure friction slope, found from previous spatially varied flow profile calculations.

The moment on the particle was computed using $A/2 = 0.223\ m^2$, where the area A was discussed in part 1 (Particle Characterization).

b) Particle moment due to form drag. See Table A-6(ii).

The equation is:

$$F_D = C_D \cdot \rho_w \cdot A \frac{V^2}{2}$$

$$\rho_w = 1000\ kg/m^3 \qquad \nu = 1 \cdot 10^{-6}\ m^2/s$$

$$\text{Assumed drag area} = \frac{1}{2}\left(\frac{\pi\, b^2}{4}\right) = 0.035\ m^2$$

The actual forward-projected area of a given particle depends on its orientation relative to the direction of flow. It was assumed that $\pi b^2/4$ is representative of the forward-projected area and that half of this area is exposed to the flow. Although the b-axis is not the largest axis, it is important to use a *representative* particle diameter within a design methodology.

The drag coefficient for a sphere is, in general, Reynolds number dependent. Figure A-6-(ii) (Diagram F in Giles 1977, SI version, used by permission), following, shows this variation. The average of the C_D value for a sphere and for a plate was assumed, since a coarse rock will not be as hydrodynamically smooth as sphere. This will also be more conservative than using C_D for a sphere only. The local velocity V was determined from the spatially varied flow computations.

Table A-6(i)

Computation of Spatially Varied Flow Profile and Related Shear Stresses

Small numbers over columns indicate corresponding column numbers for example given in Chow's "Open Channel Hydraulics" (1959), p.345.

	1 diagonal distance (m)	2 ΔX (m)	3 Z_o local bed elevation (m)	4 $\Delta d'$ Assumed drop in water level (m)	5 Z elevation at water level (m)	6 d local depth (m)	7 A area (m^2)
1	0.09		11.948		11.977	0.030	0.890
2	1.75	1.657	11.028	0.823	11.154	0.126	3.771
3	3.41	1.657	10.109	0.856	10.298	0.189	5.662
4	5.07	1.657	9.190	0.876	9.422	0.232	6.962
5	6.72	1.657	8.271	0.882	8.541	0.270	8.087
6	8.38	1.657	7.352	0.885	7.656	0.304	9.111
7	10.04	1.657	6.433	0.887	6.769	0.336	10.073
8	11.69	1.657	5.514	0.889	5.881	0.366	10.989
9	13.35	1.657	4.595	0.890	4.991	0.396	11.875
10	15.01	1.657	3.676	0.890	4.101	0.425	12.746
11	16.66	1.657	2.757	0.890	3.211	0.454	13.605
12	18.32	1.657	1.838	0.891	2.320	0.482	14.456
13	19.98	1.657	0.919	0.891	1.429	0.510	15.304
14	21.63	1.657	0	0.891	0.538	0.538	16.153

	8 Q (m^3/s)	10 Q_1+Q_2 (m^3/s)	12 ΔQ (m^3/s)	9 V (m/s)	Froude Number	11 V_2+V_1 (m/s)	13 ΔV (m/s)
1	0.5			0.54	1.000		
2	8.9	9.37	8.41	2.36	2.122	2.897	1.82
3	17.3	26.19	8.41	3.06	2.244	5.412	0.70
4	25.7	43.01	8.41	3.69	2.446	6.747	0.64
5	34.1	59.82	8.41	4.22	2.593	7.911	0.53
6	42.5	76.64	8.41	4.67	2.703	8.886	0.45
7	50.9	93.46	8.41	5.06	2.785	9.724	0.39
8	59.3	110.28	8.41	5.40	2.848	10.457	0.34
9	67.8	127.10	8.41	5.71	2.894	11.106	0.31
10	76.2	143.92	8.41	5.98	2.926	11.681	0.27
11	84.6	160.74	8.41	6.22	2.946	12.192	0.24
12	93.0	177.55	8.41	6.43	2.958	12.648	0.22
13	101.4	194.37	8.41	6.63	2.960	13.057	0.19
14	109.8	211.19	8.41	6.80	2.957	13.422	0.17

Table A-6(i) continued

Computation of spatially varied flow profile and related shear stresses

	14 $\Delta d'$ due to impact loss alone (m)	15 R hydraulic radius (m)	Manning's n	S_f pure friction slope	16 h_f head loss due to friction only (m)	17 $\Delta d'$ computed DROP in water level (m)
1						
2	0.783	0.126	0.0150	0.020	0.040	0.823
3	0.807	0.189	0.0170	0.025	0.049	0.856
4	0.808	0.232	0.0189	0.034	0.068	0.876
5	0.793	0.270	0.0209	0.044	0.089	0.882
6	0.774	0.304	0.0228	0.056	0.111	0.885
7	0.753	0.336	0.0248	0.067	0.134	0.887
8	0.730	0.366	0.0267	0.079	0.158	0.889
9	0.707	0.396	0.0287	0.092	0.183	0.890
10	0.681	0.425	0.0306	0.105	0.209	0.890
11	0.656	0.454	0.0326	0.118	0.235	0.890
12	0.631	0.482	0.0345	0.131	0.260	0.891
13	0.606	0.510	0.0365	0.143	0.286	0.891
14	0.581	0.538	0.0385	0.156	0.311	0.891

Particle area for $F_\tau = 0.223\ m^2$

Moment arm = b/2 = (0.3)/2 = 0.15 m

	Shear Stress (N/m^2)	Shear Force on Particle (N)	Clock-wise Moment (N-m)
1			
2	24.431	5.45	0.82
3	45.784	10.21	1.53
4	77.648	17.32	2.60
5	117.392	26.18	3.93
6	165.180	36.84	5.53
7	221.024	49.30	7.39
8	285.040	63.57	9.54
9	357.043	79.63	11.95
10	436.376	97.33	14.60
11	522.929	116.63	17.49
12	616.517	137.51	20.63
13	716.373	159.78	23.97
14	822.140	183.37	27.51

Table A-6(ii)

Computation of Particle Drag Force under Spatially Varied Flow

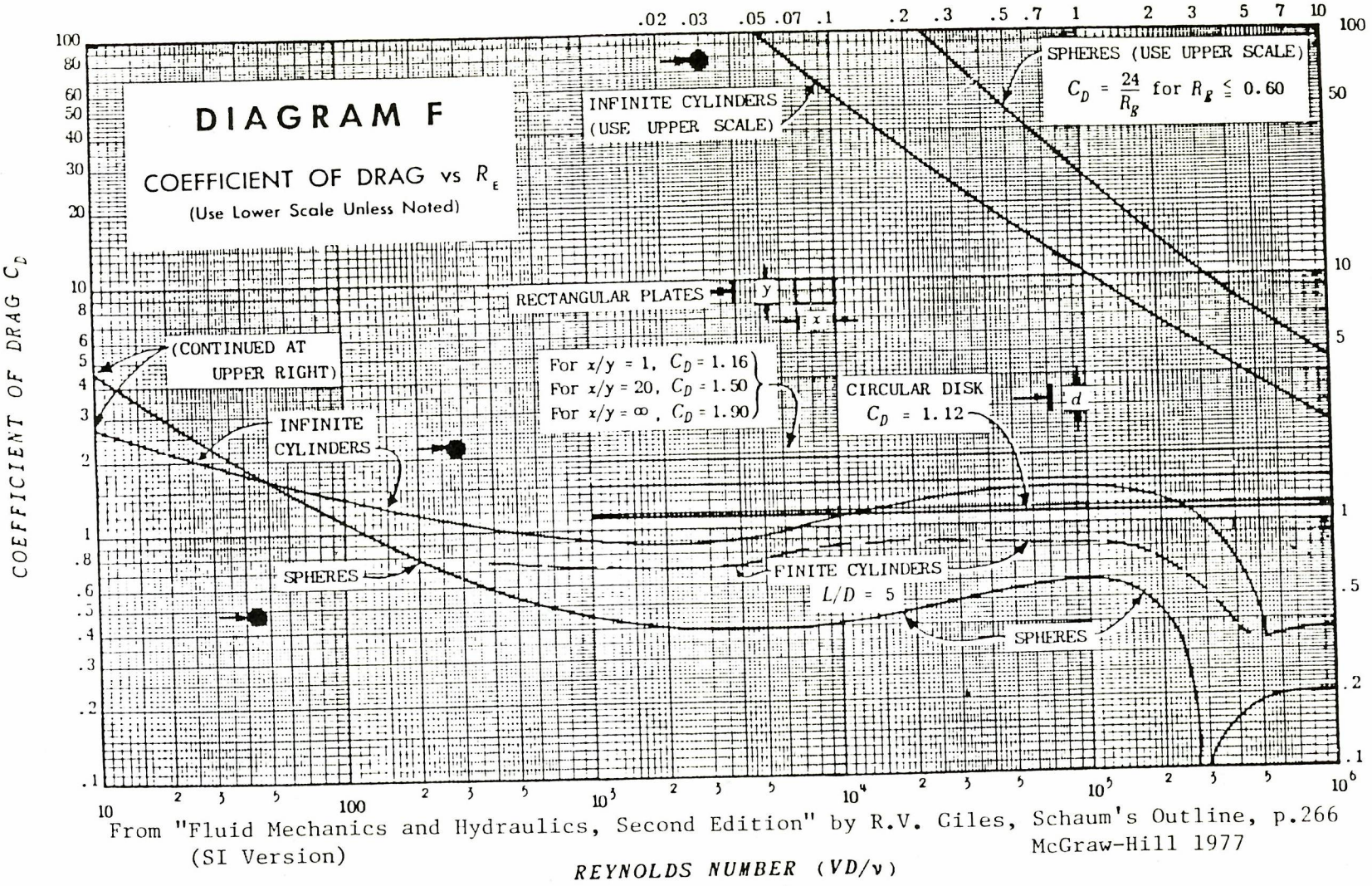
	1 Distance* (m)	2 Q (m^3/s)	3 Depth (m)	4 Flow area (m^2)	5 Velocity (m/s)
1	0.09	0.5	0.030	0.89	0.54
2	1.75	8.9	0.126	3.77	2.36
3	3.41	17.3	0.189	5.66	3.06
4	5.07	25.7	0.232	6.96	3.69
5	6.72	34.1	0.270	8.09	4.22
6	8.38	42.5	0.304	9.11	4.67
7	10.04	50.9	0.336	10.07	5.06
8	11.69	59.3	0.366	10.99	5.40
9	13.35	67.8	0.396	11.87	5.71
10	15.01	76.2	0.425	12.75	5.98
11	16.66	84.6	0.454	13.61	6.22
12	18.32	93.0	0.482	14.46	6.43
13	19.98	101.4	0.510	15.30	6.63
14	21.63	109.8	0.538	16.15	6.80

* measured along the slope surface, diagonally, from the seepage breakout point.

Forward-projected exposed particle area = $0.5 \cdot \pi \cdot (b/2)^2 = 0.035\ m^2$
Moment arm = $(b/2) = 0.15$ m

	Particle Reynolds Number	Sphere drag coeff.** C_D	Disk drag coeff. C_D	Drag force F_D (N)	Particle Moment (N-m)
1	1.61E+05	0.480	1.12	4.1	0.31
2	7.05E+05	0.200	1.12	64.7	4.85
3	9.14E+05	0.200	1.12	108.7	8.15
4	1.10E+06	0.200	1.12	158.7	11.90
5	1.26E+06	0.200	1.12	207.2	15.54
6	1.40E+06	0.200	1.12	253.6	19.02
7	1.51E+06	0.200	1.12	297.7	22.33
8	1.62E+06	0.200	1.12	339.5	25.47
9	1.71E+06	0.200	1.12	379.0	28.43
10	1.79E+06	0.200	1.12	415.7	31.18
11	1.86E+06	0.200	1.12	449.9	33.74
12	1.92E+06	0.200	1.12	481.7	36.13
13	1.98E+06	0.200	1.12	511.0	38.32
14	2.03E+06	0.200	1.12	537.9	40.34

** See Figure A-6(ii) for source of values for C_D.



From "Fluid Mechanics and Hydraulics, Second Edition" by R.V. Giles, Schaum's Outline, p.266
(SI Version) McGraw-Hill 1977

Figure A-6(ii). Variation of drag coefficient as a function of Reynolds number, for various shapes.

c) Particle moment due to seepage force.

The horizontal component of the hydraulic gradient was determined from pore pressure modelling using following equation (see Figure 2-4):

$$i_h = \frac{(h_5 - h_1)}{2\Delta x}$$

for each node on the downstream face. The seepage force on a particle basis is then:

$$F = \mathcal{V}_{min} \gamma_w i$$

$$\text{where } \mathcal{V}_{min} = e\mathcal{V}_P + \mathcal{V}_P$$

$$\text{and: } \mathcal{V}_P = \text{(average rock mass)/(density of rock)}$$

The table following shows the sequence of calculations for the particle moment due to the seepage force.

Table A-6 (iii)

Force and Moment acting on Representative Particle due to Emergent non-Darcy Seepage

Porosity n = 0.39 Void ratio e = 0.64
Minimum bulk volume to contain 1 particle = 0.0193 m^3
Moment arm = b·sinθ = 0.0832 m
No particle area required.

	Distance (m)	Horiz. gradient ih	F_{SEEP} per particle (N)	Particle moment (N-m)
1	0.09	0.56	105.96	8.8166
2	1.75	0.58	109.20	9.0856
3	3.41	0.59	112.43	9.3546
4	5.07	0.61	115.66	9.6235
5	6.72	0.63	118.89	9.8925
6	8.38	0.65	122.13	10.1615
7	10.04	0.66	125.36	10.4304
8	11.69	0.68	128.59	10.6994
9	13.35	0.70	131.82	10.9684
10	15.01	0.71	135.06	11.2373
11	16.66	0.73	138.29	11.5063
12	18.32	0.75	141.52	11.7753
13	19.98	0.77	144.75	12.0442
14	21.63	0.78	147.99	12.3132

d) Particle moments due to submerged weight.

The following values can be readily found:

Particle volume	0.012	m^3
Particle mass	31.75	kg
Displaced water mass	11.76	kg
ρ rock particle	2695.0	kg/m^3
ρ water	998.2	kg/m^3
Unsubmerged particle mass	31.75	kg
Submerged particle mass	19.99	kg
Submerged particle wgt	196.23	N
Moment from wgt force	24.49	N-m counter-clockwise

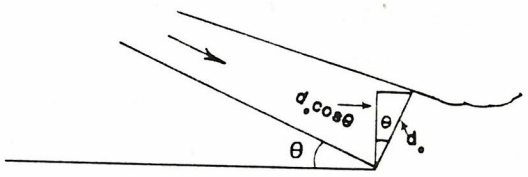
Summary: Unravelling Failure

Figure 5-9(b) shows that particles on the lower 75% of the seepage face are prone to move out of position due to the combined effects of the overflow and emergent seepage. Mesh protection is therefore recommended on the lower 75% of the downstream face of the dam. The foregoing particle moment analysis does *not* provide an estimate of bursting pressures against a mesh reinforcement. However, if massive failure is expected, the design of the restraint against massive failure will govern.

6. Pore Pressure Modelling

The upstream boundary condition for the dam is the height of the dam, equal to 20 m. For the case of no imposed tailwater (which is a conservative assumption) the downstream boundary condition is the seepage face. The seepage face, wherein the phenomenon of spatially varied flow occurs, is a *self-generated* boundary condition, unlike the upstream boundary condition, which is simply imposed. If a highly accurate downstream boundary condition were required, the analysis of non-Darcy pore pressures and the analysis of spatially varied flow would need to be linked computationally. Since both of these procedures are iterative *in their own right*, such a calculation would be difficult to perform, and would require formal coding of a specially-written computer program. In light of the degree of uncertainty regarding the role of the roughness of the bed (ie., the variation in Manning's n along the downstream face), and of the non-Darcy flow parameters, such a refinement may not be justifiable.

The suggested approach for design purposes is to assume a *linear* variation in depth for the seepage face on the downstream side of the dam. This linear variation can be described from the depth estimated at the toe, and from the total diagonal length of the seepage face. The downstream boundary condition required is the variation in the local value of $z + d\cos\theta$, the local piezometric head at the bed. This is in keeping with the standard assumptions about the pressure distribution within an open channel flow (Chow 1959), ie., that the flow occurs normal to the variation in pressure. Hence $d\cos\theta$ is used, and not simply d (see for example p.33 of Chow 1959). This is illustrated as follows for one location, the toe of the dam:



The base of the dam was assumed to be impervious, along which the following finite difference expression can be used to compute piezometric head:

$$h_c = \left(4h_1 + 2h_2 + 8h_3 + 2h_4 + 4h_5\right) / 20$$

The piezometric head at all internal nodes (see Figure 2-4) was computed using:

$$h_c = T1 \cdot (h_1 + h_3 + h_5 + h_7) + T2 \cdot T3$$

where:

$$T1 = \frac{1}{2(N'+1)}$$

$$T2 = \frac{(N'-1)}{2(N'+1)}$$

$$T3 = \left[\frac{(h_1+h_5)(h_1-h_5)^2+0.5(h_1-h_5)(h_3-h_7)(h_2+h_6-h_4-h_8)+(h_3+h_7)(h_3-h_7)^2}{(h_1-h_5)^2 + (h_3-h_7)^2}\right]$$

where:

h_n = piezometric head at a nodal point n,

N' = 1/N, where N = 2 in this case (fully-developed turbulence).

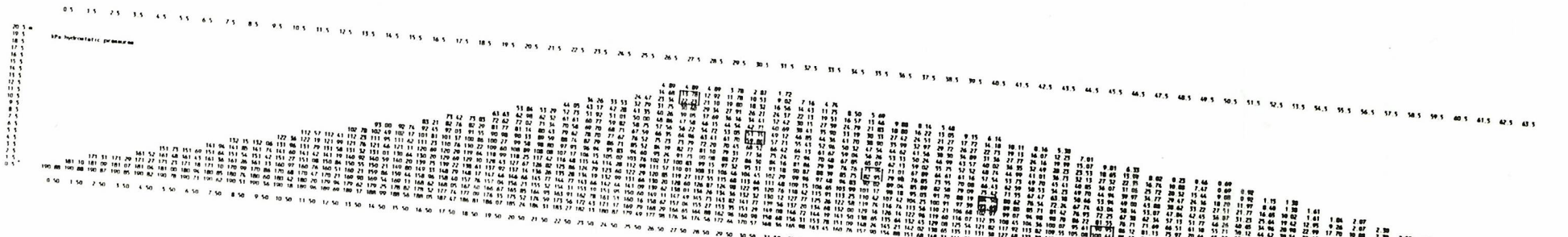
Figure A-6 (iii) shows the variation in piezometric head (also known as total head) and in pore pressure within the embankment. The pore pressure was computed as the piezometric head at each node minus the elevation at the centre of the node. These pore pressures were used in rotational failure analysis.

7. Analysis of Potential for Deep-seated Failure

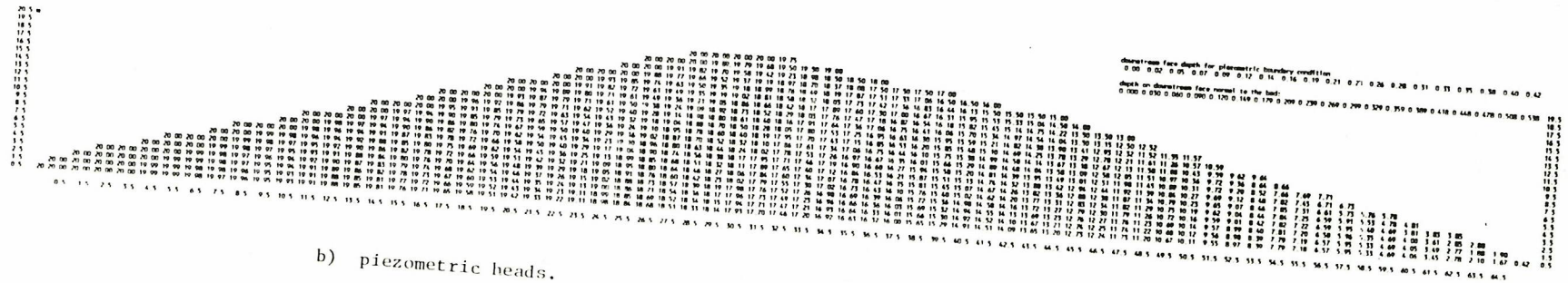
a) Rotational failure analysis.

A modified version of the FORTRAN computer program STABR (Duncan and Wong, 1985) was used to read in the non-Darcy pore pressure field and locate the slip circle with a factor of safety of one. It is of interest to find the minimum amount of reinforcement needed to prevent rotational failure. This is associated with a factor of safety (FOS) of one. As a check, the slip surface found using the modified STABR program for FOS=1 was analyzed by hand, with the result that FOS = 0.99. The slip surface and the slices above it are shown in Figure A-6(iv); the manual calculations are given in Table A-6(iv). The pore pressures at the centre of the base of each slice were interpolated from the enclosed pairs of values shown in Figure A-6(iii). The steps in this tabular calculation can be found in standard texts. For example, see p.358 of Lambe and Whitman (1979, SI version). The net effect of the upstream and downstream external hydrostatic pressures was found to be approximately 1% of the moment associated with FOS =1, and was not included in the hand calculations. As a further check, the slope shown in Figure A-6(iv) was analysed independently using the program PETAL (LCPC 1984) and the result for the moment associated with FOS=1 was within 5% of that found using the modified STABR program.

Table A-6(v) presents an example calculation of the reinforcement requirements associated with FOS = 1 and FOS = 2. These calculations do not include any estimate of the possible benefit accrued from friction between the dam and the foundation and/or abutments. Figure 5-22 shows the position and length of the reinforcing bars. As noted in Table A-6(v), the bar spacing L depends on the desired factor of safety. Other strategies could be adopted in which the rebars might be farther apart vertically, but more closely spaced along the length L.



a) pore pressures.



b) piezometric heads.

Figure A-6(iii). Results of finite difference pore pressure modelling for prototype in worked example.

γ_{sat} = 19.91 kN/m^3 γ_{unsat} = 16.09 kN/m^3 void ratio = 0.64

Angle at base of slice 7, α_7 = 5.0° Width of slice 1 = 3 m

Angle at base of slice 8, α_8 = -2.8° Width of slice 8 = 4 m

Base angle for other slices as shown. All other slice widths = 5 m

Circle centre: distance = 61.34 m, elevation = 40.87 m
Circle radius = 40.87 m

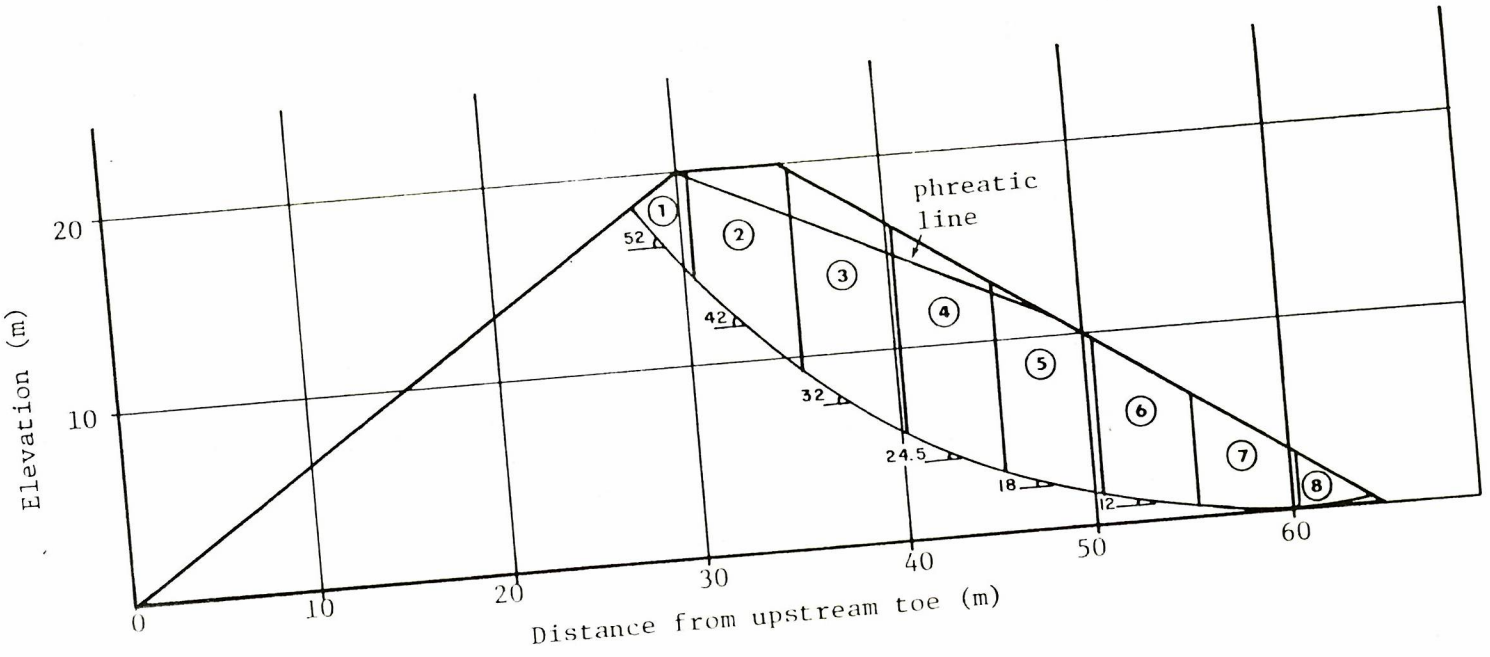


Figure A-6(iv). Layout for manual application of Bishop's Simplified Method to prototype in worked example.

Table A-6(iv)

Application of Bishop's Method of Slices to Prototype 1 for FOS=1 Slip Circle

γ_{sat} = 19.91 kN/m^3 γ_{unsat} = 16.09 kN/m^3 e = 0.64

Circle radius = 40.87 m

SLICE	1 Total Weight (kN)	2 Angle α at base of slice (degrees)	3 Downslope component of weight (kN)	4 Vertical basal pore pressure force (kN)
1	191.0	52.0	151.0	97.5
2	849.0	42.0	568.0	310.0
3	1078.5	32.0	571.5	421.0
4	1040.0	24.5	431.5	464.0
5	899.0	18.0	277.5	446.5
6	677.0	12.0	140.5	377.0
7	466.5	5.0	40.5	264.5
8	130.0	-2.0	-4.5	122.0
			sum: 2176.0 kN	

5 Total weight minus vertical basal pore pressure force (kN)	6 Shear force mobilized (kN)	7 (col.6)/M† (kN)
93.5	93.5	66.4
539.1	539.1	380.6
657.5	657.5	476.0
576.1	576.1	434.0
452.4	452.4	358.5
299.9	299.9	252.6
202.1	202.1	186.4
8.0	8.0	8.3
		sum: 2162.8 kN

FOS = (2162.8)/(2176.0) = 0.99

Moment = 40.87·2169.5 = 88675.5 kN-m

† $M = \cos\alpha \left(1 + \frac{\tan\alpha \tan\phi}{F}\right)$

Table A-6(v)
Reinforcement Against Rotational Failure

	1 Rebar elevation above base (m)	2 Moment arm (m)	3 Weighting for each bar	4 Force per bar (kN)	5 σ per bar, for 1 m L of dam (MPa)	6 Max σ per bar (MPa)	7 σ per bar for minim. FOS=2 (MPa)	8 Length of bar (m)
1	0.50	40.37	10.4%	21.3	106.38	414.0	207.0	21.6
2	1.50	39.37	10.0%	20.4	101.78	396.1	198.0	21.2
3	2.50	38.37	9.5%	19.4	97.17	378.2	189.1	20.8
4	3.50	37.37	9.1%	19.5	92.57	360.3	180.1	20.8
5	4.50	36.37	8.6%	18.6	87.97	342.3	171.2	20.8
6	5.50	35.37	8.2%	17.7	83.36	324.4	162.2	20.4
7	6.50	34.37	7.7%	16.8	78.76	306.5	153.3	20.1
8	7.50	33.37	7.3%	15.8	74.16	288.6	144.3	19.3
9	8.50	32.37	6.8%	14.9	69.56	270.7	135.3	18.9
10	9.50	31.37	6.4%	13.0	64.95	252.8	126.4	18.2
11	10.50	30.37	5.9%	12.1	60.35	234.9	117.4	17.8
12	11.50	29.37	5.5%	11.1	55.75	217.0	108.5	17.0
13	12.50	28.37	5.0%	10.2	51.14	199.0	99.5	16.7

Moment at FOS = 1 is 91,415 kN-m (overturning = resisting)

2 vertical distance to elevation of slip circle centre, = 40.87 m
3 somewhat arbitrary, higher stresses toward lower bars, linear in variation.
6 Factor of safety = 1, spacing of bars = 3.89 m between bars along L.
7 Factor of safety = 2, spacing of bars = 1.95 m between bars along L.
8 as shown in Figure 5-22, but not including hooks.

GRADE 60 rebar yield stress = 414 MPa
Rebar #15M, diameter = 16 mm, cross-sectional area of rebar = 2 cm^2

Assumptions:
1. Mesh on downstream face transmits bursting force to the rebar perfectly, without itself bursting.
2. Rebar does not fail by the mechanism of pull-out with rebar intact. Rebar fails first.

It is evident that the reinforcement requirements needed to prevent rotational failure are extensive, requiring a considerable number of relatively long sections of rebar per unit length L of dam. It is also noted that the reinforcement to prevent rotational failure, as suggested by Wilkins (1963) for a prototype (see Figure 2-7) bears much greater resemblance to Figure 5-22(a) than to Figure 5-22(b). If this type of failure is indeed a possible mechanism for deep-seated failure, this particular configuration of dam may not be economically feasible. It is noted that the mesh protection connected to the rebar layout in Figure 5-22(a) gives protection against unravelling failure to an adequate elevation.

b) Wedge failure analysis.

Section 5.2.3 and Appendix 3 present the theory behind this method. Table A-6(vi) presents the calculation of bursting pressure in tabular form. No formal computer program existed to perform this analysis, which was therefore done graphically and with the aid of an electronic spreadsheet. In general, two short sequences of information are needed to permit determination of the bursting pressure. As noted in Section 4.3.2.2, unlike the classical theory of rotational slip surfaces, the wedge method yields a bursting pressure for any trial b_{tf} (see Appendix 3-3) and angle ρ, unless ρ is quite small.

The assumption has been made that the maximum bursting pressure occurs such that the vertical plane separating the upper and lower wedges is located such that there is no shear stress available along the base of the lower wedge. The most upstream location where no shear stress was available along the base of the lower wedge was determined using the following equation for the local FOS:

Local factor of safety for a vertical segment of height h_s:

$$FOS' = F_{\tau S}/F_{SH}$$

where: $$F_{\tau S} = [(\gamma_{sat} - \gamma_w)\, h_s\, w + F_{sv}]\, \tan\phi'$$

and where: $$F_{SV} = \gamma_w w h_s \cdot \sum_{h=1}^{h_s} iv_h \qquad F_{SH} = \gamma_w w h_s \cdot \sum_{h=1}^{h_s} ih_h$$

A series of trial values of ρ were then selected. These trial planes were drawn on a printout of the vertical and horizontal gradients. The average values of the horizontal and vertical gradients between the various trial values of ρ were determined. Between any two values of ρ the i_v and i_h were therefore in hand.

The other short sequence of data was obtained analytically; this was the area of the dam subtended by each pair of ρ values. The formulae for this area computation are given in Appendix 3-3. The effective weight associated with each subtended angle was adjusted if any portion of the dam was above the phreatic line. The vertical and horizontal gradients within the upper wedge between each pair of ρ angles were then weighted according to the saturated area described by these pairs of angles. The final bursting pressure was computed using:

$$P_a = \frac{\sin(\rho + \xi - \phi)}{\cos(2\phi - \rho)} F_B$$

As shown in column 22 of Table A-6(vii) the maximum horizontal component of P_a was 228 kN over a height of 4 m, for 1 m length of dam. A reinforcement strategy to counter this bursting force, together with the seepage force in the lower wedge, is given in Table A-6(vi).

Table A-6(vi)

Rebar Stresses for Reinforcement against Wedge Failure

1 Bar Elevation (m)	2 Weighting for each bar (%)	3 "P'" Force per bar (kN)	4 Lower Wedge Seepage Force (kN)	5 Max σ per bar (MPa)	6 σ per bar for minimum FOS = 2	7 Length (m)
0	30.0%	68.4	27.1	477.57	207.3	8.0
0.5	20.0%	45.6	18.1	318.38	138.2	8.0
1.0	10.0%	22.8	9.0	159.19	69.1	7.5
1.5	10.0%	22.8	9.0	159.19	69.1	7.5
2.0	10.0%	22.8	9.0	159.19	69.1	7.0
2.5	5.0%	11.4	4.5	79.60	34.5	7.0
3.0	5.0%	11.4	4.5	79.60	34.5	6.5
3.5	5.0%	11.4	4.5	79.60	34.5	6.0
4.0	5.0%	11.4	4.5	79.60	34.5	5.5
	Totals:	227.95	90.43 kN			

5. (col.3 + col.4)/($2 \cdot 10^{-4}$ m^2)
   Rebar X-sectional area 2 cm^2.
   Rebar spaced along L every 0.434 m.
6. Grade 60 #15M rebar, yield strength 414 MPa.
7. See Figure 5-22.

Application of Wedge Method to Prototype 1, N = 2

porosity: 0.39 α = 90.00° β = 33.69°

void ratio: 0.64 ϕ = 45.00° δ = 45.00° b_{tr} = 6 m

γ_{unsat}: 16.09 kN/m^3 γ_{sat}: 19.91 kN/m^3

1 Subtended angle (degrees)	2 Total cumulative area (m^2)	3 Subtended wet area (m^2)	4 Cumulative wet area (m^2)	5 Subtended dry area (m^2)	6 Cumulative dry area (m^2)	7 Total effective weight (kN)
90.0–71.6	3.43	3.43	3.43	0.00	0.00	34.72
71.6–55.3	10.29	6.86	10.29	0.00	0.00	104.15
55.3–45.0	24.00	13.71	24.00	0.00	0.00	242.91
45.0–37.5	68.75	35.50	59.50	0.00	0.00	779.24
37.5–35.3	90.47	14.97	74.47	11.00	11.00	1067.54
35.3–30.0	149.49	58.52	132.99	8.50	19.50	1667.89
				0.50	20.00	

8 Angle ρ (degrees)	9 Subtended horiz. gradient i_h	10 Subtended vertical gradient i_v	11 Areally weighted horiz. gradient i_h	12 Areally weighted vertical gradient i_v	13 Angle γ for Fq, (degrees)
71.56	0.61	0.10	0.61	0.10	9.31
55.30	0.62	0.06	0.61	0.07	6.50
45.00	0.60	0.08	0.60	0.08	7.26
37.50	0.48	0.14	0.53	0.11	12.11
35.30	0.39	0.13	0.50	0.12	13.21
30.00	0.39•	0.13•	0.42	0.13	17.33

•assumed gradients.

14 Fq·cosγ (kN)	15 Fq·sinγ (kN)	16 Fq (kN)	17 Horiz. component of Br (kN)	18 Vertical component of Br (kN)	19 Angle ξ (degrees)	20 $\lvert F_B \rvert$ (kN)	21 P_a (kN)	22 P' (kN)
20.48	3.36	20.75	20.48	38.07	28.28	43.2	37.3	26.34
61.91	7.05	62.31	61.91	111.20	29.11	127.3	98.3	69.49
141.77	18.06	142.91	141.77	260.97	28.51	297.0	200.5	141.77
309.27	66.36	316.31	309.27	845.60	20.09	900.4	322.4	227.95
366.42	86.00	376.37	366.42	1153.54	17.62	1210.3	288.7	204.13
541.45	168.97	567.21	541.45	1836.86	16.42	1915.0	95.2	67.30

Table A-6(vii) Computations for application of wedge method to prototype in worked example.

The extent of this reinforcement in the vertical is less than the amount implied by the analysis of possible rotational failure. The closer spacing along L of the rebar for the wedge method is due to a higher weighting on bars at lower elevations and to the more limited area over which anchoring is being applied for the results of the wedge method; namely, 1m by 4m high (unit L by $b_{tf}\tan\theta$, see Appendix 3-3). Although the relatively close spacing of the rebar indicated by the wedge method might be perceived as unfavourable, it should be kept in mind that classical rotational failure analyses gives *less* guidance regarding the placement of anchors than does the wedge method. It may be that the bars at high elevations (relative to the foundation) assumed for the rotational failure analysis make a much smaller contribution to preventing failure than was simply *assumed* (see the distribution of forces in column 3 of Table A-(v)). While the wedge method indicates a bursting pressure zone of height $b_{tf}\tan\theta$, rotational failure analysis indicates no particular limit as to the height of a 'bursting pressure'; the entire downstream face of the dam is simply considered to be 'in motion' in the event of a failure.

The different strategy for reinforcement determined using the wedge failure analysis raises the question of whether to design for rotational failure or wedge failure. This question cannot be answered categorically until further research is done on the true mechanism of slope failure in prototype flowthrough rockfill dams. Certainly if rotational failure is the true mechanism, the reinforcement implied by this mechanism takes precedence over that implied by wedge failure. However, laboratory tests (see Sections 5.2.2 and 5.2.3) showed that designing for rotational failure would probably be too conservative since experimentally measured bursting forces were always much less than the observed forces needed to prevent deep-seated failure in a number of model flowthrough rockfill dams.

By applying equations [2-47] and [5-16] it was found that the horizontal seepage force in the *lower* wedge was an additional 90.4 kN (see column 4 in Table A-6(vii)). This was added to the value of P′ of 228 kN, and the anchoring adjusted accordingly. However, it is noted that it is not known how much P′sinδ (=P′sinϕ) actually contributes to the frictional resistance along the base of the entire lower wedge, and

this probably reduces the net effect of the 90.4 kN force somewhat.

Finally, it is apparent that the maximum elevation of reinforcement against wedge failure does not cover the minimum elevation requiring coverage against *unravelling* failure. Figure 5-22(b) shows the layout of two types of reinforcement; the solid lines for prevention of wedge failure, the dashed lines for the anchors connected to the external mesh needed to prevent unravelling failure. As an added safety measure the protection against unravelling failure, the entire wetted face (up to elevation 12 m) is shown protected. The longest rebar length in Figure 5-22(b) is 8 m. This is considerably less than the lengths associated with the prevention of rotational failure.

Two final points can be made. First, there must be an upper limit for the spacing of bars. If the rebar is too widely spaced the mesh will fail in tension and will not transfer the bursting force to the rebar members. Secondly, the distribution (percent weightings shown in Tables A-6(v) and A-6(vi)) of the load is open to question. Finding rigourous answers to these questions was beyond the scope of this research, but both aspects clearly affect the nature of the reinforcement strategy selected.

8. Performance in subzero temperatures

a) Growth of ice at the phreatic surface.

The ice thickness I_T in mm was experimentally found to be related to the number of degree days Ψ according to (see Section 5.2):

$$I_T = 3.5 \sqrt{\Psi}$$

Assume the number of degree days below zero to be 120 days·10 C°= 1200. This yields an approximate ice thickness at the phreatic surface of 121 mm (4.8 inches) using the above equation. Should a major spring flood occur, this thickness would likely cause the entire flow to pass over, rather than through, the rockfill dam. (This assumes that the dam does not fail in a deep-seated rotation during this flood).

b) *Possibility of frazil ice formation.*

It is of interest to whether or not the heat lost from the water passing through this prototype dam dam is greater than the heat gained by the viscous dissipation of hydraulic energy. The heat gained by the viscous dissipation of hydraulic energy is:

$$q_v = 2.342\ Q \cdot \Delta h$$

where:

q_v = heat added due to viscous dissipation (kcal/sec),
Q = discharge (m^3/s),
Δh = drop in elevation, m (in this context, from upstream pool elevation to downstream pool elevation).
2.342 = constant to convert work in kgf-m to heat in kcal.

In order for frazil ice to form a net heat loss of about 31 langleys/hr or more is required, although this is not a well-substantiated threshold (Tsang 1982, p.23). The Q-BUDGET computer program provided could be used to determine the net heat transfer coefficient for a given set of weather conditions. However, for design purposes it will suffice to consider an unusually high rate of heat loss. According to T. Prowse (Primer on Ice Covered Rivers, unpublished), values of C_o typically vary between 25 and 60 $W/(m^2C^\circ)$ for conditions in Canada, with the latter associated with "extremely cold windy conditions". A value of 60 $W/(m^2-C^\circ)$ will be assumed.

i) *Heat lost to the environment.*

Heat transfer coefficient = 60 $W/(m^2-C^\circ)$
Assume $\Delta T = 30^\circ C$ (water at zero, air at $-30^\circ C$)
Rate of heat loss is therefore 1800 W/m^2, or 154.8 langleys/hr

A travel time for water passing through the dam is required.

From geometry, volume of water in dam = 20400 m^3 (L = 30 m)
Average time water is in dam is therefore:
(20400 m^3)/(109.8 m^3/s) = 185.8 seconds = 0.05 hours.

Heat loss = (154.77 langleys/hr)·(0.05 hours) = 7.99 langleys
= 79.88 $kcal/m^2$
(1 langley = 1 cal/cm^2)

In order to convert this to a quantity of heat, an area is required, through which the heat flux takes place. Using the governing non-Darcy

flow equation found in Part 2 of this worked example, and applying it to the hydraulic gradient at every finite difference (FD) node (as determined from the FD model of this prototype), the mean of the velocity computed at every FD node was found to be 0.2005 m/s.

Average distance travelled = (185.8 sec)(0.2005 m/s) = 37.25 m
Area for heat flux = 37.25·L = 37.25·30 = 1117.5 m^2

∴ Heat lost to the environment=(117.5m^2)(79.88 kcal/m^2)= $8.93 \cdot 10^4$ kcal

ii) *Heat added by the viscous dissipation of hydraulic energy.*

For Δh = 20 m, discharge = 109.9 m^3/s, q_v is 5143 kcal/sec.

Heat added per unit volume = (5143 kcal/sec)/(109.8 m^3/s) = 47 kcal/m^3

∴ Heat added = (47 kcal/m^3)(20400m^3) = $9.56 \cdot 10^5$ kcal

Ratio: (heat IN)/(heat OUT) = $(9.56 \cdot 10^5)(8.93 \cdot 10^4)$ = 10.7

In general it is therefore unlikely that a net heat loss from the body of water within the dam could occur such that freezing would take place spontaneously within a flowthrough rockfill dam.

This concludes the worked example.

Example input and output screens for program Q-BUDGET

INPUT SCREEN (interactive):

Program computes net heat flux from a body of water

Enter albedo of water surface (typical value is 0.1): 0.1

Enter cloud cover, a number between 0 (clear) and 10 (overcast): 5

Do you wish to change the value for shortwave insolation (presently set at 9.2 Langleys per hour) ? (y/n):n

Enter air temperature in degrees Celcius: -15

Enter relative humidity as a number between 0 and 100: 40

Enter elevation of cloud cover in meters: 2000

Enter wind speed at 2 m height in m/s: 0.5

Enter depth rate of snowfall in cm/hr: 0.25

Hit return after performing print screen.

OUTPUT SCREEN:

Summary of Results

(All heat fluxes in Langleys/hr unless otherwise noted)

Shortwave gain, Tsang: 5.423
Shortwave gain, Devik: 4.554
Net longwave loss: -8.460
Convective heat loss, Rimsha-Donchenko: -9.450
Convective heat loss, Tsang: -2.600
Evaporative heat loss, Tsang: -0.325
Evaporative heat loss, Rimsha-Donchenko: -1.130
Snowfall heat loss: -2.180

NET HEAT FLUX IN LANGLEYS PER HOUR IS: -12.40

NET HEAT FLUX IN WATTS PER SQUARE METER IS: -144.21

HEAT TRANSFER COEFFICIENT IN WATTS/SQUARE METER/CELCIUS DEGREE: 9.61

Do you wish to rerun the program ?

Appendix 7-2

Program Q-Budget for Estimating Heat Flux from a Body of Water

Written in Microsoft GW-BASIC version 1.0

```
1000 REM  The author makes no warranty or representation, either express or
          implied, with respect to this software, its quality, performance,
1050 REM  or fitness for a particular purpose.  This software is distributed
          "as-is" and you the user are assuming the entire risk as to its
1100 REM  quality and performance.  In no event will the authors be liable
          for direct, indirect, special, incidental, or consequential
1150 REM  damages arising out of the use or inability to use this software.
1200 CLS:KEY OFF
1250 REM  Written by David Hansen.
1300 PRINT:PRINT "Program computes net heat flux from a body of water."
1350 PRINT "-------------------------------------------------":PRINT
1400 INPUT "Enter albedo of water surface (typical value is 0.1): ",ALPHA
1450 PRINT
1500 INPUT "Enter cloud cover, a number between 0 (clear) and 10 (overcast):
",C
1550 PRINT:INSOL = 9.2
1600 INPUT "Do you wish to change the value for shortwave insolation
(presently set          at 9.2 langleys per hour) ? (y/n):",RR$
1650 IF RR$="y" OR RR$="Y" THEN 1800
1700 IF RR$="n" OR RR$="N" THEN 1850
1750 GOTO 1600
1800 PRINT:INPUT "Enter value for shortwave insolation in langleys per hour:
",INSOL
1850 PRINT
1900 INPUT "Enter air temperature in degrees Celsius: ",TAIR
1950 PRINT
2000 INPUT "Enter relative humidity as a number between 0 and 100: ",RH
2050 PRINT
2100 IF C=0 THEN 2250
2150 INPUT "Enter elevation of cloud cover in meters: ",H
2200 PRINT
2250 INPUT "Enter wind speed at 2 m height in m/s: ",VA2
2300 PRINT
2350 INPUT "Enter depth rate of snowfall in cm/hr: ",DRATE:PRINT
2400 INPUT "Hit return after performing print-screen.",ANY$:CLS
2450 PRINT:PRINT:PRINT "Summary of Results."
2500 PRINT "-------------------":PRINT "(All heat fluxes in Langleys/hr
unless otherwise noted.)":PRINT
2550 REM                    Tsang, equation 11, p. 13
2600 QSW1=INSOL*(1-ALPHA)*(.35+.061*(10-C)):PRINT "Shortwave gain, Tsang:
";QSW1
2650 REM                    Devik, eqn 13, p.14
2700 QSW2=INSOL*(1-ALPHA)*(1-9.000001E-02*C):PRINT "Shortwave gain, Devik:
";QSW2
2750 QSW=(QSW1+QSW2)/2
2800 LWOUT=-.97*4.879E-09*273.15^4
2850 REM   The eqn for ES following appears in Linsley, Kohler,
Paulhus, (1975) 2nd ed., page 35 , eqn. 2-5.
2900 ES=33.8639*((.00738*TAIR+.8072)^8-.000019*ABS(1.8*TAIR+48)+.001316)
```

```
2950 EA=ES*RH/100
3000 REM                A, eqn 18 p.16 Tsang.
3050 REM                B, eqn 19 p.16 Tsang.
3100 A=.74+.025*C*EXP(-.000192*H)
3150 B=.0049-.00054*C*EXP(-.000197*H)
3200 REM                LWINAIR, eqn 16, p.15 Tsang.
3250 LWINAIR=(.68+.036*EA)*4.789E-09*(TAIR+273)^4
3300 REM                LWINCLOUDS, eqn 17, p.16 Tsang.
3350 LWINCLOUDS=(A+B*EA)*4.879E-09*(TAIR+273)^4
3400 IF C=0 THEN NETLW=LWINAIR+LWOUT
3450 IF C>0 THEN NETLW=LWINCLOUDS+LWOUT
3500 PRINT "Net longwave loss: ";NETLW
3550 REM   RIMSHA-DONCHENKO EQUATION (eqn 26, p.20 Tsang)
3600 QCONV1=-(.33+.0146*(-TAIR)+.1625*VA2)*(-TAIR):PRINT "Convective heat
loss, Rimsha-Donchenko: ";QCONV1
3650 REM  Tsang eqn 25, p.19
3700 QCONV2=-(.08+.186*VA2)*(-TAIR):PRINT "Convective heat loss, Tsang:
";QCONV2
3750 QCONV=(QCONV1+QCONV2)/2
3800 REM                QEVAP1, TSANG, eqn 24, p.19 Tsang.
3850 QEVAP1=-(.131+.306*VA2)*(ES-EA):PRINT "Evaporative heat loss, Tsang:
";QEVAP1
3900 REM                QEVAP2, RIMSHA-DONCHENKO, eqn 27, p.20 Tsang.
3950 QEVAP2=-(.52+.02275*(-TAIR)+.253*VA2)*(ES-EA):PRINT "Evaporative heat
loss, Rimsha-Donchenko: ";QEVAP2
4000 QEVAP=(QEVAP1+QEVAP2)/2
4050 CS=.5:HL=79.7:RHO=.1:PS=RHO*DRATE
4100 QSN = -PS*(HL + CS*(-TAIR)):PRINT "Snowfall heat loss: ";QSN:PRINT
4150 SUMMATION=QSW+NETLW+QCONV+QEVAP+QSN
4200 SUMMATIONW=SUMMATION*11.63
4250 NETCO=SUMMATIONW/TAIR
4300 PRINT "-------------------------------------------------"
4350 PRINT USING "NET HEAT FLUX IN LANGLEYS PER HOUR IS:
####.##";SUMMATION:PRINT
4400 PRINT USING "NET HEAT FLUX IN WATTS PER SQUARE METER IS:
####.##";SUMMATIONW:PRINT
4450 PRINT USING "HEAT TRANSFER COEFFICIENT IN WATTS/SQUARE METER/CELCIUS
DEGREE: ###.##";NETCO:PRINT
4500 INPUT "Do you wish to rerun the program ";R$
4550 IF R$="Y" OR R$="y" THEN 1200
4600 REM  ********************************************************
4650 REM  *                                                      *
4700 REM  *  Equations used in this program were found in:        *
4750 REM  *                                                      *
4800 REM  *  Frazil and Anchor Ice - A Monograph                 *
4850 REM  *  by Gee Tsang, Ph.D.                                 *
4900 REM  *  NWRI CCIW Burlington, February 1982, 92 pp.         *
4950 REM  *                                                      *
5000 REM  ********************************************************
5050 REM
5100 END
```

Appendix 8

On Using a Spreadsheet for non-Darcy Pore Pressure Computations

Olsthoorn (1985) has pointed out that although the inventor of the electronic spreadsheet may have been seeking a better way to solve the accounting problems of the business world, the uses of this software have gone considerably beyond this application. For seepage problems the use of spreadsheets is efficient in terms of model development. The advantages include:

1. A combined visual presentation of the problem and its solution. A model is viewed and saved as a single file. This visual presentation of the problem is particularly advantageous when prescribing boundary conditions.

2. The ability to plot some of the results directly.

3. The absence of formal coding. Finite difference (FD) definitions such as those given by equations [2-38] and [5-20] through [5-22] are entered directly at the appropriate locations. Boundary conditions are entered next to the appropriate cells. When this has been done, the model development is complete and iterative relaxation of the grid can begin. No debugging of the logic is required because no formal computer language is used.

The main disadvantage of using a spreadsheet, particularly for large (3100 cells) non-linear flow problems of the type described here, is that the computational speed is poor. It was found that a 4.77 MHz 8088 computer with no numeric coprocessor required about 5 minutes to perform 1 relaxation of the grid, while a 80386 computer operating at 25 MHz with a 80387 numeric coprocessor required about 11 seconds to perform the same task. Resolving the grids associated with Tests 1 and 2 in this study required about 5300 and 22000 relaxations of the grid, respectively. For 5000 relaxations, about 17 days of continuous operation would be needed for an ordinary 8088 PC, but only about 15 hours of operation on a 80386 desktop computer with an 80387 numeric coprocessor.

Although *developing* spreadsheets to solve te FD problems described in Section 5.2.1 was less time consuming than writing FORTRAN code, the following points are important to note in the development of a worksheet of this type:

1. The spreadsheet used had a limit of 239 characters for the definition of a single cell (or node). In order to fit equation [2-38] into a single cell, values for T1 and T2 must be placed in fixed locations and absolute references to these fixed locations must be used.

2. When building the worksheet, cells defined with a FD formula should not be moved using the MOVE command. If this is done the result will be a FD definition in which some of the connections between nodes are of incorrect length. Instead of moving cells it is necessary to COPY the cell to the new location and then erase the definition in the old location.

3. If ERR (indicating "error") appears in a given cell, it should be erased before proceeding with model development. This is because if the command to iterate is inadvertently given, the ERR message for a single cell will propagate to every node defining the embankment. If this happens the numerical model has been destroyed. There appears to be no remedy for this once it has happened so that the zone containing FD definitions will have to be completely redeveloped. Equation [2-38] is more prone to ERR appearing and propagating than equation [2-36] because of the possibility of either division by zero or raising a negative number to a fractional power in equation [2-38]. It is therefore prudent to keep a statement of equation [2-38] in a safe location in the worksheet by surrounding a single node so defined by nine arbitrary numbers which give a non-ERR answer.

An efficient way to "build" the embankment within the worksheet is to enter all boundary conditions and the Darcy FD layer first, and then use the programmable keystroke feature (a so-called "macro") to fill in the interior. One such macro used was:

'/C~{R}.{END}{R}{L}~

The above macro copies a single definition, such as that given by equation [2-38], into the width of the FD field.

The following macro was used to check the convergence of the numerical scheme:

+AQ47~RV~~{D}
[CALC]
+AQ47~RV~~{D}
[CALC]

etc.

The file size for tests GF25 and GF26 was about 700 Kb each. Once convergence was achieved the entire worksheet was converted from formula definitions to numerical values. This resulted in a file about one seventh the size of the original file. This numbers-only file was much faster to load and analyse than the file containing formulae definitions.

The electronic spreadsheet was found to be an efficient tool for solving a number of FD equations by the relaxation method. Hydraulic gradients arising from computed piezometric heads were readily determined. However the computational requirements of such a model are such that the use of a state-of-the art desktop computer was the only reasonably efficient way to achieve a solution. Temporarily seeding the FD grid area with fixed values was found to assist in achieving a more rapid solution.